

Calculation of Coupled Bunch Effects in the Synchrotron Light Source BESSY VSR

DISSERTATION

zur Erlangung des akademischen Grades

doctor rerum naturalium
(Dr. rer. nat.)

im Fach Physik
Spezialisierung: Experimentalphysik

eingereicht an der
Mathematisch-Naturwissenschaftlichen Fakultät
der Humboldt-Universität zu Berlin

von
Dipl.-Phys. Martin Ruprecht

Präsident der Humboldt-Universität zu Berlin:
Prof. Dr. Jan-Hendrik Olbertz

Dekan der Mathematisch-Naturwissenschaftlichen Fakultät:
Prof. Dr. Elmar Kulke

Gutachter: 1. Prof. Dr. Andreas Jankowiak
 2. Prof. Dr. Jens Knobloch
 3. Prof. Dr. Riccardo Bartolini

Tag der mündlichen Prüfung: 22.02.2016

Abstract

In the last decades, accelerator based synchrotron radiation (SR) has become a central tool for spectroscopic and structural imaging of samples for a wide range of scientific fields, including solid state physics, life science and information technology. The increasing demand for high brilliance and short pulse length is continuously leading to the upgrade or new construction of SR facilities, among which BESSY Variable Pulse Length Storage Ring (BESSY VSR) is the upgrade project for the third generation light source BESSY II, located at Helmholtz-Zentrum Berlin für Materialien und Energie GmbH (HZB), Germany. It will provide a previously uncovered time regime of intense ps bunches in a multi-user facility, achieved by the novel concept of utilizing super conducting (SC) multi-cell cavities. New technological and accelerator physical challenges need to be addressed. This includes coupled bunch effects, a beam-cavity interaction that causes coupled bunch instabilities (CBIs) and transient beam loading. The former are transverse or longitudinal bunch oscillations that spoil the beam quality and the latter is a steady distortion of the longitudinal dynamics, introduced by unevenness in the bunch fill pattern affecting the bunch length and synchronous phase.

In the scope of this thesis, the strength of CBIs driven by longitudinal monopole higher order modes (HOMs) and transverse dipole and quadrupole HOMs is evaluated for BESSY VSR, based on analytic calculations and tracking simulations, and compared to the performance of an active bunch-by-bunch feedback (BBFB). Algorithms for tracking codes are derived, and a semi-empirical formula for the estimation of transverse quadrupole CBIs is presented. CBI studies are an integral part of the benchmarking of the cavity models for BESSY VSR and have been accompanying and influencing their entire design process. Based on the BESSY VSR cavity model with highly advanced HOM damping, beam stability is likely to be reached with a BBFB system, independent of the bunch fill pattern. Additionally, measurements of CBIs have been performed at BESSY II and the Metrology Light Source of the Physikalisch-Technische Bundesanstalt (MLS), where the longitudinal long range impedance was characterized.

Transient beam loading is evaluated by means of analytic formulas and new experimentally verified tracking codes. For the baseline bunch fill pattern of BESSY VSR, it is shown that the particular setup of cavity frequencies amplifies the transient effect on the long bunch, limiting its elongation and potentially resulting in increased Touschek losses, which has already triggered studies regarding alternative bunch fill pattern.

Keywords: collective effects, coupled bunch instabilities, short bunches, synchrotron light source, transient beam loading

Zusammenfassung

Von Elektronenbeschleunigern erzeugte Synchrotronstrahlung hat sich in den letzten Jahrzehnten zu einem zentralen Werkzeug für spektroskopische und strukturelle Analysen in vielen Wissenschaftsbereichen entwickelt, einschließlich Festkörperphysik, Lebenswissenschaften, und Informationstechnologie. Der steigende Bedarf nach hoher Brillanz und kurzen Pulsen führt zum Um- und Neubau von Synchrotronstrahlungsquellen. BESSY Variable Pulse Length Storage Ring (BESSY VSR) ist das Ausbauprojekt von BESSY II, einer Synchrotronstrahlungsquelle der dritten Generation des Helmholtz-Zentrum Berlin für Materialien und Energie GmbH (HZB) in Deutschland. Durch den neuartigen Einsatz von supraleitenden mehrzelligen Hohlraumresonatoren wird es intensive Elektronenpakete (Bunche) in einem bisher nicht abgedeckten Picosekundenzeitbereich bieten. Neue technologische und beschleunigerphysikalische Herausforderungen müssen darin adressiert werden, einschließlich der gekoppelten Effekte auf Elektronenpakete. Ursprung des obigen Effekts ist die Strahl-Hohlraumresonator-Wechselwirkung, die zu einer Multibunch-Instabilität (MBI) führen kann, bei der longitudinale oder transversale Elektronenpaketoszillationen die Strahlqualität zerstören. Außerdem kann sie bei Variationen in der Speicherringfüllung zu transientser Strahllast (engl. beam loading) führen, welche die Länge und synchrone Phase der Elektronenpakete stört.

Im Rahmen dieser Dissertation wird die Stärke der MBI, die von longitudinalen Dipol-, transversalen Dipol- und Quadrupolschwingungsmoden höherer Ordnung getrieben werden mithilfe von analytischen Rechnungen und Trackingsimulationen untersucht und mit dem vorhanden aktiven Dämpfungssystem verglichen. Algorithmen für Trackingsimulationen werden hergeleitet und eine halbempirische Formel zur Abschätzung der transversalen quadrupolaren MBI wird präsentiert. MBI Studien bilden einen wesentlichen Teil der Beurteilung der BESSY VSR Hohlraumresonatoren und begleiteten und beeinflussten ihren Entwicklungsprozess. Mit Berechnungen auf Grundlage des neusten BESSY VSR Hohlraumresonatormodels kann Strahlstabilität als wahrscheinlich und unabhängig vom Füllmuster angesehen werden. Des weiteren wurden Messungen der MBI an BESSY II und der Metrology Light Source (MLS) der Physikalisch-Technischen Bundesanstalt durchgeführt, bei welcher die longitudinale langreichende Impedanz charakterisiert wurde.

Transiente Strahllast wird in dieser Arbeit mit analytischen Formeln und neuen, experimentell überprüften Trackingsimulationen berechnet. Für das Standardfüllmuster von BESSY VSR wurde gezeigt, dass die besondere Konfiguration der Hohlraumresonatorfrequenzen zu einer relativ starken Beeinflussung der langen Elektronenpakete führt. Diese verkürzt das Elektronenpaket und vergrößert die Touschekverluste, was bereits Studien bezüglich alternativen Füllmustern anstieß.

Schlagwörter: Kollektive Effekte, Kurze Elektronenpakete, Multibunch-Instabilitäten, Synchrotronstrahlungsquelle, Transiente Strahllast

Contents

Abstract	iii
Zusammenfassung	v
List of Abbreviations	ix
List of Symbols	xi
1. Introduction	1
1.1. Synchrotron Radiation	1
1.2. BESSY II	4
1.3. BESSY VSR	9
1.4. Coupled Bunch Effects in BESSY VSR	13
1.5. Motivation of this Thesis	15
2. Theory of Coupled Bunch Instabilities	17
2.1. Wakes and Impedances	17
2.2. Higher Order Modes in Cavities	25
2.3. Longitudinal Bunch Motion for Even fill	26
2.4. Longitudinal Bunch Motion for Uneven Fill	34
2.5. Longitudinal Landau Damping	35
2.6. Transverse Bunch Motion	37
3. Tracking Codes for Coupled Bunch Effects	43
3.1. Beam Interaction with Resonator Impedances	43
3.2. Implementations in Tracking Codes	49
3.3. General CBI Findings Obtained from Tracking Codes	51
4. Observation of Coupled Bunch Instabilities	59
4.1. Bunch-by-Bunch Feedback Systems	59
4.2. Methods and Example Measurements at the MLS	63
4.3. Measurements of Longitudinal CBMs at the MLS	73
4.4. Measurements at BESSY II	76

5. Predictions of Coupled Bunch Instabilities for BESSY VSR	79
5.1. Threshold Impedance	79
5.2. Uncertainty of HOM Frequencies	86
5.3. Fill Pattern Dependency	94
5.4. Low- α Operation	104
5.5. Instabilities Driven by Fundamental Modes	105
5.6. Booster Synchrotron	106
6. Transient Beam Loading	109
6.1. Definition and Methods of Calculation	109
6.2. Experiments at BESSY II	116
6.3. Predictions for BESSY VSR	122
7. Conclusion	131
A. Appendix	133
A.1. Transverse Moments in Cartesian Coordinates	133
A.2. Longitudinal Higher Order Motion	134
A.3. Principle of Phasor Addition	135
A.4. Minimal Demonstrative Tracking Code	136
A.5. Justification of Margin a in the Statistical Approach	137
A.6. Quality Factor Measurements of Landau cavities at BESSY II	138
References	141
Acknowledgment	151

List of Abbreviations

ADC	analog-to-digital converter, 60
BBFB	bunch-by-bunch feedback, iii, 41, 57, 59–65, 69, 72–74, 76–82, 84, 85, 91–93, 106, 108, 118, 127–129, 131, 132, 135
BESSY VSR	BESSY Variable Pulse Length Storage Ring, iii, v, 1, 3, 4, 6, 8–13, 15–18, 25, 26, 33, 41, 50, 58, 59, 62, 77, 79, 80, 82, 84–86, 88, 92, 94, 95, 99, 102, 104–106, 109, 115, 122–125, 127–129, 131, 132, 134, 137
BPM	beam position monitor, 59, 60, 72
CBI	coupled bunch instability, iii, 14, 16, 17, 26, 29–31, 34, 37–41, 43, 50, 51, 54, 57–59, 61, 63, 66, 68, 73, 76–79, 81, 82, 84–86, 88, 94, 104–108, 131, 132
CBM	coupled bunch mode, 28, 29, 31–34, 38, 63, 64, 68–79, 86, 88, 94, 95, 98, 101–103, 105
cdf	cumulative distribution function, 87, 88, 90–93
CSR	coherent synchrotron radiation, 3, 8, 10
CW	continous wave, 15
DBA	double bend achromat, 6, 83
EFEM	even fill eigen mode, 28, 34, 70
ERL	energy recovery linac, 3, 40, 86, 92
FEL	free-electron laser, 3
FIR	finite impulse response, 60
FPGA	field-programmable gate array, 60
HOM	higher order mode, iii, 14–17, 23, 24, 26, 30, 31, 34–41, 43, 50, 51, 54–59, 76, 79–82, 85–94, 99, 104, 106, 108, 127, 131, 132, 134, 135, 137, 138
HZB	Helmholtz-Zentrum Berlin für Materialien und Energie GmbH, iii, v, 3, 4, 80, 102, 103, 151
ID	insertion device, 2, 5–7
l.h.s.	left hand side, 20, 30, 37, 75
linac	linear particle accelerator, 3, 4
MLS	Metrology Light Source of the Physikalisch-Technische Bundesanstalt, iii, 2, 59, 63, 64, 66–69, 72–76, 151
NC	normal conducting, 10, 11, 106, 108
pdf	probability density function, 88
pmf	probability mass function, 87, 88

List of Abbreviations

r.h.s.	right hand side, 20, 28, 30, 36, 44, 74, 127
RF	radio frequency, 6, 9–11, 13, 14, 16, 21, 25, 33, 60, 64, 76, 79, 105–108, 115, 120, 121, 151
rms	root mean square, 6, 8, 14, 39, 82, 85, 126, 134
SC	super conducting, iii, 6, 7, 9–11, 13, 15–17, 33, 79, 83, 84, 86, 104–106, 122, 123, 131, 132, 137
SPM	same passband mode, 24, 26, 57, 58, 81, 85, 92, 131
SR	synchrotron radiation, iii, 1–3, 6, 8–10, 15

List of Symbols

Sym.	Description	Unit	Page List
A_{lm}	Matrix whose eigenvalues give the coherent frequencies for uneven fill	s^{-1}	34, 35, 40, 95–97, 99, 100
A	Amplitude of phasor at last bunch passage	V	45
$c\Delta\vec{p}_m^\perp$	Transverse m -th order wake potential	eV	19–21
$c\Delta\vec{p}$	Wake potential	eV	19, 43
$c\Delta p_m^\parallel$	Longitudinal m -th order wake potential	eV	19–21
c	Speed of light	ms^{-1}	21–23, 38, 39, 44, 48, 49, 55, 57
d	Dispersion function used in Landau theory	$V rad s^{-1}$	35, 36, 126, 127
E	Electron energy	eV	6, 8, 28, 30, 32, 34, 35, 37–41, 55, 57, 58, 64, 74, 79, 80, 83, 107
e	Elementary charge	C	8, 20, 21, 28, 30, 32, 34, 35, 37–41, 43, 55, 57, 58, 74, 79, 80
f_{beam}	Frequency of a beam harmonic close to the phenomenon of interest	Hz	32, 33
f_{rev}	Beam revolution frequency	Hz	6, 8, 31, 33, 57, 58, 64, 72, 74, 75, 88–90, 92, 94, 96, 106, 107, 110
Δf_r	Detuning w. r. t. a beam harmonic	Hz	11, 32, 33, 46, 111
f_r	Resonance frequency	Hz	8, 32, 51, 75, 76, 89, 90, 92, 134, 139
f_s	Unperturbed synchrotron frequency	Hz	6, 8, 62, 64, 72, 74, 75, 83, 102, 104, 106–108, 118, 126–128

List of Symbols

Sym.	Description	Unit	Page List
\vec{F}	Force of the electromagnetic fields	N	19, 43
I_{DC}	Average (DC) beam current	A	5, 6, 11, 28, 30, 32, 34–41, 55, 57, 58, 64, 76, 79, 80, 83, 107, 110, 127, 129
I_{thr}	Threshold current of bursting instability	A	9
i_k	Current stored in the k -th bunch	A	34, 111, 113–115
I_p	p -th element of the complex beam spectrum	A	34, 94, 95, 110–112
L	A distance much longer than the extension of the localized source of the wake	m	19, 43
M_1	Transverse dipole moment of the beam	m	21, 48
M_2	Transverse quadrupole moment of the beam	m ²	21, 41, 49, 53, 55, 80–82
M_m	Transverse m -th moment of the beam	m ^{m}	17, 18, 20, 21, 133, 134
M	Number of buckets	1	26, 28–32, 34–36, 38–40, 57, 63, 68, 72, 75, 94, 96, 110, 111, 113, 127
P_{diss}	Dissipated power in resonator	W	25
Q_x	Horizontal betatron tune	1	6, 39
Q_y	Vertical betatron tune	1	6
Q	Quality factor of resonator	1	6, 11, 22–25, 44–46, 48–52, 55–58, 85, 90, 92, 99, 110, 111, 116, 120, 122, 131, 135, 139
q	Bunch charge	C	20, 21, 44–46, 48, 49, 55
R_a	Shunt impedance in accelerator definition	Ω	25
R_s	Shunt impedance in circuit def.	Ω	25, 89, 90
$R_{s,0}$	$m = 0$ shunt impedance in circuit def.	Ω	6, 11, 25, 36, 44, 46, 56–58, 75, 76, 90, 105, 110, 111, 116, 120, 122, 129, 135
$R_{s,1}$	$m = 1$ shunt impedance in circuit def.	Ωm^{-2}	25, 48, 51, 56–58, 90

Sym.	Description	Unit	Page List
$R_{s,2}$	$m = 2$ shunt impedance in circuit def.	Ωm^{-4}	49, 51, 55, 56
$R_{s,m}$	m -th order shunt impedance in circuit def.	Ωm^{-2m}	21–24, 27
t_{last}	Time at last bunch passage	s	45, 47
T_{rev}	Beam revolution period	s	35
Δt_k	Arrival time difference of k -th bunch w.r. t. its nominal bucket position	s	114
Δt	Bunch arrival time difference w.r. t. its nominal bucket position	s	116–118
U	Energy stored in the resonator field	J	24, 25
$\vec{V}_{\text{acc}}^{\perp}$	Effective transverse accelerating voltage	V	25, 48, 49, 55
\vec{V}_{acc}	Effective accelerating voltage	V	43
V'	Time derivative of the effective accelerating voltage	Vs^{-1}	8, 9, 12, 15, 45, 118, 124
$V_{\text{acc}}^{\parallel}$	Effective longitudinal accelerating voltage	V	8, 24, 25, 44, 45, 47–49, 116, 120
V_{op}	Operating voltage of a cavity	V	8
V	Complex voltage phasor	V	45–49, 55, 135
W'_0	Longitudinal $m = 0$ wake function	VC^{-1}	21, 26, 44, 45
W'_1	Longitudinal $m = 1$ wake function	$\text{VC}^{-1}\text{m}^{-2}$	21
W_1	Transverse $m = 1$ wake function	$\text{VC}^{-1}\text{m}^{-1}$	21
W'_m	Longitudinal m -th order wake function	$\text{VC}^{-1}\text{m}^{-2m}$	20, 21, 23
W_m	Transverse m -th order wake function	$\text{VC}^{-1}\text{m}^{-2m+1}$	19–21, 23
Z_0^{\parallel}	Longitudinal $m = 0$ impedance	Ω	28, 30, 32, 34–37, 74–76, 90, 94, 110, 111, 127, 134
Z_1^{\perp}	Transverse $m = 1$ impedance	Ωm^{-1}	38–40
Z_2^{\perp}	Transverse $m = 2$ impedance	Ωm^{-3}	41, 55
$Z_{\text{th}}^{\parallel}$	Longitudinal threshold impedance	Ω	79, 80, 90
Z_{th}^{\perp}	Transverse $m = 1$ threshold impedance	Ωm^{-1}	79, 80, 90
Z_{th}	Threshold impedance	see text	89, 90
Z_m^{\parallel}	Longitudinal m -th order impedance	Ωm^{-2m}	21, 22
Z_m^{\perp}	Transverse m -th order impedance	Ωm^{-2m+1}	21, 22
$Z_{2,\text{th}}^{\perp}$	Transverse $m = 2$ threshold impedance	Ωm^{-1}	80–82
Z_{lm}	Longitudinal mode-coupling impedance	Ω	34, 94–96
Z_l^{\perp}	Transverse mode-coupling impedance	Ωm^{-1}	40, 99

List of Symbols

Sym.	Description	Unit	Page List
α	Momentum compaction factor	1	6–9, 11, 28, 30, 32–35, 37, 39, 57, 64, 72–74, 79, 83, 104, 105, 107, 108, 131, 137
β	Value of the betatron function (horizontal or vertical) at the localized impedance	m	6, 7, 38, 40, 41, 55, 57, 58, 79, 80, 82–84, 104, 105, 107
γ	Lorentz factor	1	1
δ	Relative momentum deviation	1	39
δ_0	Relative natural energy spread	1	6, 8
δ_n	Dissipative damping rate	s^{-1}	35–37, 127
ϵ_x	Horizontal emittance	nm rad	6, 82
ϵ_y	Vertical emittance	nm rad	6
λ_μ	Eigenvalue of CBM μ	rad s^{-1}	34, 40
μ	CBM index	1	28, 30–34, 38, 39, 72–76
$\tilde{\mu}$	Condensed machine parameter	$V^{-1}s^{-1}$	35–37, 127
ξ	Chromaticity (horizontal or vertical)	1	39
σ	Bunch length	s	14, 39, 134
σ_0	Zero current bunch length	s	6, 8, 124
τ^{-1}	Growth rate	s^{-1}	32, 36, 37, 41, 55, 57, 58, 74, 86, 134, 135
τ_d^{-1}	Damping rate	s^{-1}	79, 80, 84
τ_{fb}^{-1}	Damping rate of the bunch-by-bunch feedback system (longitudinal or transverse)	s^{-1}	77, 78, 80, 82, 91, 93, 108, 127
τ_μ^{-1}	Growth rate of CBM μ	s^{-1}	29, 30, 34, 38, 40, 70, 104
τ_c	Characteristic fill time of a cavity	s	56–58, 116
$\tau_{ }$	Longitudinal radiation damping time	s	6, 64, 74, 107, 118, 122
τ_{\perp}	Transverse radiation damping time	s	6, 64, 81, 82, 107
ϕ	Phase of phasor at last bunch passage	rad	45
$\Delta\omega$	(Real) angular frequency shift	rad s^{-1}	32
$\Delta\omega_\mu$	(Real) angular frequency shift of CBM μ	rad s^{-1}	29, 30, 34, 38, 40
$\Delta\omega_\xi$	Chromatic betatron angular frequency shift	rad s^{-1}	39

Sym.	Description	Unit	Page List
Ω	Complex coherent angular frequency of synchrotron or betatron oscillation	rad s^{-1}	28, 34–37, 40, 126, 127
ω_β	Angular betatron frequency (horizontal or vertical)	rad s^{-1}	37–41
ω_{beam}	Angular frequency of a beam harmonic close to the phenomenon of interest	rad s^{-1}	32, 35–37, 41, 110, 127, 129
ω_{rev}	Angular beam revolution frequency	rad s^{-1}	28, 30–32, 34, 37–41, 55, 57, 58, 79, 80, 83, 94
ω_r	Angular resonance frequency	rad s^{-1}	22–25, 44–46, 48, 49, 55, 57, 58, 90, 110, 114, 116, 134, 135
ω_{sq}	Unperturbed angular synchrotron frequency of bunch q	rad s^{-1}	35, 36, 127
ω_s	Unperturbed angular synchrotron frequency	rad s^{-1}	26, 28–32, 34, 36, 37, 57, 79
ω_μ	Complex coherent angular frequency of CBM μ	rad s^{-1}	28–30, 34, 38–40
ω_p	Angular frequency of the p -th revolution harmonic	rad s^{-1}	110–113

1. Introduction

The first section of this chapter, Section 1.1, shortly introduces synchrotron radiation, accelerator based sources and its relevance for the scientific community.

After that, the BESSY II [1] storage ring and the concept of BESSY Variable Pulse Length Storage Ring (BESSY VSR) [2] are described in Sections 1.2 and 1.3 alongside an introduction to selected aspects of beam dynamics, necessary to follow the discussions in this thesis.

Finally, the specific topic of coupled bunch effects is introduced in Section 1.4, and its particular importance for BESSY VSR is highlighted, leading to the motivation of this thesis.

1.1. Synchrotron Radiation

Synchrotron radiation (SR) is the electromagnetic radiation emitted by ultra-relativistic charged particles when they are accelerated perpendicular to their trajectory. For instance, relativistic electrons passing through magnetic fields will generate SR.

Due to the Lorentz boost from the ultra-relativistic electrons to the laboratory frame, the SR is shifted to high photon energies and is radiated in a cone directed forward parallel to the momentary velocity vector of the electrons with a half opening-angle of $\theta \approx 1/\gamma$, inversely proportional to the Lorentz factor γ . In typical synchrotron light sources with electron energies in order of 1 GeV to 10 GeV, the SR is a highly collimated photon beam with a small divergence and small source size defined by the properties of the electron beam. The energy spectrum of the SR created in a bending magnet is continuous with its maximum at a photon energy in the order of a few keV, depending on the electron energy and the magnetic field.

Since its first observation in 1947 [3], SR has become an increasingly demanded and indispensable tool for a wide range of scientific communities. At present SR facilities, the SR is used from THz radiation up to hard x-ray photons in the order of 100 keV for a large variety of experiments, where the interaction of the photons with the sample matter reveals its properties that are otherwise inaccessible.

The scientific questions addressed with the experiments with SR cover many of the grand scientific and societal challenges of mankind, including energy technologies, environmental remediation, climate change, information technology, material science, chemistry, biology and medicine [4]. More specifically, spectroscopic and structural imaging

1. Introduction

of nanoscale regions of homogeneous or inhomogeneous materials can be performed with nm spatial resolution and the temporal evolution of electrons, spins, atoms and chemical reactions can be studied down to the fs range [4]. For instance, modern molecular biology would not exist without the high-throughput determination of the structures of proteins by x-ray crystallography performed at SR facilities [4]. Additionally, SR can serve as a primary source standard, as done for example at the Metrology Light Source of the Physikalisch-Technische Bundesanstalt (MLS) [5].

The SR used for experiments is produced in bending magnets or insertion devices (IDs). An ID consists of a series of alternatingly oriented magnets that force the beam on an undulated path where the emitted SR can coherently interact leading to an intense photon beam. Depending on the field strength and period length of the magnets, an ID may be called undulator, wiggler or wavelength shifter. In the former, the emitted synchrotron radiation is monochromatic, otherwise, a continuous spectrum is found, similar as produced by bending magnets.

Depending on the particular experiment, important figures of merit of the SR include photon flux, brightness, i. e., flux per solid angle, brilliance, i. e., brightness per spot size, coherence and the time structure of the pulsed photon beams.

The first experiments with SR were performed parasitically at electron or positron storage rings dedicated for high energy physics. They are called first generation light sources.

The second generation synchrotron light sources are electron or positron storage rings dedicated for the generation and usage of SR with the first being Tantalus [6].

As the demand of the users of SR continuously increases in terms of the quality of the photon beam, the third generation synchrotron light sources were optimized to deliver a much smaller beam emittance, i. e., transverse beam size and divergence, leading to higher brilliance and are designed to provide space for many IDs. The bunch length in third generation synchrotron light sources is typically in the order of 10 ps to 100 ps. BESSY II is a typical third generation synchrotron light with a focus primarily on the soft x-ray regime.

Presently, the development in accelerator based light sources continues in three directions.

First, improvements of the electron storage ring based light sources are emerging, considered as an enhanced third generation where recent technological advances are utilized and well established schemes are optimized, leading to a reduction of the emittance by about one to two orders of magnitude [7], with the MAX IV 3.0 GeV storage ring [8] the first of its kind. The trend is towards the so called diffraction limited light sources, where an additional reduction of the beam emittance no longer increases the brilliance of the photon beam as the beam emittance is in the same order as the intrinsic photon emittance given by the diffraction limit at the desired photon energy. However, in the present schemes of this kind, the longitudinal dynamics is affected in a sense that it is more difficult to achieve a short bunch length.

Second, free-electron lasers (FELs) [9] are another class of accelerator based sources for SR, basically consisting of a linear particle accelerator (linac) and a section with a long undulator. A strong enhancement in the emitted SR is obtained by the fact that the emitted photons at the beginning of the undulator modulate the substructure of the electron bunch, which in turn causes it to radiate coherently, i.e., with a power proportional to the square of the number of electrons. In addition, the electrons are used only for a single pass, i.e., the beam properties are mainly defined by the source. Thus, the photon beam produced in FELs has a very high peak brilliance and additionally, its pulse length can be as short as a few fs which is far below the typical bunch length of third generation light sources. As the beam is dumped at the end of the undulator, it is impossible to sustain a high average current at high energies, thus the repetition rate of FELs is usually several orders of magnitude below a storage ring based facility. Furthermore, the light from a FEL can only be delivered to one user at a time. The much larger need for accelerating structures, the low repetition rate and the limitation to one experiment at a time causes FEL experiments to be much more expensive than experiments at a storage ring based facility. FELs are presently available and considered complementary to third generation light sources.

Third, the concept of energy recovery linacs (ERLs) [10] is becoming increasingly recognized. In a simplified manner, it combines the single pass advantages of an FEL with the energy efficiency of storage rings. This is achieved by decelerating the beam before it is dumped and simultaneously transferring its energy to other electrons that are being accelerated. Thus, the electrons are exchanged each turn but the energy is reused. ERLs are presently still in a phase of development, for instance, the test facility bERLin-Pro [11] is currently under construction at the Helmholtz-Zentrum Berlin für Materialien und Energie GmbH (HZB), Berlin, Germany.

Apart from enhanced brilliance by means of emittance, the temporal structure of SR is gaining increasing interest, both in the regime of shortest pulses produced by FELs as well as in the intermediate regime, from a few 100 fs to a few ps seconds range [12, 13]. In addition, the short pulses at storage rings are used as a source for THz radiation as the bunches emit coherent synchrotron radiation (CSR) up to a frequency inversely proportional to their length, reaching to higher frequencies with shorter bunches.

The project BESSY VSR intends to satisfy demands for intense short pulses in a regime which is presently unoccupied in terms of repetition rate and pulse length, see Fig. 1.1, by providing short pulses in the standard user operation of a third generation light source.

A similar project is discussed in [14] along with alternative options to produce short pulses of SR at third generation light sources, for example [15–17]. A method that is successfully operated since several years at a number of light sources is the laser-slicing [18]. However, the latter can only provide limited pulse intensities at low repetition rates.

1. Introduction

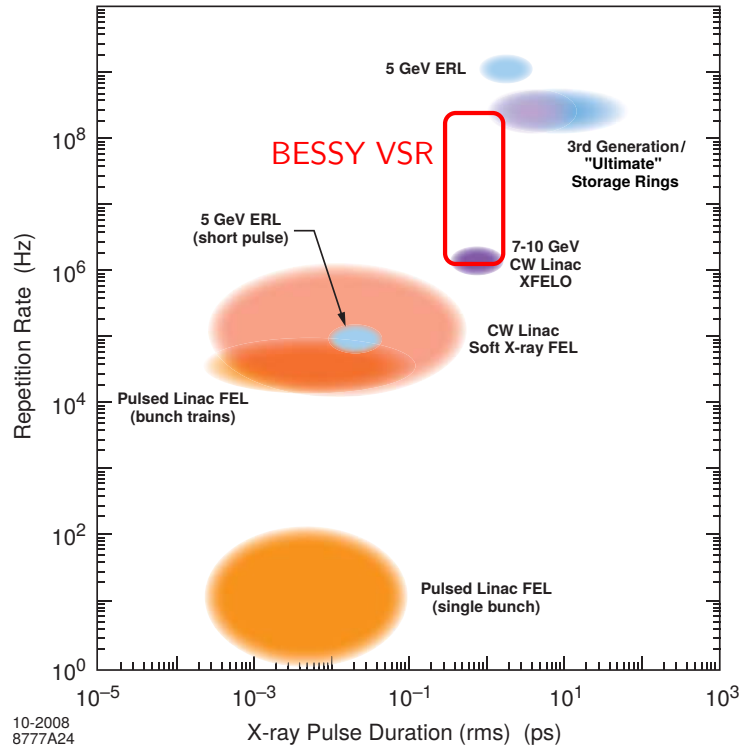


Figure 1.1.: Approximate performance range of BESSY VSR in comparison to present and future synchrotron radiation facilities in terms of repetition rate and pulse duration. Figure extracted from [12] and modified.

1.2. BESSY II

BESSY II [1] is a third generation synchrotron light source located at the HZB, Berlin, Germany, which is in user operation since 1998. The drawing of the storage ring along with the booster synchrotron and the experimental hall is shown Fig. 1.2 and a summary of basic machine parameters is given in Tab. 1.1.

At the very beginning of the process of acceleration, the electrons are emitted from a cathode in the electron gun and accelerated to a kinetic energy of 90 keV [20]. From the electron gun, they enter the linac where they are accelerated to 50 MeV and transferred to the booster synchrotron, see Fig. 1.2.

The booster synchrotron serves the purpose of accelerating the electrons to the final energy of 1.7 GeV. Its magnets are wired in a “White circuit” [21] allowing for resonant oscillations between a state suitable for the injection energy of 50 MeV and a state for high energy somewhat above the needed 1.7 GeV. At 1.7 GeV, the electrons are extracted from the booster and transferred to the storage ring.

In the storage ring, the electrons of each booster cycle are accumulated until the nominal

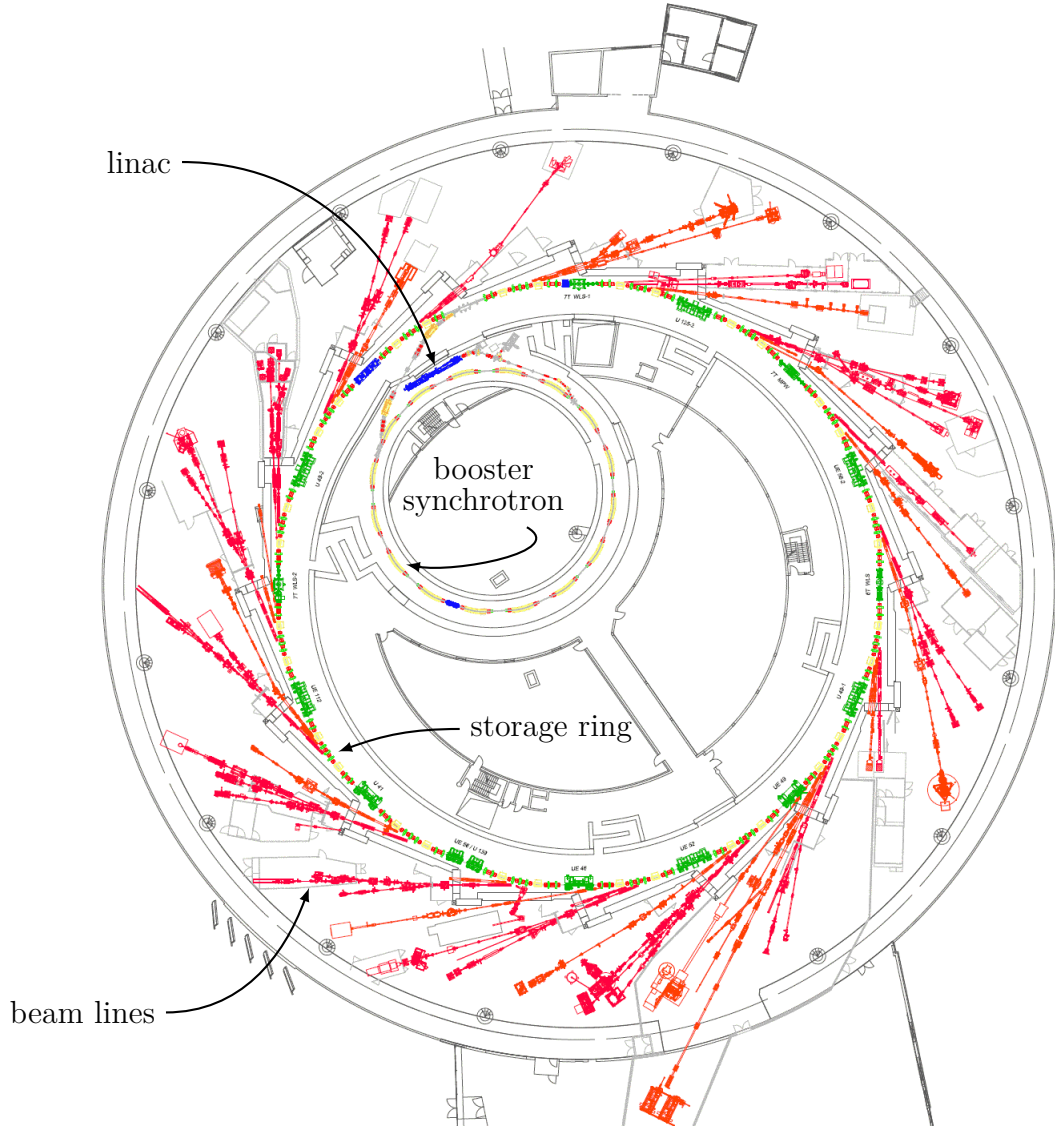


Figure 1.2.: Floor plan of the synchrotron light source BESSY II with the linac, the booster synchrotron, the 1.7 GeV electron storage ring and its beam lines stretching tangentially outwards into the experimental hall. Bending magnets are colored yellow, quadrupole magnets red, sextupole magnets green, cavity structures blue and IDs are dark green.

current of $I_{DC} = 300 \text{ mA}$ is reached. After that, electrons are only injected every few minutes to compensate continuous electron losses, hence the nominal current is maintained. This is called top-up operation.

The BESSY II storage ring has a circumference of 240 m and consists of 32 bending

1. Introduction

Table 1.1.: Relevant machine parameters of BESSY II standard user operation and BESSY VSR. Note: Some values may slightly deviate from [2, Tab. 1.1]. The deviation is always below the claimed accuracy of the predictions made in this thesis and can therefore be ignored.

Parameter	Value
Energy E	1.7 GeV
Horizontal emittance ϵ_x	5 nm rad
Coupling ϵ_y/ϵ_x	2 %
Momentum compaction factor α , nominal	7.3×10^{-4}
Relative natural energy spread, root mean square (rms) δ_0	7×10^{-4}
Total beam current I_{DC}	300 mA
Circumference	240 m
Revolution frequency f_{rev}	1.25 MHz
Harmonic number	400
Fundamental RF frequency	500 MHz
Fundamental RF sum voltage	1.5 MV
Fundamental RF quality factor Q	26 700 ^a
Fundamental RF sum shunt impedance $R_{\text{s},0}$	12.4 M Ω ^a
Synchrotron frequency f_{s}	8.0 kHz ^b
Zero-current bunch length σ_0	10.0 ps ^b
Transverse tunes Q_x, Q_y	17.85, 6.74
Betatron functions at super conducting (SC) cavities β_x, β_y	4 m ^c
Longitudinal radiation damping time τ_{\parallel}	8 ms
Transverse radiation damping time τ_{\perp}	16 ms
Landau cavity RF frequency	1.5 GHz
Landau cavity RF sum voltage	0.225 MV

^aCorresponding to the original BESSY II cavities before their replacement [19].

^bCorresponds to the long bunch in BESSY VSR and BESSY II without Landau cavities.

^cConservative number, see Fig. 5.3.

magnets, arranged in 16 arcs, connected by 16 straight sections where two are needed for the injection and the radio frequency (RF) cavities and the rest is occupied by IDs, see Fig. 1.2.

The magnet structure, also called lattice or optics, is a so called double bend achromat (DBA) lattice [22], where the dispersion function is small in the straight sections, hence the name “achromat”. A vanishing or small dispersion function in the straight sections is typical for third generation synchrotron light sources because it ensures a small beam size, thus high brilliance for the SR from IDs.

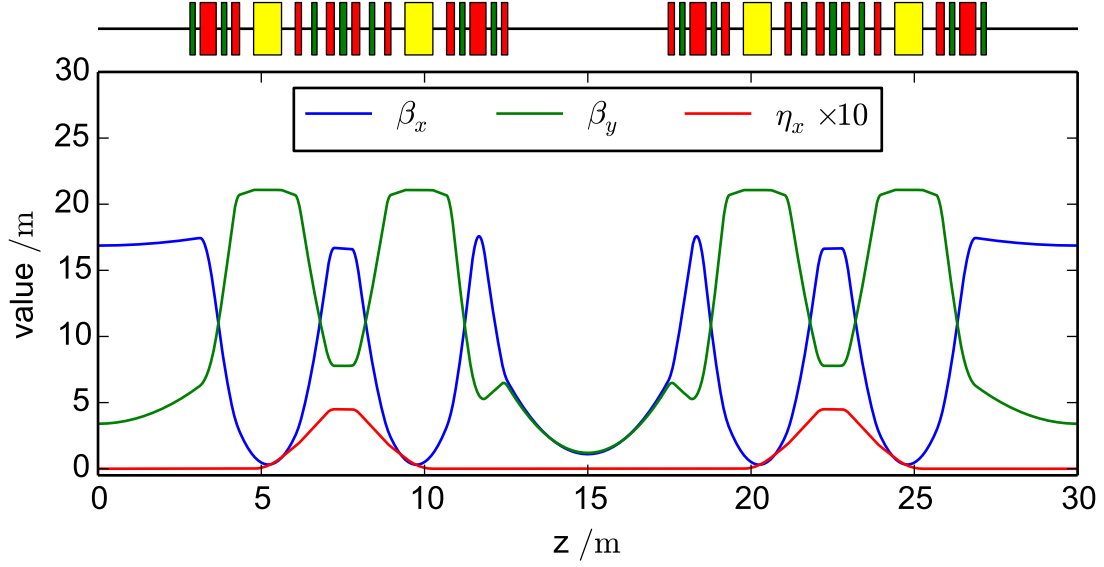


Figure 1.3.: Magnet lattice of BESSY II with horizontal betatron function (β_x), vertical betatron function (β_y) and 10 fold magnified horizontal dispersion function (η_x) in the standard user operation. Rectangles illustrate the length and position of magnets where bending magnets are yellow, quadrupole magnets are red and sextupole magnets are green.

The BESSY II lattice along with the horizontal and vertical betatron functions and the horizontal dispersion function for the standard user operation are shown for an eighth of the ring in Fig. 1.3. Due to extra quadrupoles placed at the edges of every other straight section, the 16-fold symmetry is broken resulting in a remaining 8-fold symmetry. As a result, half of the straight sections have a relatively large horizontal beta function of $\beta_x > 15$ m and are called high- β straight sections. The other half is called low- β straight sections as β_x reaches a local minimum of about $\beta_x \approx 1$ m, see Fig. 1.3. The low β is required for the SC IDs of BESSY II with magnetic fields up to 7 T which would otherwise noticeably worsen the emittance. Additional asymmetries, such as an adjustment of the lattice for improved injection and requirements for in-vacuum undulators are not discussed here.

Part of the magnets of BESSY II can be powered individually, offering the possibility of alternative lattices. For about two weeks a year, the machine is set to the so called low- α lattice, where the momentum compaction factor α is reduced by a factor of approximately 20 compared to its nominal value. This leads to a reduction of the bunch length of a factor of approximately 5 according to the formula for the zero-current bunch length [22,

1. Introduction

Eq. 8.48],

$$\sigma_0 = \delta_0 \sqrt{\frac{E|\alpha|}{ef_{\text{rev}}|V'|}}, \quad (1.1)$$

with the relative natural energy rms spread δ_0 , the electron energy E , the momentum compaction factor α , the elementary charge e , the revolution frequency f_{rev} and the time derivative of the net accelerating voltage at the bunch position V' . In this thesis, the bunch length is measured in units of time and is an rms value, more precisely it is equal to the one standard deviation of a bunch with Gaussian shape. The use of absolute values are introduced here in order to leave the sign conventions open.

If no explicit time dependence stated, V' is assumed to be the time derivative of the net accelerating voltage evaluated at the bunch position,

$$V' = \left. \frac{dV_{\text{acc}}^{\parallel}(t)}{dt} \right|_{\text{bunch position}}, \quad (1.2)$$

with $V_{\text{acc}}^{\parallel}(t)$ the momentary effective accelerating voltage a bunch experiences when passing the cavity at a time t .

The gradient V' of a single cavity system with resonance frequency f_r and operating voltage V_{op} can be estimated as follows if it is operated close to its resonance frequency and close to zero-crossing:

$$|V'| \approx 2\pi f_r V_{\text{op}}. \quad (1.3)$$

This approximations are valid for the active cavities of BESSY II and BESSY VSR.

Equation 1.1 can also be expressed in terms of the synchrotron frequency f_s [22, Eq. 6.35],

$$\sigma_0 = \frac{|\alpha|\delta_0}{2\pi f_s}, \quad (1.4)$$

with the following explicit expression for f_s :

$$f_s = \frac{1}{2\pi} \sqrt{\frac{ef_{\text{rev}}|\alpha||V'|}{E}}. \quad (1.5)$$

A drawback of low- α operation is the appearance of a single bunch instability, the so called microwave instability or bursting instability, driven by CSR, see for example [23, 24]. The name bursting refers to a non-equilibrium state where the emitted CSR, usually in the THz regime, appears in bursts instead of a quasi continuous radiation. Correlated with the bursts are modulations of the bunch structure. Usually no beam loss occurs, but the average bunch length and energy spread can be significantly increased. The SR from a beam in this state is unusable for most applications. As a consequence, the total stored current in low- α operation needs to be reduced to about 15 mA to achieve stability. This is done in 50% of the scheduled low- α runs, while the rest of the time, a current of 100 mA

is stored with a certain level of bursting that can be accepted by some but not all users. In low- α operation, most other users of SR are unable to perform regular experiments, either because the intensity is too low or the beam is too unstable.

At constant bunch length, the threshold current for this instability primarily scales with α ,

$$I_{\text{thr}} \propto \alpha. \quad (1.6)$$

A more detailed discussion on the expected scaling for the parameter space of BESSY VSR is given in [2].

Another effect that changes the bunch length at realistic currents is the potential well effect [25], a single bunch effect caused by the machine impedance. For BESSY II and BESSY VSR, where the bunch current of most bunch types is in a stable regime close to the threshold current, this effect increases the bunch length by about 50%.

1.3. BESSY VSR

The purpose of BESSY VSR [2] is to provide short bunches with high intensity in the multi-user facility BESSY II in the standard operation mode without reducing the beam quality or availability for user experiments that are transparent to the time structure.

As was discussed before, low- α cannot provide this demands, thus an alternative approach has been perused. It became clear, that with a massive increase of V' , the bunch length can also be significantly reduced while only slightly reducing the threshold current of the microwave instability [26], see Eqs. 1.1 and 1.6. The idea presented therein utilizes SC multi-cell cavity structures operated at high fields to provide an increase of V' in the order of a factor of 100 which allows to store stable bunches at high current with a 10 times reduction in length.

If a single RF frequency was used for the additional focusing cavities, all bunches in the ring would be short. In BESSY II, a setup with 300 mA stored current in short bunches is believed to be impossible due to the strong impedance heating caused by short bunches [2].

The solution is an alternating bunch length scheme, presented in [27], now known as BESSY VSR [2], where only every other bunch is short and the total current can be distributed in short and long bunches according to the need of the users and possible limitations of the machine. Typically, the majority of the total current will be stored in long bunches, where no impedance issues are expected and only a small fraction of the beam is stored in short bunches with high bunch current. This satisfies the demands of both user groups, those who are transparent to the time structure as a high average current is provided and those who use short pulses, as there are a few, intense short bunches continuously available.

The multi-functionality of this scheme is illustrated in the BESSY VSR baseline fill pattern shown in Fig. 1.4. The bunch fill pattern includes two trains of long bunches,

1. Introduction

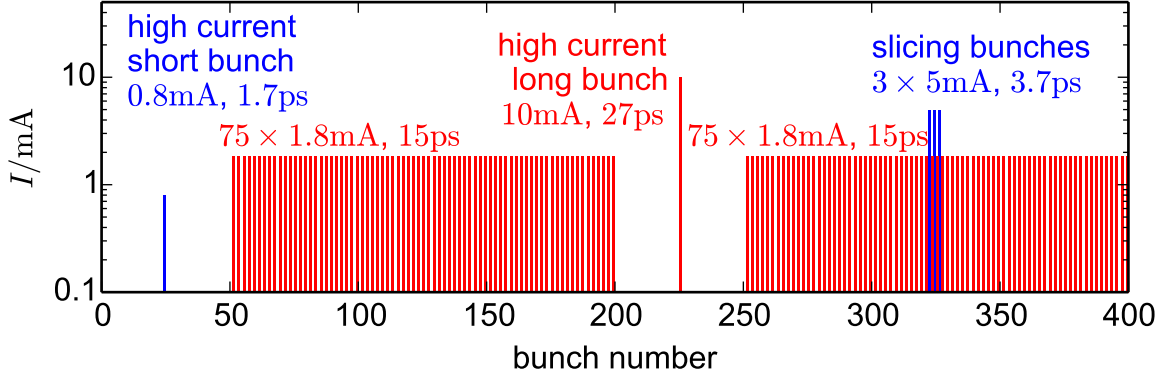


Figure 1.4.: Baseline fill pattern of BESSY VSR showing two chopper gaps and indicating the bunch current and expected bunch length for each bunch type [2].

providing the average current for users who are transparent to the time structure. The trains are interrupted by a gap of 100 ns each, which is enough to allow a separation of the SR of this fraction of the fill from the rest by means of a mechanical chopper wheel [2]. For this purpose, a single short bunch and a single high current long bunch are placed in the center of the first and second gap respectively, which appear as pure single bunches at the experiments where the choppers are applied. The chopper wheel is the baseline scheme for the separation of long and short bunches; other means are discussed in [2]. Other fill patterns are possible, e.g., all short bunches in the bunch trains can be filled with a reduced bunch charge to provide intense CSR in the THz regime.

The bunch currents and bunch lengths shown in Fig. 1.4 are based on scaling laws for the microwave instability, illustrated in Fig. 1.5, and estimations including the lengthening by CSR and potential well lengthening [2]. The single short bunch is operated close to the threshold of the microwave instability. The shift of the threshold current at constant bunch length by a factor of 80 for the short bunches in BESSY VSR is depicted in Fig. 1.5. Analogously, the RF upgrade reduces the bunch length approximately by a factor of 9 at constant current.

The alternating bunch length of BESSY VSR is achieved by the voltage beating of two SC multi-cell cavity systems of difference frequency, resulting in a beat frequency of 250 MHz, i.e., alternatingly long and short bunches of 500 MHz bunch repetition rate. The basic RF parameters of the two cavity systems are given in Tab. 1.2 and the superposition of the two SC cavity systems and the normal conducting (NC) 500 MHz cavity system is shown in Fig. 1.6.

At even bucket positions, i.e., $t = n \times 2$ ns with n even, all gradients add up with the same sign, see Fig. 1.6. This results in a large focusing, thus a small bunch length via Eq. 1.1. At odd bucket positions, i.e., $t = n \times 2$ ns with n odd, the gradients of the two SC cavity systems have opposite sign, thus cancel each other and lead to long

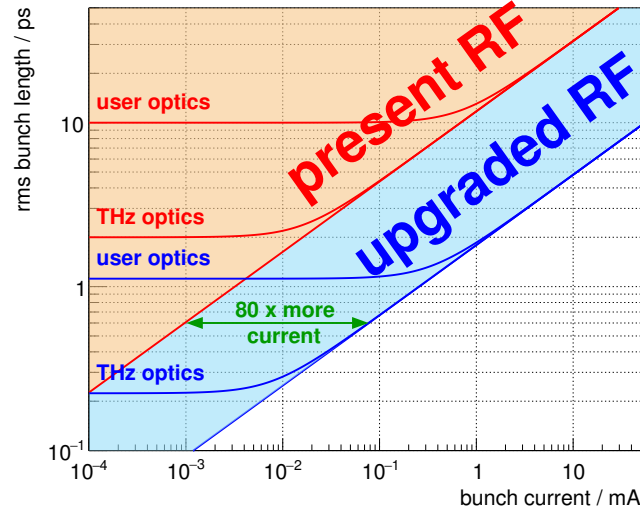


Figure 1.5.: Expected scaling of bunch length and current for the present BESSY II RF system (red) and the short bunches in the BESSY VSR RF system (blue) [2]. The curved solid lines represent the thresholds for different magnet optics, where “user optics” is the standard user operation and “THz optics” is a low- α optics. Deviations from this simplified scaling are discussed in [2].

Table 1.2.: Relevant RF parameters of the SC cavity systems for BESSY VSR [2, Tab. 3.1].

Parameter	Value	
RF frequency	1.5 GHz	1.75 GHz
Operating voltage	20 MV	17.14 MV
Number of cavities and cells	2×5	2×5
Normalized shunt impedance $R_{s,0}/Q$	500Ω	500Ω
Loaded quality factor Q	5×10^7	5×10^7
Cavity detuning Δf_r at $I_{DC} = 300$ mA	-11.25 kHz	15.3 kHz

bunches whose length is defined by the remaining gradient given by the NC cavity. The long bunch approximately matches the properties of the bunches in BESSY II in standard user operation.

With the frequencies and voltages of the SC cavity systems from Tab. 1.2 and the NC cavity system from Tab. 1.1 and ignoring beam loading, cavity detuning, and energy

1. Introduction

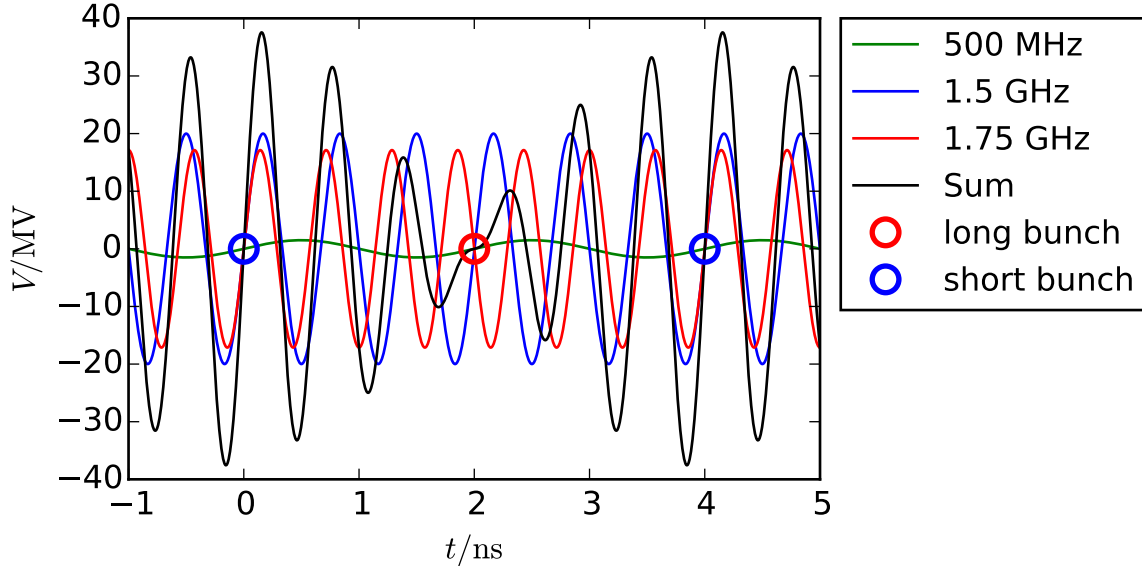


Figure 1.6.: Superposition of cavity voltages at BESSY VSR. At $t = 0$ ns and $t = 4$ ns, the sum voltage (black curve) has a large slope leading to short bunches (blue circles). In between, i.e., $t = 2$ ns, the sum voltage is almost flat, leading to long bunches (red circles). No beam loading, cavity detuning, or energy losses are considered.

losses, the gradients of the three cavity systems can be calculated:

$$|V'|_{500 \text{ MHz}} = 2\pi \times 1.5 \text{ MV} \times 0.5 \text{ GHz} = 2\pi \times 0.75 \text{ MV GHz} \quad (1.7)$$

$$|V'|_{1.5 \text{ GHz}} = 2\pi \times 20 \text{ MV} \times 1.5 \text{ GHz} = 2\pi \times 30 \text{ MV GHz} \quad (1.8)$$

$$|V'|_{1.75 \text{ GHz}} = 2\pi \times 17.14 \text{ MV} \times 1.75 \text{ GHz} = 2\pi \times 30 \text{ MV GHz} \quad (1.9)$$

The net gradient at even and odd buckets is found to be

$$|V'|_{\text{even}} = |V'|_{500 \text{ MHz}} + |V'|_{1.5 \text{ GHz}} + |V'|_{1.75 \text{ GHz}} = 2\pi \times 60.75 \text{ MV GHz} \quad (1.10)$$

$$|V'|_{\text{odd}} = |V'|_{500 \text{ MHz}} + |V'|_{1.5 \text{ GHz}} - |V'|_{1.75 \text{ GHz}} = 2\pi \times 0.75 \text{ MV GHz}, \quad (1.11)$$

which means the focusing gradient of the short bunches is 81 times larger than for the long bunches. Thus, the short bunches are expected to be 9 times shorter than the long bunches. With a zero-current bunch length for the long bunches of 10 ps, the zero-current bunch length of the short bunches is around 1.1 ps. If the current dependent

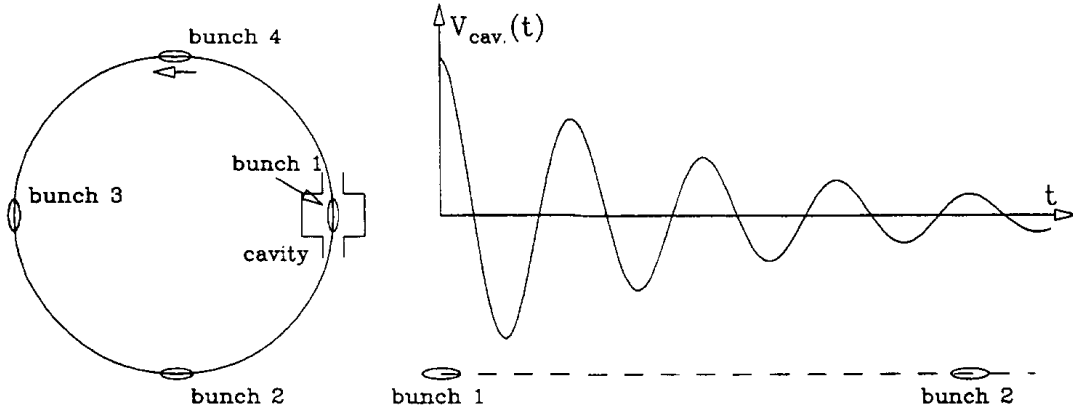


Figure 1.7.: Illustration of bunch coupling transmitted by the electromagnetic field induced by the interaction of a bunch with a cavity. Figure reproduced from [28].

bunch lengthening is considered, the expected bunch length is 1.7 ps, see Fig. 1.4. This is significantly shorter than anything presently offered at reasonably high bunch currents at synchrotron light sources.

1.4. Coupled Bunch Effects in BESSY VSR

Coupled bunch effects describe phenomena where the bunches influence each other in contrast to single bunch effects which are independent of the existence or behavior of other bunches. In this thesis, the bunches are considered to be coupled only through the electromagnetic interaction with RF cavities, because the installation of SC multi-cell cavities is the major change from BESSY II to BESSY VSR. Hence, the focus of this thesis is on coupled bunch effects that are caused by the introduction of the SC multi-cell cavities.

The interaction of the bunches with an RF cavity is illustrated in Fig. 1.7. If a bunch passes an RF cavity, it induces an oscillating electromagnetic field which remains for some time in the cavity after the bunch has passed. At the same time, the bunch interacts with the electromagnetic fields already present in the cavity, e.g., fields produced by an RF generator or previous bunches. In this case, the electromagnetic fields can be expressed as an sinusoidally oscillating and decaying voltage that acts accelerating or decelerating on a bunch. Thus, energy is transmitted by the interactions of the bunches with the fields in the cavity and couples the bunches to each other.

As the bunch interaction repeats each revolution, it is plausible that under certain conditions, the electromagnetic fields may add up from turn to turn and reach a significant field strength. In such a situation, there are two effects possible. On the one hand, it

1. Introduction

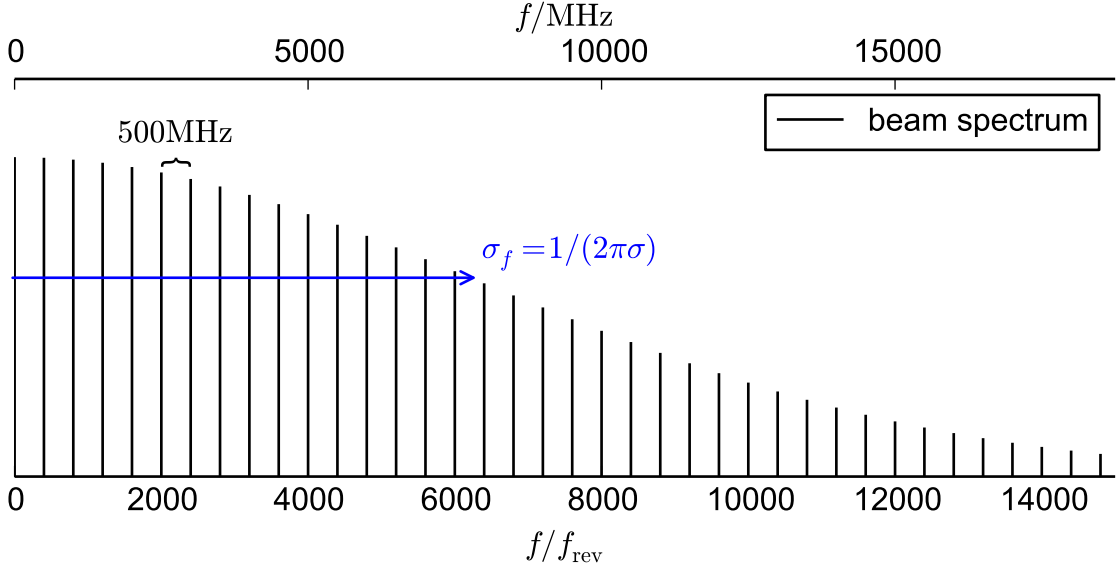


Figure 1.8.: Beam spectrum of BESSY II for even bunch fill pattern with 400 bunches, 2 ns bunch spacing and $\sigma = 20$ ps bunch length.

can lead to a constant voltage without beam motion, known as beam loading, covered in Chapter 6. On the other hand, it can lead to an instability where the bunches oscillate longitudinally or transversely with increasing amplitude until a saturation occurs or the beam is lost, known as the coupled bunch instability (CBI), explained in detail in Chapter 2.

For further understanding, it is convenient to consider the effect in the frequency domain. The bunch fill pattern is Fourier transformed to obtain the beam spectrum. The beam spectrum is illustrated in Fig. 1.8 for BESSY II parameters with even bunch fill pattern, i. e., all bunches have the same current, 2 ns bunch spacing and a bunch length of $\sigma = 20$ ps. The bunch length determines the frequency limit of the amplitude of the beam spectrum, which is given by a Gaussian envelop with rms value of $\sigma_f = 1/(2\pi\sigma)$.

The cavity is represented by a sum of impedances, where the fundamental mode and all higher order modes (HOMs) are each described by a resonator impedance. The interaction of the beam with the impedance is, in a simplified form, the product of beam spectrum with impedance.

As illustrated in Fig. 1.9, interaction occurs where an impedance overlaps with the beam spectrum or its side bands generated by longitudinal motion (synchrotron oscillations) or transverse motion (betatron oscillations). In operation with even bunch fill pattern, there are no beam spectrum components other than at multiples of the fundamental RF frequency. However, as will be shown later in this thesis, in a manner of speaking, the impedance is still sampled at the side bands of all revolution harmonics. The side bands are located at both sides at multiples of the revolution frequency with a distance

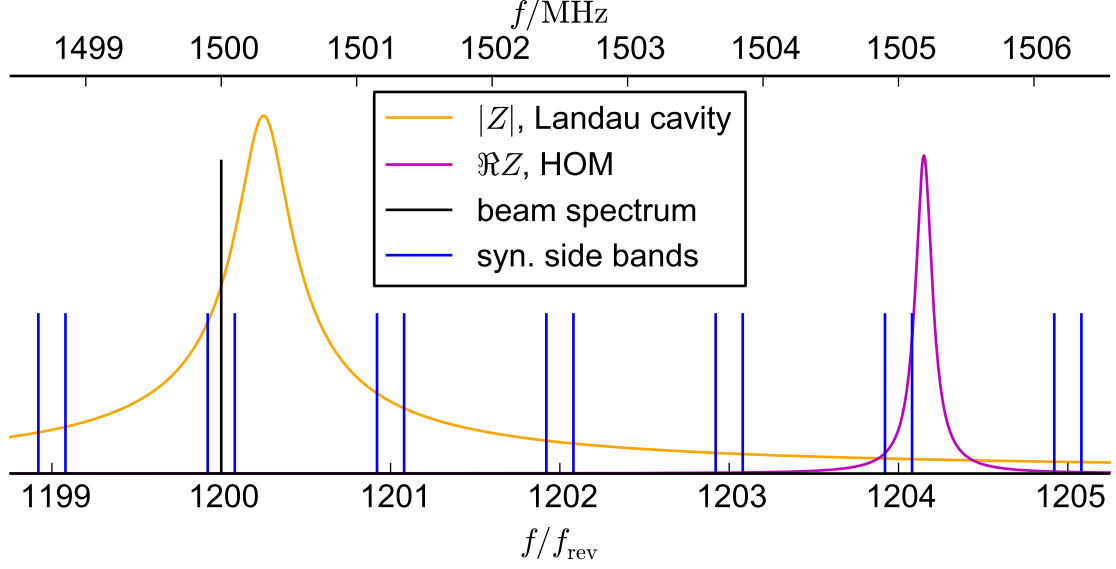


Figure 1.9.: Beam spectrum for even bunch fill pattern with location of synchrotron side bands indicated. As an example, a typical location of a passive Landau cavity (orange curve) and a possible position of an HOM (magenta curve) are shown.

corresponding to the synchrotron frequency or a betatron frequency, respectively.

In Fig. 1.9, the synchrotron side bands are schematically drawn to indicate at which frequencies the impedances are sampled. If the beam spectrum (black line) overlaps with an impedance, a constant voltage is induced, e.g., a passive Landau is driven as illustrated in Fig. 1.9. If a synchrotron side band (blue line) overlaps with an impedance, an instability might be driven. This may occur close to a beam spectrum component, e.g., a passive Landau cavity, or far away at any other harmonic, e.g., an HOM.

The cavities for BESSY VSR need to be operated in continuous wave (CW) and provide very high focusing gradients V' within the limited space of one straight section of the BESSY II storage ring. This requires high frequency, large accelerating voltages, a multi-cell design and super conductivity.

1.5. Motivation of this Thesis

The novel approach of BESSY VSR, i.e., using SC multi-cell cavities in an storage ring based light source leads to great technological and accelerator physical challenges, among which the coupled bunch effects play a major role.

In a synchrotron light source, beam stability is crucial in all three planes in order to guarantee the high quality of the SR for the user experiments. At BESSY VSR, the particular risk are strong HOMs, typical for high-frequency SC multi-cell cavities,

1. Introduction

potentially leading to CBIs, with the theory described in Chapter 2 and methods for tracking simulations in Chapter 3 and measurements in Chapter 4.

Therefore, one major goal of this thesis is the investigation of the expected appearance and strength of CBIs in BESSY VSR, covered in Chapter 5. Further, an estimation needs to be given how much the HOM damping or other countermeasures, such as beam based damping mechanisms, need to be improved in order to reach stability.

The other major aspect covered by this thesis is the previously unanswered question of transient beam loading in BESSY VSR, induced by unevenness in the bunch fill pattern by the interaction with the SC cavities. As the scheme of BESSY VSR relies on the almost complete cancellation of the large RF gradients to obtain the long bunches, as depicted in a Fig. 1.6, a disturbance of the amplitude or phases of the SC cavities may significantly change the longitudinal dynamics, particularly for the long bunch. Thus, this effect is investigated in Chapter 6 and predictions are made for the baseline fill pattern of BESSY VSR in terms of expected bunch length, synchronous phase positions and spread in synchrotron frequency leading to Landau damping.

2. Theory of Coupled Bunch Instabilities

The theory of CBIs is thoroughly described in [29, 30]. This chapter will review the theory, use formulas from both sources and point out important aspects that are needed for the cases discussed in this work.

In Section 2.1, the concept of wakes and impedances is introduced. This thesis will restrict on CBIs that are driven by localized impedances, described by the resonator model derived from the LRC equivalent circuit, as discussed in Section 2.1.4. This covers the HOMs of the SC cavities, described in Section 2.2, which are the only type of impedances that are expected to change in BESSY VSR compared to BESSY II. Other causes for CBIs, e.g., driven by ions, geometric impedances and resistive wall impedances are not discussed, as those effects are equally present at BESSY II where they seem to be under control.

Sections 2.3 and 2.4 describe the longitudinal CBIs for the case of even and uneven bunch fill pattern, followed by a brief introduction of longitudinal Landau damping in Section 2.5. The transverse dipole CBIs for even and uneven fill are described in Section 2.6, along with a discussion of the transverse quadrupolar CBI.

2.1. Wakes and Impedances

The concept of wakes and impedances is essential to study CBIs driven by a cavity, as the entire beam-cavity interaction can be described in terms of relatively simple expressions of wake functions or impedances respectively. This section describes a definition of the wake function, the shunt impedance, their relation to each other and other relevant quantities that allow for a complete and unambiguous description of the physics in terms of a multipole decomposition in transverse beam moments.

2.1.1. Decomposition in Terms of m -th Moment of the Beam

The major decomposition to describe the interaction of the beam with its surrounding structure, is made in *transverse beam moments*. It means that the interaction of the beam with its surrounding through electromagnetic fields is decomposed in the transverse multipoles of the beam. The transverse m -th moment M_m of the beam or a single bunch

2. Theory of Coupled Bunch Instabilities

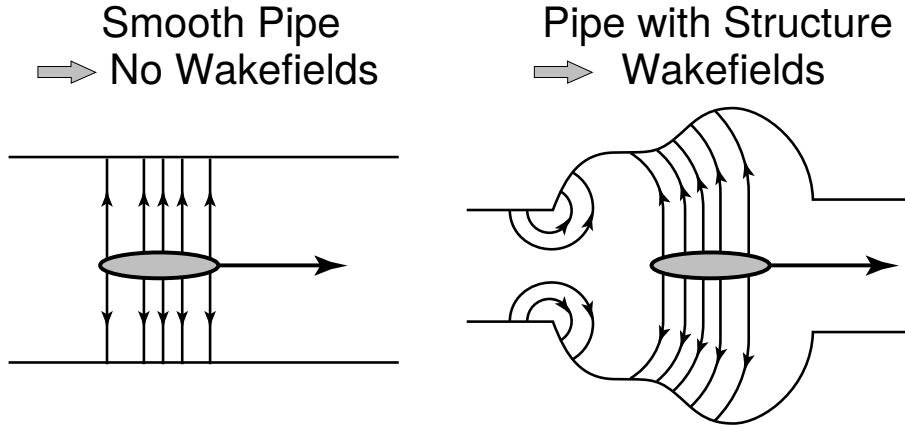


Figure 2.1.: Illustration of wakes appearing if the surrounding shows a structure. Perfectly conducting walls are assumed. Figure reproduced from [31].

is defined as

$$M_m = \langle r^m \cos m(\theta - \theta_0) \rangle, \quad (2.1)$$

where the angle brackets indicate the averaging of the expression in the brackets given all cylindrical coordinates (r, θ) of the electrons of the beam or a single bunch and θ_0 is a constant indicating an absolute orientation. In Cartesian coordinates, the freedom of choosing θ_0 results in two components of the m -th moment, a normal and a skewed one, out of which the normal one is always used in this thesis, without loss of generality. The normal transverse m -th moment in Cartesian coordinates can then be calculated by

$$M_m = \left\langle \sum_{k=0}^m \binom{m}{k} x^k y^{m-k} \cos \left(\frac{1}{2}(m-k)\pi \right) \right\rangle, \quad (2.2)$$

with (x, y) the transverse coordinates of the electrons. See Appendix A.1 for a derivation of this formula.

The electromagnetic fields that arise during the interaction of a bunch with its surrounding are also called wakes due to their apparent similarity to the disturbance a boat inflicts on a water surface. For a beam pipe with infinity conductivity, wakes appear only if the beam pipe exhibits a change in the cross section, see Fig. 2.1. For finite conductivity, the phenomenon commonly referred to as resistive wall occurs and the arising wakes can become significant¹. However, as mentioned above, this effect is not discussed in this thesis, as they are not expected to change in BESSY VSR. The interaction of each beam multipole M_m is fully described by a so called wake function or equivalently by an impedance.

¹In a more generalized context, wakes and impedances can also be used to describe phenomena such as coherent synchrotron radiation, e.g. [32], or active elements, such as feedback systems.

Note, the decomposition indicated by m is a priori different from the ordering of solutions of the Maxwell equations of a pillbox cavity, which may also be called “monopole”, “dipole”, etc. In fact, solutions to the Maxwell equations of a realistic cavity must be decomposed [33] in orders of m to be of use in the instability theory described in this thesis.

2.1.2. Wake Function and Wake Potential

At high energies, the beam can be considered rigid, i. e., during its interaction with the surrounding neither its velocity, nor its direction of path, nor its shape changes. Hence, the net effect of the wake on a test particle can be obtained by integrating the force \vec{F} of the electromagnetic fields along the longitudinal coordinate z over a distance L that includes the localized source of the electromagnetic interaction:

$$c\Delta\vec{p} = \int_{-L/2}^{L/2} dz \vec{F}. \quad (2.3)$$

The integral describes the net effect on the test particle and is called the wake potential $c\Delta\vec{p}$ or the *integrated wake force impulse*. For instance, the sources for the electromagnetic interaction can be a cavity structure, i. e., a relatively short structure where the approximations are well justified.

With those assumptions, the Panofsky-Wenzel theorem [34] follows, forming the basis of potentials and impedances [30, p. 3]. It relates the transverse and longitudinal wake potentials, via [30, Eq. 1.12]

$$\frac{\partial}{\partial z}(c\Delta\vec{p}_m^\perp) = \vec{\nabla}(c\Delta p_m^\parallel), \quad (2.4)$$

stating that the transverse derivative of the longitudinal impulse is equal to the longitudinal derivative of the transverse impulse.

Furthermore it is assumed that the structure is axially symmetric and cylindrical coordinates can be used to describe the dynamics. This leads to the definition of the wake function, $W_m(z)$, a quantity closely related to the wake potential. It is a function solely dependent on z , the distance of the test particle from the source particle. If the wake function is known, neither the calculation of the force \vec{F} is needed, nor is it necessary to perform an integration over the distance L . In this sense, the wake function already comprises the integrated effect of the localized source. Or in other words, quoting [29, p. 59], the wake function *describes the shock response of the vacuum chamber environment to a δ -function beam which carries an m -th moment*, where z describes the distance of the test particle from the δ -function beam and $z > 0$ means the test particle is ahead of the beam.

In the ultra-relativistic limit, as always assumed in this thesis, the wake function must

2. Theory of Coupled Bunch Instabilities

be zero for $z > 0$. The relation of the wake function to the wake potential for all orders of m can be expressed in cylindrical coordinates as [29, Eq. 2.50]

$$\begin{aligned} c\Delta p_m^{\parallel} &= -eqM_m W'_m(z) r^m \cos m\theta \\ c\Delta \vec{p}_m^{\perp} &= -eqM_m W_m(z) m r^{m-1} (\hat{r} \cos m\theta - \hat{\theta} \sin m\theta), \end{aligned} \quad (2.5)$$

with M_m the m -th moment of the beam, q the total charge of the beam and e the charge of the test particle. Note that $W'_m(z)$ is the derivative of $W_m(z)$,

$$W'_m(z) = \frac{d}{dz} W_m(z). \quad (2.6)$$

The fact that both the longitudinal and transverse wake potentials, i. e., the net forces on the particles, can be described by a single quantity and its derivative is a consequence of the Panofsky-Wenzel theorem.

In Eq. 2.5, the beam is the source that generates the wake, and can also be a single bunch. Note that if the charge of the test and source particle have the same sign, a positive value of W'_m must lead to deceleration of the test particle. If the wake function is known for a structure, Eq. 2.5 can be used to calculate the kick that a particle experiences if it passes the structure.

The wake function $W_m(z)$ contains all information about the structure causing the interaction with the beam through the wake. The derivative of the wake function with respect to z , $W'_m(z)$, relates to the longitudinal wake potential $c\Delta p_m^{\parallel}$ while the wake function $W_m(z)$ itself relates to the transverse wake potential $c\Delta \vec{p}_m^{\perp}$. Therefore, $W_m(z)$ is also called the *transverse wake function* and $W'_m(z)$ the *longitudinal wake function*. For the case of resonators that can be described with the equivalent circuit, $W_m(z)$ takes a simple explicit form, as discussed in the next sections. The relation for the first four beam moments is given explicitly in Tab. 2.1 in Cartesian coordinates.

Strictly speaking, Eq. 2.5 is only valid for axially symmetric structures. In non-axially symmetric structures, different orders of the impedance are mixed, i. e., different orders may contribute to the same multipole order of motion. In other words, the wake potentials $c\Delta p_m^{\parallel}$ on the left hand side (l.h.s.) of Eq. 2.5 would not only have a single contributing $W'_m(z)$ on the right hand side (r.h.s.), but a sum of contributing wake functions of all different orders of m . Covering this behavior requires a generalized definition of impedance and wakes where different orders are allowed to couple [35]. For realistic cavities, this effect is expected to be small and therefore ignored in this thesis. In non-axially symmetric structures, the transverse wake function can be separated into two perpendicular wake functions, indicated by x and y respectively.

Table 2.1.: Relation of wake potentials to wake functions for the first four orders of m . The test particle with charge e and coordinates (x, y) follows the beam at a distance $|z|$. The wake is created by the beam with charge q and transverse normal moment M_m which can be calculated with the coordinates (\bar{x}, \bar{y}) of its electrons. \hat{x} and \hat{y} are the unit vectors indicating the transverse direction of the resulting wake forces.

m	M_m	$c\Delta p_m^\parallel$	$c\Delta \vec{p}_m^\perp$
0	$\langle 1 \rangle$	$-eqW'_0(z)$	0
1	$\langle \bar{x} \rangle$	$-eqM_1xW'_1(z)$	$-eqM_1W_1(z)\hat{x}$
2	$\langle \bar{x}^2 - \bar{y}^2 \rangle$	$-eqM_2(x^2 - y^2)W'_2(z)$	$-2eqM_2W_2(z)(x\hat{x} - y\hat{y})$
3	$\langle \bar{x}^3 - 3\bar{x}\bar{y}^2 \rangle$	$-eqM_3(x^3 - xy^2)W'_3(z)$	$-3eqM_3W_3(z)[(x^2 - y^2)\hat{x} - 2xy\hat{y}]$

2.1.3. Impedance

The impedance is defined by a Fourier transform of the wake function [29, Eq. 2.69, Eq., 2.71],

$$Z_m^\parallel(\omega) = \int_{-\infty}^{\infty} \frac{dz}{c} e^{-i\omega z/c} W'_m(z) \quad (2.7)$$

$$Z_m^\perp(\omega) = i \int_{-\infty}^{\infty} \frac{dz}{c} e^{-i\omega z/c} W_m(z), \quad (2.8)$$

where Z_m^\parallel is called longitudinal impedance and Z_m^\perp transverse impedance. The dimensions of Z_m^\parallel and Z_m^\perp are $\Omega \text{ m}^{-2m}$ and $\Omega \text{ m}^{-2m+1}$ respectively. The Fourier transform adds the dimension of seconds to the wake functions, hence the dimensions of $W'_m(z)$ and $W_m(z)$ are $\text{VC}^{-1} \text{ m}^{-2m}$ and $\text{VC}^{-1} \text{ m}^{-2m+1}$ respectively.

The wake function and the impedance are equivalent methods to describe the physics. The wake function is a function of longitudinal position, i. e., applicable in the time domain while the impedance is a function of frequency, used in the frequency domain. Depending on the particular problem, the most suitable method is used.

2.1.4. Resonator in LRC Model (Equivalent Circuit)

Impedances, such as those extracted from the modes of a RF cavity can be described by a parallel LRC resonator circuit with a resistance $R_{s,m}$, an inductance L_m and a capacitance C_m . For the longitudinal impedance at an angular frequency ω , the following is obtained,

2. Theory of Coupled Bunch Instabilities

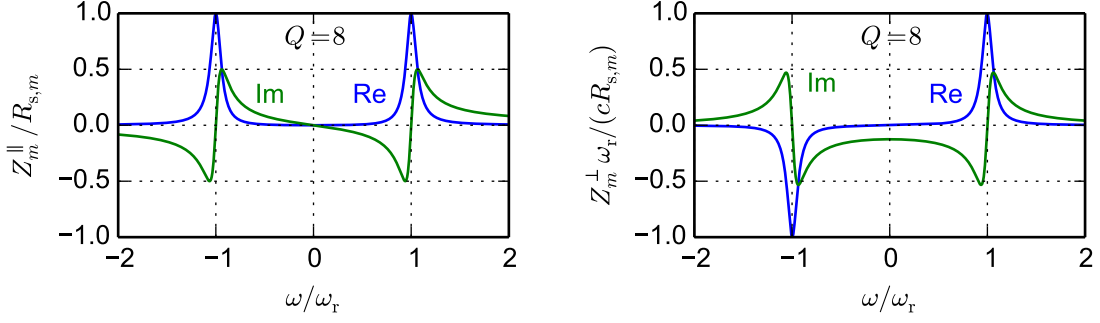


Figure 2.2.: Real and imaginary component of the resonator impedance for $Q = 8$ for the longitudinal case (left) and the transverse case (right).

$$\frac{1}{Z_m^{\parallel}(\omega)} = \frac{1}{R_{s,m}} + \frac{i}{\omega L_m} - i\omega C_m, \quad (2.9)$$

which can be rearranged with the substitutions $Q = R_{s,m}\sqrt{C_m/L_m}$ and $\omega_r = 1/\sqrt{C_m L_m}$ to yield an explicit expression for the impedance [30, Eq. 1.56]

$$Z_m^{\parallel}(\omega) = \frac{R_{s,m}}{1 + iQ\left(\frac{\omega_r}{\omega} - \frac{\omega}{\omega_r}\right)}, \quad (2.10)$$

with the quality factor Q and the angular resonance frequency ω_r where the index m is omitted as those quantities have the same dimensions for all m . In accelerator physics, the quantity $R_{s,m}$ is called shunt impedance² and has the dimension $\Omega \text{ m}^{-2m}$. The transverse resonator impedance, valid for $m > 0$, is then given by [30, Eq. 1.57]

$$Z_m^{\perp}(\omega) = \frac{c}{\omega} \frac{R_{s,m}}{1 + iQ\left(\frac{\omega_r}{\omega} - \frac{\omega}{\omega_r}\right)}, \quad (2.11)$$

with the speed of light c . The longitudinal $m = 0$ and the transverse $m = 1$ case are shown in Fig. 2.2.

²See Section 2.1.6 for a discussion on the different definitions of the shunt impedance used in literature.

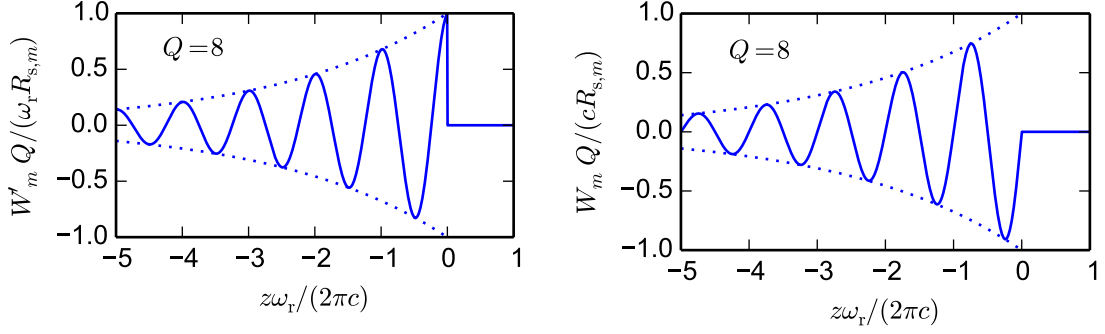


Figure 2.3.: Longitudinal (left) and transverse (right) resonator wake function.

With Eq. 2.7 the longitudinal wake function is given by [29, Eq. 2.84]

$$W'_m(z) = \begin{cases} 0 & , \quad z > 0 \\ \frac{\omega_r R_{s,m}}{2Q} & , \quad z = 0 \\ \frac{\omega_r R_{s,m}}{Q} e^{\frac{\omega_r z}{2Qc}} \left(\cos \frac{\bar{\omega} z}{c} + \frac{\omega_r}{2Q\bar{\omega}} \sin \frac{\bar{\omega} z}{c} \right) & , \quad z < 0, \end{cases} \quad (2.12)$$

with $\bar{\omega} = \sqrt{\omega_r^2 - \left(\frac{\omega_r}{2Q}\right)^2}$ and $Q > \frac{1}{2}$ assumed. The transverse wake function is obtained analogously. With the approximation of a sharply peaked resonator, i.e., $Q \gg 1$, the wake functions simplify significantly to the following for $z < 0$ [29, Eq. 2.86, Eq. 2.90]:

$$W'_m(z) = \frac{\omega_r R_{s,m}}{Q} e^{\frac{\omega_r z}{2Qc}} \cos \frac{\omega_r z}{c} \quad (2.13)$$

$$W_m(z) = \frac{c R_{s,m}}{Q} e^{\frac{\omega_r z}{2Qc}} \sin \frac{\omega_r z}{c}. \quad (2.14)$$

This approximation is clearly valid for fundamental modes but also for HOMs of a cavity with typical Q values of at least a few hundred. The wake functions of Eq. 2.13 and Eq. 2.14 are depicted in Fig. 2.3.

2.1.5. Extraction of Shunt Impedance from Cavity Fields

Cavity modes are eigenmodes of the Maxwell equations where the cavity geometry and surface defines the boundary conditions. The fundamental mode of a cavity is the longitudinal mode which is used for acceleration. In a single-cell cavity, this is usually the mode with the lowest resonance frequency. In general, all eigenmodes of cavity with a

2. Theory of Coupled Bunch Instabilities

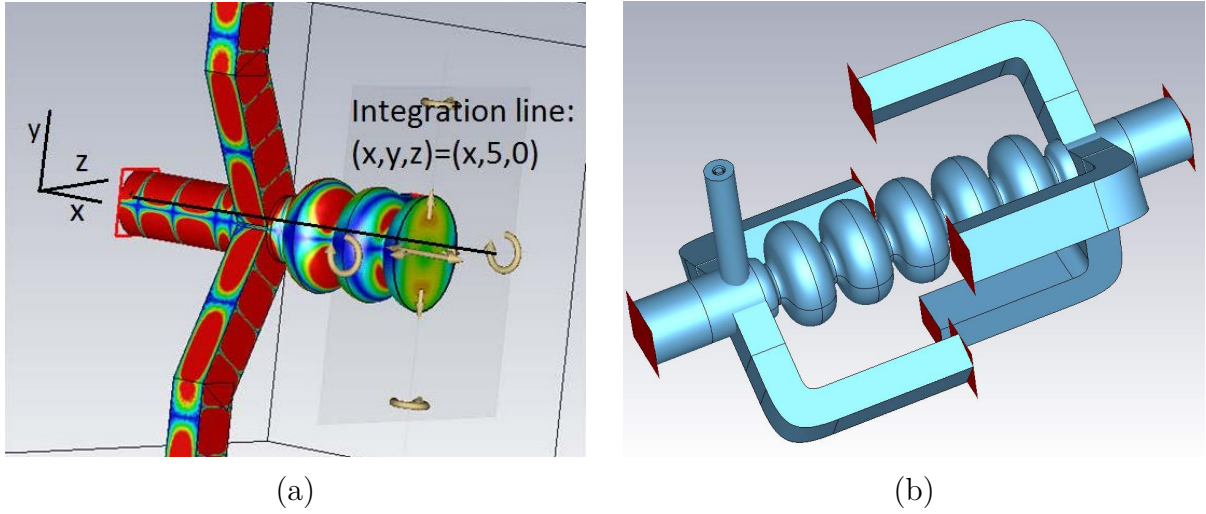


Figure 2.4.: (a) Example of a dipolar HOM [2]. (b) Five-cell cavity model “HZB 2c coax. coupler” as of May 2015 [37].

frequency larger than the fundamental mode are called HOMs. In case of a multi-cell cavity, the fundamental mode is usually the highest frequency of the fundamental band. In this case, the other modes of the fundamental band are called same passband modes (SPMs).

A realistic cavity is not exactly axially symmetric and the eigenmodes need to be decomposed according to impedances ordered in m in order to describe their interaction with the beam [33]. In consideration of the numerical uncertainties of computed cavity models, this is a good approximation whose error can be ignored, even if the decomposition in Eq. 2.5 itself is strictly speaking only valid for axial symmetry.

If an eigenmode of a cavity is known to be a resonator impedance of the order m , the normalized shunt impedance $R_{s,m}/Q$ can be obtained by integration through the electromagnetic fields [36, Eq. 2.66],

$$\frac{R_{s,m}}{Q} = \frac{|V_{\text{acc}}^{\parallel}(r)|^2}{2\omega_r U r^{2m}}, \quad (2.15)$$

where $V_{\text{acc}}^{\parallel}$ represents the integrated longitudinal accelerating voltage parallel to the longitudinal axis at an offset r , ω_r the angular resonance frequency and U the energy stored in the field. The procedure is graphically illustrated in Fig. 2.4a for a dipole mode. Note that both the azimuth and the overall phase have to be chosen such that $V_{\text{acc}}^{\parallel}(r)$ is at its maximum. In case of $m > 0$, the azimuth then defines the orientation of the impedance in the transverse plane.

The special case of $m = 1$ can also be calculated by on-axis integration of the transverse

force [36, Eq. 15.55],

$$\frac{R_{s,1}}{Q} = \frac{|\vec{V}_{\text{acc}}^\perp(r=0)|^2 \omega_r}{2Uc^2}, \quad (2.16)$$

with the integrated transverse voltage $|\vec{V}_{\text{acc}}^\perp|$. The validity of this formula becomes clear when looking at Eq. 2.5 or Tab. 2.1, as on-axis ($x = 0$, $y = 0$) contributions to the transverse force are zero for all orders but $m = 1$.

With the relation of the quality factor Q to the dissipated power P_{diss} given by [22, Eq. 15.49]

$$Q = \frac{\omega_r U}{P_{\text{diss}}}, \quad (2.17)$$

Eq. 2.15 can be written for $m = 0$ in the following, frequently used form [36, Eq. 2.63]:

$$R_s \equiv R_{s,0} = \frac{V_{\text{acc}}^\parallel{}^2}{2P_{\text{diss}}}. \quad (2.18)$$

When considering the fundamental mode, the shunt impedance is loosely speaking, the amount of accelerating voltage V_{acc}^\parallel obtained for a given power dissipated in the cavity with the typical goal of making acceleration as efficient as possible [38]. For this reason, R_s is a very important quantity and frequently introduced via Eq. 2.18, especially when the subject is addressed from a more technical view and the discussion of $m > 0$ is neglected.

2.1.6. Other Definitions of Shunt Impedance

In accelerator physics, there are different definitions of shunt impedance, especially when only the fundamental mode, $m = 0$, is discussed. They mostly differ by a factor of two. The definition $R_{s,0}$ of this thesis is the so called *circuit definition*, named after the fact that the shunt impedance is equal to the resistance that appears in the equivalent circuit, see Section 2.1.4.

Another common definition is the so called *accelerator definition*, denoted in this thesis with an index a, where the numerical values are twice as large as in the circuit definition [36, Eq. 2.63],

$$R_a = 2R_s. \quad (2.19)$$

2.2. Higher Order Modes in Cavities

The RF cavities considered in this thesis are designed to provide a high shunt impedance of the fundamental mode which is used for acceleration in longitudinal direction. For the purpose of BESSY VSR, the cavities need to provide a very large time derivative of the accelerating voltage. This is achieved by the combination of high frequency (1.5 GHz and

2. Theory of Coupled Bunch Instabilities

1.75 GHz) and high electric fields. As the space is limited, a multi-cell design was chosen and superconductivity is mandatory due to the required operation in continuous wave.

Figure 2.4b shows the 1.5 GHz cavity model “HZB 2c coax. coupler” presently in the development for BESSY VSR [37]. Unfortunately, the strength of HOMs increases with frequency, the number of cells and with the transition from normal conductivity to superconductivity. Despite significant progress in the HOM damping [37, 39], the HOM spectrum cannot be fully suppressed. Figure 2.4a shows an example of a dipolar HOM along with the integration line used for the calculation of the shunt impedance.

The entire impedance spectrum up to 3.0 GHz of the cavity model “HZB 2c coax. coupler” is shown in Fig. 2.5. It is based on calculations that were stopped at 3.0 GHz due limited computationally resources.

The fundamental mode, having the largest longitudinal impedance, can be seen at 1.5 GHz. The other four modes of the fundamental band, the SPMs, have frequencies slightly below the fundamental and a significantly lower impedance. Longitudinal HOMs are visible around 2.7 GHz. Dipole modes seem to appear in four bands below 3.0 GHz with the strongest modes around 2.8 GHz. Quadrupole modes show two bands with the strongest modes also located around 2.8 GHz.

2.3. Longitudinal Bunch Motion for Even fill

This section presents the derivation of the longitudinal bunch motion under the influence of a longitudinal resonator impedance with the goal of obtaining expressions for the tune shift and growth rate of the CBI for the case of a homogeneous bunch fill pattern, also called even fill, i.e., all buckets filled with the same charge.

Up until here, all formulas are valid for arbitrary longitudinal bunch profiles. In the following discussions, the bunches are assumed to be point charges in the longitudinal direction, which is a justified approximation as the typical bunch length is much smaller than the wave length of the resonant structure, see Appendix A.2 for a quantitative estimate.

In time domain, the equations of motion for M equally spaced bunches are given by [29, Eq.4.121],

$$\ddot{z}_n + \omega_s^2 z_n \propto \sum_k \sum_{l=0}^{M-1} W'_0(l, k), \quad (2.20)$$

with the longitudinal coordinate z_n of bunch $n = 0, \dots, M - 1$ as a function of time, ω_s the unperturbed synchrotron frequency, k an index representing points in time of bunch passages in the time range $-\infty \dots t$ and W'_0 a longitudinal wake function given in parameters of l and k . Equation 2.20 is a system of M differential equations coupled by the wake fields of all other bunches produced by all their previous passages. This formula is only shown to depict the general structure of the dynamics, namely the positions of the

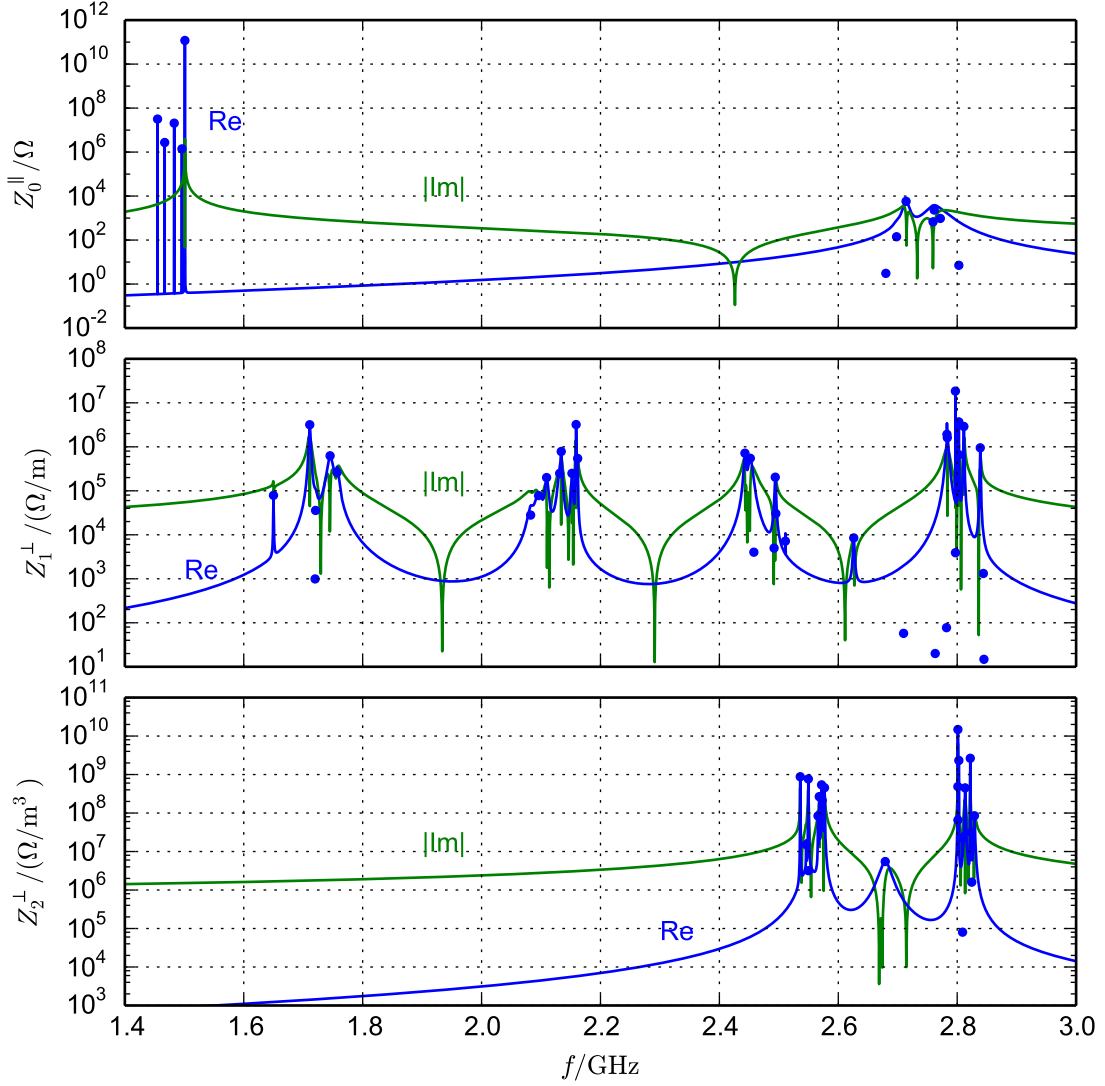


Figure 2.5.: Impedance spectrum of the 1.5GHz cavity model “HZB 2c coax. coupler” [37]. Real part (blue line) and absolute value of imaginary part (green line) of longitudinal $m = 0$ impedance (top), transverse $m = 1$ impedance (center) and transverse $m = 2$ impedance (bottom) corresponding to the sum of longitudinal modes (top), dipole modes (center) and quadrupole modes (bottom). Blue dots correspond to the $R_{s,m}$ values of the individual cavity modes.

bunches are affected by all wake fields previously produced, in a form not yet specified.

In Eq. 2.20, a small amplitude approximation was applied on the terms that form the

2. Theory of Coupled Bunch Instabilities

r.h.s. so that the expression is a driven harmonic oscillator. This is well justified as the purpose of this instability theory is to determine the onset of an instability at arbitrarily small amplitudes. Statements about the behavior of the motion at larger amplitudes, such as a possible saturation are not covered with this approach.

With the typical ansatz to solve a harmonic oscillator and the introduction of a coherent frequency Ω for z_n ,

$$z_n(t) = \tilde{z}_n e^{-it\Omega}, \quad (2.21)$$

with \tilde{z}_n a constant complex amplitude, Eq. 2.20 can be transformed into the frequency domain which turns the wake function into an impedance, in analogy to [29, Eq. 4.126]. The equations of motion of the M bunches are then still coupled to each other. The decoupling can be performed by the following ansatz, which implies a fixed phase relation from bunch to bunch given by the number of full phase revolutions per turn μ

$$\tilde{z}_n \propto e^{in2\pi\mu/M}. \quad (2.22)$$

The bunch modes described by Eq. 2.22 are the coupled bunch modes (CBMs). More specifically, they are called the even fill eigen mode (EFEM), as they are only exact solutions if the bunch fill pattern is even. With those EFEM, Eq. 2.20 decouples and using [29] or [30], the following, very central equation that forms the starting point for many of the following discussions, can be stated:

$$\omega_\mu^2 - \omega_s^2 = -i \frac{\omega_{\text{rev}} I_{\text{DC}} \alpha}{2\pi E/e} \sum_{p=-\infty}^{\infty} \left[pM\omega_{\text{rev}} Z_0^{\parallel}(pM\omega_{\text{rev}}) - ((pM + \mu)\omega_{\text{rev}} + \omega_\mu) Z_0^{\parallel}((pM + \mu)\omega_{\text{rev}} + \omega_\mu) \right]. \quad (2.23)$$

It consists of M equations with μ the number of the CBM, ω_{rev} the angular revolution frequency, I_{DC} the average (DC) beam current, α the momentum compaction factor, E the electron energy and e the elementary charge. The solutions to this equation, ω_μ , are the coherent angular frequencies of the CBM μ . Equation 2.23 is a full description of the bunch dynamics in the frequency domain including the interaction with the impedance that may consists of a large number of longitudinal resonators. The CBMs for a case of $M = 4$ are illustrated in Fig. 2.6.

In case of a single bunch $M = 1$, $\mu = 0$, the index μ can be omitted and Eq. 2.23 simplifies to [29, Eq. 4.8]

$$\Omega^2 - \omega_s^2 = -i \frac{\omega_{\text{rev}} I_{\text{DC}} \alpha}{2\pi E/e} \sum_{p=-\infty}^{\infty} \left[p\omega_{\text{rev}} Z_0^{\parallel}(p\omega_{\text{rev}}) - (p\omega_{\text{rev}} + \Omega) Z_0^{\parallel}(p\omega_{\text{rev}} + \Omega) \right], \quad (2.24)$$

with the coherent frequency $\Omega = \omega_1$.

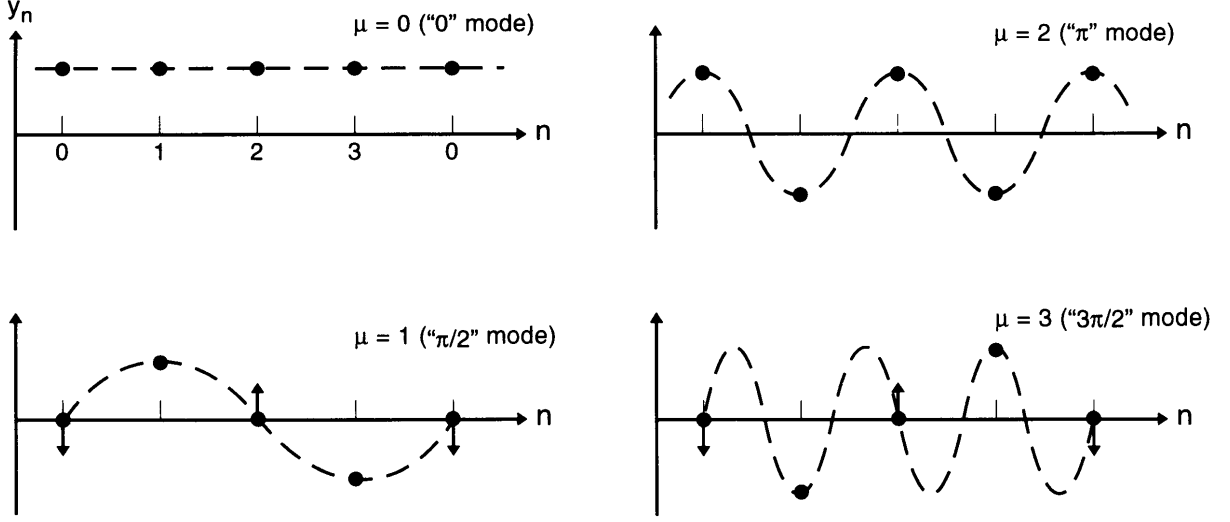


Figure 2.6.: Illustration of all CBMs for the case of four bunches $M = 4$. The bunch number is drawn on the horizontal axis. All bunches are drawn at one point in time with y_n expressing their momentary amplitude of the coordinate of interest (e. g., longitudinal or transverse position). Arrows indicate the momentary momentum. Its absence identifies a turning point. Figure reproduced from [29].

2.3.1. Growth Rate and Frequency Shift

The complex angular frequencies ω_μ are directly related to the growth rate and the frequency shift caused by the impedances. As $z \propto e^{-it\omega_\mu}$, see Eq. 2.21, the real part of ω_μ determines the oscillating frequency of the bunch motion while the imaginary part of ω_μ determines whether the amplitude of the motion is exponentially growing or decaying. The angular frequency shift $\Delta\omega_\mu$ and growth rate τ_μ^{-1} can then be defined as

$$\Delta\omega_\mu = \Re(\omega_\mu) - \omega_s \quad (2.25)$$

$$\tau_\mu^{-1} = \Im(\omega_\mu). \quad (2.26)$$

A positive growth rate indicates that the amplitude of the motion increases exponentially, i. e., a CBI is occurring. Analogously, negative τ_μ^{-1} indicates damping. A frequency shift does not influence the stability in this context and is usually ignored in the discussions of stability.

2. Theory of Coupled Bunch Instabilities

2.3.2. Case of Small Complex Frequency Shift

A common approximation is the case of small complex frequency shift, namely

$$\omega_\mu \approx \omega_s, \quad (2.27)$$

which is given when the induced field is not too strong. At full current, this approximation is valid for all realistic HOMs considered in this thesis. However, for the fundamental mode of a cavity, this approximation is typically violated. For the other modes of the fundamental pass band it must be checked on a case to case basis.

In this approximation, the l.h.s. of Eq. 2.23 can be written as $(\omega_\mu - \omega_s)2\omega_s$ which yields a linear algebraic equation in ω_μ . Furthermore, ω_μ on the r.h.s. can be replaced by ω_s , resulting in the following explicit expression for ω_μ :

$$\omega_\mu - \omega_s = -i \frac{\omega_{\text{rev}} I_{\text{DC}} \alpha}{4\pi\omega_s E/e} \sum_{p=-\infty}^{\infty} \left[pM\omega_{\text{rev}} Z_0^{\parallel}(pM\omega_{\text{rev}}) - ((pM + \mu)\omega_{\text{rev}} + \omega_s) Z_0^{\parallel}((pM + \mu)\omega_{\text{rev}} + \omega_s) \right]. \quad (2.28)$$

This expression can also be separated in real and imaginary parts to obtain the growth rate and the frequency shift [29, Eq. 4.9, Eq. 4.10]:

$$\Delta\omega_\mu = \frac{\omega_{\text{rev}} I_{\text{DC}} \alpha}{4\pi\omega_s E/e} \sum_{p=-\infty}^{\infty} \left[pM\omega_{\text{rev}} \Im Z_0^{\parallel}(pM\omega_{\text{rev}}) - ((pM + \mu)\omega_{\text{rev}} + \omega_s) \Im Z_0^{\parallel}((pM + \mu)\omega_{\text{rev}} + \omega_s) \right] \quad (2.29)$$

$$\tau_\mu^{-1} = \frac{\omega_{\text{rev}} I_{\text{DC}} \alpha}{4\pi\omega_s E/e} \sum_{p=-\infty}^{\infty} ((pM + \mu)\omega_{\text{rev}} + \omega_s) \Re Z_0^{\parallel}((pM + \mu)\omega_{\text{rev}} + \omega_s). \quad (2.30)$$

Despite the assumptions and simplifications, Eq. 2.30 is the most useful formula in the study of HOM driven longitudinal CBIs. Hence, a short discussions is presented in the following.

Equation 2.30 reveals the scaling of the growth rate with all relevant machine parameters. The appearance of most of the parameters in Eq. 2.30 can be justified readily. The growth rate scales with the average current, the value of the impedance and inversely to the beam energy. The latter via the beam rigidity. The proportionality to the revolution frequency becomes clear if it is considered that it describes how often the bunch passes the impedance in a given time. The more often it passes, the more kicks are accumulated and the more voltage is induced. The proportionality to the frequency of the induced voltage, $(pM + \mu)\omega_{\text{rev}} + \omega_s$, is plausible if it is considered that the synchrotron frequency is related not only to the voltage but to the product of voltage and frequency, as known

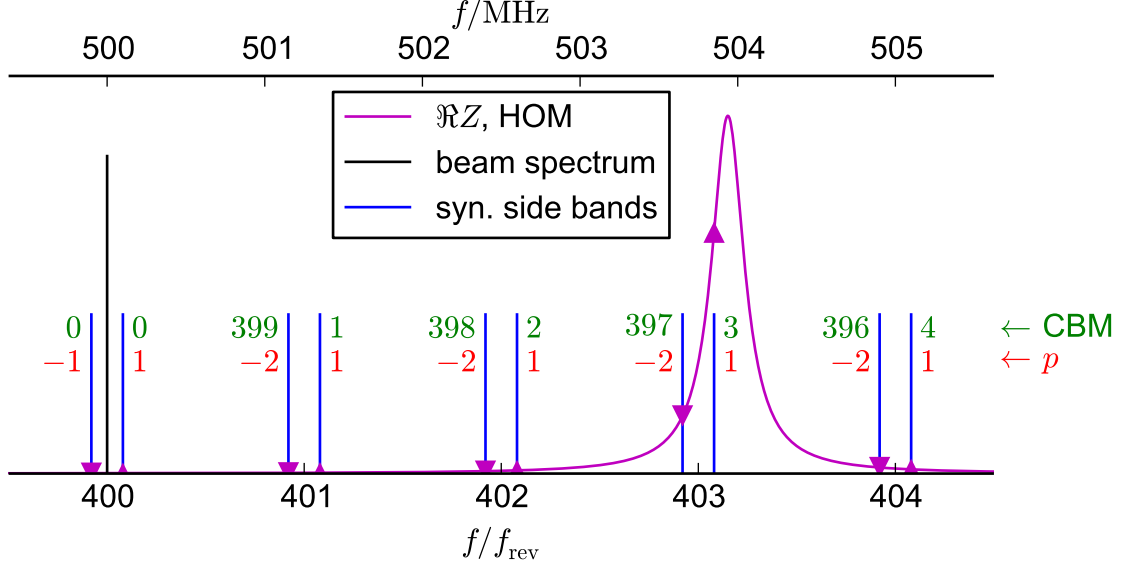


Figure 2.7.: Qualitative illustration of beam spectrum and CBM numbering for an even beam fill pattern at BESSY II along with the real part of the impedance of an HOM. For each side band, the triangles indicate the magnitude (vertical position) and sign (vertical pointing direction) of the contribution to the growth rate to the CBM. The CBM and p are defined as in Eq. 2.30.

from Eqs. 1.3 and 1.5.

Furthermore, Eq. 2.30 explains the relation of the CBMs to the frequencies of the beam spectrum. The even fill beam spectrum of BESSY II with its synchrotron side bands and the numbering of the CBMs and p along with an illustrative HOM impedances is shown in Fig. 2.7, i.e., it depicts the term $((pM + \mu)\omega_{\text{rev}} + \omega_s)$ in Eq. 2.30. In analogy to a spectrum analyzer, negative frequencies are mirrored into the positive frequency space. They can be identified by a negative p value. In even fill, the beam spectrum has components only at multiples of $Mf_{\text{rev}} = 500$ MHz. However, the possibility to sample the impedance and drive CBIs is equally large at all synchrotron side bands of all revolution harmonics. In a spectrum analyzer, a particular synchrotron side band is only visible if the beam performs an oscillation in the corresponding CBM, as used in the measurements explained in Section 4.2.2.

Figure 2.7 shows an example of an HOM with a resonance frequency close to 504 MHz. As can be seen, this particular HOM causes $\mu = 3$ to be unstable and $\mu = 397$ to be damped as indicated by the vertical position and pointing direction of the triangles. At other CBMs, the contribution to growth and damping is rather small.

2. Theory of Coupled Bunch Instabilities

Single sharply peaked resonator impedance

If the impedance consists of a single sharply peaked resonator impedance, i. e., described by Eq. 2.10, it is driven significantly at most by the two synchrotron side bands of one positive beam harmonic $pM + \mu$ with its angular frequency $\omega_{\text{beam}} = (pM + \mu)\omega_{\text{rev}}$. Thus, the summation over p can be omitted and only two CBMs remain, $\mu_+ = \mu$ and $\mu_- = M - \mu_+$. With another well justified approximation, $\omega_{\text{beam}} \gg \omega_s$, the following expression for the frequency shift and growth rate is obtained,

$$\Delta\omega_{\mu\pm} = \frac{\omega_{\text{rev}} I_{\text{DC}} \alpha}{4\pi\omega_s E/e} \left[\delta_{0\mu} \omega_{\text{beam}} \Im Z_0^{\parallel}(\omega_{\text{beam}}) - \omega_{\text{beam}} \Im Z_0^{\parallel}(\omega_{\text{beam}} \pm \omega_s) \right] \quad (2.31)$$

$$\tau_{\mu\pm}^{-1} = \pm \frac{\omega_{\text{rev}} I_{\text{DC}} \alpha}{4\pi\omega_s E/e} \omega_{\text{beam}} \Re Z_0^{\parallel}(\omega_{\text{beam}} \pm \omega_s), \quad (2.32)$$

with the Kronecker delta $\delta_{0\mu}$ indicating that the first term in Eq. 2.31 vanishes for $\mu \neq 0$. The first term in Eq. 2.31 is the static contribution induced by the beam spectrum itself, not its synchrotron side bands. As an even fill is assumed in this section, it has no other contributions but $\mu = 0$.

Case of $\mu = 0$ or AC Robinson instability

The special case of $\mu = 0$ of Eq. 2.31 reveals the so called AC Robinson instability [40] in the approximation of a small complex frequency shift, i. e., a relatively weak disturbance of the longitudinal dynamics. It is used to calculate the complex frequency shift of a fundamental cavity or of a higher harmonic cavity, such as a passive Landau cavity. For $\mu = 0$, μ_+ and μ_- are identical and zero, $\mu = \mu_+ = \mu_- = 0$, hence omitted in the following formulas for the angular frequency shift and growth rate:

$$\Delta\omega = \frac{\omega_{\text{rev}} I_{\text{DC}} \alpha}{4\pi\omega_s E/e} \omega_{\text{beam}} \left[2\Im Z_0^{\parallel}(\omega_{\text{beam}}) - \Im Z_0^{\parallel}(\omega_{\text{beam}} + \omega_s) - \Im Z_0^{\parallel}(\omega_{\text{beam}} - \omega_s) \right] \quad (2.33)$$

$$\tau^{-1} = \frac{\omega_{\text{rev}} I_{\text{DC}} \alpha}{4\pi\omega_s E/e} \omega_{\text{beam}} \left[\Re Z_0^{\parallel}(\omega_{\text{beam}} + \omega_s) - \Re Z_0^{\parallel}(\omega_{\text{beam}} - \omega_s) \right]. \quad (2.34)$$

If Eq. 2.34 gives a positive growth rate (instability), the so called AC Robinson instability is occurring. The sign of τ^{-1} is given by the difference of the real part of the impedance sampled at the left and right synchrotron side band. For a positive momentum compaction factor α , and recalling the shape of the real part of a longitudinal resonator impedance, Fig. 2.2 left, it is clear that the sign of τ^{-1} depends on the sign of the detuning Δf_r , i. e., whether the resonance frequency of the cavity is tuned above or below the beam frequency. The detuning Δf_r is defined as

$$\Delta f_r = f_r - f_{\text{beam}}, \quad (2.35)$$

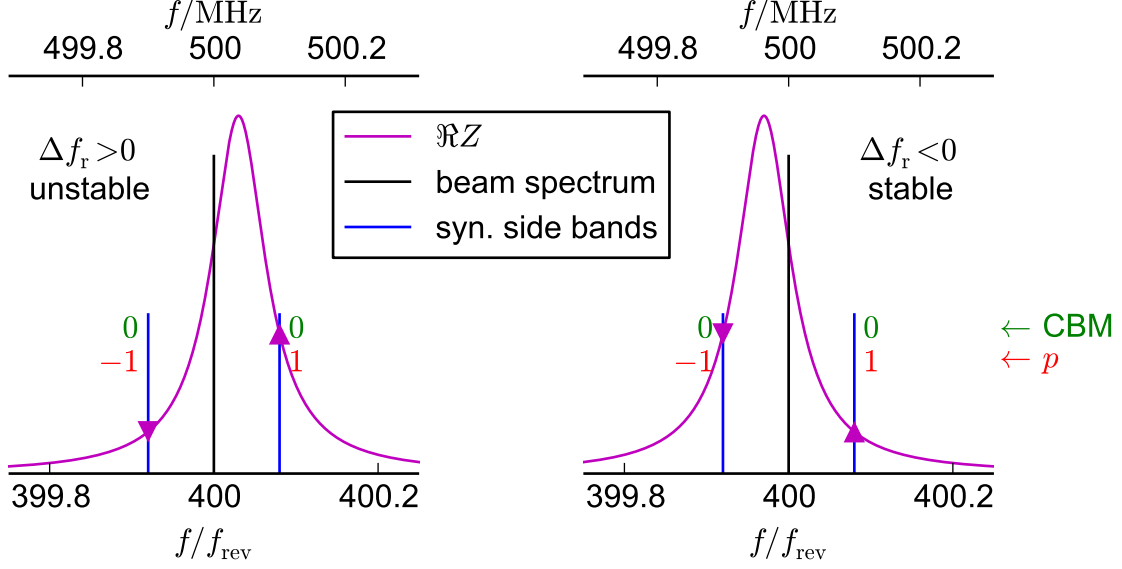


Figure 2.8.: Qualitative illustration of the AC Robinson stability criterion in the approximation of small frequency shift for positive α . For each side band, the triangles indicate the magnitude (vertical position) and sign (vertical pointing direction) of the contribution to the growth rate to the CBM $\mu = 0$. The CBM μ and p are defined as in Eq. 2.30. Left: Instability as $\Delta f_r > 0$. Right: Stability as $\Delta f_r < 0$.

with f_{beam} the frequency of a beam harmonic, e. g., $f_{\text{beam}} = 400f_{\text{rev}}$ for the fundamental RF cavities of BESSY II. The symbol f_{beam} is intentionally defined in a loose manner in order to be applicable to a wide range of problems where the appropriate beam harmonic depends on the particular case.

The application of Eq. 2.34 for the case of BESSY II, i. e., positive α , is illustrated in Fig. 2.8 for the fundamental RF cavities where the magnitude of the contribution of the side bands is indicated by triangles with the triangles pointing upwards for positive growth rates and pointing downwards for negative growth rates. The left panel shows a situation with $\Delta f_r > 0$, i. e., unstable because the right synchrotron side band samples an impedance value that is greater than the value where the left synchrotron side bands samples the impedance. Thus, the net impedance sampled by the CBM 0 is positive and the oscillation amplitude grows. The opposite situation, i. e., stability, is shown in the right panel.

Note that Eqs. 2.33 and 2.34 are not applicable for the SC cavities in BESSY VSR which are intended to provide very high fields to dominate the longitudinal dynamics instead of being a minor perturbation. Hence, the assumption in Eq. 2.27 is strongly violated for most cases. Further discussion on the subject of Robinson instabilities in BESSY VSR can be found in Section 5.5.

2.4. Longitudinal Bunch Motion for Uneven Fill

The case of small complex frequency shift discussed in Section 2.3.2, e.g., applicable for HOM driven CBIs, can be extended to arbitrary fill pattern, also called uneven fill in contrast to the even fill discussed above [41]. In an even fill, the solutions to the equations of motion, the CBMs, are the so called EFEMs defined in Eq. 2.22, together with the eigenvalue given by the complex coherent frequency ω_μ . In case of an uneven fill, the CBMs are a different set of solutions, consisting of linear combinations of the EFEMs. Their eigenvalues, corresponding to the complex tune shift, also take different values, meaning the instability threshold, defined by the fastest growing CBM, may be enhanced or reduced. The problem of obtaining the new CBMs along with their new eigenvalues reduces to a M -dimensional eigenvalue problem [30, Eq. 8.143],

$$(\Omega - \omega_s) \bar{z}_l = i \sum_{m=0}^{M-1} A_{lm} \bar{z}_m, \quad (2.36)$$

with l the index of the vector $\bar{\mathbf{z}} = (\bar{z}_1, \dots, \bar{z}_M)$ with the $M \times M$ matrix A_{lm} defined as [30, Eq. 8.144]

$$A_{lm} = \frac{\omega_{\text{rev}} I_{\text{DC}} \alpha}{4\pi \omega_s E / e} M \omega_{\text{rev}} I_{l-m} Z_{lm}(\omega_s), \quad (2.37)$$

with the usual constants and with I_{l-m} the complex amplitude of the $(l-m)$ -th revolution harmonic in the beam spectrum I_p defined as

$$I_p = \sum_{k=0}^{M-1} i_k e^{-i2\pi kp/M}, \quad (2.38)$$

where $p = 0, \dots, M-1$ indicates the harmonic, i_k the current of the k -th bunch and the so called mode-coupling impedance Z_{lm} , given by

$$Z_{lm}(\omega) = \frac{1}{M \omega_{\text{rev}}} \sum_{p=-\infty}^{\infty} \left[(pM \omega_{\text{rev}} + l \omega_{\text{rev}} + \omega) Z_0^{\parallel}(pM \omega_{\text{rev}} + l \omega_{\text{rev}} + \omega) - (pM \omega_{\text{rev}} + (l-m) \omega_{\text{rev}}) Z_0^{\parallel}(pM \omega_{\text{rev}} + (l-m) \omega_{\text{rev}}) \right]. \quad (2.39)$$

There are M solutions to Eq. 2.36, labeled with the CBM index μ , yielding M eigenvectors $\bar{\mathbf{z}}_\mu$ expressed in the basis of EFEM along with their M eigenvalues $\lambda_\mu = -i(\omega_\mu - \omega_s)$. The angular frequency shift $\Delta\omega_\mu$ and growth rate τ_μ^{-1} are then given by

$$\Delta\omega_\mu = \Re(\omega_\mu) - \omega_s = -\Im(\lambda_\mu) \quad (2.40)$$

$$\tau_\mu^{-1} = \Im(\omega_\mu) = \Re(\lambda_\mu). \quad (2.41)$$

Common methods of linear algebra can be applied. In this thesis, a software in C++ was written which delivers the complex synchrotron frequencies based on input files specifying the machine parameters and the impedance spectrum and further provides a graphical output of the eigenvectors. A similar program exists but does not supply the needed flexibility for this thesis [42, 43]. The software in this thesis utilizes the “ROOT” libraries [44] and the “Eigen” library [45] for the eigendecomposition of the complex matrix A_{lm} . Applications of the software along with a description of its full workflow are presented in Section 5.3.

2.5. Longitudinal Landau Damping

In accelerator physics, Landau damping, refers to a phenomenon where coherent oscillations are damped by means of decoherence. It is named after Lev Davidovich Landau who first described the general effect [46] which is now widely used in instability theory for accelerator physics, see references in [47] for details.

In this thesis, Landau damping will be discussed for cases where there is a frequency spread from bunch to bunch but not within individual electrons of a single bunch. For the cases presented in this thesis, i. e., transient beam loading in Chapter 6, this is the dominating effect. The theory is the same in both cases.

A very thorough analysis of longitudinal Landau damping in electron storage rings is given in [47]. The result extracted from that work and presented here describes the problem of Landau damping in terms of an equation for the angular coherent synchrotron frequency Ω , called the dispersion relation. By numerically solving this equation, solutions for Ω are obtained which immediately tell about the stability of the system. The dispersion relation can be considered as a generalization of Eq. 2.24, allowing each bunch to have its own synchrotron frequency.

The dispersion relation for a single HOM is defined as [47],

$$d(\Omega) = I_{\text{DC}}\omega_{\text{beam}}Z_0^{\parallel}(\omega_{\text{beam}} + \Omega), \quad (2.42)$$

with the dispersion function d ,

$$d(\Omega) = \left(i \frac{\tilde{\mu}}{M} \sum_{q=1}^M \frac{1}{\omega_{\text{sq}}^2 - \Omega^2 + 2i\delta_n\Omega} \right)^{-1}, \quad (2.43)$$

and the “condensed machine parameter” $\tilde{\mu}$,

$$\tilde{\mu} = \frac{\alpha}{T_{\text{rev}}E/e}, \quad (2.44)$$

with Ω the angular coherent frequency, I_{DC} the beam current, ω_{beam} some harmonic of the

2. Theory of Coupled Bunch Instabilities

revolution frequency, Z_0^\parallel a longitudinal resonator impedance of an HOM, M the number of bunches, ω_{sq} the unperturbed angular synchrotron frequency of bunch q , δ_n the dissipative damping rate (e. g., radiation damping) and the usual constants.

Solving Eq. 2.42 is not trivial as it is a nonlinear algebraic equation in the complex space. However, a simplification can be made if only the threshold of the instability is of interest. In this case, the search for solutions can be limited to cases where the growth rate is zero,

$$\tau^{-1} = -\Im(\Omega) = 0. \quad (2.45)$$

This reduces the parameter space for Ω from \mathbb{C} to \mathbb{R} , thus greatly enhancing the speed of a numerical calculation. Graphically, the search for Ω can be expressed by first plotting d for all real Ω in a reasonable interval and then increasing I_{DC} until the r.h.s. of Eq. 2.42 intersects with the line drawn by d .

If the resonance frequency of the HOM is not exactly known, it is reasonable to take a worst case approach which is realized by plotting the r.h.s. of Eq. 2.42 not only for a small interval of Ω but for all real Ω . This draws a circle with both the center and radius equal to $I_{\text{DC}}\omega_{\text{beam}}R_{\text{s},0}/2$ with $R_{\text{s},0}$ the shunt impedance of the HOM. Then, I_{DC} is increased until the circle intersects with the line drawn by d anywhere. Examples and applications of this method are shown in Section 6.3.4.

2.5.1. Small Effect Approximation and Vanishing Landau Damping

Instead of a complete deviation of the dispersion relation, it will only be shown that Eq. 2.42 is indeed a generalization of the formulas obtained in Section 2.3.

For small expected synchrotron shifts and small frequency spread, $\omega_{\text{sq}} \approx \Omega \approx \omega_{\text{s}}$, the same approximations as in Eq. 2.28 can be applied to Eq. 2.42, which yields the following relation,

$$d(\Omega) = \left(i \frac{\tilde{\mu}}{M} \sum_{q=1}^M \frac{1}{(\omega_{\text{sq}} - \Omega)2\omega_{\text{sq}} + 2i\delta_n\omega_{\text{sq}}} \right)^{-1} = I_{\text{DC}}\omega_{\text{beam}}Z_0^\parallel(\omega_{\text{beam}} + \omega_{\text{s}}). \quad (2.46)$$

This is not a linear equation in Ω , however the r.h.s. of Eq. 2.42 has become a constant, especially independent of Ω . The threshold is given by the largest I_{DC} where all Ω that solve Eq. 2.46 have no positive imaginary part.

If it is additionally assumed that there is no frequency spread from bunch to bunch, $\omega_{\text{s}} = \omega_{\text{sq}}$, the dispersion function becomes

$$d(\Omega) = \left(i \frac{\tilde{\mu}}{M} \frac{M}{\omega_{\text{s}}^2 - \Omega^2 + 2i\delta_n\Omega} \right)^{-1} = \frac{-i}{\tilde{\mu}}(\omega_{\text{s}}^2 - \Omega^2 + 2i\delta_n\Omega). \quad (2.47)$$

The dispersion relation then yields

$$(\omega_s^2 - \Omega^2) = i\tilde{\mu}I_{\text{DC}}\omega_{\text{beam}}Z_0^{\parallel}(\omega_{\text{beam}} + \Omega) - 2i\delta_n\Omega. \quad (2.48)$$

If the small amplitude approximation is used again on the l.h.s., i.e., $\omega_s^2 - \Omega^2 \approx (\omega_s - \Omega)2\omega_s$ the following is obtained,

$$(\omega_s - \Omega) = i\frac{\tilde{\mu}I_{\text{DC}}\omega_{\text{beam}}Z_0^{\parallel}(\omega_{\text{beam}} + \Omega)}{2\omega_s} - i\delta_n. \quad (2.49)$$

Again, the imaginary part of Ω relates to the growth rate. Note that due to the definition made in Eq. 2.42, the sign is opposite to what is used elsewhere in this thesis, compare Eq. 2.26. The growth rate can be calculated as

$$\begin{aligned} \tau^{-1} &= -\Im(\Omega) = \Im(\omega_s - \Omega) = \Im\left(i\frac{\tilde{\mu}I_{\text{DC}}\omega_{\text{beam}}\Re Z_0^{\parallel}(\omega_{\text{beam}} + \Omega)}{2\omega_s} - i\delta_n\right) \\ &= \frac{\omega_{\text{rev}}I_{\text{DC}}\alpha}{4\pi\omega_s E/e}\omega_{\text{beam}}\Re Z_0^{\parallel}(\omega_{\text{beam}} + \Omega) - \delta_n, \end{aligned} \quad (2.50)$$

which is identical to Eq. 2.32 if the term of the dissipative damping rate, δ_n , is dropped and only the upper side band is considered.

2.6. Transverse Bunch Motion

In this section, formulas for the HOM driven transverse CBIs will be derived. The formulas for the dipole oscillation, i.e., oscillations of the center of mass, use a point charge approximation. Consequently, the formulas are very similar to the longitudinal cases studied above, both for even and uneven fill. In addition, transverse quadrupolar motion, i.e., density oscillations may occur in the interaction with quadrupolar HOMs, more precisely with $m = 2$ resonator impedances, as described in Section 2.6.4.

2.6.1. Even Fill

In point charge approximation, the bunches can perform only dipole betatron oscillations in the horizontal or vertical plane. Due to the strong focusing in the transverse planes, the angular betatron oscillation frequency ω_β is much larger than the angular synchrotron frequency, i.e., $\omega_\beta \gg \omega_s$. As a consequence, the approximation of a small perturbation to the betatron oscillation frequency ω_β is almost always well justified. In this thesis, it is justified for all applications because the transverse impedance is given by HOMs of moderate strength.

2. Theory of Coupled Bunch Instabilities

In this approximation and assuming even fill, an algebraic equation for the coherent frequencies can be obtained in analogy to the longitudinal case, Eq. 2.28. The complex betatron frequency shift $\omega_\mu - \omega_\beta$ is given by [29, Eq. 4.114]

$$\omega_\mu - \omega_\beta = -i \frac{\omega_{\text{rev}} I_{\text{DC}}}{4\pi E/e} \frac{c}{\omega_\beta} \sum_{p=-\infty}^{\infty} Z_1^\perp((pM + \mu)\omega_{\text{rev}} + \omega_\beta), \quad (2.51)$$

with ω_μ the coherent betatron frequency of CBM μ , Z_1^\perp the transverse $m = 1$ impedance and the other M the number of equidistant bunches. It can be applied to both the horizontal or vertical plane.

There is no static term in the transverse case, i.e., proportional to $Z_1^\perp(pM\omega_{\text{rev}})$ for even fill, because the transverse force of the $m = 1$ wake potential does not depend on the offset [29, p. 174]. Without the static contribution, there is no transverse Landau damping effect expected from uneven fill patterns unlike in the longitudinal case [30, p. 348].

This formula can be made more accurate by the substitution $c/\omega_\beta = \beta$, which takes the value of the betatron function β as a weight for the localized impedance [30, Eq. 9.5] instead of a sort of averaged value. The betatron frequency shift and the growth rate are then given by

$$\Delta\omega_\mu = \frac{\omega_{\text{rev}} I_{\text{DC}}}{4\pi E/e} \beta \sum_{p=-\infty}^{\infty} \Im Z_1^\perp((pM + \mu)\omega_{\text{rev}} + \omega_\beta) \quad (2.52)$$

$$\tau_\mu^{-1} = -\frac{\omega_{\text{rev}} I_{\text{DC}}}{4\pi E/e} \beta \sum_{p=-\infty}^{\infty} \Re Z_1^\perp((pM + \mu)\omega_{\text{rev}} + \omega_\beta). \quad (2.53)$$

Equation 2.53 is the most useful formula for the calculation of HOM driven CBIs for the transverse case, similar to the meaning of Eq. 2.30 for the longitudinal case. The scaling with machine parameters is the same as in Eq. 2.30 for the revolution frequency, the current, the impedance and the current. A difference is the fact that the growth rate does not scale with the product of frequency and impedance, but only with the impedance itself. This is plausible, as the tune shift is not achieved by the time dependence of the field but only depends on its amplitude. The scaling with β is plausible as it describes how transverse momentum is translated into transverse displacement, i.e., a large β amplifies the feedback loop of the instability mechanism.

2.6.2. Chromaticity Dependence of Transverse CBIs

The mechanism of increasing the stability of transverse CBIs by increasing the chromaticity is not completely understood [48]. Apart from the effect described below, chromaticity causes transverse Landau damping which may contribute to increased stability. As will be shown, in terms of the effect described below, chromaticity is not particularly effective to increase the stability of HOM driven CBI, hence it is ignored in most parts of this

thesis.

In the transverse planes, the chromaticity ξ is defined via

$$\Delta Q_x = \xi \delta, \quad (2.54)$$

with δ the relative momentum deviation and ΔQ_x the horizontal chromatic tune shift respectively. The vertical plane is defined analogously. The betatron angular frequency shift due to chromaticity $\Delta\omega_\xi$ is defined as

$$\Delta\omega_\xi = \frac{\xi\omega_{\text{rev}}}{\alpha}, \quad (2.55)$$

with the momentum compaction α .

Among other parameters, the effect of the chromaticity on transverse instabilities in general strongly depends on the type of impedance and the bunch length. For long bunches in combination with a broad band impedances, such as the resistive wall impedance, chromaticity can have a strong effect on stability [49].

For a narrow impedance, such as cavity HOM, the effect of the chromaticity can be estimated by an additional form factor [49]. Equation 2.51 then becomes

$$\omega_\mu - \omega_\beta = -i \frac{\omega_{\text{rev}} I_{\text{DC}}}{4\pi E/e} \frac{c}{\omega_\beta} \sum_{p=-\infty}^{\infty} Z_1^\perp(\omega) F'_0(\omega - \Delta\omega_\xi), \quad (2.56)$$

with $\omega = (pM + \mu)\omega_{\text{rev}} + \omega_\beta$ and a form factor that can be estimated for Gaussian bunch shape by

$$F'_0(\omega) \approx h_0(\omega) \approx \exp\left(-\frac{\omega^2}{(2\pi/\sigma)^2}\right) \quad (2.57)$$

and $h_0(\omega)$ the squared absolute value of the envelope of the beam spectrum and σ the rms bunch length measured in units of time. For BESSY II, the form factor is nearly one for reasonable chromaticity values. For instance, for $\sigma = 20$ ps and an unreasonably large chromaticity of $\xi = 20$, the form factor is about 0.65. This is not a very significant reduction and considering the fact that the chromaticity is typically restricted to values $\xi \lesssim 5$ by other machine parameters, such as dynamic aperture, chromaticity is not a useful handle to reduce transverse CBIs driven by HOMs.

2.6.3. Uneven Fill

Equation 2.51 can also be extended to the case of uneven fill. Analogous to the longitudinal case, Section 2.4, the task of solving the equations of motion can be expressed as a M -

2. Theory of Coupled Bunch Instabilities

dimensional eigenvalue problem

$$(\Omega - \omega_\beta)\bar{z}_l = i \sum_{m=0}^{M-1} A_{lm}\bar{z}_m, \quad (2.58)$$

with l the index of the vector $\bar{\mathbf{z}} = (\bar{z}_1, \dots, \bar{z}_M)$ with the $M \times M$ matrix A_{lm} defined as,

$$A_{lm} = \frac{\omega_{\text{rev}} I_{\text{DC}}}{4\pi E/e} \beta M \omega_{\text{rev}} I_{l-m} Z_l^\perp(\omega_\beta), \quad (2.59)$$

with the usual constants, the complex amplitude of the beam spectrum defined in Eq. 2.38 and the so called transverse mode-coupling³ impedance Z_l^\perp , given by

$$Z_l^\perp(\omega) = \sum_{p=-\infty}^{\infty} Z_1^\perp(pM\omega_{\text{rev}} + l\omega_{\text{rev}} + \omega). \quad (2.60)$$

As explained above, the static term does not exist in the transverse case, leading to the increased simplicity of Eq. 2.59 compared to Eq. 2.37.

Again, there are M solutions to Eq. 2.58, yielding M eigenvectors with their eigenvalues $\lambda_\mu = -i(\omega_\mu - \omega_\beta)$. The angular frequency shift $\Delta\omega_\mu$ and growth rate τ_μ^{-1} are again given by

$$\Delta\omega_\mu = \Re(\omega_\mu) - \omega_\beta = -\Im(\lambda_\mu) \quad (2.61)$$

$$\tau_\mu^{-1} = \Im(\omega_\mu) = \Re(\lambda_\mu). \quad (2.62)$$

The computer code presented in this thesis includes the transverse case as well.

2.6.4. Quadrupolar Higher Order Modes

The effect of quadrupolar HOMs of cavities in circular accelerators does not seem to be a subject of studies published to date. Generally, longitudinal cavity HOMs can be considered to be the most critical plane in circular accelerators. HOM driven transverse dipole CBIs are typically much weaker compared to their longitudinal counterpart and often even below a recognizable limit [50, 51]. Transverse quadrupole HOMs are expected to be even weaker in comparison to transverse dipole HOMs, thus are usually not of interest.

However, in ERLs, the transverse instabilities are typically more critical than the longitudinal instabilities and instability studies for both, dipole and quadrupole HOMs are available [52–55].

³This unfortunate naming convention must not lead to a confusion with the mode-coupling instabilities in the sense of e.g. [30, Chap. 11].

2.6. Transverse Bunch Motion

In the context of BESSY VSR, where a new class of cavities is going to be installed in an electron storage ring, it is also possible that a parameter space is being entered where the quadrupole HOMs may not be negligible anymore. Thus, a method for the estimation of transverse quadrupole CBIs has been developed in this thesis.

The following formula for the growth rate of transverse quadrupole CBIs in a circular accelerator has been found empirically based on numerical studies with the tracking software presented in Section 3.2.1, based on the algorithm described in Section 3.1.4,

$$\tau^{-1}(M_2) \approx \frac{M_2}{2} \frac{\omega_{\text{rev}} I_{\text{DC}}}{4\pi E/e} \beta \Re Z_2^\perp(\omega_{\text{beam}} + 2\omega_\beta), \quad (2.63)$$

with M_2 the transverse quadrupole moment w. r. t. the reference orbit. Unlike the $m = 0$ and $m = 1$ case, the growth rate explicitly depends on the amplitude of the oscillation, i. e., the momentary quadrupole moment. Hence, the growth as a function of time of a point-like bunch with coordinate x , $M_2 = x^2$, is much faster than exponential,

$$x(t) \propto e^{x(t)^2 t \frac{\tau^{-1}(x_0^2)}{x_0^2}}, \quad (2.64)$$

with $x_0 > 0$ some constant.

Unfortunately, no experimental measurements to further validate Eq. 2.63 exists today. This naturally lies in the weak nature of quadrupolar HOMs, which has made it neither particularly pressing nor easy to measure and characterize the phenomenon in existing electron storage rings. Future experimental validation would require a cavity with strong quadrupolar HOMs and a suppression of dipolar HOM driven CBIs during the measurement, e. g., by means of a bunch-by-bunch feedback (BBFB).

3. Tracking Codes for Coupled Bunch Effects

This chapter depicts how the physics of coupled bunch effects can be addressed in the time domain by means of tracking codes based on the wake potential of a resonator impedance. In Section 3.1, the basic formulas for the interaction of the beam with a resonator impedances are derived explicitly for the longitudinal case and the transverse dipole and quadrupole case. Moreover, instructions for self-consistent algorithms are stated that are applicable to study CBIs as well as transient beam loading.

Some examples for the implementation of the algorithms are given in Section 3.2. In Section 3.3, general findings regarding HOM driven CBIs are obtained with the tracking codes which complement and extend the analytic results of Chapter 2.

3.1. Beam Interaction with Resonator Impedances

This section describes formulas necessary for the implementation of a self-consistent tracking code that describes the interaction of the beam with a resonator impedance.

The interaction of transverse beam moments of infinitesimally small longitudinal extension with resonator impedances of the first four orders in m are given by the relation of wake potentials to the wake functions in Tab. 2.1 and the wake functions of the resonator impedance Eqs. 2.13 and 2.14. The approximations made in Eqs. 2.13 and 2.14 are well justified for the cases studied in this thesis.

The accelerating voltage a bunch¹ experiences from a wake which was induced by a previous bunch¹ is given by the wake potential $c\Delta\vec{p}$ defined in Eq. 2.3, divided by the charge of the test particle, e ,

$$\vec{V}_{\text{acc}} = \frac{1}{e} \int_{-L/2}^{L/2} dz \vec{F}. \quad (3.1)$$

In this section, the bunches are assumed to be short compared to the wave length of

¹or a longitudinal slice thereof or an individual electron

3. Tracking Codes for Coupled Bunch Effects

the resonator impedances².

3.1.1. Longitudinal Case

The lowest order, $m = 0$, describes longitudinal resonators. As can be read out from Tab. 2.1, the transverse wake potential is zero, i. e., no transverse kicks are to be expected from such a resonator impedance. Furthermore, the longitudinal wake potential scales with the $m = 0$ beam moment, i. e., the charge q , hence it is independent of the transverse extension of the beam.

For $m = 0$, the accelerating voltage a bunch experiences from the wake induced by a previous bunch of charge q at a distance $-z$ can be written using Eqs. 2.5, 2.13 and 3.1,

$$V_{\text{acc}}^{\parallel}(z) = -qW'_0(z) = -q\frac{\omega_r R_{s,0}}{Q}e^{\frac{\omega_r z}{2Qc}}\cos\frac{\omega_r z}{c}. \quad (3.2)$$

The bunch also experiences a kick from its own induced field. According to the so called fundamental theorem of beam loading [56], the accelerating voltage the bunch experiences equals half the voltage it induces in the resonator impedance. For a bunch of charge q , the self-induced field is then given by

$$V_{\text{acc}}^{\parallel}\Big|_{\text{self}} = -\frac{q}{2}W'_0(0^-) = -\frac{q}{2}\frac{\omega_r R_{s,0}}{Q}, \quad (3.3)$$

with 0^- indicating that the function is evaluated at a negative value very close to zero. In order to comply with conservation of energy, the voltage in Eq. 3.3 must act decelerating, which is in accordance with the sign convention mentioned in Section 2.1.

The term on the r.h.s. of Eq. 3.3 represents the incoherent impedance losses which are sometimes described by means of a so called loss factor in literature [36, 57, 58].

With $t = -z/c$, time dependent wake functions can be defined and Eq. 3.2 can be written in time coordinates, expressing the accelerating voltage a probe would experience passing the impedance at a time $t > 0$ after a bunch with charge q has induced the wake,

$$V_{\text{acc}}^{\parallel}(t) = -qW'_0(t) = -q\frac{\omega_r R_{s,0}}{Q}e^{-\frac{\omega_r t}{2Q}}\cos\omega_r t. \quad (3.4)$$

In a circular accelerator, the bunches pass the impedance resonator many times and if there are multiple bunches in the ring, also many different bunches induce wakes in the impedance resonator. Hence, the accelerating voltage of a resonator impedance depends

²The restriction to short bunches is not a requirement to derive the formulas in this section and is only done to simplify the wording. E.g., Eq. 3.2 can also be used for long bunches if it is described as the accelerating voltage an infinitesimally small longitudinal slice of a bunch experiences from the wake induced by a previous infinitesimally small longitudinal slice of charge q at a distance $-z$. The effect on a slice is then the superposition of the wakes of all previous slices.

3.1. Beam Interaction with Resonator Impedances

on all previous bunch passages by all bunches,

$$V_{\text{acc}}^{\parallel}(t) = - \sum_{t_i=t_0}^{t_k} q(t_i) W_0'(t - t_i), \quad (3.5)$$

where t_0, \dots, t_k are the times at which a bunch has passed the impedance and $q(t_i)$ is the bunch charge of the bunch that passes at time t_i . A tracking code works as an iterative calculation, where the momentary acceleration field is calculated based on the last known field previously calculated. The time behavior of the wake function, Eq. 3.4, consists of an exponentially decaying term and a sinusoidal function. The frequency and the rate of the exponential decay are constants which allows to use trigonometric identities to reduce any sum of such wake functions to a single expression, characterized by an amplitude and a phase, see Appendix A.3. This means, the history of previous bunch interactions does neither need to be kept in memory, nor is it needed to compute the exact phasor at present time, which dramatically lowers the computational effort. For other types of wakes, e. g., the resistive wall wake, a reduction similar to Appendix A.3 is not possible [59].

The momentary acceleration field at time t can be calculated if the amplitude $A(t_{\text{last}})$ and phase $\phi(t_{\text{last}})$ of the last calculation are known,

$$A(t) = A(t_{\text{last}}) e^{-\frac{\omega_r(t-t_{\text{last}})}{2Q}} \quad (3.6)$$

$$\phi(t) = \phi(t_{\text{last}}) + \omega_r(t - t_{\text{last}}) \quad (3.7)$$

$$V_{\text{acc}}^{\parallel}(t) = A(t) \cos \phi(t). \quad (3.8)$$

Instead of amplitude and phase, it is more convenient to use the phasor notation in the complex plane. The accelerating voltage $V_{\text{acc}}^{\parallel}$ is represented by the real part of the complex phasor V . The phasor at time t and the accelerating voltage can be obtained by

$$\Delta\phi = \omega_r(t - t_{\text{last}}) \quad (3.9)$$

$$V(t) = V(t_{\text{last}}) e^{i\Delta\phi} e^{-\frac{\Delta\phi}{2Q}} \quad (3.10)$$

$$V_{\text{acc}}^{\parallel}(t) = \Re V(t), \quad (3.11)$$

with $\Delta\phi$ the angle by which the phasor needs to be rotated since the last passage. Conveniently, the imaginary part of the phasor, $\Im V$, is proportional to the time derivation of $\Re V$, hence it is proportional to the focusing gradient V' defined in Eq. 1.2,

$$V'(t) = \omega_r \Im V(t), \quad (3.12)$$

where an arbitrary sign convention has been chosen. For instance, V' can be used to obtain the synchrotron frequency for point-like bunches using Eq. 1.5.

The interaction of a bunch with charge q with the impedance at the time t simply adds

3. Tracking Codes for Coupled Bunch Effects

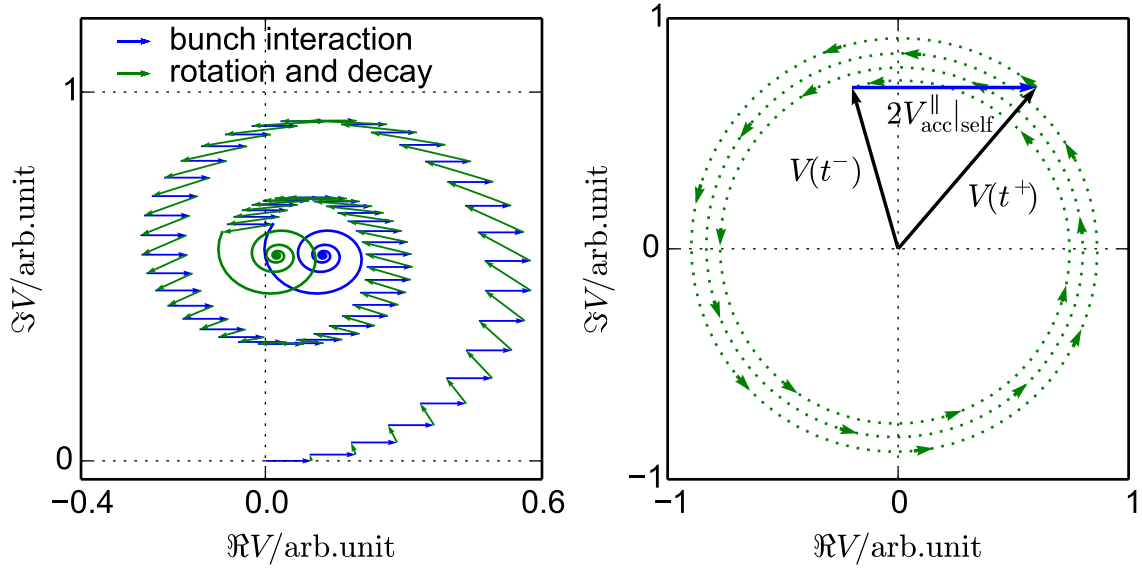


Figure 3.1.: Examples of the phasor representation of the beam impedance interaction and phasor rotation and decay in the complex plane. Left: Transient behavior of bunch interaction (blue arrows) and bunch rotation and decay (green arrows) for 60 consecutive bunch passes. The tips of the arrows converge to the steady state phasor values just before and after a bunch pass and are indicated by solid lines after the first 60 bunches for better visualization. Right: Steady state of a passive third harmonic Landau cavity tuned to bunch lengthening for even bunch fill pattern with 400 bunches. The steady state is manifested in the fact that the induced field of each bunch (blue arrow) exactly equals the net effect of decay and rotation (green spiral arrow). For bunch lengthening, a positive detuning, i.e., $\Delta f_r > 0$, is required. As a consequence, the phasor rotates faster than the third harmonic of the bunch frequency, resulting in a little more than three full revolutions, visualized by the spiral arrow.

a constant to the real part of the phasor,

$$V(t^+) = V(t^-) - q \frac{\omega_r R_{s,0}}{Q}. \quad (3.13)$$

The imaginary part of the phasor is unchanged.

Figure 3.1 shows two examples to illustrate the behavior of the phasor V . The instantaneous change of the phasor due to the bunch interaction, Eq. 3.13, is expressed by blue arrows. Green arrows indicate the rotation and decay of the phasor between two consecutive bunch passes, Eq. 3.10, where the arrow either represents the net effect (straight arrow) or the entire path (spiral arrow).

3.1. Beam Interaction with Resonator Impedances

The energy lost or gained by the bunch by this interaction is described by the self-induced losses, Eq. 3.3, plus the energy loss or gain by the accelerating field given by the present state of the phasor, Eq. 3.11. Together, the net voltage a bunch experiences by the interaction at time t reads as

$$V_{\text{acc}}^{\parallel} = V_{\text{acc}}^{\parallel} \Big|_{\text{self}} + \Re V(t^{-}). \quad (3.14)$$

A tracking code only needs three steps for a self-consistent treatment of the bunch-impedance interaction:

1. Keep the values of t_{last} and $V(t_{\text{last}})$ in memory (3 floating point scalars).
2. Calculate the new values of V at each passage of bunch with Eqs. 3.9, 3.10 and 3.13.
3. Calculate the new energy of the bunch after each passage with Eq. 3.14.

Similar implementations with phasor addition and rotation can be found in other tracking codes [59–65].

3.1.2. Feedback Controlled Cavities

The scheme discussed in Section 3.1.1 can also be used for the fundamental mode of a cavity which results in a realistic behavior of a passive cavity. An active cavity can be described as a passive cavity that is continuously driven by a generator current [36]. In this thesis, a very simplified model of a the generator is used, as described in the following.

First, target values are set for the active cavity in terms of phase and amplitude. After each turn, the feedback loop compares the target values with the momentary values and calculates the difference in terms of phase an amplitude. The calculated difference is then added to cavity phasor in equal discrete steps over the course of the next turn. The discrete steps are chosen such that the phasor addition takes place between the arrival times of nominal bucket positions.

The motivation of this implementation is to obtain a feedback that does not react within a turn but reacts quickly from one turn to another. This resembles a realistic feedback in the sense that for times scales in the order of the revolution period, a feedback can barely react [2], but it is relatively fast in reaching the equilibrium state that any slow feedback will eventually reach. Hence, the simplified model allows to study quite realistically transient beam loading induced by uneven fill, see Chapter 6.

Similar work with the goal to implement feedback controlled cavities in a tracking code for beam dynamics is ongoing at another laboratory [66]. Other simulation codes, for example [67, 68], come with a much stronger focus on realistic cavity control theory and are considered complementary to the software presented in this thesis.

3. Tracking Codes for Coupled Bunch Effects

3.1.3. Transverse $m = 1$ Case

The next order, $m = 1$, describes dipolar resonators. Unlike the $m = 0$ case, both the transverse wake potential and the longitudinal wake potential are non-zero, see Tab. 2.1, and scale with the $m = 1$ beam moment, i.e., the transverse dipole moment. The longitudinal wake potential further scales with the transverse coordinate of the probing bunch while the transverse wake potential is independent of the transverse coordinate, which equals the behavior of common dipole magnet.

For $m > 0$, there are two orthogonal multipoles possible for each m . Without loss of generality, the bunch is assumed to possess a purely normal dipole in x direction. The $m = 1$ transverse moment of the bunch is given by,

$$M_1 = \langle x \rangle, \quad (3.15)$$

where the angle brackets indicate the averaging over the x coordinates of all electrons of the bunch. M_1 is the center of mass in x direction.

The phasor can be defined by its calculation after a bunch passage with charge q and dipole moment M_1 ,

$$V(t^+) = V(t^-) - M_1 q \frac{\omega_r R_{s,1}}{Q}, \quad (3.16)$$

and the transformation rules given in Eqs. 3.9 and 3.10. Here, the important point is the usage of the charge and the dipole moment of the bunch as a weight when the wake functions are added to form a phasor. The longitudinal and transverse kicks on the bunch that passes the impedance are given by Tab. 2.1,

$$V_{\text{acc}}^{\parallel} = -M_1^2 \frac{q}{2} \frac{\omega_r R_{s,1}}{Q} + x \Re V(t^-) \quad (3.17)$$

$$\vec{V}_{\text{acc}}^{\perp} = -\frac{c}{\omega_r} \Im V(t) \hat{x}, \quad (3.18)$$

with \hat{x} the unit vector in x direction. The first term in Eq. 3.17 is the energy loss due to its self induced fields. The transverse kick, Eq. 3.18, is obtained from the transverse wake function given in Eq. 2.14 and the fact that the transverse wake function is defined as the derivative of the longitudinal wake function with respect to z , yielding the relation

$$\frac{d}{dz} \Im V(t) = -\frac{1}{c} \frac{d}{dt} \Im V(t) = \frac{\omega_r}{c} \Re V(t). \quad (3.19)$$

The transverse kick does not have a self-induced component, as the transverse wake function goes as a sine, i.e., it is zero at small arguments.

A self-consistent tracking code can be written following the steps in Section 3.1.1 and

using Eqs. 3.16 to 3.18 instead of Eqs. 3.13 and 3.14.

3.1.4. Transverse $m = 2$ Case

In the $m = 2$ case describes the interaction with quadrupolar resonator impedances. Compared to the $m = 2$ case, the transverse wake potential is additionally dependent on the transverse coordinates of the probing bunch. The dependence equals the behavior of a common quadrupole magnet.

The normal $m = 2$ transverse moment of the bunch is given by

$$M_2 = \langle x^2 - y^2 \rangle, \quad (3.20)$$

see Tab. 2.1, where the angle brackets indicate the averaging over both transverse coordinates over all electrons of the bunch. M_2 is the normal quadrupole moment in the $x - y$ plane. The phasor can be defined by its calculation after a bunch passage with charge q and quadrupole moment M_2 ,

$$V(t^+) = V(t^-) - M_2 q \frac{\omega_r R_{s,2}}{Q}, \quad (3.21)$$

and the transformation rules given in Eqs. 3.9 and 3.10. Again, the charge and the moment of the bunch are used as a weight when the wake functions are added to form a phasor. The longitudinal and transverse kicks on the electrons of the bunch that passes the impedance are given by Tab. 2.1 and depend on the position x and y of the electron within the bunch,

$$V_{\text{acc}}^{\parallel}(x, y) = -(x^2 - y^2) M_2 \frac{q \omega_r R_{s,2}}{2Q} + (x^2 - y^2) \Re V(t^-) \quad (3.22)$$

$$\vec{V}_{\text{acc}}^{\perp}(x, y) = -2(\hat{x}x - \hat{y}y) \frac{c}{\omega_r} \Im V(t), \quad (3.23)$$

with \hat{x} and \hat{y} the unit vectors in x and y directions. The fact that the position information appears in a squared form, i. e., independent of the sign, gives rise to a potential quadrupolar motion. The structure of Eqs. 3.22 and 3.23 can be explained as above and a self-consistent tracking code can again be written following the steps in Section 3.1.1 and using Eqs. 3.21 to 3.23 instead of Eqs. 3.13 and 3.14.

3.2. Implementations in Tracking Codes

A number of implementations of the algorithms above have been written in the course of this thesis. This includes a very demonstrative Python code, a more complex longitudinal C++ code, and personal extensions to the existing software “mbtrack” [69].

3. Tracking Codes for Coupled Bunch Effects

3.2.1. Minimal Demonstrative Code

The Python source code of a so called minimal working example of the $m = 1$ and $m = 2$ implementations described in Sections 3.1.3 and 3.1.4 is presented in Appendix A.4. The coupling between the transverse and longitudinal plane has been ignored and only one transverse coordinate, the horizontal one, is considered. Another simplification is the fact that only one bunch is in the machine, consisting of one macro particle. Otherwise, the BESSY VSR parameters are used. Despite the simplifications, the code is very useful as it allows to study scenarios not covered with the analytic formulas, e. g., their validity in terms of Q , see Section 3.3.4. In addition, it was used to provide an empirical formula for the prediction of the growth rate of the CBI for the $m = 2$ case, see Section 3.3.2.

3.2.2. Longitudinal Stand-alone Tracker

A somewhat more advanced, self-consistent tracking code for the longitudinal plane was written in C++. The bunches are still described by one macro particle each, but any number of bunches and bunch fill pattern can be simulated. The effect of the magnet optics on the longitudinal dynamics is expressed by a constant momentum compaction factor. The transverse planes are not simulated.

The cavities can be modeled either by exact sinusoidal functions applying a kick without being affected by the beam or they can be feedback controlled cavities that are continuously powered by a generator and interact with the beam as a resonator impedance, as explained in Section 3.1.2.

An individual constant energy loss per turn for each bunch, Gaussian noise and exponential damping of the energy coordinate are available to emulate the effects of synchrotron radiation losses, quantum excitation and radiation damping.

Longitudinal resonators, e. g., passive cavities or HOMs, are treated by the method described in Section 3.1.1.

The tracking code can be used to study longitudinal CBI for arbitrary fill pattern, including its fill pattern dependency and Landau damping from the bunch to bunch spread in synchrotron frequencies [70]. Furthermore, the effects of transient beam loading induced by the fundamental modes of any number of active and passive cavities can be studied [2, 71]. See Section 6.1.3 for examples presented in this thesis.

3.2.3. Extensions to the Third Party Software “mbtrack”

In addition to the stand-alone tracking codes described above, a personal copy of the full-feature three dimensional tracking code “mbtrack” [69] was extended for this thesis to support the interaction of the beam with transverse $m = 1$ and $m = 2$ resonator impedances. Longitudinal resonator impedances are already supported by “mbtrack” [59, 72]. In the course of writing the extensions for transverse resonator impedances, an

3.3. General CBI Findings Obtained from Tracking Codes

implementation of the longitudinal case was also written and agreement with “mbtrack”’s original functions could be shown.

“mbtrack” is a multi-particle tracking code. The implementations were done in three different longitudinal methods. In the first method, only the longitudinal center of mass is taken to calculate the induced field and the kick which is the same for all electrons of the bunch. Second, a binned method was implemented, very similar to the existing methods in “mbtrack”. In those methods, the longitudinal bunch distribution is binned and each slice is treated consecutively. This allows for intra-bunch effects transmitted by long range resonators. The third implementation is an unbinned calculation, meaning the entire set of macro particles is ordered by arrival time and each macro particle induces its own field and experiences a kick depending on the field already present and induced by previous macro particles. Obviously, the computational efforts strongly increase from the first to the third method, if the number of macro particles is large.

For short bunches, the center of mass mode is usually accurate enough, see Appendix A.2. However, longitudinal intra-bunch Landau damping can be seen only in binned or unbinned methods.

Another tracking code that was not used in this thesis but officially supports $m \leq 2$ resonator impedances is described in [73].

3.3. General CBI Findings Obtained from Tracking Codes

All the general findings obtained from tracking simulations in this section are obtained with the Python code described in Section 3.2.1 and printed in Appendix A.4. However, the general dynamics of the longitudinal stand-alone tracker described in Section 3.2.2 has also been successfully cross checked against analytic expectations. Hence, the same results in the longitudinal cases can also be obtained from this code as well.

3.3.1. Comparison of Growth Rate with Analytic Formulas

In this section, the tracking algorithm is applied to the case of HOM driven CBIs and compared to the analytic expressions given in Eqs. 2.53 and 2.63.

The code can be used to obtain the growth rate of the instability by fitting an exponential function to the envelop of the transverse coordinate of the trajectory. The transverse coordinate along with the imaginary part of the phasor is shown in Figs. 3.2 and 3.3. Those plots are obtained from the arrays produced in the code segments labeled “demo 1” and “demo 2” shown in Appendix A.4. Except for the export and plotting of the arrays \mathbf{ax} and \mathbf{aV} , the code shown in Appendix A.4 is complete for the exact reproduction of the trajectories shown in the figures. It includes the BESSY II standard parameters from Tab. 1.1 and realistic HOM parameters with $f_r \approx 1 \text{ GHz}$, $Q = 1 \times 10^4$, $R_{s,1} \approx 1.9 \times 10^8 \Omega \text{m}^{-2}$, $R_{s,2} = 1 \times 10^{13} \Omega \text{m}^{-4}$ and a horizontal start amplitude of 1 mm.

3. Tracking Codes for Coupled Bunch Effects

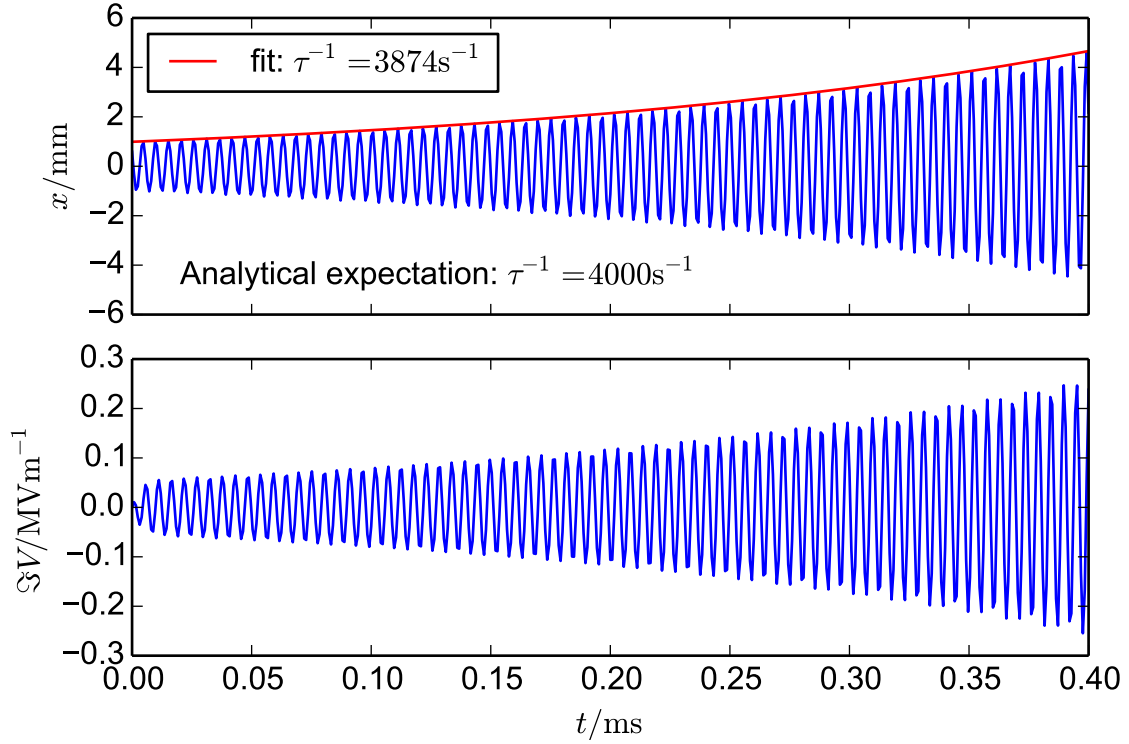


Figure 3.2.: Simulation of a transverse $m = 1$ impedance with the code described in Section 3.2.1. Transverse coordinate and fit to its envelop (top) and imaginary part of phasor (bottom) as a function of time. The analytic expectation for the growth rate is obtained by means of Eq. 2.53.

One difference to a realistic scenario is the fact that only one bunch containing the entire charge is simulated in the ring, which does not change the results unless Q becomes too small, as discussed in Section 3.3.4.

As can be seen, the agreement in terms of growth rate of simulation and analytic expectation is in the order of 95% for the $m = 1$ case. The remaining difference can be attributed to the discrete nature of the simulation and the finite number of simulation steps. For the $m = 2$ case, no analytic expectation for the growth rate is available which is why the analytic expression given in Eq. 2.63 was derived based on studies with this very code. The agreement of simulation and the expectation is then given by construction, of course.

3.3.2. Empirical Formula for the $m = 2$ Growth Rate

The empirical formula for the $m = 2$ growth rate given in Eq. 2.63 has been found by evaluating the scaling of all input parameters in the simulation code. Furthermore, a

3.3. General CBI Findings Obtained from Tracking Codes

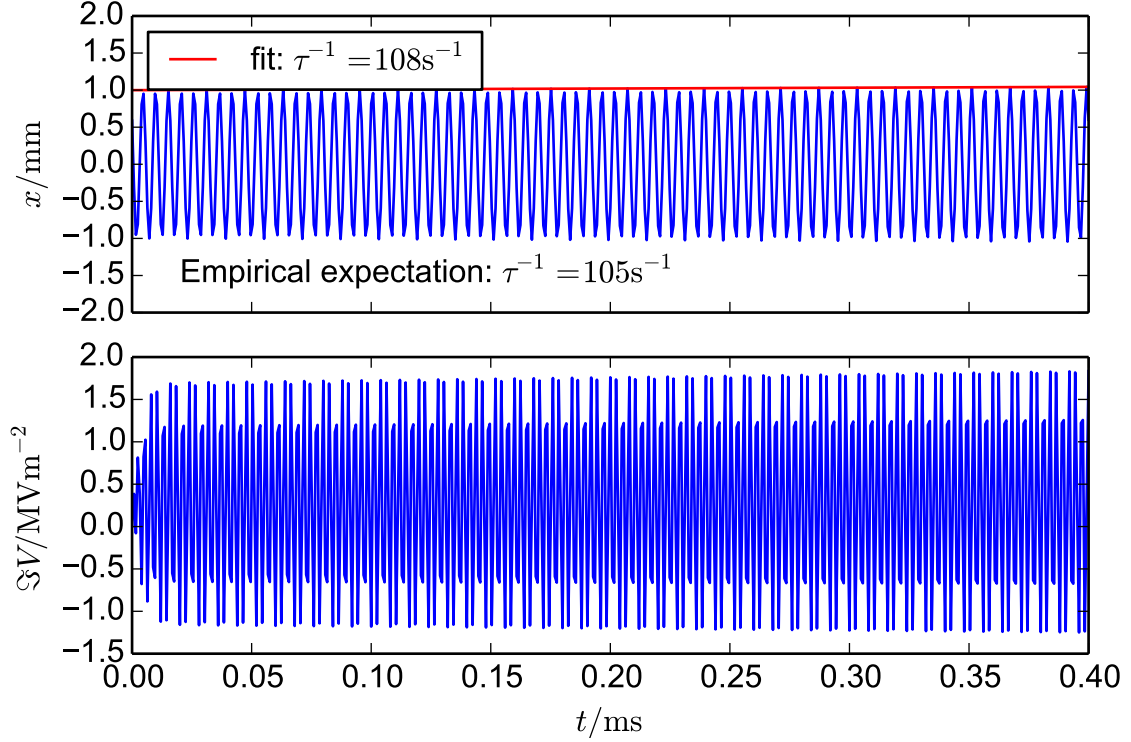


Figure 3.3.: Simulation of a transverse $m = 2$ impedance with the code described in Section 3.2.1. Transverse coordinate and fit to its envelop (top) and imaginary part of phasor (bottom) as a function of time. The expectation for the growth rate is obtained by means of Eq. 2.63.

comparison with the known $m = 1$ formula given in Eq. 2.53 was made and finally a numerical comparison revealed another constant factor of two.

The major difference of $m = 2$ compared to $m = 1$ and the longitudinal $m = 0$ case is the amplitude dependence of the growth rate, i. e., the scaling with M_2 . In the $m = 1$ and $m = 0$ cases, the frequency and growth rate do not depend on the amplitude of the oscillation, as expected from a perfect harmonic oscillator. In reality, an amplitude dependence might still occur in those cases but it is usually very small.

In contrast, the amplitude dependence for the $m = 2$ growth rate seems to be very strong, as illustrated in Fig. 3.4 for simulation runs with different starting values for the transverse coordinate x_{start} . In Fig. 3.4 left, it can be seen that the growth is faster than exponential. The right panel of Fig. 3.4 shows that the growth rate scales with $M_2 = x_{\text{start}}^2$ up until a point where the growth is so fast that the amplitude has grown too much in the interval that is used to fit the growth rate.

3. Tracking Codes for Coupled Bunch Effects

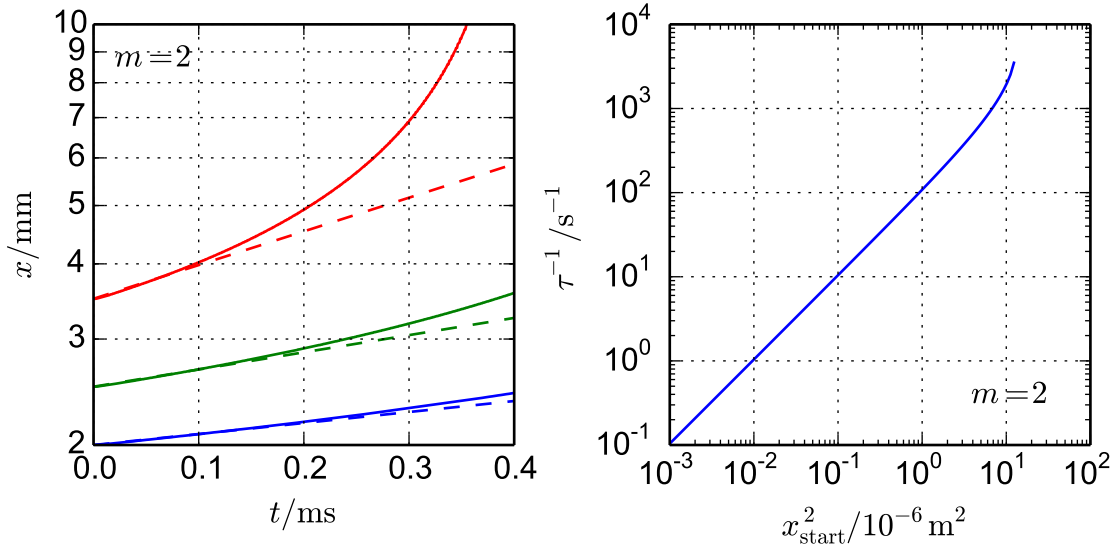


Figure 3.4.: Left: Tracking simulation of time behavior of the envelop of the transverse coordinate (solid lines) during an instability driven by a transverse $m = 2$ impedance for three different starting amplitudes (colors). Dashed lines indicate the expected behavior for the hypothesis of exponential growth. Right: Tracking simulation of growth rate as a function of squared starting amplitude. The linearity is clearly visible until very large growth rates where the change of amplitude during the course of the simulation is large and the fit of the growth rate by applying an exponential function begins to fail.

3.3.3. Dependence of Transverse HOM Offset

The simulation code can also be used to study the effect of a transverse displacement of the electromagnetic HOM center with respect to the reference orbit of the beam. This may happen by misalignment of the cavities, by steering the beam through the cavities with an offset or by HOMs with an intrinsically shifted center, see for example [33].

The equations describing the HOM interaction of the longitudinal $m = 0$ case are independent of the transverse coordinate, so no offset dependence can occur. In the transverse $m = 1$ case, transverse coordinate appears in the equations and the question of the influence of a transverse offset on the dynamics has to be studied. From analytic considerations, the growth rate of the CBI is not expected to be dependent on the transverse offset. Instead, the center of oscillation of the CBI will be changed to the offset. The independence of the offset is confirmed by the simulations shown in the tracking simulations in the left panel in Fig. 3.5, where the growth rate is virtually constant over the entire range of realistic transverse HOM offsets for the $m = 1$ case.

In the $m = 2$ case, the situation is very different. It shows a strong dependence on the offset, as shown in the tracking simulation in Fig. 3.5 right panel. The relationship of the

3.3. General CBI Findings Obtained from Tracking Codes

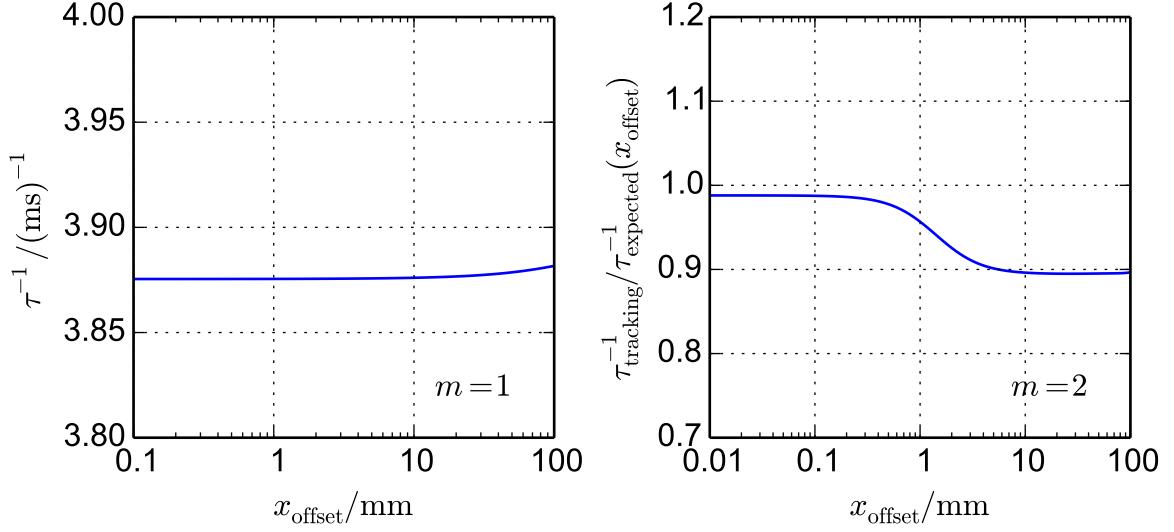


Figure 3.5.: Left: Tracking simulation of growth rate of an instability driven by a transverse $m = 1$ impedance as a function of transverse HOM offset. Right: Tracking simulation of growth rate divided by the expected growth rate evaluated by Eq. 3.24 for an instability driven by a transverse $m = 2$ impedance as a function of transverse HOM offset.

transverse HOM offset x_{offset} to the growth rate can be expressed by an explicit formula,

$$\tau_{\text{expected}}^{-1}(M_2, x_{\text{offset}}) \approx \frac{M_2 + \frac{1}{2}x_{\text{offset}}^2}{2} \frac{\omega_{\text{rev}} I_{\text{DC}}}{4\pi E/e} \beta \Re Z_2^\perp(\omega_r). \quad (3.24)$$

which is a generalization of Eq. 2.63. The approximate validity of this formula is shown in Fig. 3.5 right panel where the tracking simulation differs by no more than about 10% for realistic values of x_{offset} .

The x_{offset} dependence of quadrupolar HOMs can also be understood by looking at Eqs. 3.21 and 3.23. If small oscillation amplitudes x_0 are considered at a constant offset, i.e., setting $x = x_0 + x_{\text{offset}}$ with $x_0 \ll x_{\text{offset}}$ in those equations and implying $y = 0$ and $M_2 = x^2$, the phasor addition and kick take the following form:

$$V(t^+) = V(t^-) - M_2 q \frac{\omega_r R_{s,2}}{Q} \approx V(t^-) - (x_{\text{offset}}^2 + 2x_0 x_{\text{offset}}) q \frac{\omega_r R_{s,2}}{Q} \quad (3.25)$$

$$\vec{V}_{\text{acc}}^\perp = -2\hat{x}x \frac{c}{\omega_r} \Im V(t) \approx -2\hat{x}x_{\text{offset}} \frac{c}{\omega_r} \Im V(t). \quad (3.26)$$

The approximations $(x_0 + x_{\text{offset}})^2 \approx x_{\text{offset}}^2 + 2x_0 x_{\text{offset}}$ and $(x_0 + x_{\text{offset}}) \approx x_{\text{offset}}$ were used to obtain the results. As can be seen, the x_0 dependence of those equations is now exactly as in the $m = 1$ case, see Eqs. 3.16 and 3.18. In other words, a transversely

3. Tracking Codes for Coupled Bunch Effects

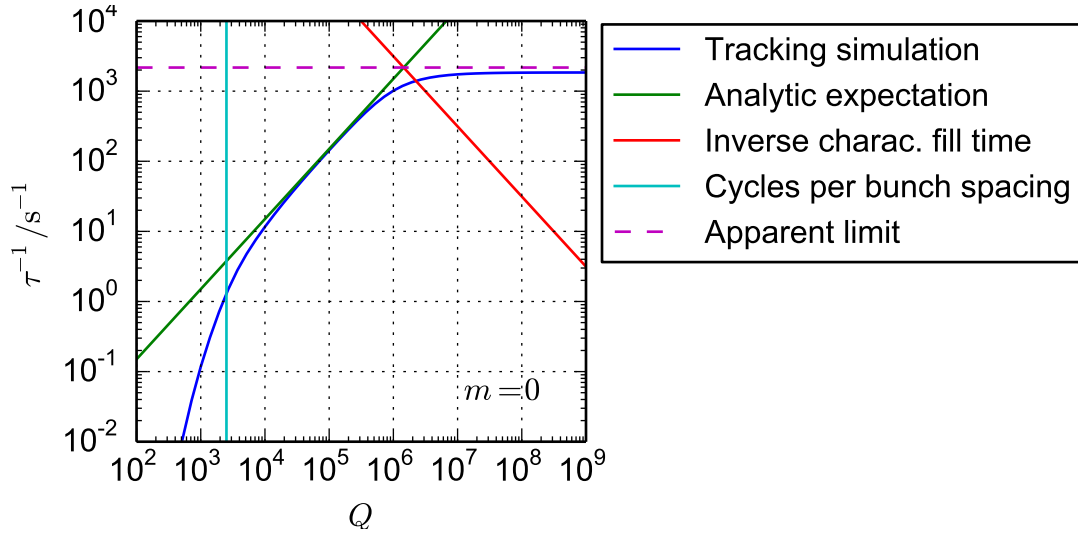


Figure 3.6.: Growth rate of longitudinal $m = 0$ case as a function of Q for constant $R_{s,0}/Q$. The tracking simulation (blue) is compared to the analytic estimation given by Eq. 2.30 (green). The cycles per bunch spacing define a lower limit for Q while an upper limit is given by the inverse of the characteristic fill time τ_c .

shifted quadrupole impedance acts like a dipole impedance with an equivalent $m = 1$ shunt impedance given by the offset x_{offset} ,

$$(R_{s,1})_{\text{equivalent}} = 4x_{\text{offset}}^2 R_{s,2}. \quad (3.27)$$

The factor $4x_{\text{offset}}^2$ complies with the comparison of Eq. 2.53 with Eq. 3.24.

3.3.4. Q Limits for Analytic Formulas

The tracking code can also show the limits of the analytic estimations of the growth rates, Eqs. 2.30 and 2.53, in terms of the quality factor Q .

Longitudinal $m = 0$ case

With slight changes in the tracking code described in Section 3.2.1, the longitudinal $m = 0$ case described in Section 3.1.1 can be studied as well.

The comparison of the growth rate obtained with the tracking code and Eq. 2.30 is shown in Fig. 3.6 for a reasonable parameter set. As can be seen, a lower and an upper limit for the validity of Eq. 2.30 in terms of Q appears.

The lower limit can be explained by the fact that the estimations in Eq. 2.30 require that the HOM field has not decayed significantly between two bunch passes. This is expressed by the relation of oscillation cycles to bunch repetition frequency and defines a

3.3. General CBI Findings Obtained from Tracking Codes

lower limit for Q as $\omega_r/2/(Mf_{\text{rev}})$. In this case, the lower limit for Q is $\omega_r/2/f_{\text{rev}}$ because only one bunch is simulated in the machine for simplicity. For more realistic calculations, e. g., even fill with 400 bunches and an HOM at $\omega_r = 2.0$ GHz, the lower limit for Q is estimated as 12.5, which is a very low quality factor, even for strongly damped HOMs. Hence, the lower limit is not expected to become relevant for the calculation of HOM driven CBIs.

An upper limit in Q for the validity of Eq. 2.30 is given by the characteristic fill time of a resonator,

$$\tau_c = \frac{2Q}{\omega_r}. \quad (3.28)$$

As the name suggests, it describes how fast a resonator, e. g., a cavity, is filled when a constant current is applied. In the theory of CBIs, the field in the resonator grows proportionally to the oscillation amplitude of the bunches. If τ_c is very large, i. e., high Q , the growth is limited and does not scale linear with Q anymore as Eq. 2.30 would normally suggest for constant $R_{s,1}/Q$. Instead, the simulation suggests that the growth rate does actually reach a limit given by

$$\tau_{\text{limit}}^{-1} = \omega_r \sqrt{\frac{1}{2} \frac{R_{s,0}}{Q} \frac{\omega_{\text{rev}} I_{\text{DC}} \alpha}{4\pi\omega_s E/e}}, \quad (3.29)$$

to be found at the intersection of the curves given by the inverse of τ_c and given by formula for the analytic approximation. The Q value for this intersection defines the limit at

$$Q_{\text{limit}} = \frac{1}{\sqrt{2 \frac{R_{s,0}}{Q} \frac{\omega_{\text{rev}} I_{\text{DC}} \alpha}{4\pi\omega_s E/e}}}. \quad (3.30)$$

As an example, the SPMs are a candidate where the upper Q limit may be reached as they posses very high Q at very low $R_{s,0}/Q$ values. Table 3.1 shows the calculation of the growth rate and its limit for the cavity model “HZB 2c coax. coupler”. The calculations indeed show that the analytic formula given in Eq. 2.30 overestimates the expected growth rates by factors up to several hundred. Hence, the SPMs appear to be much less hazardous than expected from their shunt impedance $R_{s,0}$ alone. With those results, only one SPM exceeds the BBFB threshold by a factor of about two, see also discussions in Chapter 5.

Transverse $m = 1$ case

The equivalent comparison for the $m = 1$ case is shown in Fig. 3.7. An empirical limit for the growth rate in terms of Q is found to be

$$\tau_{\text{limit}}^{-1} = \sqrt{\frac{c}{2} \frac{R_{s,1}}{Q} \frac{\omega_{\text{rev}} I_{\text{DC}}}{4\pi E/e}} \beta, \quad (3.31)$$

3. Tracking Codes for Coupled Bunch Effects

Table 3.1.: Longitudinal growth rates of the CBI given if the SPMs of the cavity model “HZB 2c coax. coupler” are driven on resonance for BESSY VSR parameters. The growth rate τ^{-1} is estimated with the analytic formula given in Eq. 2.30 and τ_{limit}^{-1} is calculated with Eq. 3.29.

Frequency GHz	Q 1×10^8	$R_{s,0}/Q$ Ω	τ^{-1} $(\text{ms})^{-1}$	τ_{limit}^{-1} $(\text{ms})^{-1}$
1.455	15.1	0.0210	464.66	1.19
1.467	4.19	0.0065	40.19	0.67
1.483	2.38	0.0865	307.79	2.45
1.496	2.15	0.0065	21.06	0.68

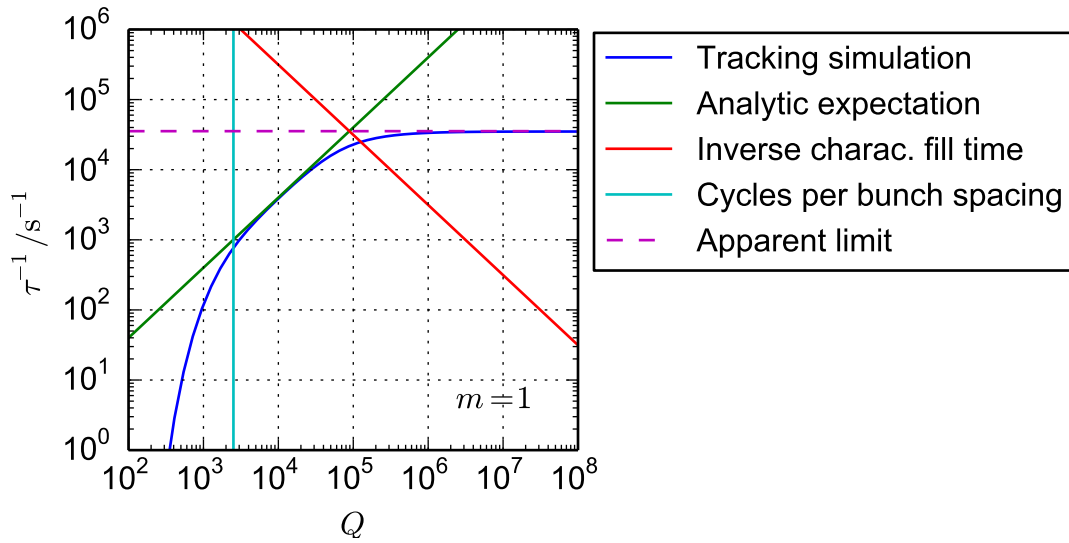


Figure 3.7.: Growth rate of transverse $m = 1$ case as a function of Q for constant $R_{s,1}/Q$. The tracking simulation (blue) is compared to the expectation (green) given by Eq. 2.53. It is limited by the cycles per bunch spacing, here $\omega_r/2/f_{\text{rev}}$, for low Q and by the inverse characteristic fill time τ_c^{-1} for high Q .

with the corresponding quality factor defining this limit,

$$Q_{\text{limit}} = \frac{\omega_r}{\sqrt{2c \frac{R_{s,1}}{Q} \frac{\omega_{\text{rev}} I_{\text{DC}}}{4\pi E/e} \beta}}. \quad (3.32)$$

Calculations show that the growth rate of transverse HOMs is not limited by the mechanism described here for a realistic cavity model, such as “HZB 2c coax. coupler”

4. Observation of Coupled Bunch Instabilities

This chapter covers examples of the observation of CBIs along with crucial methods of the analysis and implementation of the measurements. First, Section 4.1 covers BBFB systems as they are the most important tool to observe CBIs. In Section 4.2, different methods of observation are presented by means of examples, combined with the purpose of demonstrating the general behavior and features of the CBI, confirming the applicability of the theoretical and numerical models presented earlier in Chapters 2 and 3.

Sections 4.3 and 4.4 present additional measurements, including the characterization of the longitudinal long range impedance at the MLS and measurements evaluating the performance of the BBFB system at BESSY II, a crucial parameter for the calculation of the instability threshold in BESSY VSR.

4.1. Bunch-by-Bunch Feedback Systems

A BBFB system is a very effective tool to suppress all types of dipole instabilities, i. e., instabilities where the center of mass of the bunches are oscillating in the longitudinal or transverse plane [74]. Among others, this includes some ion instabilities, the transverse resistive wall instability and HOM driven CBIs. Instabilities that primarily lead to density oscillations with unchanged center of mass cannot be damped with such a feedback. A BBFB system is routinely in operation at many synchrotron light sources, including BESSY II and the MLS.

4.1.1. Hardware

Figure 4.1 shows the block diagram of the BBFB system of BESSY II [75] manufactured by [76]. The same system is installed at the MLS.

When a bunch passes the beam position monitor (BPM), it induces signals in the four pickups according to its transverse position and its charge.

The so called hybrid network takes differences and sums of the four signals of the pickups of the BPM to provide simultaneously three signals corresponding to the horizontal and vertical displacement (x, y) and the sum signal which is used to detect the longitudinal position (t) [77].

4. Observation of Coupled Bunch Instabilities

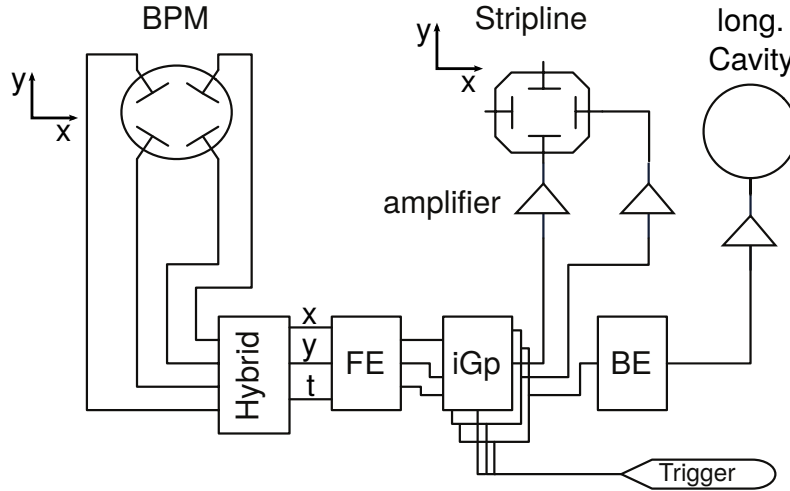


Figure 4.1.: Block diagram of the present BBFB system at BESSY II showing the beam position monitor (BPM), the hybrid network (Hybrid), the front end (FE), the digital processing units (iGp), the back end (BE), the amplifiers, the stripline kicker (Stripline), the longitudinal kicker cavity (long. Cavity) and an external source for trigger signals (Trigger). See text for details. Figure extracted from [75] and changed.

The analog front end receiver (FE) performs further tasks of signal processing [78], most importantly, the measured signal is mixed with a multiple of the fundamental RF frequency, which turns the sum signal into a signals whose amplitude is proportional to the bunch arrival time.

Each signal is then passed to a digital processing unit called iGp [76], consisting of a 12-bit analog-to-digital converter (ADC) and a finite impulse response (FIR) filter with 32 coefficients implemented on a field-programmable gate array (FPGA) with the full digital chain running at 500 MHz.

Note that this BBFB treats each bunch in the storage ring completely independently from all other bunches. A correlated bunch motion is neither assumed, nor is it used in order to damp the oscillation.

The filtered signals are then converted back to an analog signal and transmitted to the amplifiers and finally to a stripline to perform horizontal or vertical kicks and to a cavity to perform longitudinal kicks [79]. In the longitudinal case, the signal first passes a backend (BE) which transforms the signal to a higher band, i. e., close to the resonance frequency of the longitudinal kicker cavity of 1.374 GHz.

Additionally, the digital processing unit can be triggered to synchronize its data acquisition with external events, such as beam loss or injection.

4.1.2. Data Acquisition

The digital BBFB system can be used for diagnostics as the digitized input data can be written to an internal memory and from there it can be transferred to and stored on other computers. In the case of the hardware discussed here, the data with a length of about 1.25×10^7 samples can be read out twice a second. This corresponds to a duty cycle of about 5%.

However, for the study of CBIs, continuous data taking is usually not needed. Instead, transient measurements, e. g., turning on or off of the feedback, provide the highest amount of information. More details and applications are presented in Section 4.2.

Another valuable application of the data acquisition are the studies of beam loss events.

4.1.3. Damping

Typically, the coefficients of the filter, also known as taps, are set to a pure sine function with a suitable phase and with a frequency that corresponds to the betatron or synchrotron frequency. With that, the filter becomes nothing but a frequency filter and phase shifter. In order for the feedback to damp bunch motion most efficiently, the phase must be selected such that the kick applied to the bunch is delayed by 90° compared to its input signal. This is because the input signal is proportional to the amplitude coordinate of the motion but the kick is applied on the momentum coordinate of the motion. They are related by their time derivatives, i. e., shifted by 90° for sinusoidal motion. By changing the sign, anti-damping is achieved.

The output from a 32-tap filter is simply obtained by multiplying the coefficients with the last 32 turns of the measured bunch signals (input). As a formula, the output signal o_n from a 32-tap filter with coefficients a_i is given by

$$o_n = \sum_{i=1}^{32} s_{n-32+i} a_i, \quad (4.1)$$

with s_n the input signal and n the turn number. Conventions may differ regarding the ordering of the taps.

Figure 4.2 illustrates the working principle of a sinusoidal tap filter. The coefficients of the filter are plotted in the left panel of Fig. 4.2. In the right panel, a noisy input signal is drawn along with the output signal obtained with the given tap filter and Eq. 4.1. As can be seen, the filter rejects the noise, i. e., acts as a frequency filter, and provides an output with a well defined phase relation to the input, i. e., a phase shift is obtained. In this case, the phase shift is 90° to provide damping/anti-damping with highest efficiency.

4. Observation of Coupled Bunch Instabilities

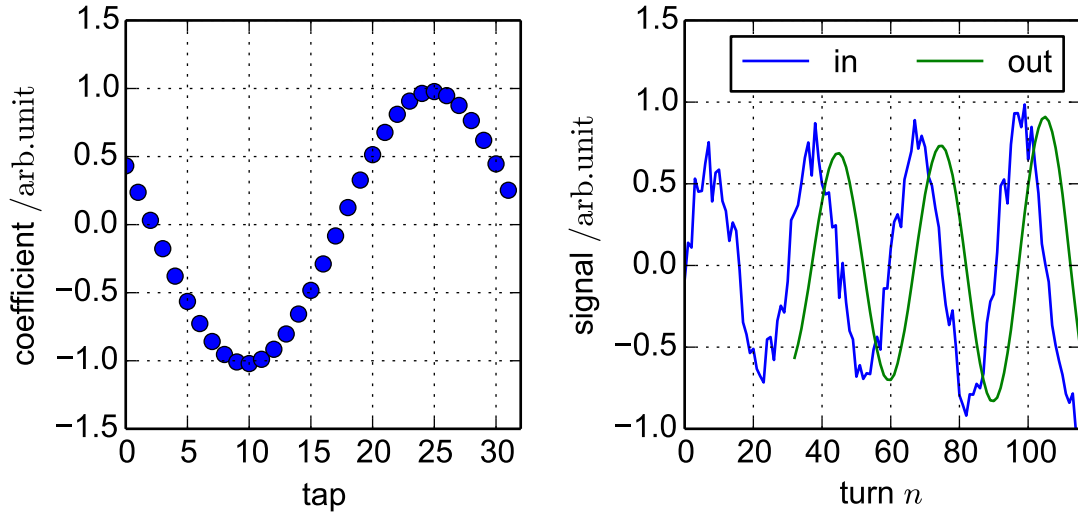


Figure 4.2.: Illustration of working principle of a BBFB with a sinusoidal tap filter. Left: Tap filter matching the frequency of the input signal and causing a phase shift of approximately 90° between input and output signal. Right: Noisy input signal (blue) and output signal (green) obtained by the tap filter on the left.

4.1.4. Limitations and Future Ideas

At this point, some qualitative discussions on some limitations of the damping performance of a BBFB system are presented. Among other parameters, the strength of the kicker is an important factor.

The damping rate of a BBFB system scales approximately linearly with the strength of the kicker [74, Eqs. 25 and 30]. Hence, to raise the damping rate, either the power of the amplifiers that drive the existing kickers can be increased (scaling with square root of power), or the number of kickers with new amplifiers can be increased (linear scaling with number of kickers), if there is enough space in the storage ring. For BESSY VSR, this can be considered both for the transverse planes and the longitudinal plane.

However, an additional limit will manifest itself in the longitudinal plane, where the synchrotron frequency is rather low compared to the betatron frequencies.

A sinusoidal tap filter, as explained above, only works efficiently if the filter length includes a significant fraction of one synchrotron oscillation period. The exact size of the fraction of one period is not discussed here. If it is assumed the needed filter length is one full period, this means for BESSY VSR with $f_s = 8 \text{ kHz}$, that the filter length is about $125 \mu\text{s}$ or approximately 150 turns. Thus, the delay from amplitude detection until the kick is applied is of the order of $125 \mu\text{s}$. In other words, the kick is applied about 150 turns after the amplitude has been measured. It becomes plausible, that if an instability has a

growth rate comparable to the inverse of this time interval, i.e., 8000 s^{-1} , a fundamental limit arises if such a filter is used. It is likely that in such a case the damping performance will no longer scale linearly with the strength of the kicker.

From a CBM theory's point of view, the fact that it should be waited for 150 turns after an amplitude has been measured before the corrector kick is applied, appears unnecessary, as explained in the following. If all bunches are considered individually, as done in the present implementation of the BBFB, it is indeed necessary to sample the synchrotron motion for a significant fraction of a period in order to determine its present phase.

However, if all bunches in the storage ring are measured and correlated to each other, already after one turn, the amplitudes and phases of all bunches are known up to the determination of their mirror CBMs, e.g., CBM 1 is indistinguishable from CBM399. With a correlation over time, i.e., after at least two turns, this ambiguity is resolved as well. This works for bunch fill pattern that are approximately even, because it is known from CBM theory that the bunches can perform correlated motion in exactly M different CBMs.

Essentially, the idea is to combine a mode based feedback [74] with a digital BBFB and in the case of BESSY II use 400 times more information for the kicks applied on the bunches. With this argumentation, the delay in the longitudinal plane could dramatically reduced, hence the damping rate could be increased.

Potential pitfalls of this idea and questions of technical realizations are subject to future studies.

4.2. Methods and Example Measurements at the MLS

Three methods to observe CBIs are presented in this section. The procedures are described with example measurements taken at the MLS.

1. Bunch-by-bunch data acquisition and active beam manipulation with a BBFB system as explained in Section 4.1. This is the most valuable method of diagnostics for CBI.
2. Spectrum analysis at electronic pickup. With a spectrum analyzer attached to an electronic pickup that is sensitive to transverse or longitudinal bunch motion, the transverse or longitudinal CBMs can directly be measured as the side bands of the revolution harmonics.
3. Streak camera imaging. The longitudinal position of individual bunches can be measured with a streak camera which allows to see the CBMs directly on the camera image. This method is not shown in this thesis.

Note that the last two options are basically only suitable for situations where the oscillation amplitude of the CBI saturates without beam loss. This is usually the case for

4. Observation of Coupled Bunch Instabilities

Table 4.1.: Relevant machine parameters of the MLS in the standard user operation mode [24]. Some numbers are rounded.

Parameter	Value
Energy E	629 MeV
Momentum compaction factor α	0.03
Total beam current I_{DC}	200 mA
Fill pattern	homogeneous
Circumference	48 m
Revolution frequency f_{rev}	6.2457 MHz
Harmonic number	80
Fundamental RF frequency	499.654 MHz
Synchrotron frequency f_s	105 kHz
Longitudinal radiation damping time τ_{\parallel}	11 ms
Transverse radiation damping time τ_{\perp}	22 ms

the longitudinal plane but not the transverse planes. The focus in this thesis will be on the observations with the BBFB. Relevant machine parameters of the MLS are given in Tab. 4.1.

4.2.1. Bunch-by-bunch Data and Active Beam Manipulation

This section describes the procedure of obtaining the growth rate and tune shift of each CBM from bunch-by-bunch data, taken at a single pickup on the basis of an example obtained with the longitudinal BBFB of the MLS showing 10 ms of a growth-damp experiment at $I_{\text{DC}} = 124$ mA. The theory presented here can be found in [41, 80]. MATLAB[®] [81] scripts for this purpose come along with the delivery of the BBFB systems manufactured by [76]. In the context of this thesis, implementations of the procedure have been written by the author in C++ and Python. The latter is a more recent implementation that is now collaboratively maintained in-house and is available for online diagnostics in the control systems of BESSY II and the MLS, see Fig. 4.3.

The procedure can be separated into three steps. First, the Hilbert transform, which is used to obtain the desired information on the oscillation of each bunch individually. Second, the Fourier transform that gives the correlation from bunch to bunch, i.e., the CBMs. Finally, the fitting of CBM amplitudes which yields the growth rate and tune shift for each CBM.

4.2. Methods and Example Measurements at the MLS

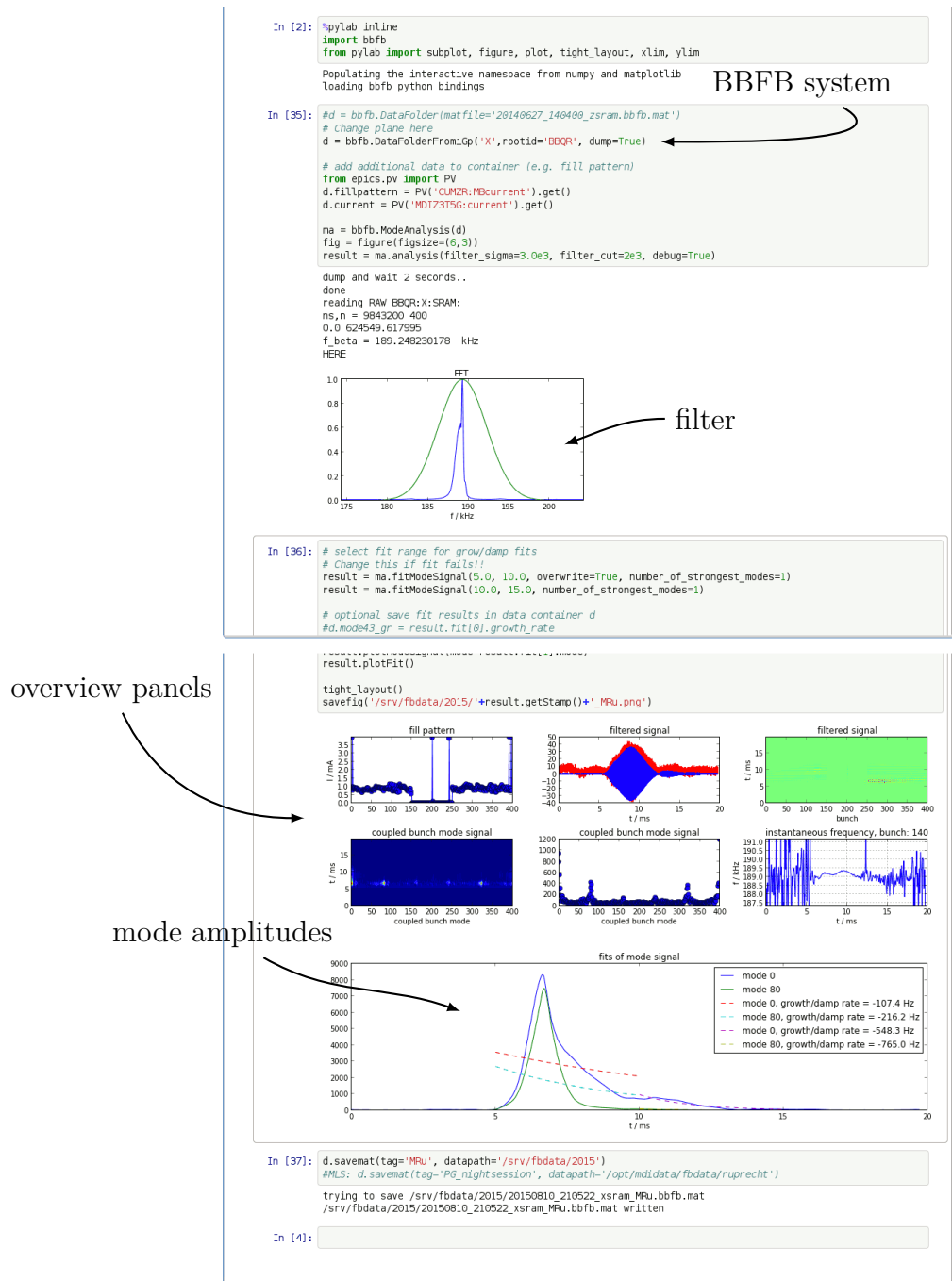


Figure 4.3.: Screen capture of the iPython [82] interface in the BESSY II control room for online diagnostics of bunch-by-bunch data of the BBFB systems.

4. Observation of Coupled Bunch Instabilities

Hilbert transform: Individual bunch motion

The raw signals of the example measurement, a longitudinal growth-damp experiment performed at the MLS, are shown in Fig. 4.4a for all bunches. Even though the actual synchrotron oscillations are well resolved by the data acquisition, they are not resolved by the binning in the particular image shown here. Nonetheless, areas with large oscillation amplitudes are still visible due to the binning effect. The raw signal of a single bunch is shown in Fig. 4.4b. Here, the mechanics of the grow-damp measurement can be nicely seen. First, the feedback is switched off and the instability grows until about 6 ms when the feedback is switched on again and the motion is damped again, indicated by vertical dashed lines in Figs. 4.4b, 4.4d and 4.4f. The exact time between the switch-off of the feedback until the visible onset of the growth is of statistical nature as random fluctuations create the initial conditions for the CBI.

Now, a Hilbert transform is applied on the raw signals to obtain a so called analytic signal. In contrast to the measured raw signals, the analytic signal is complex valued. The real part of the analytic signal corresponds to the raw signals but the added value lies in the fact that the imaginary part is available, thus the amplitude of the motion and its phase is given at every single point. This assumes that the motion is dominated by one oscillation frequency so that the resulting phase is given with respect to that oscillation. To ensure this, a frequency filter is applied along with the Hilbert transform, see below. Logically, the increase of information, i. e., the knowledge of the phase, is explained by the fact that the Hilbert transform takes the entire time series of a bunch into consideration instead of processing the data points individually. The amplitudes, i. e., the envelop of the synchrotron oscillation, is shown in Fig. 4.4c for each bunch. The real part of the analytic signal along with its envelop are shown in Fig. 4.4d for a single bunch. As can be seen from the comparison with the raw signal in Fig. 4.4b, any motion other than the synchrotron motion is removed from the signal. This includes a constant offset, slow drifts and low and high frequency noise.

The phase information of the analytic signal can also be used to extract the instantaneous frequency of the motion, i. e., the phase advance from one data point to another divided by the time interval, see Fig. 4.4f. For non-existing oscillation and very low oscillation amplitudes until about 4 ms, no clear frequency signal is obtained with this method. After that, from about 4 ms to about 6 ms, the synchrotron frequency shows a decline with increasing amplitude. A possible explanation is the non-linearity of the longitudinal dynamics resulting in a tune shift with amplitude. When the feedback is turned on, at about 6 ms, the behavior gets more complex which is plausible as the feedback, acting as an impedance, changes the synchrotron frequency in a non-trivial way. As mentioned before, the Hilbert transform works best if a filter is applied. In this case, a Gaussian filter that fully encompasses the synchrotron frequency has been used, see Fig. 4.4e.

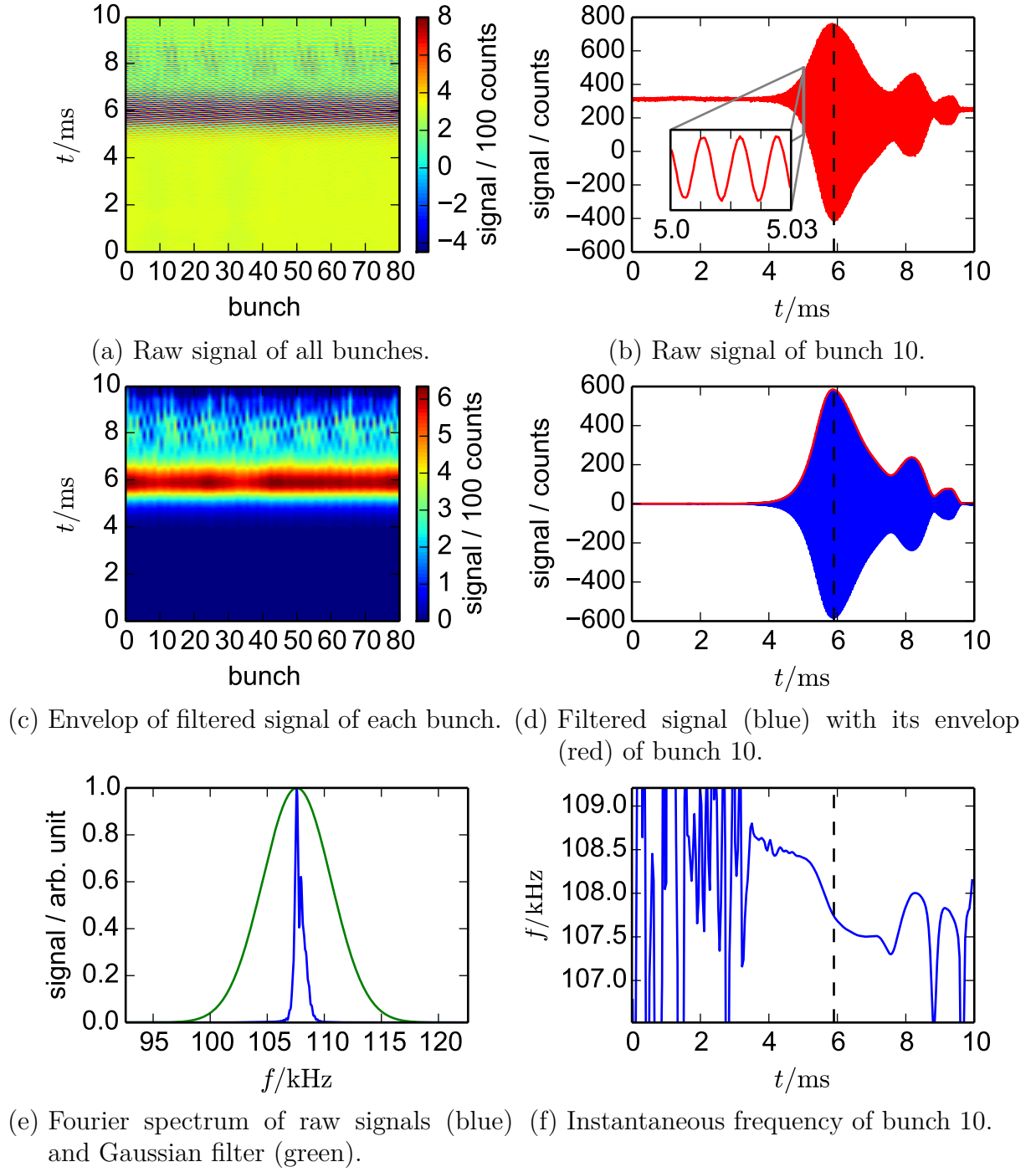


Figure 4.4.: Illustration of the Hilbert transform in the analysis of bunch-by-bunch data of a grow-damp experiment at the MLS.

4. Observation of Coupled Bunch Instabilities

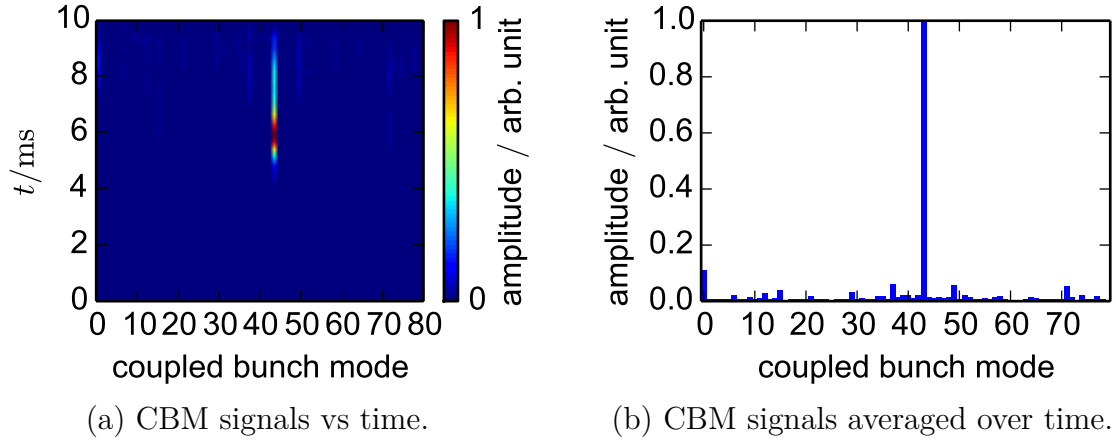


Figure 4.5.: Illustration of the amplitude of the CBMs obtained from the analysis of bunch-by-bunch data taken at the MLS.

Fourier transform: Correlation of bunch motions

With the analytic signal, it is now possible to obtain the CBMs simply by applying a complex Fourier transform along the bunches at each point in time individually. The amplitude of the CBM is then given by the absolute value of the Fourier transform. The CBMs as a function of time are shown in Fig. 4.5a and averaged over time in Fig. 4.5b. It can be seen that CBM 43 is the strongest mode, arising simultaneously with the amplitude of the oscillation. In other words, it is shown that the bunch oscillations seen in Fig. 4.4 are in fact correlated, hence a CBI is occurring.

This can also be nicely visualized by looking at the phase of the oscillation. Figure 4.6a displays the phase as a function of time for all bunches. Note that the actual oscillation is not resolved in the binning that is displayed, however, the regular pattern visible from about 3 ms to 6 ms appears due to a regularity in the phase relations from bunch to bunch. This is confirmed by looking into a close magnification in time. Figure 4.6b top shows an interval around 5 ms where the bunch phases are fully correlated. The center plot is a snapshot of one turn at around 5 ms. The phase advance from bunch to bunch can be read out directly from Fig. 4.6b center, confirming that the dominating mode is the CBM 43 with a phase advance from bunch to bunch of $\frac{43}{80}2\pi$. At an interval close to zero, the bunch phases are mostly uncorrelated with a slight dominance of CBM 0, see Fig. 4.6b bottom.

If the real signals, i. e., raw signals, were taken instead of the analytic signal, the Fourier transform along the bunches would result in a symmetric spectrum which contains less information. More precisely, the CBM μ would be indistinguishable from its mirror mode $M - \mu$ with M the number of bunches.

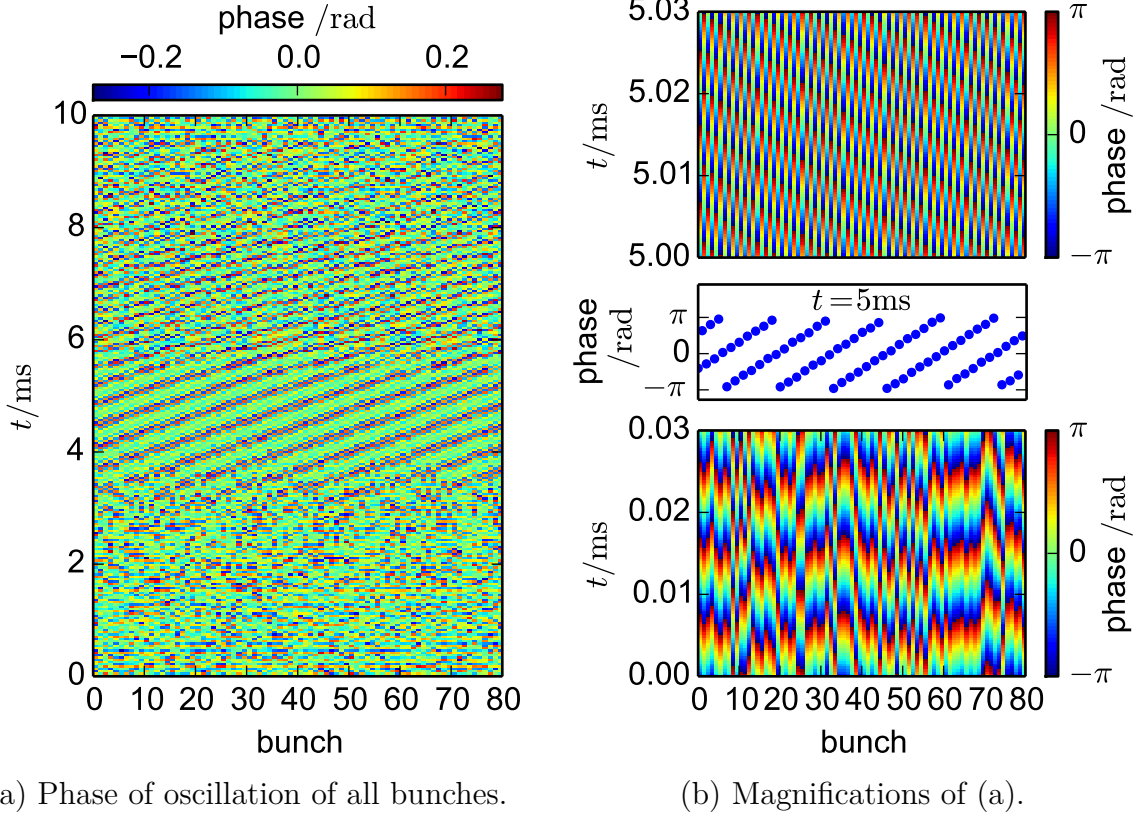


Figure 4.6.: Illustration of the phase of the synchrotron oscillations obtained from the analysis of bunch-by-bunch data taken at the MLS.

Fitting the CBM amplitudes: Growth rate and tune shift

With the amplitudes of all CBMs as a function of time, the growth rate can be obtained by applying an exponential fit. The amplitudes of the 8 strongest CBMs are shown in Fig. 4.7 along with their fits to exponential functions and the obtained growth rates. For the selection of the strongest modes, the strength of the CBMs were determined by their amplitudes at 4.5ms which is a time well within the period of growth but before non-linearities in the longitudinal dynamics limit the growth. In general, the non-linearities in the longitudinal dynamics eventually lead to a saturation of the amplitudes without beam loss even if the BBFB is not switched on again.

The fits are performed as least square fits of a straight line in the logarithmic amplitude. The lower fit limit is set to a factor of 5 above the noise level of the mode while the upper fit limit is set to a point where the mode has reached the third of its maximum value. The uncertainty shown in Fig. 4.7 corresponds to the standard deviation errors on the slope of the straight line, i. e., it is a statistical uncertainty. This value is very small as the data set consists of 5×10^3 to 1×10^4 data points for each mode, depending on the choice

4. Observation of Coupled Bunch Instabilities

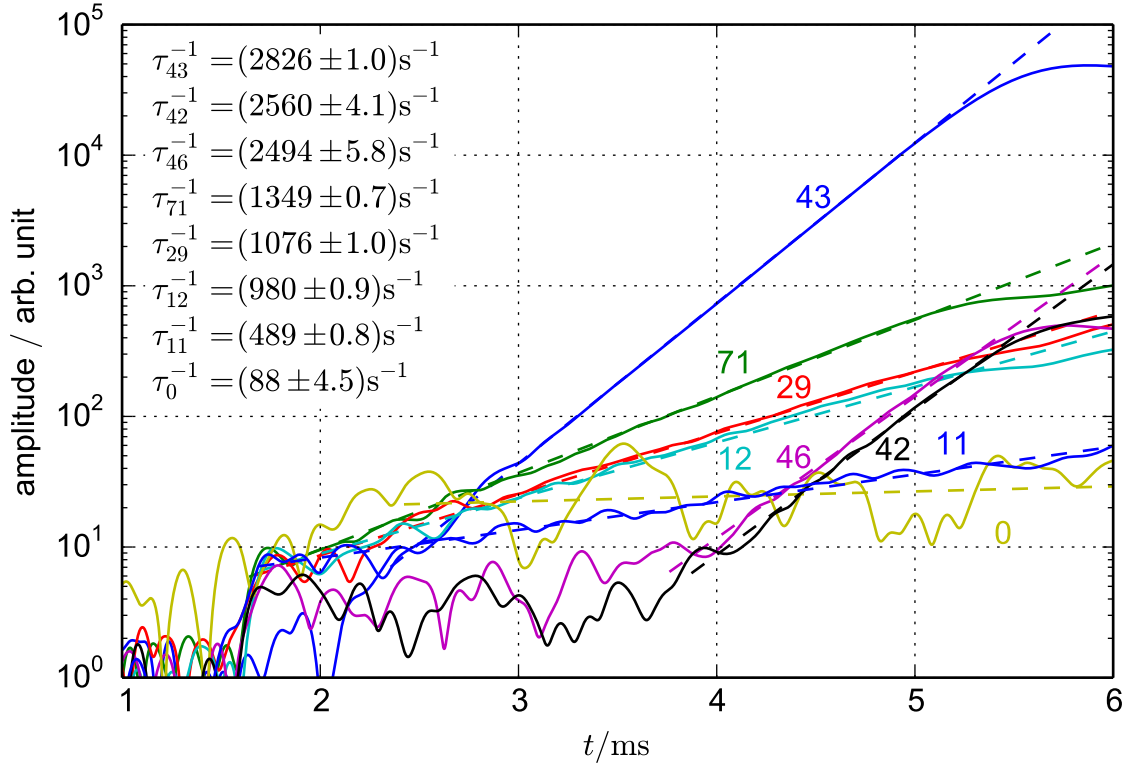


Figure 4.7.: Amplitude of CBMs (solid lines) with exponential fits (dashed lines) and fitted growth rates τ_{μ}^{-1} displayed. The annotations in the vicinity of the lines indicate the CBM.

of the fit limits. It is not a direct measure of how well the data points follow a straight line. Strictly speaking, the CBM signals are not a series of independent measurements anymore but they are correlated as a consequence of the frequency filter applied in the Hilbert transform. Those subtleties are ignored as the statistical uncertainties are most certainly much smaller than possible sources of systematic uncertainties.

As can be seen, CBM 43 has the largest growth rate, as expected from previous discussions. After 43, the strongest modes seem to be 71, 29, 12 and 11. Note that modes 42 and 46 grow almost proportional to CBM 43 but with a much smaller amplitude. This suggests that the modes 42 and 46 are not actually independent modes but there is a physical eigenmode that is made up of a linear combination of the EFEM 43, 42 and 46. This analysis performs a decomposition in EFEMs while in reality a slightly uneven fill was present, explaining the different set of eigenmodes, see also Section 2.4. However, this effect is typically small and can be neglected in all measurements presented in this thesis.

Obtaining the tune shift of the CBMs appears to be a more difficult task. Figure 4.8 shows the attempt for the four strongest modes. The frequency, extracted from the mode

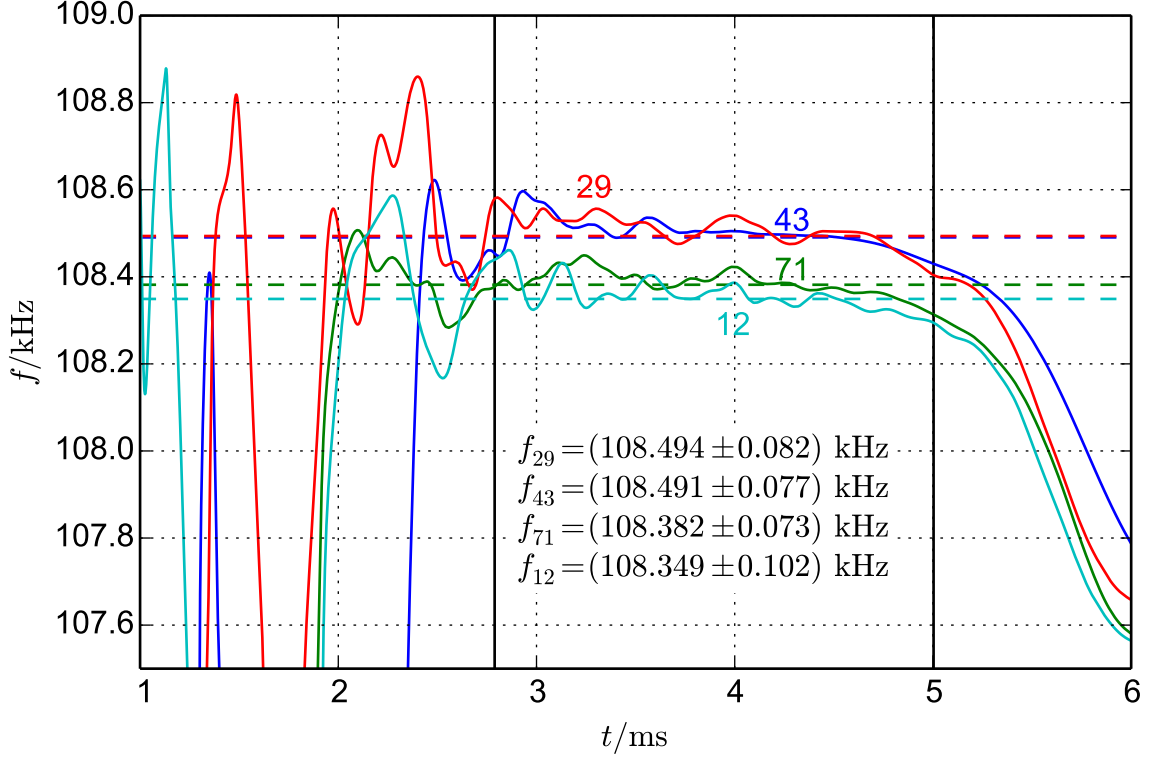


Figure 4.8.: Frequency of CBMs (solid lines) with their averages (dashed lines and numbers displayed) calculated in the interval limited by the vertical black lines. The frequency is smoothed out by a moving average in the entire range plotted. The colored annotations in the vicinity of the lines indicate the CBM.

signal is rather noisy and smoothing with a moving average has been applied in the graph. Furthermore, the range where the frequency is calculated needs to be chosen carefully as a rather strong amplitude dependence seems to dominate the growth-damp measurements.

The uncertainty stated corresponds to the standard deviation errors of the mean value found on the interval. As can be seen, the frequencies of the strongest CBMs do not deviate much. At most, the difference is about 150 Hz, between CBM 29 and CBM 12, with an uncertainty almost of the same order. It is noteworthy that the frequency of CBM 43 does not deviate much from those of the other modes. This suggests that the beam samples the impedance that drives CBM 43 closely to its resonance frequency, where the real part is much larger than the imaginary part, i.e., a strong growth rate and little frequency shift.

4. Observation of Coupled Bunch Instabilities

4.2.2. Spectrum Analysis at Electronic Pickup

The amplitude of the oscillation that the bunches perform in a certain CBM μ can be read out directly from the amplitude of the spectral component at the corresponding frequency. The signal can be obtained from a BPM. For the longitudinal plane, where the synchrotron frequency f_s is much smaller than the revolution frequency f_{rev} , the corresponding frequencies for each μ are given by

$$f_\mu = pMf_{\text{rev}} + \mu f_{\text{rev}} + f_s, \quad (4.2)$$

with p an integer and M the number of buckets. Even though this equation is exact only for even bunch fill pattern, it can be applied for uneven fill pattern as well. Projected onto positive frequencies, as done by a spectrum analyzer, the corresponding positive frequencies are

$$f_\mu = pMf_{\text{rev}} + \begin{cases} \mu f_{\text{rev}} + f_s & , \quad 0 \leq \mu < M/2 \\ (M - \mu)f_{\text{rev}} - f_s & , \quad M/2 \leq \mu < M. \end{cases} \quad (4.3)$$

This means, the entire set of CBMs can be obtained from any spectral interval of the length $Mf_{\text{rev}}/2$, i. e., 250 MHz for BESSY II and the MLS.

As $f_s \ll Mf_{\text{rev}}/2$, some spectrum analyzers cannot provide the needed range and resolution simultaneously to obtain the full set of CBMs. Hence, a simple software, similar to [51, 83], has been written in LabVIEWTM [84] to interact with a spectrum analyzer and automatically obtain the amplitudes of longitudinal CBMs at the MLS, see Fig. 4.9. During measurement, the software applies the appropriate frequency range and center frequency consecutively to the corresponding CBM frequencies f_μ and reads the amplitude of the peak. The software can be used to measure the amplitudes of all CBMs or repetitively the amplitude of an individual CBM. The simplicity and possible sensitivity are advantages of this method compared to measurements with a BBFB system. In a scan of decreasing current with more than one hundred points of measurement, the method showed very good agreement with BBFB measurements.

The particular measurement shown in Fig. 4.9 was taken during a MLS machine setting with negative α . As the growth rate is proportional to α , see for example Eq. 2.30, a change in the sign of α changes unstable into stable CBMs and vice versa. If the synchrotron frequency is smaller than the revolution harmonic and approximately smaller than the width of the resonator impedance that drives the instability, each damped mode μ has a corresponding anti-damped mode with the index $M - \mu$ and approximately the same absolute value of the growth/damping rate. With nominal alpha, the most unstable CBM in the MLS is $\mu = 43$ as shown in detail in Section 4.3. Hence, if operated with negative α , $\mu = 37$ is expected to be unstable while $\mu = 43$ is damped by the same resonator impedance, which is exactly what is seen in Fig. 4.9.

4.3. Measurements of Longitudinal CBMs at the MLS

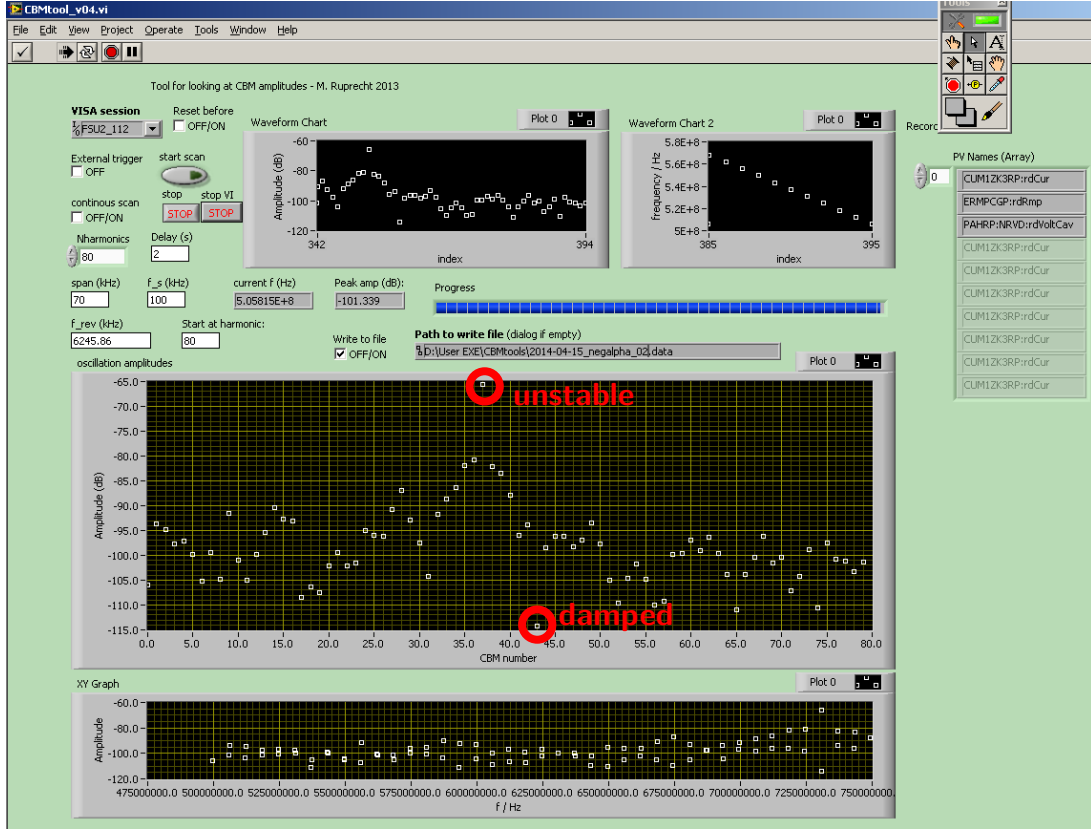


Figure 4.9.: Screenshot of simple LabVIEWTM program to interact with a spectrum analyzer in order to automatically obtain amplitudes of the CBMs. The central graph shows the amplitudes of the CBMs. This measurement was taken during a machine setting with negative α which explains why $\mu = 37$ is the most unstable mode (largest amplitude) in contrast to the usual mode $\mu = 43$, which is highly damped (smallest amplitude) in this case, see red circles.

4.3. Measurements of Longitudinal CBM at the MLS

With its high diagnostic capabilities, the MLS is a good example to study CBI. While there are no transverse CBIs visible in the typical operation modes, the longitudinal plane clearly shows CBIs driven by narrowly peaked resonators at the nominal momentum compaction factor $\alpha = 0.03$ [50].

At nominal α , the threshold current given by longitudinal radiation damping is rather low, around 10 mA. If operated above this threshold, the beam is unstable and so called grow-damp measurements with the BBFB are needed to obtain the growth rate and frequency shift of the CBMs.

This has been done in an automated over-night scan where data has been taken after

4. Observation of Coupled Bunch Instabilities

each step of reducing the stored current. The data is used to obtain the growth rate as a function of current, see Fig. 4.10, where each point is obtained from the fit procedure explained above. A number of cuts have been applied on the data set to remove measurements where the evaluation of the growth rates of the modes was less successful. This occurs throughout the automated scan, as the growth contains a stochastic behavior leading to a fluctuation in the degree of success of the growth rate extraction. The cuts include a lower limit on the maximum amplitude, a lower limit on the amplitude normalized w.r.t. the current, an upper limit on the current and an upper limit on the uncertainty of the fit of the growth rate of less than 1%, hence the individual error bars are not shown.

As can be seen, the scaling of the growth rates is quite linear, as expected from the analytic consideration, e.g., Eq. 2.30. The uncertainties stated in Fig. 4.10 are the standard deviation errors on the fit parameters of the straight lines. Again, this is a statistical uncertainty with limited applicability to the question how well the data matches the assumption of a straight line.

The growth rate of CBM 43 can be obtained with the highest precision as it is the strongest mode and produces the strongest signals. Generally, the measurement confirms that Eq. 2.30 is applicable for the case of the MLS despite its various approximations. Especially, the growth rate is not “too strong” for the small disturbance approximation used for Eq. 2.30 which would appear as a deviation from the linear scaling towards high currents.

Note that the extrapolated growth rate of CBM 43 for zero current is $-357 \pm 3 \text{ s}^{-1}$, corresponding to a damping time of approximately 3 ms. This is much smaller than the radiation damping time at the MLS which is $\tau_{\parallel} = 11 \text{ ms}$. This is an indication for other damping effects, for example caused by the interaction with other impedances or ions. A similar discrepancy has been found at another storage ring [65], where the argument is given that the BBFB system only detects the center of mass motion and no higher order motion, e.g., bunch lengthening.

4.3.1. Aliased Resonator Impedance

The fit results obtained in Fig. 4.10 can be used to obtain the aliased resonator impedance, i.e., the information about the source of the instability.

The expression for the growth rate, Eq. 2.30, can be rearranged such that all known parameters are shown on the r.h.s.,

$$f_{\mu} \Re Z_0^{\parallel}(f_{\mu}) = \frac{d\tau^{-1}}{dI} \cdot \frac{2E/ef_s}{f_{\text{rev}}\alpha}. \quad (4.4)$$

Only a single resonator is assumed here and $\frac{d\tau^{-1}}{dI}$ is the slope of the growth rate τ^{-1} as a function of current I , obtained from the fit results shown in Fig. 4.10. The corresponding

4.3. Measurements of Longitudinal CBMs at the MLS

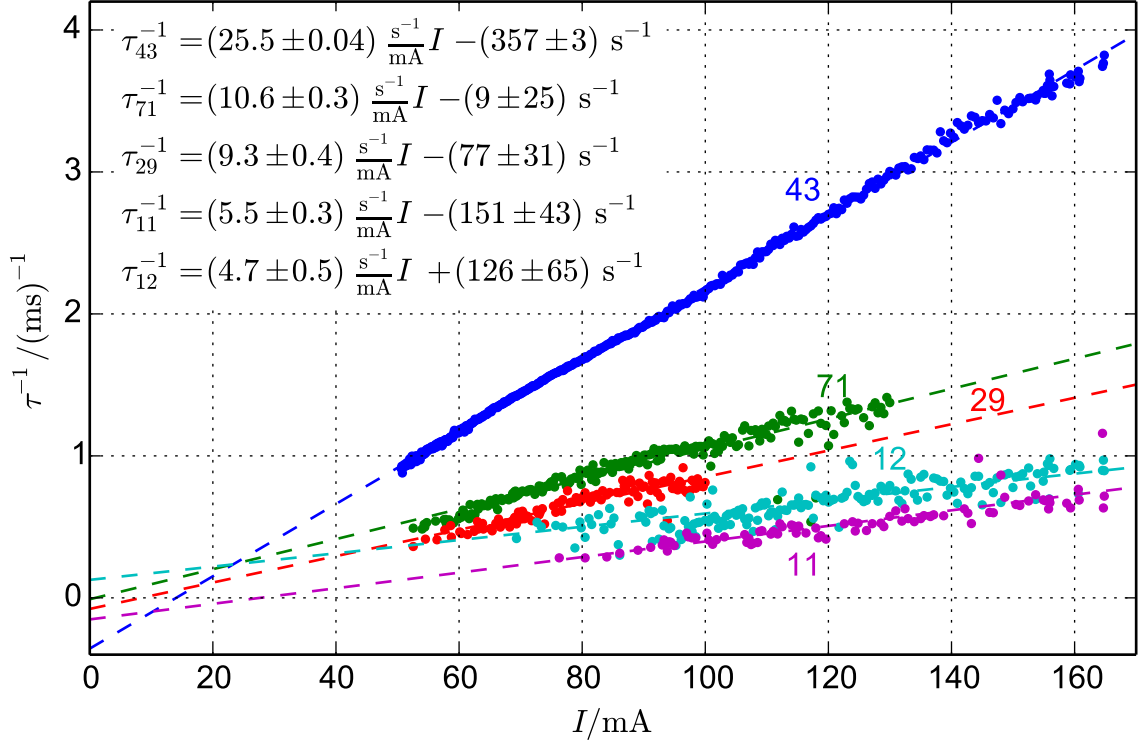


Figure 4.10.: Measured growth rate of the strongest longitudinal CBMs at the MLS in standard user settings as a function of stored beam current (dots) and linear fit (dashed lines) with its result written in the top left corner. The colored annotations in the vicinity of the lines indicate the CBM.

frequencies f_μ for each μ are

$$f_\mu = pMf_{\text{rev}} + \mu f_{\text{rev}} + f_s, \quad (4.5)$$

where p is a non-negative integer as only unstable modes are observed.

The l.h.s. of Eq. 4.4 is called the aliased resonator impedance because it is multiplied with a frequency that is only known up to multiples of 500 MHz. Thus, the measurements only yield the product of frequency and impedance. A combination with measurements of the phase transient could be used in future studies to obtain the unaliased frequencies [85].

If it is assumed that the resonator is driven closely to its resonance frequency, i. e., $f_r \approx f_\mu$, the value of the measured impedances approximately equals the shunt impedance of the resonator, i. e., $R_{s,0} = \Re Z_0^\parallel(f_r) \approx \Re Z_0^\parallel(f_\mu)$.

With this approximation, the results from Fig. 4.10 are summarized in Tab. 4.2 for some reasonable choices for p . The statistical uncertainty, obtained from the fit in Fig. 4.10 is given in percent. The systematic uncertainties have not been studied quantitatively

4. Observation of Coupled Bunch Instabilities

Table 4.2.: Possible combinations of shunt impedance $R_{s,0}$ and resonance frequency $f_r \approx f_\mu$ of the three strongest longitudinal resonator impedances at the MLS, obtained from the fit results of the measurements shown in Fig. 4.10.

CBM	$f_\mu \Re Z_0^\parallel(f_\mu)$ GHz k Ω	p	f_μ MHz	$R_{s,0}$ k Ω	Stat. Uncertainty %
43	17.98	0	268.67	66.9	0.2
		1	768.32	23.4	
		2	1267.98	14.2	
		3	1767.63	10.2	
71	7.47	0	443.55	16.8	2.8
		1	943.20	7.9	
		2	1442.86	5.2	
		3	1942.51	3.8	
29	6.56	0	181.23	36.2	4.3
		1	680.88	9.6	
		2	1180.54	5.6	
		3	1680.19	3.9	

but it can be suggested that they include the uncertainty of the exact machine setting at the time of measurement, the uncertainty of the current measurement, the fill pattern unevenness and other impedances that may influence the growth and damping behavior.

The source of the strong longitudinal impedances at the MLS is not known. Possible candidates are HOMs of the RF cavity [19] or the impedance of the slotted-pipe kicker magnet [86]. If the possible frequencies in Tab. 4.2 are compared with HOM measurements of the RF cavity [87], no direct agreement can be found, which is an indication that the longitudinal impedances are not the HOMs of the RF cavity.

4.4. Measurements at BESSY II

BESSY II is equipped with the same digital BBFB systems as the MLS. In standard user operation, the BBFB is active and needed in all three planes to ensure stability at the maximum current of $I_{DC} = 300$ mA.

The strongest CBIs usually occur in the horizontal plane which is why this plane was chosen for characterizations of the transverse damping performance of the BBFB system at BESSY II [50]. The damping performance of BESSY II is approximately equal in both transverse planes.

Figure 4.11 shows a recent grow-damp measurement in the horizontal plane at BESSY II, taken during machine commissioning in August 2015. The four strongest

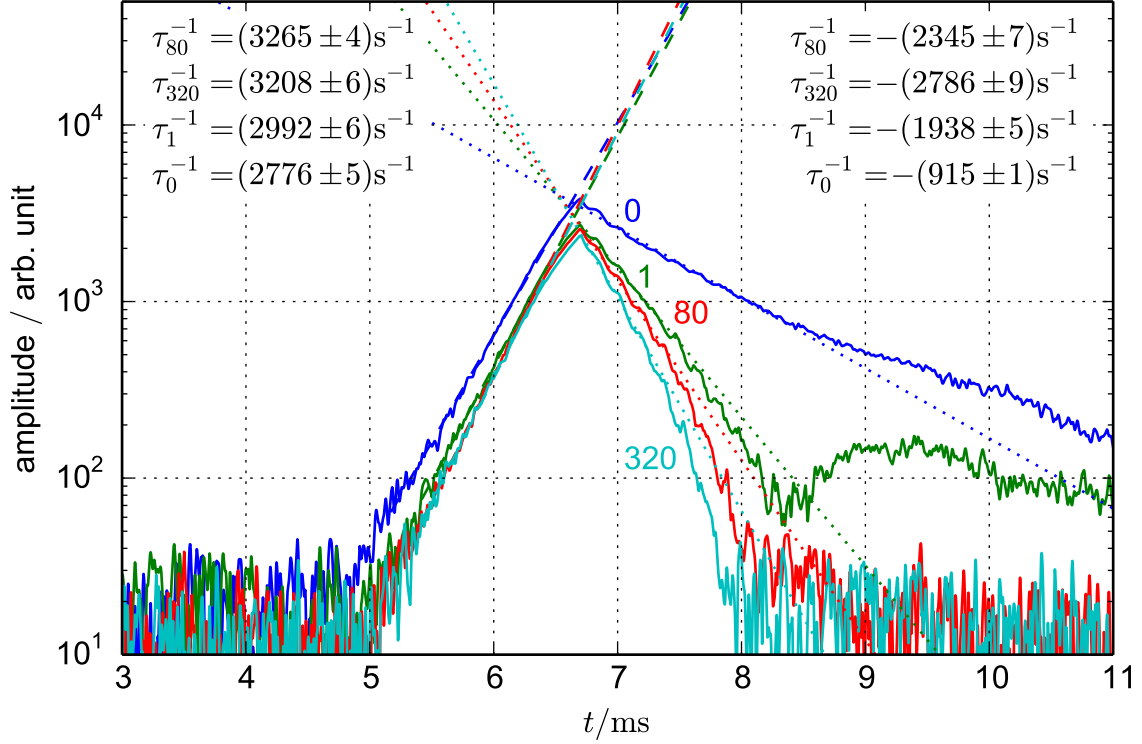


Figure 4.11.: Amplitude of CBMs (solid lines) with exponential fits for growth (dashed lines) and decay (dotted lines) and resulting growth rates (top left corner) and damping rates (top right) in a grow-damp experiment at BESSY II in the horizontal plane. The annotations in the vicinity of the lines indicate the CBM.

CBMs are shown and their growth rates and damping rates are fitted the same way as in Fig. 4.7. In this case, several CBMs are strong, including very low mode numbers. The strongest mode seems to be CBM 0. The damping performance of the BBFB can be estimated by the evaluating of the CBM with the strongest amplitude, where the growth rate of the instability has to be added to the observed damping rate. With the values shown in Fig. 4.11 for mode 0, the damping performance is approximately $2776 \text{ s}^{-1} + 915 \text{ s}^{-1} \approx 3.7 \times 10^3 \text{ s}^{-1}$.

In [50], the number of $\tau_{\text{fb}}^{-1} = 4000 \text{ s}^{-1}$ was found as the damping performance of the BBFB system, which is in good agreement with the single measurement shown in Fig. 4.11, as fluctuations from measurement to measurement as well as dependencies on the precise machine settings are expected. The number from [50] is used throughout this thesis whenever calculations for BESSY VSR are done where growth rates of transverse CBIs are compared to the damping performance of a BBFB, see for example Chapter 5.

Similar measurements have been done with the longitudinal BBFB system. An example

4. Observation of Coupled Bunch Instabilities

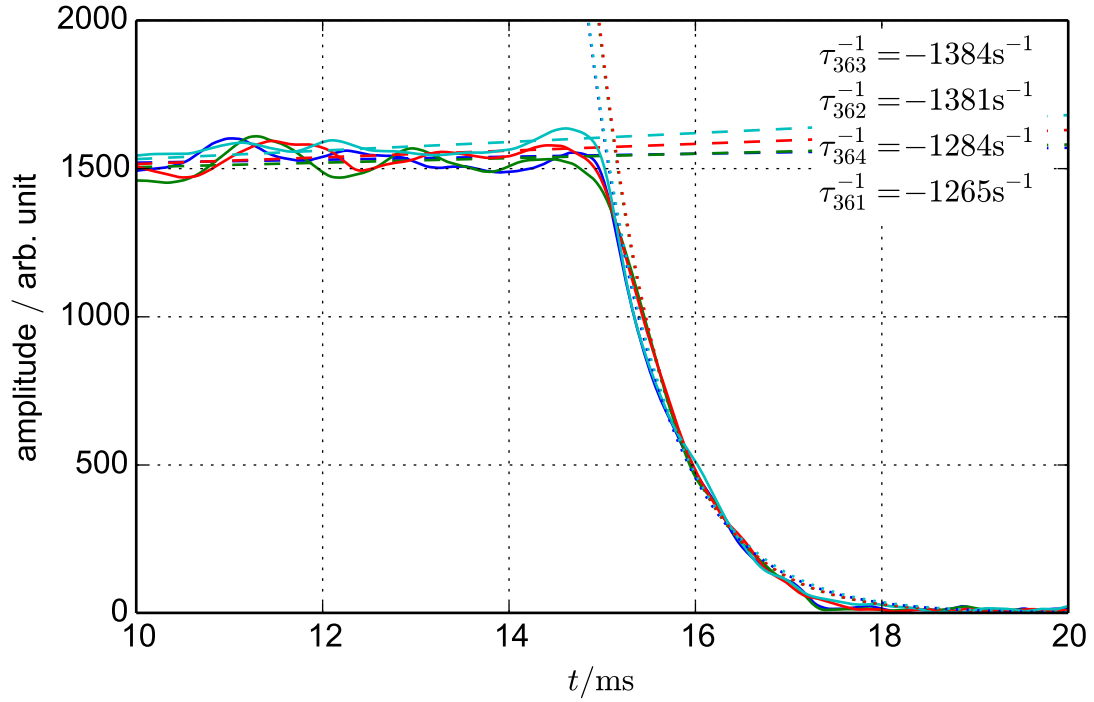


Figure 4.12.: Amplitude of CBMs (solid lines) with slow growth (dashed lines) and fast decay (dotted lines) and resulting damping rates (top right) in a grow-damp experiment at BESSY II in the longitudinal plane [50]. The four lines correspond to the CBMs 361 to 364.

of the measurements used in [50] is shown in Fig. 4.12. In this example, the longitudinal growth rate was very slow, resulting in oscillations at an almost constant amplitude. From those studies, the damping performance in the longitudinal plane was estimated as $\tau_{\text{fb}}^{-1} = 1.33 \times 10^3 \text{ s}^{-1}$, which is the number used in this thesis when longitudinal CBIs are compared with the damping capabilities provided by the BBFB system.

5. Predictions of Coupled Bunch Instabilities for BESSY VSR

This chapter covers calculations for the predictions of CBIs for BESSY VSR. In Section 5.1, the CBIs are estimated based on the simple method of impedance thresholds where first conclusions are already given. In Section 5.2, a more complex method is applied that includes the frequency uncertainty of the HOMs. Section 5.3 presents the effects of different fill pattern on CBIs in BESSY VSR. Finally, Sections 5.4 to 5.6 shortly discuss possible CBIs in the low- α mode in BESSY VSR, CBIs driven by the fundamental mode of the SC cavities and potential CBIs arising in the BESSY II booster synchrotron with upgraded RF.

5.1. Threshold Impedance

5.1.1. The $m = 0$ and $m = 1$ Case

For reasonably weak HOMs, the well established formulas given in Eqs. 2.30 and 2.53 can be used to calculate the lowest order longitudinal and transverse growth rate for each HOM. The threshold of the instability is defined by the point where the growth rate equals the damping rate of the system, typically given by radiation damping or the BBFB systems, see Section 4.1. For a given damping rate τ_d^{-1} , a frequency dependent threshold impedance can also be calculated.

By rearranging Eq. 2.30 and Eq. 2.53, the longitudinal and transverse threshold impedance Z_{th}^{\parallel} and Z_{th}^{\perp} are found as

$$Z_{th}^{\parallel}(\omega, \tau_d^{-1}) = \frac{\tau_d^{-1}}{\omega} \frac{4\pi\omega_s E/e}{\omega_{rev} I_{DC} \alpha} \quad (5.1)$$

$$Z_{th}^{\perp}(\tau_d^{-1}) = \frac{\tau_d^{-1}}{\beta} \frac{4\pi E/e}{\omega_{rev} I_{DC}}, \quad (5.2)$$

with the usual constants mentioned before and summarized in the List of Symbols on Page xi. The summation over p in Eq. 2.30 and Eq. 2.53 has been omitted, which means that the unlikely case of several HOMs contributing significantly to the same CBM has been ignored.

5. Predictions of Coupled Bunch Instabilities for BESSY VSR

Comparing a cavity impedance spectrum with the threshold impedance is a common measure to evaluate the HOM damping of a cavity, see for example [2, 37, 51, 70, 88–91].

Unless otherwise stated, the strongest damping mechanism for BESSY VSR is assumed to be the BBFB system with damping rates equal to the performance of the present feedback system of BESSY II [50]. The damping rate of the BBFB system τ_{fb}^{-1} then takes the following numerical values depending on the plane [50]:

$$\tau_{\text{fb}}^{-1} = \begin{cases} 1.33 \times 10^3 \text{ s}^{-1} & \text{long.} \\ 4.0 \times 10^3 \text{ s}^{-1} & \text{trans.} \end{cases} \quad (5.3)$$

With the parameters given in Tab. 1.1, the frequency dependent longitudinal and transverse threshold impedance can be stated numerically:

$$Z_{\text{th}}^{\parallel}(f, \tau_{\text{fb}}^{-1}) = 132 \text{ k}\Omega \times \frac{\text{GHz}}{f} \quad (5.4)$$

$$Z_{\text{th}}^{\perp}(\tau_{\text{fb}}^{-1}) = 9.07 \text{ M}\Omega \text{ m}^{-1}. \quad (5.5)$$

A comparison of the impedance spectra of different cavity models with the threshold impedance given by the BBFB system can be seen in Fig. 5.1¹. For an additional comparison, the threshold impedance given by radiation damping is also shown with the damping rates given in Tab. 1.1. The cavity models “HZB 2c” and “HZB 2c coax. coupler” refer to two recent developments at HZB, with “HZB 2c coax. coupler” being the most recent considered in this thesis. They are also compared with another 1.5 GHz high current cavity developed at Jefferson Lab, the “JLab HC” [92, 93]. The “JLab HC” cavity is suitable for a comparison as it matches the BESSY VSR requirements in terms of field strength, frequency and compactness. Moreover, the cavity has already been manufactured and simulations have been compared with measurements made with a copper model [92].

5.1.2. The $m = 2$ Case

The growth rate of the instability induced by transverse $m = 2$ impedances can be estimated by the empirical formula given in Eq. 2.63. With this formula, the transverse $m = 2$ threshold impedance can be given in analogy to Eq. 5.2,

$$Z_{2,\text{th}}^{\perp}(\tau_{\text{d}}^{-1}, M_2) \approx \frac{2}{M_2} \frac{\tau_{\text{d}}^{-1}}{\beta} \frac{4\pi E/e}{\omega_{\text{rev}} I_{\text{DC}}}. \quad (5.6)$$

¹A very similar comparison has been presented in [37].

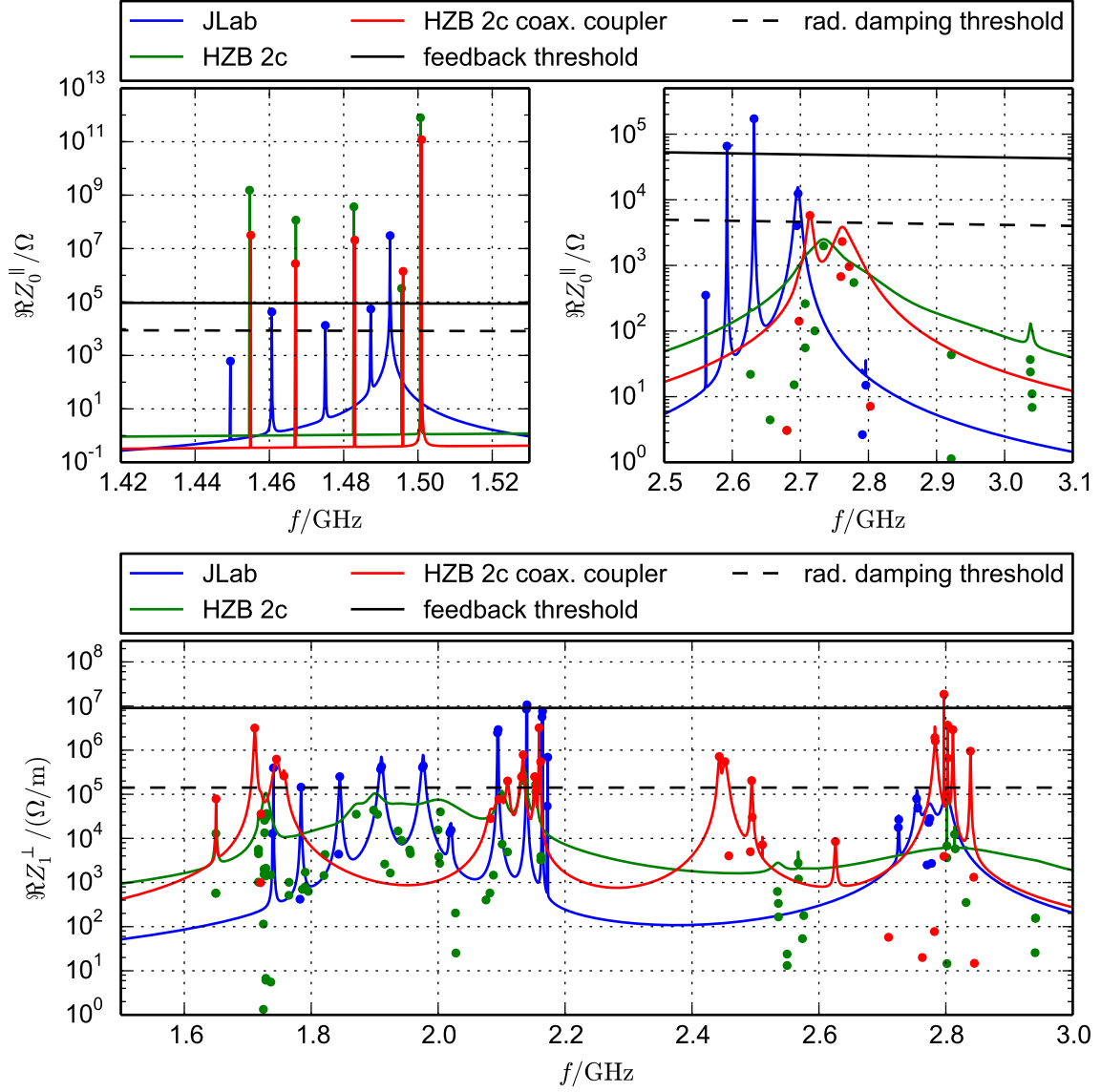


Figure 5.1.: Comparison of impedance spectra of different cavity models with the CBI threshold impedance given by the damping performance of the present BBFB of BESSY II and radiation damping. Other parameters are given in Tab. 1.1. See text for details. Top: Longitudinal $m = 0$ impedance with SPMs (left) and HOMs (right). Bottom: Transverse $m = 1$ impedance of HOMs.

With the transverse radiation damping time given in Tab. 1.1 a semi-numerical expression can be stated,

$$Z_{2,\text{th}}^{\perp}(\tau_{\perp}^{-1}, M_2) \approx 283 \text{ k}\Omega\text{m}^{-3} \times \frac{1 \text{ m}^2}{M_2}. \quad (5.7)$$

5. Predictions of Coupled Bunch Instabilities for BESSY VSR

In order to state a number, plausible values of M_2 have to be given. The following items are considered as plausible, though extreme, scenarios:

- The beam is stable and M_2 is made up of the transverse dimensions of the beam. At BESSY VSR as well as BESSY II, the beam has a low horizontal-vertical coupling. As a consequence, the beam is flat, i. e., its horizontal extension is much greater than the vertical extension, see Tab. 1.1. With the values for the emittance and the value of the betatron function taken from the same table, the quadrupole moment is $M_2 = \epsilon_x \beta = 2 \times 10^{-8} \text{ m}^2$.
- The beam has a momentary displacement from its reference orbit, i. e., it is performing dipole betatron oscillations. With a displacement of $x = 5 \text{ mm}$ at the position of the HOM, the quadrupole moment is $M_2 = x^2 = 2.5 \times 10^{-5} \text{ m}^2$. Note that in this case, the oscillation can be damped by a BBFB providing much stronger damping than radiation. This includes also the case of a static displacement of the beam with respect to the HOM center. According to Eq. 3.24, the equivalent static displacement would be $\sqrt{2} \times 5 \text{ mm}$.
- The beam is momentarily extended in horizontal direction, i. e., it is performing quadrupole betatron oscillations. With a horizontal rms width of $\sigma_x = 1 \text{ mm}$ at the position of the HOM, the quadrupole moment is $M_2 = \sigma_x^2 = 1 \times 10^{-6} \text{ m}^2$. In this case the beam performs pure density oscillations which are transparent to a BBFB system.

With those scenarios, three numbers for the threshold impedance are stated:

$$Z_{2,\text{th}}^\perp(\tau_\perp^{-1}, 2 \times 10^{-8} \text{ m}^2) \approx 1.42 \times 10^{13} \Omega \text{m}^{-3} \quad (5.8)$$

$$Z_{2,\text{th}}^\perp(\tau_{\text{fb}}^{-1}, 2.5 \times 10^{-5} \text{ m}^2) \approx 7.25 \times 10^{11} \Omega \text{m}^{-3} \quad (5.9)$$

$$Z_{2,\text{th}}^\perp(\tau_\perp^{-1}, 1 \times 10^{-6} \text{ m}^2) \approx 2.83 \times 10^{11} \Omega \text{m}^{-3}. \quad (5.10)$$

A comparison of the transverse $m = 2$ impedance spectrum of different cavity models with those three numbers for the threshold impedance can be seen in Fig. 5.2.

5.1.3. Discussions

All important direct means to influence the thresholds of CBIs are covered with the simple formulas presented in Section 5.1.

This includes many machine parameters, for example, the longitudinal threshold scales with the synchrotron frequency whilst the transverse instabilities scale with the value of the betatron function.

In case of BESSY VSR, most machine parameters are tightly constrained, i. e., cannot be used to influence the thresholds of CBIs. In detail, the restrictions of the machine parameters are discussed in the following:

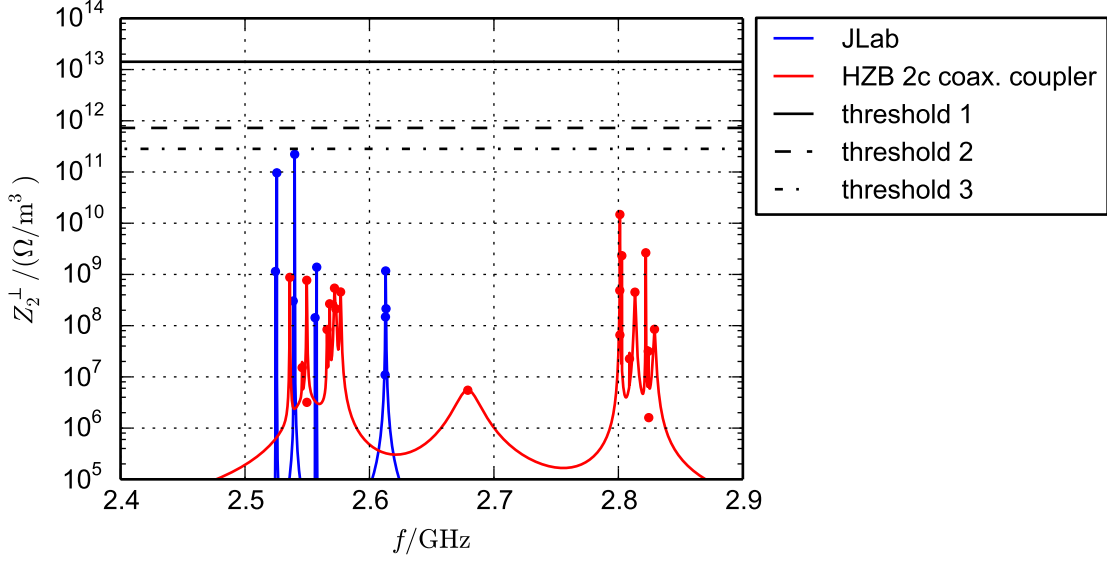


Figure 5.2.: Comparison of transverse $m = 2$ impedance of different cavity models with three possible thresholds for the instability as described in the text.

α Restrained as the DBA will be kept as basic lattice layout.

E Restrained by demands of the users of synchrotron radiation.

ω_{rev} Restrained by the circumference of the ring.

I_{DC} Restrained by demands of the users of synchrotron radiation.

β Restrained by the transverse beam optics at the location of the SC cavities. As transverse impedances are effectively weighted by the value of the beta function, see Eq. 5.2, the place for the module containing the SC cavities was chosen to be a so called low- β straight section, where the values of the horizontal and vertical betatron function are small, see Fig. 5.3. From this figure, it can be seen that all cavities are located at positions where both betatron functions are below 4 m. Thus, a value of $\beta = 4$ m was chosen as a conservative value for all calculations.

f_s Restrained by impedance heating and transient beam loading. Impedance heating gives an upper limit for f_s because high f_s means the bunches are short which can lead to problems of impedance heating if the amount of current that is stored in short bunches is large [2]. As shown in Chapter 6, the maximum elongation of long bunches is limited by the bunch fill pattern. Realistic values for the average synchrotron frequency are expected to be similar to the nominal value of f_s , hence no significant change is expected. In terms of beam lifetime, long bunches, i. e., low f_s is also desirable [2].

5. Predictions of Coupled Bunch Instabilities for BESSY VSR

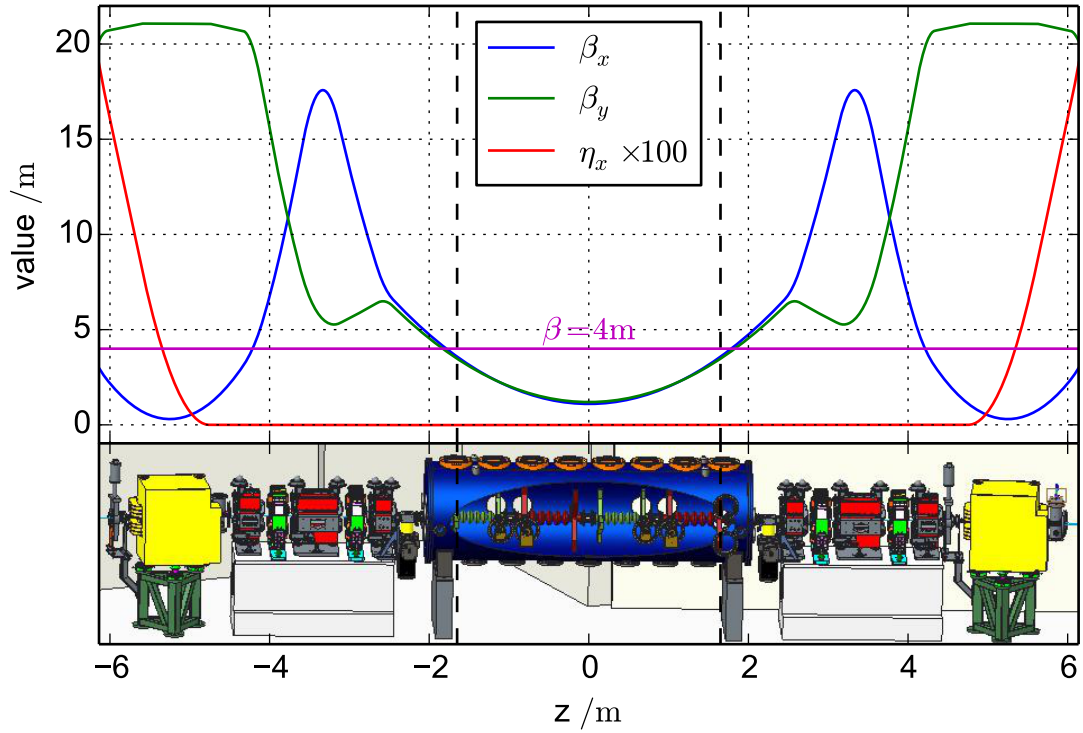


Figure 5.3.: Top: Horizontal betatron function (β_x), vertical betatron function (β_y) and 100 fold magnified horizontal dispersion function (η_x) of BESSY II, shown near a so called low- β straight section. Bottom: Drawing of the BESSY VSR cryomodule (blue) between quadrupole magnets (red), sextupole magnets (green) and dipole magnets (yellow), drawn to scale. Image extracted from [2]. The beginning and end of the SC cavities is indicated by vertical dashed lines.

τ_d^{-1} No direct restriction. Increasing the damping rate does not conflict any other aspect of machine operation, thus it is a good handle to influence CBIs. Indeed, it is the strongest handle from the beam dynamics point of view. The BBFB is typically the strongest damping mechanism and increasing the performance of the BBFB is a good way to raise the CBIs threshold. Physical and technical limits for the performance of the BBFB systems may arise, see Section 4.1.4.

5.1.4. Conclusions

Already at this point, first conclusions regarding CBIs at BESSY VSR can be made. Except for increasing the damping rate provided by a BBFB system, none of the machine

parameters can significantly be changed to raise the instability thresholds. Thus, the question of stability depends almost only on the impedance spectrum and the performance of the BBFB system.

From Fig. 5.2, it can be seen that the quadrupole CBI is generally weak and no quadrupole HOM of the cavity model “HZB 2c coax. coupler” seems to threaten the stability.

A similar behavior is seen with the longitudinal HOMs of “HZB 2c coax. coupler”, which are about a factor of ten below the BBFB threshold, see Fig. 5.1 top right panel. The SPMs shown in Fig. 5.1 top left panel, exceed the threshold significantly. However, it must be noted that Eq. 5.1 overestimates the growth rate of such modes with a very high Q value, as discussed in Section 3.3.4 and explicitly calculated in Tab. 3.1. With this consideration, only one SPM exceeds the threshold, thus the likelihood of this instability to occur is not very large.

The transverse dipole HOMs are also found below the CBI threshold except for a single outlier, see Fig. 5.1 bottom panel.

Essentially, the latest cavity model, “HZB 2c coax. coupler”, performs well in a sense that HOM driven CBIs are expected to be under control by the present BBFB system if the final cavity has the same HOM spectrum².

The fact that those calculations are made for one 1.5 GHz cavity only does not diminish their validity as simply increasing the number of cavities does not necessarily increase the strongest impedance³. In fact, the fabrication uncertainties leading to a spread in the HOM frequencies make it unlikely that the strongest HOMs exactly overlap.

5.1.5. Restrictions Regarding the Reliability of CBI Predictions

It is not part of this thesis to estimate HOM spectra or their uncertainty. However, as the HOM spectra and their uncertainty have such a large influence on one of the key questions of this thesis, some comments are in order.

It is not known if the final 1.5 GHz cavity will have the same HOM spectrum as the calculated spectrum of the “HZB 2c coax. coupler” cavity model. Generally, the finite fabrication precision leads to a randomization of the shunt impedance, the quality factor and the frequency for each HOM, which is characterized by a rms spread. While the spread in the shunt impedance and quality factor has not been evaluated for the BESSY VSR cavities, the spread in the HOM frequency can be estimated and is used in Section 5.2 for a statistical study.

In addition to the uncertainty of shunt impedance and quality factor, limitations in the simulation software are known [94] and the 1.75 GHz cavity is not designed yet.

Furthermore, the four cavities of BESSY VSR need to be brought closely together and connected to the beam pipes at both ends, forming a super-structure. The impedance

²Comments on this question are given in Section 5.1.5

³However, bringing multiple cavities close together may result in an entirely new impedance spectrum, see Section 5.1.5.

5. Predictions of Coupled Bunch Instabilities for BESSY VSR

spectrum of the super-structure may have significant additional contributions from the sections between the cavities and the transitions to the beam pipes that are not included in the sum of the impedance spectra of the individual cavities [94]. The design and study of the BESSY VSR superstructure is presently ongoing.

With the impedance data available to date, the question of HOM driven CBIs looks promising in a sense that stability can be reached. However, the situation needs to be reevaluated with upcoming information on fabrication uncertainties, the overcome of limitations in the simulation software, the design of the 1.75 GHz cavity, the final HOM spectrum of the super-structure, results from measurements with copper models and finally with the results from a SC niobium prototype.

5.2. Uncertainty of HOM Frequencies

The statistical approach presented in the following is an extension to the simple method of using impedance thresholds to address HOM driven CBIs, as discussed in Section 5.1. This approach includes the frequency spread of HOMs due to fabrication and yields additional information about the likelihood of HOM excitation that helps to judge how critical a scenario is in terms of CBIs, especially if there are HOMs close or above the impedance thresholds. The approach has been used in [70]⁴. The spread of shunt impedance or quality factor has not been evaluated as those uncertainty studies for the BESSY VSR cavities are not concluded yet.

The question of stability in HOM driven CBIs is to be determined whether the growth rate τ^{-1} of the fastest growing CBM is larger or smaller than the damping rate available to the system. A statistical approach to the question of stability is reasonable if the frequencies of the HOMs are not precisely known. For evaluations based on calculated HOM spectra, such as always in this thesis, this is the case because the fabrication at finite mechanical precision introduces a randomized disturbance to the modeled geometry. In turn, the frequencies of the HOMs of each final cavity take random values with a certain spread compared to the predicted value obtained from calculation. The distribution is usual Gaussian with a typical relative frequency spread σ_f/f of 1×10^{-3} to 5×10^{-3} , which is for HOMs with $f > 1.5$ GHz a value in the order of several MHz [95].

5.2.1. Algorithm Using Tracking Software

Statistical approaches similar to the one described in this section are well known in the calculation of the so called beam break up instability in ERLs, see for example [96–98]. However, there is a difference, namely the fact that those studies usually take a large number of cavities into account whilst here only the HOMs of one cavity are considered.

⁴Results shown in this thesis may vary from values presented in [70] up to a factor of two due to overestimations of the impedance data that was used for the publication.

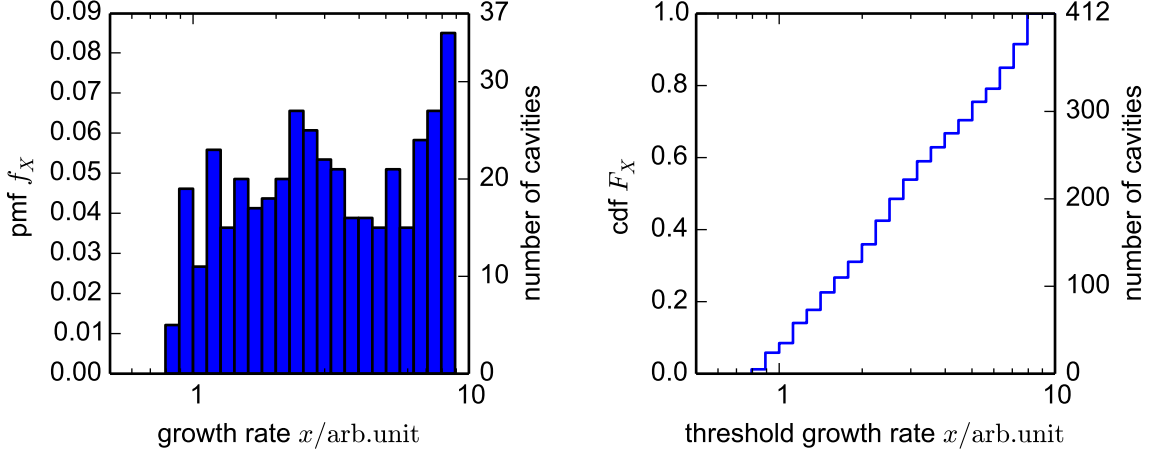


Figure 5.4.: Illustration of the statistical approach for a discrete case with tracking simulation of a statistical sample of 412 generated cavities [70]. Left: Probability mass function (pmf) or equivalently the number of cavities at each growth rate x . Right: Cumulative distribution function (cdf) showing the probability of stability for a given threshold growth rate x or equivalently the number of cavities with a growth rate less or equal to the threshold growth rate x .

The statistical approach can be formulated in terms of discrete probability theory and is realized with the use of tracking software.

In a practical scenario, a so called Monte Carlo approach is used. A finite number of cavities is created, each with a set of HOM frequencies that was randomly generated according to the expected frequency spread of the HOMs. Each cavity is then evaluated by means of tracking simulations to obtain the threshold growth rate. For instance, the threshold growth rate can be retrieved by increasing an artificial damping mechanism in the simulation by discrete steps until stability is found. The result is binned and drawn in a histogram, see Fig. 5.4 left. If it is drawn in a normalized histogram, it represents the probability mass function (pmf),

$$f_X = P(X = x), \quad (5.11)$$

of the random variable X where the outcome of X is the growth rate of the instability and x the threshold growth rate.

If an accumulated summation over the histogram is performed, a quantity is obtained that shows how many of the simulated cavities have a growth rate equal to or below a certain threshold growth rate, see Fig. 5.4 right. For a normalized histogram, it describes

5. Predictions of Coupled Bunch Instabilities for BESSY VSR

the probability of stability P , given by the cumulative distribution function (cdf) $F_X(x)$,

$$F_X(x) = P(X \leq x) = \sum_{x=0}^X f_X(x). \quad (5.12)$$

Figure 5.4 shows the statistical sample used in [70] with the pmf shown in left panel and the cdf in the right panel. It consists of 412 generated cavities, each with a finite number of longitudinal HOMs.

5.2.2. Algorithm Using Analytic Formulas

In the case of BESSY VSR, the simple analytic formulas Eqs. 5.1 and 5.2 are in most situations sufficiently valid to study CBIs, avoiding time consuming tracking simulations. In addition, the Monte Carlo approach can be replaced by formulas that explicitly state a probability. Considering this, the statistical approach can be formulated purely on explicit analytic expressions, making its calculation very fast.

The growth rate induced by an HOM depends on the relative spectral location of its resonance frequency to the beam spectrum. By varying either quantity, the growth rate may change significantly and even become negative, i. e., damped. The beam samples the HOM spectrum at intervals of the revolution frequency f_{rev} , i. e., if an HOM resonance frequency is shifted by f_{rev} , the growth rate remains equal and only the index of the CBM has changed by one. Therefore, the problem of driving the HOM can be reduced to the frequency interval of f_{rev} , i. e., the frequencies are “aliased” resulting in an aliased spectrum, as shown in the figures introduced later in this section.

The growth rate is determined by the maximum real part of the impedance at any of the spectral beam components. As the spread due to fabrication is expected to be larger than f_{rev} , the Gaussian distribution can be approximated by a continuous uniform distribution in the aliased spectrum. The impedance is then equally likely to be sampled at any point in the aliased spectrum of width f_{rev} . The likelihood of the growth rate to be above a given value can then be read out by the range on the frequency axis in the aliased spectrum where the real part of the impedance is above a certain value, see Fig. 5.5. The mathematical description in terms of probability theory is given in the following.

Let N be the number of HOMs of a cavity, then N random variables X_n can be defined where the outcome is the growth rate of the instability induced by the n -th HOM. The variables X_n itself follow a non-trivial probability density function (pdf), which appears very difficult to obtain. However, as the frequency distribution can be assumed uniform, the cdf $F_{X_n}(x) = P(X_n \leq x)$ can be obtained more easily as described in the following and illustrated in Fig. 5.5.

The probability of stability given by the n -th HOM, i. e., the growth rate X_n is equal or below a threshold growth rate x , is given by a modified width w_n of the impedance

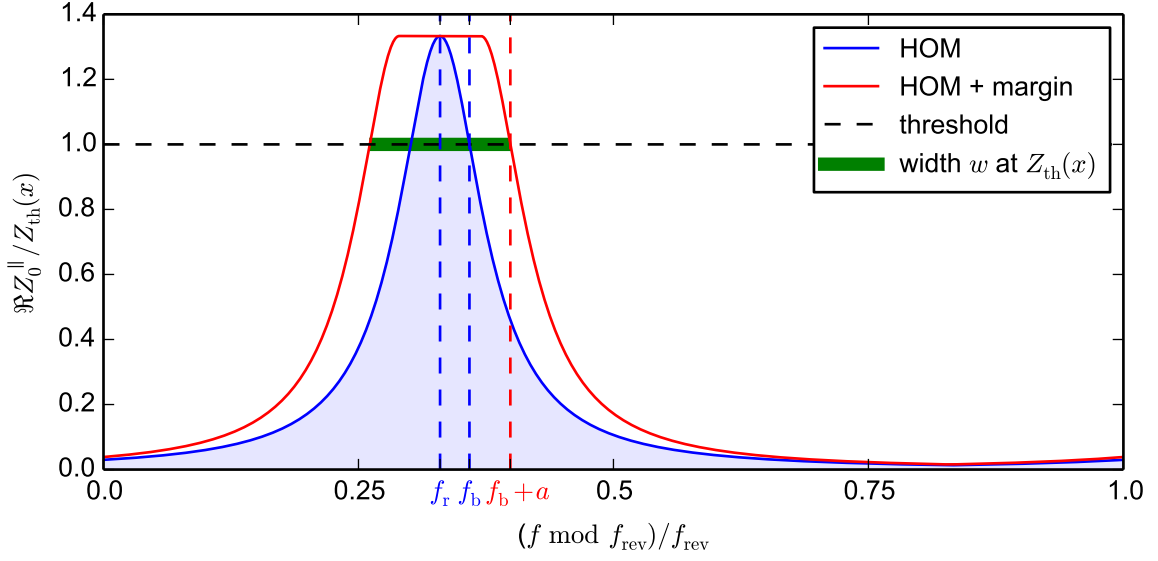


Figure 5.5.: Illustration of the calculation of the probability of stability for one HOM at a given threshold growth rate x . The width w of the HOM is evaluated at the threshold impedance Z_{th} corresponding to the threshold growth rate x and includes an additional safety margin a . The probability can then be read out by comparing w (green bar) with the length of the interval, f_{rev} . The symbol \bmod is the modulo operation. The operation $(f \bmod f_{\text{rev}})/f_{\text{rev}}$ is implicitly also applied to all other variables that are shown on the horizontal axis.

peak at the threshold impedance Z_{th}

$$F_{X_n}(x) = P(X_n \leq x) = \frac{f_{\text{rev}} - w_n(Z_{\text{th}}(x))}{f_{\text{rev}}}, \quad (5.13)$$

see Fig. 5.5 for an illustration. The width w_n is defined as follows

$$w_n(Z_{\text{th}}) = \begin{cases} 0 & \text{for } R_s \leq Z_{\text{th}}, \\ f_{\text{rev}} & \text{for } 2(f_b + a - f_r) > f_{\text{rev}}, \\ 2(f_b + a - f_r) & \text{otherwise,} \end{cases} \quad (5.14)$$

5. Predictions of Coupled Bunch Instabilities for BESSY VSR

with

$$f_b = f_r \left[\frac{2Z_{\text{th}}Q^2 - Z_{\text{th}} + R_s}{2Z_{\text{th}}Q^2} + \sqrt{\frac{-4Z_{\text{th}}^2Q^2 + Z_{\text{th}}^2 + 4Z_{\text{th}}Q^2R_s - 2Z_{\text{th}}R_s + R_s^2}{4Z_{\text{th}}^2Q^4}} \right]^{\frac{1}{2}}, \quad (5.15)$$

with f_r the resonance frequency of the n -th HOM, Q the quality factor of the n -th HOM, and $a = 50 \text{ kHz}$ an extra safety margin that is added to both sides of the peak in order to account for relative changes of the resonance frequency of the HOMs w. r. t. the beam spectrum during deployment, see Appendix A.5. All relevant parameters are shown in Fig. 5.5 to illustrate their graphical representation.

Equation 5.15 is the analytic expression of a solution to the equation $\Re(Z_0^{\parallel}(f)) - Z_{\text{th}} = 0$, with Z_0^{\parallel} the longitudinal resonator impedance, Eq. 2.10. The equation has four solutions for $Z_0^{\parallel} < R_s$ out of which the solution with the frequency $f > f_r$ was chosen. It is basically the inverse of the Lorentzian function, which allows to calculate the frequency as a function of the impedance value, i. e., it tells about the width of the Lorentzian peak as a function of its height. A special case would be the full width half maximum, defined as $f_{\text{FWHM}} = f_r/Q$ for a resonator impedance. It can be obtained as $2(f_b - f_r) \approx f_{\text{FWHM}}$ by setting $Z_{\text{th}} = 0.5R_s$ and $Q \gg 1$.

The threshold impedance $Z_{\text{th}}(x)$ explicitly depends on the threshold growth rate x and the angular frequency ω at which the impedance is sampled. However, as a reasonable approximation, this frequency can be set constant over the interval of f_{rev} and equal to the resonance frequency of the HOM, f_r . The threshold impedance Z_{th} then only depends on the threshold growth rate x .

The shunt impedance R_s and the threshold impedance Z_{th} are kept general in the formulas above and can be replaced by the following expressions depending on whether the longitudinal or transverse case is calculated:

$$R_s = \begin{cases} R_{s,0} & \text{long.} \\ R_{s,1} & \text{trans.} \end{cases} \quad Z_{\text{th}}(x) = \begin{cases} Z_{\text{th}}^{\parallel}(\omega_r, x) & \text{long.} \\ \frac{\omega_r}{c} Z_{\text{th}}^{\perp}(x) & \text{trans.} \end{cases} \quad (5.16)$$

The definitions of $Z_{\text{th}}^{\parallel}$ and Z_{th}^{\perp} can be found in Eq. 5.1 and Eq. 5.2 respectively. The factor ω_r/c in front of Z_{th}^{\perp} is introduced to avoid a redefinition of f_b for the transverse case.

The random variables X_n are all independent. Therefore, the probability of global stability is then given by the multivariate cdf $F_X(x)$ which can be defined in a simplified form as all random variables X_n are considered at the same outcome x ,

$$F_X(x) = P(X_1 \leq x) \cdot P(X_2 \leq x) \cdots P(X_N \leq x). \quad (5.17)$$

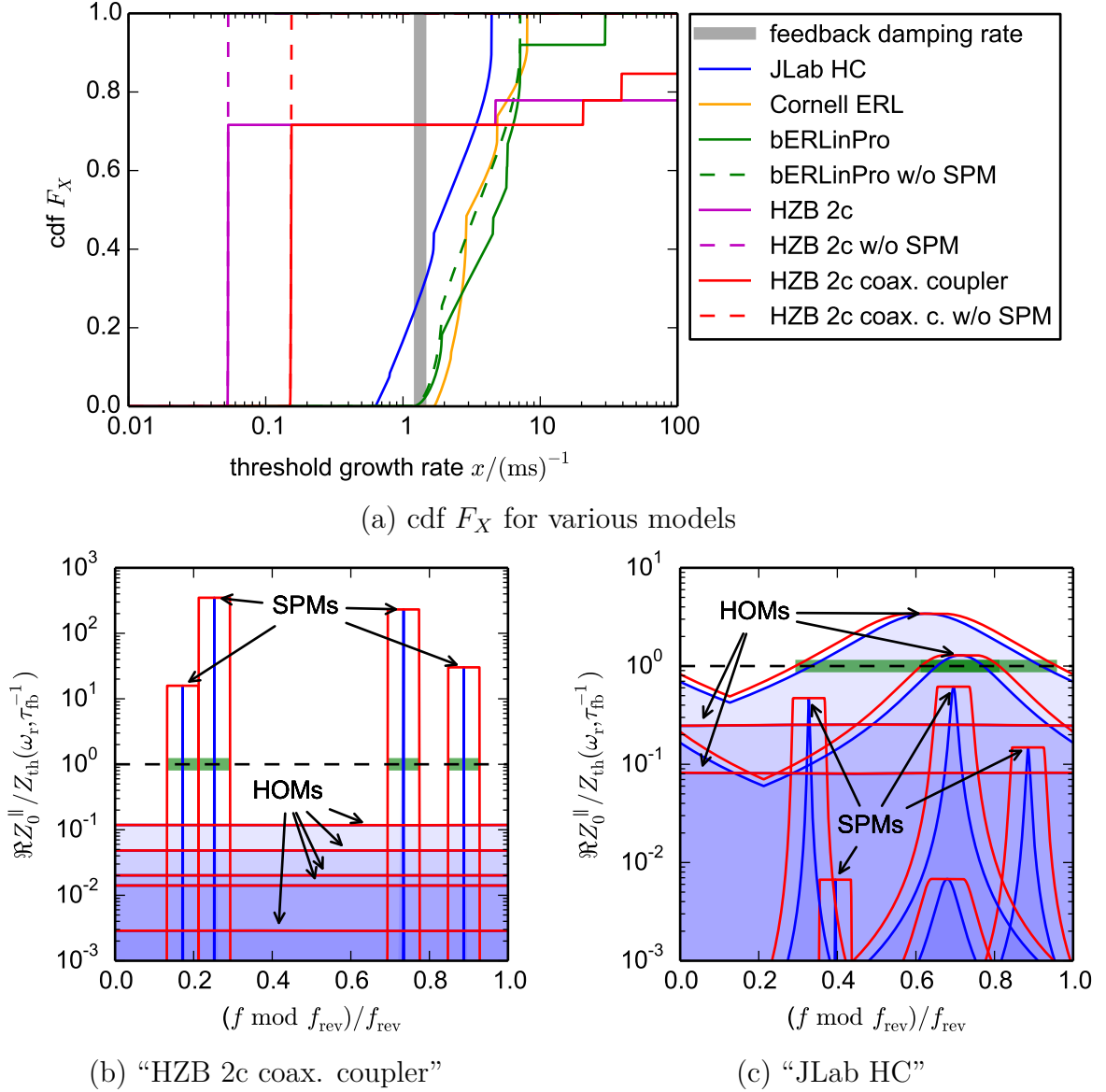


Figure 5.6.: (a) Cumulative distribution function (cdf) F_X stating the probability of stability vs. threshold growth rate x for the longitudinal case. (b) and (c) Aliased HOM impedance illustrating the calculation of the probability of stability for each HOM at the threshold growth rate equal to the BBFB damping performance τ_{fb}^{-1} for different cavity models. Colors and line styles see Fig. 5.5.

In other words, the probability of global stability is simply obtained by multiplying the individual probabilities of stability given by each HOM. The function $F_X(x)$, i.e., global stability, is plotted for a number of cavity models in Fig. 5.6a for the longitudinal case

5. Predictions of Coupled Bunch Instabilities for BESSY VSR

and in Fig. 5.7a for the transverse case. Note that the cdf $F_X(x)$ is exactly the same quantity as shown in Fig. 5.4 with the difference that here it is a continuous function.

The HZB models [37] and the “JLab HC” model [92] are 1.5 GHz cavities with five cells. The models “Cornell ERL” [53] and “bERLinPro” [99] are 1.3 GHz cavities with seven cells designed as main linac cavities for the ERL projects Cornell ERL [100] and bERLinPro [11] respectively.

5.2.3. Discussion

Figures 5.6 and 5.7 show the results of the calculation, the probability of stability for BESSY VSR as a function of threshold growth rate, e. g., given by the performance of the BBFB system for a number of different cavity models. For two cavity models, “HZB 2c coax. coupler” and “JLab HC”, the aliased impedance spectrum is additionally shown.

In the longitudinal case, the effect of the SPMs is somewhat special in BESSY VSR where they will have very high Q values, hence be very narrow. The solid lines of the model “HZB 2c coax. coupler” in Fig. 5.6a tell that the probability of stability is approximately $(1 - 2a/f_{\text{rev}})^4 \approx 70\%$ if no precautions to actively avoid the excitation of the SPMs are considered. The number is obtained by the multiplication of four narrow modes, each having a width at the threshold approximately equal to twice the extra margin a .

Note that the analytic formulas used in this section seem to overestimate the growth rate of SPMs, as discussed in Section 3.3.4. Using the conclusions in Section 3.3.4, the probability of stability would be given by only one SPM above the threshold, i. e., $1 - 2a/f_{\text{rev}} \approx 92\%$.

If repetitive steps of mechanical deformation and tuning of the cavity are performed until no SPM is close to a beam harmonic, the question of stability is not a statistical anymore and stability could be ensured.

The longitudinal HOMs of the latest HZB models seem to pose no thread to stability.

The transverse HOMs of the latest HZB model are also well below the threshold except for one mode which is of very narrow type. The probability of instability by exciting this mode is small, namely about $2a/f_r \approx 8\%$.

Generally, it is confirmed that a small number of narrow HOMs pose a low risk on the instability, as already suspected in Section 5.1.4.

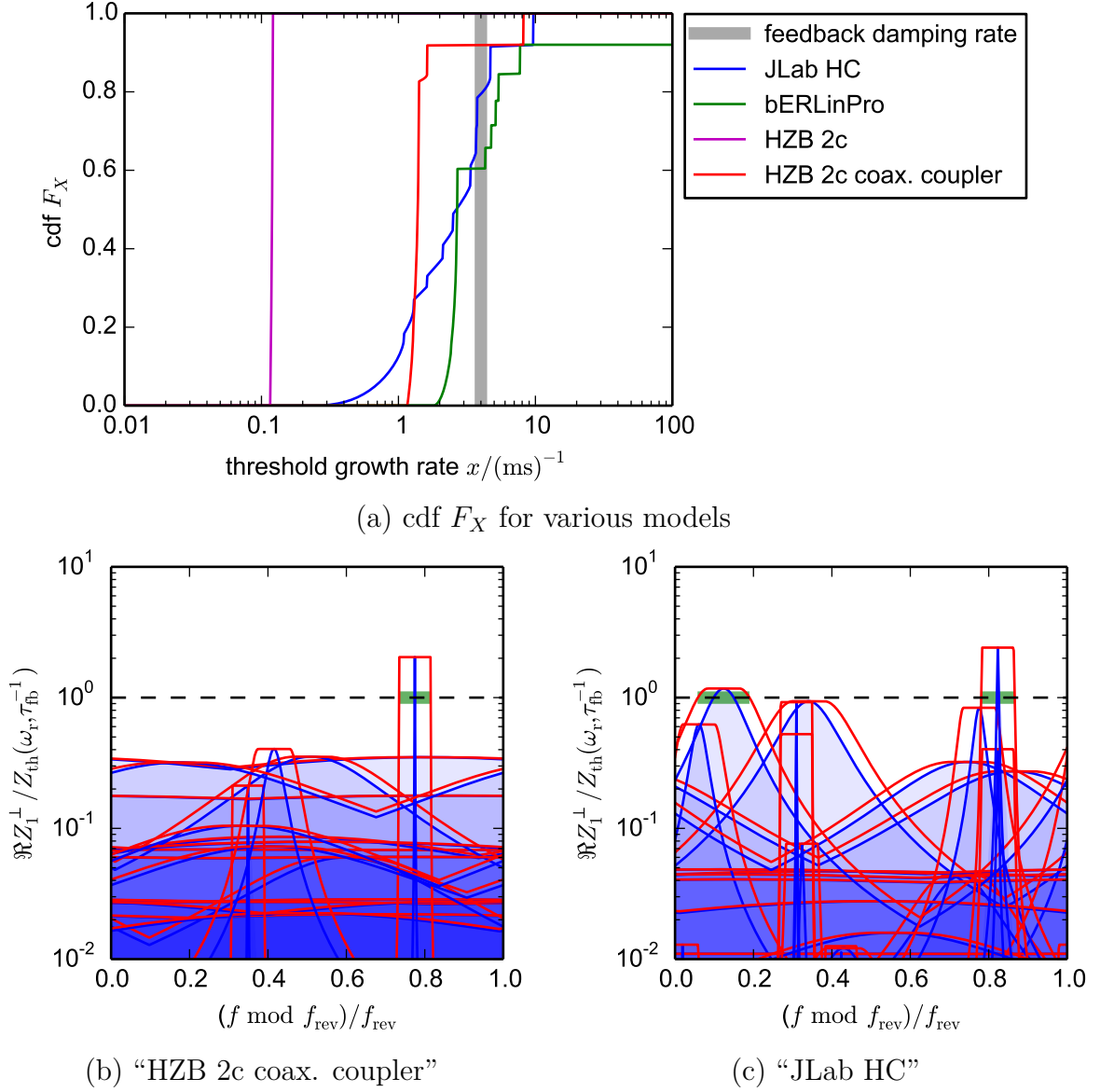


Figure 5.7.: (a) Cumulative distribution function (cdf) F_X stating the probability of stability vs. threshold growth rate x for the transverse case. (b) and (c) Aliased HOM impedance illustrating the calculation of the probability of stability for each HOM at the threshold growth rate equal to the BBFB damping performance τ_{fb}^{-1} for different cavity models. Colors and line styles see legend in Fig. 5.5.

5.3. Fill Pattern Dependency

The theory of fill pattern dependent CBI was discussed in Section 2.4 and Section 2.6.3. Note that the following discussion does neither include the Landau damping induced by the effect of transient beam loading in the fundamental modes of the cavities nor the Landau damping provided by a spread in the synchrotron tune induced by HOMs. It is assumed that the unperturbed synchrotron frequencies are identical for every bunch, even though the (small) tune spread induced by HOMs is calculated by this algorithm. As will be shown in this section, the sole effect of uneven fill has a minor impact on the instability. Unlike, e. g., Landau damping caused by transient beam loading in the longitudinal case.

In the following, the algorithm will be explained along with the calculation of an example in the longitudinal and the transverse plane. After that, a number of fill patterns are studied with respect to CBIs and general conclusions are stated.

5.3.1. Longitudinal Case

Figures 5.8 to 5.11 show the calculation steps for the BESSY VSR baseline fill pattern Fig. 1.4 and the longitudinal HOMs of the 1.5 GHz cavity model called “HZB 2c coax. coupler”.

First, the beam spectrum is calculated by means of Eq. 2.38. The fill pattern and the absolute value of the beam spectrum components I_p are shown in Fig. 5.8. As can be seen, the beam spectrum has a very strong component at $p = 200$, corresponding to a frequency of 250 MHz which is caused by the fact that the majority of the current is placed in odd buckets, i. e., long bunches. Only a small fraction of the current occupies even buckets, i. e., short bunches. The two gaps in the fill pattern are manifested as relatively strong components at $p = 2$ and $p = 398$.

Next, the mode-coupling impedance Z_{lm} , defined in Eq. 2.39, must be computed. It contains the information about the impedance spectrum, i. e., the sum of all resonator impedances, at discrete points. The first index, l , adds the contribution of the impedance spectrum sampled at the frequency of the side bands of CBM l multiplied with the frequency, i. e., it is the dynamic contribution. The second index, m , adds the contributions of the impedance spectrum sampled at the frequency of the beam harmonic $l - m$ multiplied with the frequency, i. e., it is the static contribution. For $l = m$, the static contribution is zero for all harmonics except for multiples of the beam frequency, i. e., pMf_{rev} , which then equals the even fill case.

Thus, the diagonal elements Z_{ll} have a simple interpretation. They are the product of the impedance Z_0^{\parallel} and the frequency f of CBM l . Here, the frequency f can be positive or negative, hence the real values of Z_{ll} can be positive or negative, even though $\Re(Z_0^{\parallel}) > 0$ for all resonators. A positive real value, i. e., $\Re(Z_{ll}) > 0$, indicates that the CBM l will have a positive growth rate. Analogously, $\Re(Z_{ll}) < 0$ indicates a damped CBM. The normalization with $M\omega_{\text{rev}}$ in Eq. 2.39, cancels the angular frequency in the dimension

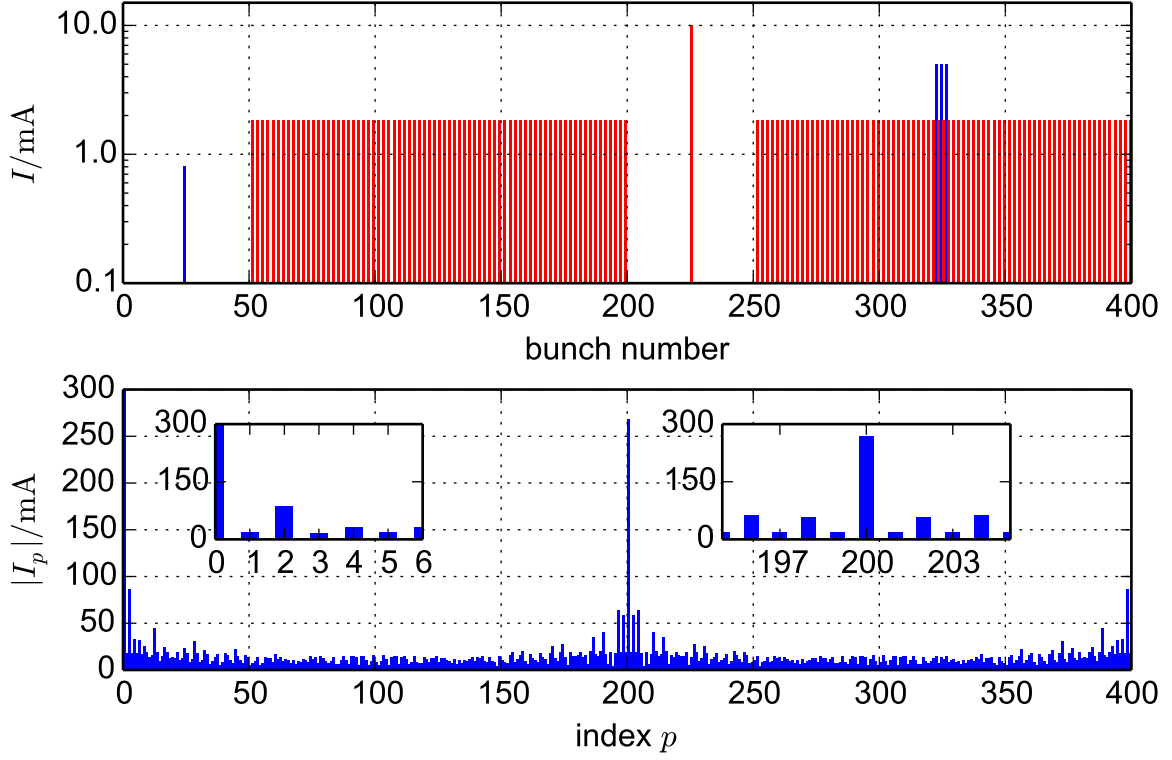


Figure 5.8.: Top: BESSY VSR baseline fill pattern, also shown in Fig. 1.4. Bottom: Absolute value of the corresponding beam spectrum I_p .

and Z_{lm} remains an impedance with units in Ω . For even fill, $\Re(Z_{ll})$ is proportional to the growth rate of CBM l and $\Im(Z_{ll})$ is proportional to the tune shift of CBM l . The real and imaginary part of the diagonal elements of the mode-coupling impedance Z_{lm} are shown in Fig. 5.9.

Third, the A_{lm} matrix, defined in Eq. 2.37 has to be calculated. Basically, the calculation of A_{lm} is the multiplication of the impedance with the current and all other machine parameters.

In case of even fill, I_p is non-zero only for $p = 0$ and Z_{lm} becomes diagonal. The complex frequency shift, i. e., the growth rate and tune shift, of all CBMs can then directly be read out from the diagonal elements of A_{lm} .

For uneven fill, the multiplication of I_p and Z_{lm} leads to the so called mode coupling, which may influence the growth rate of the strongest growing mode [101]. Figure 5.10 depicts the absolute value of the A_{lm} matrix as a 400×400 color-code image. Values significantly other than zero are only visible along the diagonal axis and along the diagonal lines shifted by ± 200 columns. The latter is a consequence of the fact that the fill pattern almost exclusively consists of long bunches with a spacing of two buckets, leading to 200

5. Predictions of Coupled Bunch Instabilities for BESSY VSR

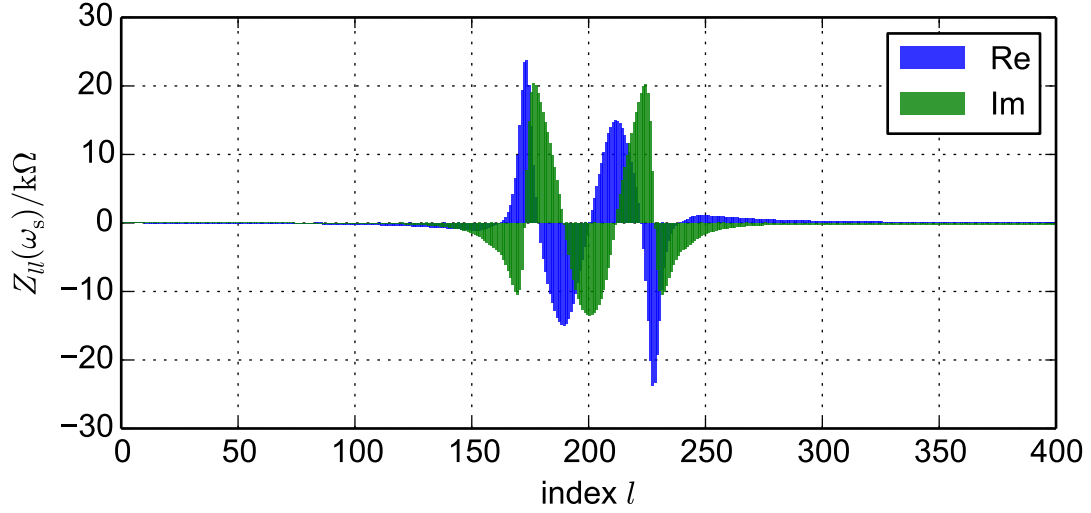


Figure 5.9.: Longitudinal case. Real and imaginary part of the diagonal elements of the so called mode-coupling impedance Z_{lm} . It corresponds to the product of frequency and impedance sampled by the synchrotron side bands summed over all harmonics of Mf_{rev} . See text for details.

pairs of almost identical eigenvalues.

Fourth, the eigenvalues of A_{lm} need to be obtained. In case of even fill, A_{lm} is diagonal and the diagonal elements are the eigenvalues. For uneven fill, common methods of linear algebra are applied. The eigenvalues obtained from the eigendecomposition of the matrix A_{lm} are directly related to the tune shift and growth rate of the coherent frequencies, see Eqs. 2.40 and 2.41. The growth rate and tune shift obtained from the eigenmodes of the uneven fill are shown in Fig. 5.11 in comparison with the case of even fill.

Note that the eigenvalues of the uneven solution are not ordered by any particular criterion by the numerical algorithm. Thus, a sorting was applied based on the similarity of the absolute values of the eigenvectors with the M -dimensional unit vectors, using an M -dimensional Euclidean norm, i. e., the similarity S of the complex eigenvector \vec{a} with the n -th unit vector \hat{e}_n is given by,

$$S(\vec{a}, n) = \|\vec{a} - \vec{e}_n\|_2 = \sqrt{\sum_{i=0}^M (|\vec{a}_i| - \hat{e}_{n,i})^2}, \quad (5.18)$$

where $|\vec{a}|$ means the absolute values of \vec{a} are taken elementwise and i is the index for the elements of the vectors. This sorting is not perfect, but it can be seen that the even fill and uneven fill case look rather similar in Fig. 5.11, thus the effect of the fill unevenness

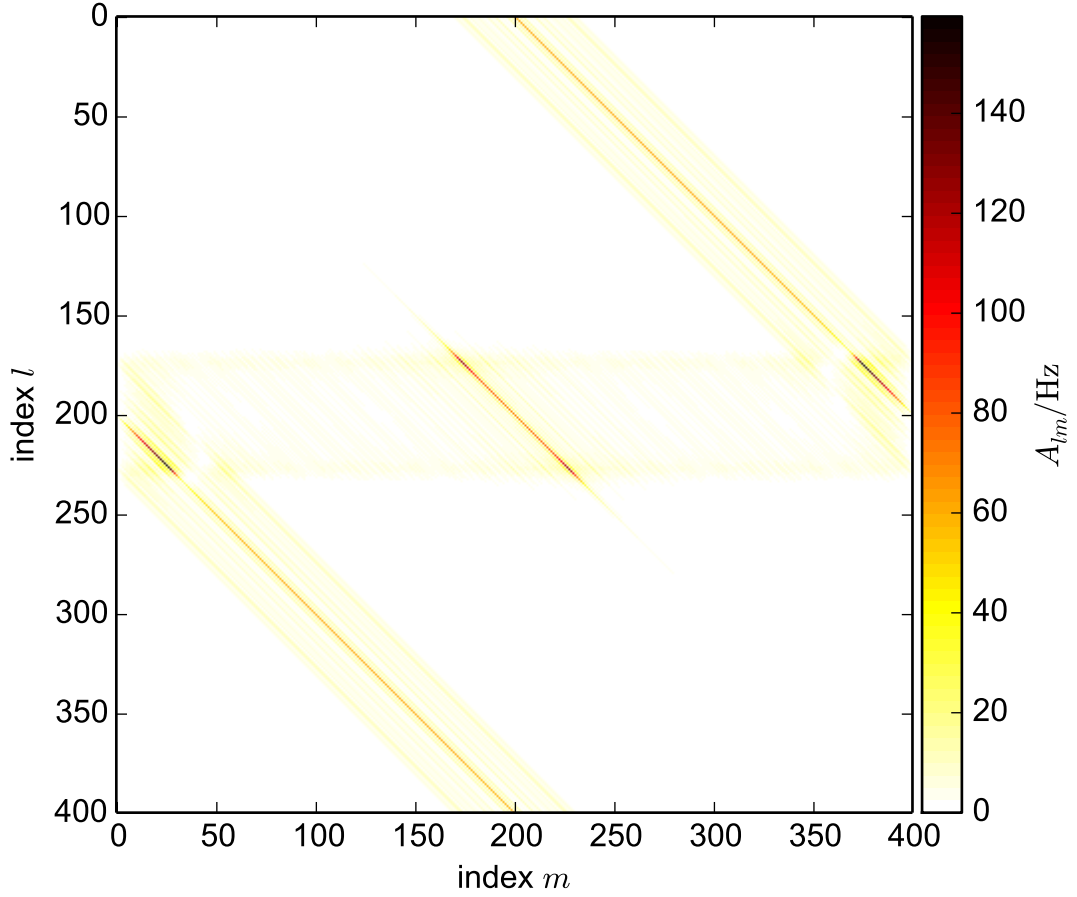


Figure 5.10.: Longitudinal case. Absolute values of the A_{lm} matrix whose eigenvalues are the coherent frequencies for uneven fill, yielding the growth rate and tune shift.

is not very strong on the growth rates in this example.

In addition to the ordering, Fig. 5.11 bottom panel shows a more significant difference between the cases of even and uneven fill. This stems from the tune shift induced by the static contributions, i. e., the beam spectrum and not its synchrotron side bands. Those contributions only occur at uneven fill and only in the longitudinal case.

The corresponding eigenvectors can also be obtained but as the ordering of the eigenvalues is different compared to the even fill, showing the eigenvectors adds little value to the understanding of the algorithm.

5. Predictions of Coupled Bunch Instabilities for BESSY VSR

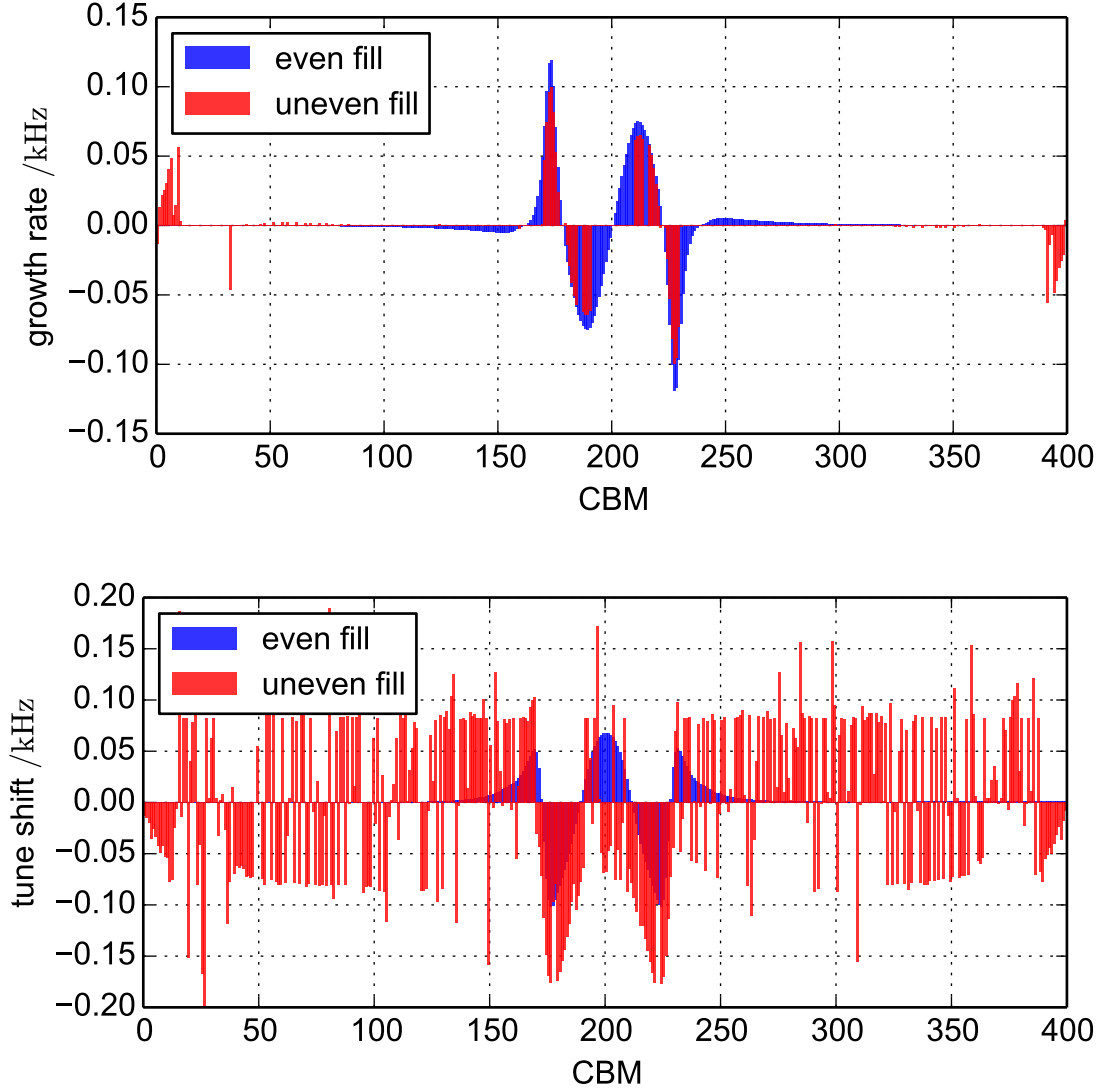


Figure 5.11.: Longitudinal case. Top: Growth rate for even fill and uneven fill, corresponding to the real part of the eigenvalues. Bottom: Angular frequency shift, corresponding to the negative imaginary part of the eigenvalues. Note that the CBMs labeled in the horizontal axis are different for the even and uneven fill as they correspond to a different set of eigenvectors.

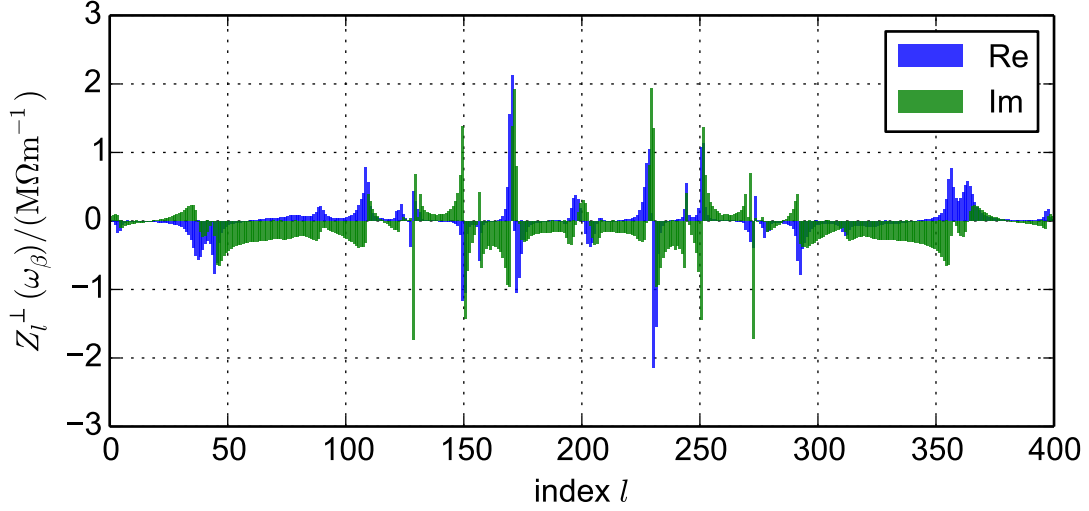


Figure 5.12.: Transverse case. Real and imaginary part of the so called transverse mode-coupling impedance Z_l^\perp , corresponding to the product of frequency and impedance sampled by all betatron side bands. See text for details.

5.3.2. Transverse Case

Figures 5.12 to 5.14 show the calculation steps for the BESSY VSR baseline fill pattern Fig. 1.4 and the transverse HOMs of the “HZB 2c coax. coupler” cavity model.

The fill pattern and the beam spectrum is the same as above, see Fig. 5.8. The Real and imaginary part of the transverse mode-coupling impedance Z_l^\perp is shown in Fig. 5.12. In the transverse case, there is no static contribution and Z_l^\perp directly corresponds to the product of frequency and impedance spectrum at the all side bands. Compared to the longitudinal case, the spectrum contains more HOMs including some with very high and low Q .

Figure 5.13 depicts the absolute value of the A_{lm} matrix as a 400×400 color-code image. Similar to the longitudinal case, values significantly other than zero are only visible along the diagonal axis and along the diagonal lines shifted by ± 200 columns.

The eigenvalues and in turn the growth rate and tune shift obtained from the eigendecomposition of the matrix A_{lm} are shown in Fig. 5.14 in comparison with the case of even fill. The same sorting as for the longitudinal case has been used and the similarity of the solutions of even fill and uneven fill case can be seen.

5. Predictions of Coupled Bunch Instabilities for BESSY VSR

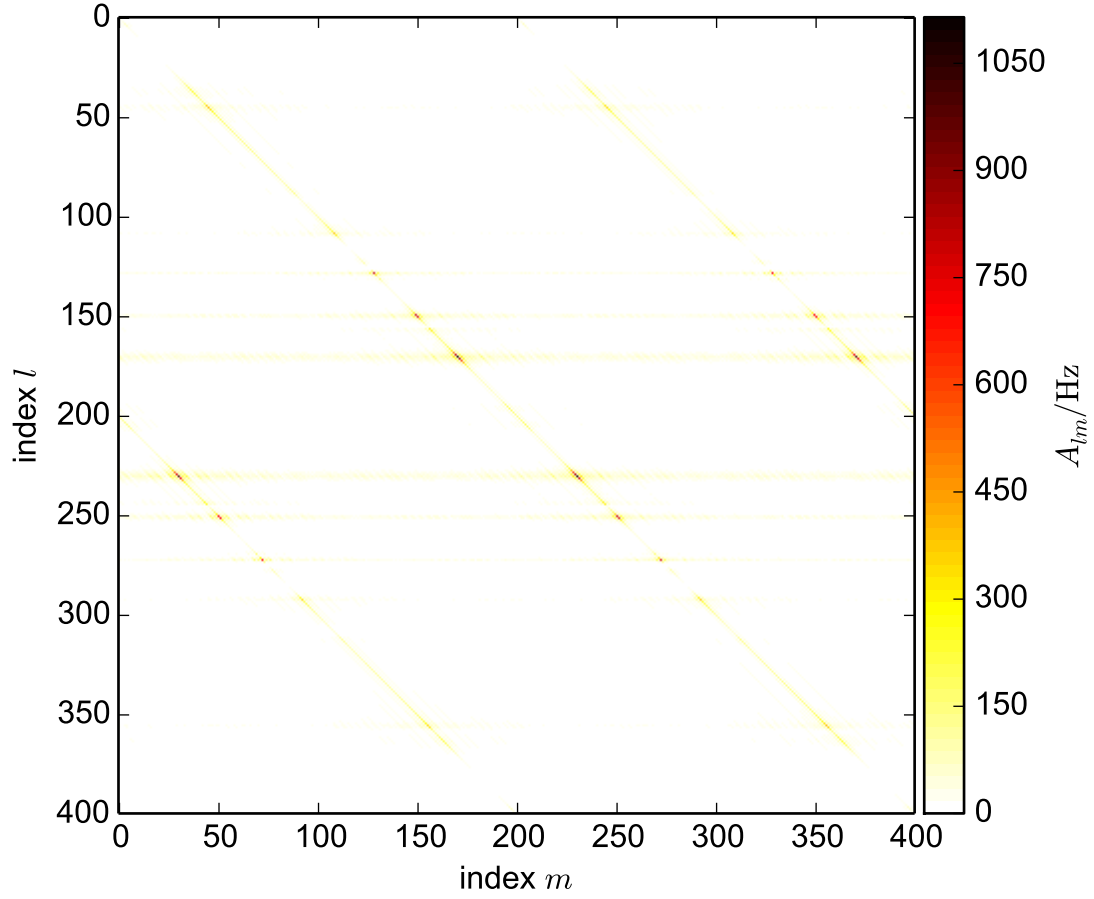


Figure 5.13.: Transverse case. Absolute values of the A_{lm} matrix whose eigenvalues are the coherent frequencies for uneven fill, yielding the growth rate and tune shift.

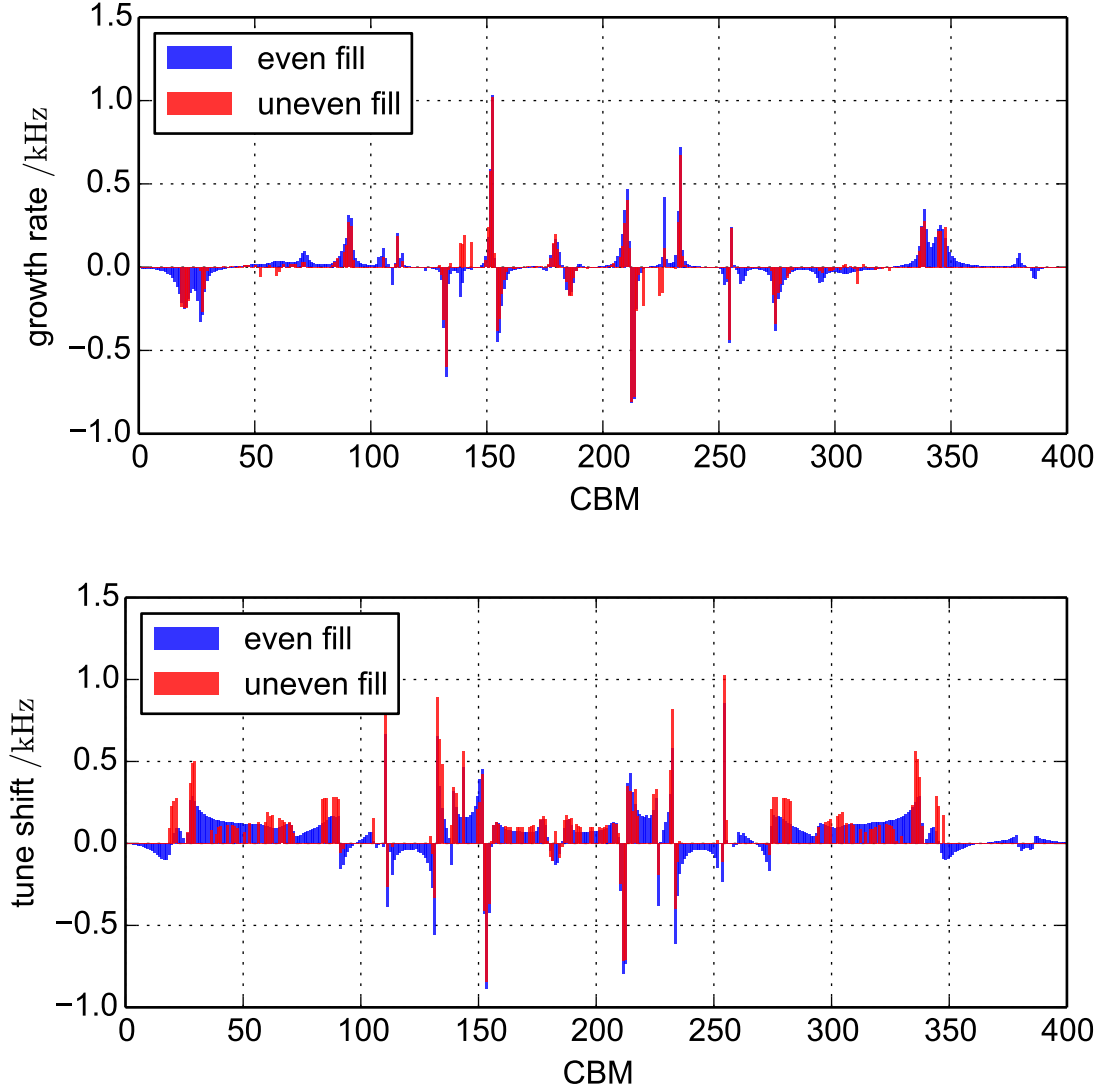


Figure 5.14.: Transverse case. Top: Growth rate for even fill and uneven fill, corresponding to the real part of the eigenvalues. Bottom: Angular frequency shift, corresponding to the negative imaginary part of the eigenvalues. Note that the CBMs labeled in the horizontal axis are different for the even and uneven fill as they correspond to a different set of eigenvectors.


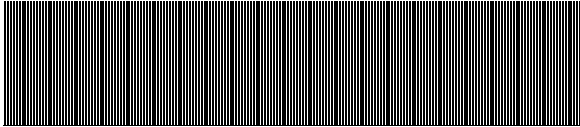

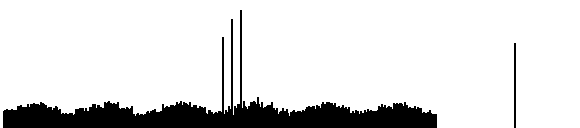


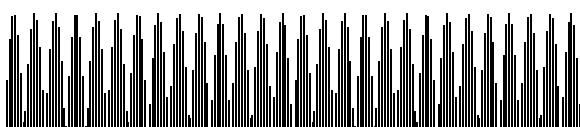
5.3.3. Results

The same calculation as above has been done for a number of fill patterns shown in Tab. 5.1. The average current of all fills is 300 mA and the synchrotron frequency is assumed to be exactly $f_s = 8$ kHz for all 400 possible bunches. Hence, neither the effect of Landau damping, nor the longitudinal decoupling of long and short bunches is taken into account. The description of the fill patterns of Tab. 5.1 and a discussions of the results of the calculations are given in the following:

- (a) Even fill with 400 bunches. All following growth rates are normalized to the results of this even fill.
- (b) Even fill with 200 bunches, corresponding to long bunches in BESSY VSR. Very small effect on growth rates.
- (c) BESSY VSR baseline fill pattern defined in Fig. 1.4. The effect on the growth rates appears to be very small, except for the longitudinal modes of the HZB cavity where the maximum growth rate is reduced by about 17%.
- (d) A realistic BESSY II fill pattern with rather strong variations, a 200 ns gap and four high current bunches. The effect on the growth rates appears to be about 10% or less.
- (e) Another realistic BESSY II fill pattern with variations introduced by the injection system, a 200 ns gap and four high current bunches. The effect on the growth rates appears to be similar as to fill pattern (d).
- (f) A fill pattern tailored to maximize the so called mode coupling of the fastest growing longitudinal CBM with its mirror mode for the HZB cavity. Essentially, it is a sinusoidal fill pattern with period length of 1.156 buckets, for details on the method of calculation see [101, 102]. As desired, the growth rate of the fastest growing longitudinal CBM is reduced for the HZB cavity. However, the reduction is only about 40%.
- (g) A fill pattern tailored to maximize the mode coupling of the fastest growing longitudinal CBM with its mirror mode for the “JLab HC” cavity. With the same approach as above, it is a sinusoidal fill pattern with period length of 1.869 buckets. Similar to the case above, the growth rate of the fastest growing longitudinal CBM is reduced by about 40% for the “JLab HC” cavity.

5.3. Fill Pattern Dependency

Table 5.1.: Fill pattern dependency of longitudinal and transverse relative growth rate of fastest growing CBM for different fill pattern and two cavity models at a fixed tuning setting (not necessarily optimized). The cavity models are the HZB model “HZB 2c coax. coupler” [37] and the “JLab HC” model [92]. More details on the fill pattern (a) to (g) are given in the text.

Fill Pattern		Relative CBI Growth Rate			
		HZB		“JLab HC”	
		long.	trans.	long.	trans.
(a)		1	1	1	1
(b)		1.002	1.040	1.000	1.049
(c)		0.836	0.994	0.987	1.001
(d)		0.875	0.892	0.998	0.919
(e)		0.908	0.896	0.999	0.933
(f)		0.618	1.043	1.029	0.960
(g)		0.669	1.256	0.616	0.984

5.3.4. Conclusion

As was shown, the sole effect of the fill pattern on CBIs is small. Even with a specially tailored fill pattern, Tab. 5.2f and Tab. 5.2g, the effect on CBIs stays below a factor of two. In this case, the specially tailored fill pattern are unfeasible due to the high single bunch charge. Similar findings have been made at other machines and experimentally confirmed [102]. The effect of realistic fill pattern, such as the BESSY VSR baseline fill pattern, Tab. 5.2c or the realistic BESSY II fill patterns with additional variations, Tab. 5.2d and Tab. 5.2e, are generally small and in all cases below 20%. If the number of buckets is much larger than the number of strong HOMs, such as in the scenarios evaluated here, the modulation coupling introduced from the uneven fill is likely to couple a strongly growing mode with a non-growing one, which explains why most fill patterns lead to a small reduction of the maximum growth rate.

5.4. Low- α Operation

The option to operate the storage ring in a low- α optics will remain in BESSY VSR and is in consideration for a special operation mode for shortest bunches [2]. With an optics similar to the low- α optics of BESSY II, a momentum compaction factor of $\alpha = 3.5 \times 10^{-5}$ will lead to a reduction of the bunch lengths by a factor of approximately 5.

As discussed in Sections 1.2 and 1.3, the microwave instability will then limit the bunch current. For BESSY VSR, it is estimated that a non-bursting low- α mode would be operated with about 13 mA current, divided approximately equally to short and long bunches [2]. If a bursting beam is accepted, a current in the order of 100 mA could be possible.

In terms of CBIs, those changes significantly affect the growth rate of the instability. For transverse CBIs, it will be the scaling with the current that linearly reduces the growth rate, see Eq. 2.53. However, the change of the linear optics also changes the value of the vertical betatron function at the location of the SC cavities, see Fig. 5.15. With a value of $\beta_y = 9$ m, the growth rate is then increased by factor of approximately two compared to the standard user optics.

The growth rate of the longitudinal CBIs is reduced by the current and additionally by the low momentum compaction factor. This can be seen from Eq. 2.30 when the synchrotron frequency is replayed by $f_s \propto \sqrt{\alpha}$, according to Eq. 1.5. The effective scaling is then given by the following expression if only α is changed:

$$\tau_\mu^{-1} \propto \sqrt{\alpha}. \quad (5.19)$$

Thus, an additional reduction of 5 in the growth rate of longitudinal CBI is expected in the low- α optics.

It can be concluded, that CBIs are significantly suppressed in BESSY VSR low- α mode.

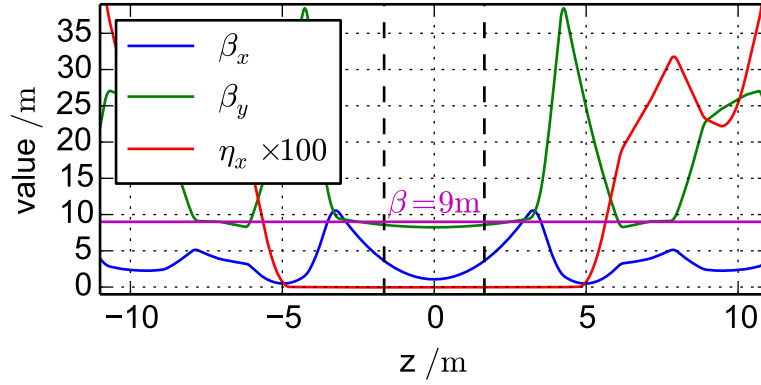


Figure 5.15.: Horizontal betatron function (β_x), vertical betatron function (β_y) and 100 fold magnified horizontal dispersion function (η_x) of BESSY II in a specialized low- α mode [103] shown near the low- β straight section of the SC cavities. The beginning and end of the SC cavities is indicated by vertical dashed lines.

The growth rate goes down linearly with the current in all planes and an additionally suppression of a factor of 5 is given for the longitudinal plane. However, a moderate increase of the vertical transverse growth rate is expected.

5.5. Instabilities Driven by Fundamental Modes

The interaction of the beam with the fundamental modes of the SC cavities can also lead to instabilities, the so called Robinson instabilities [40].

The Robinson instabilities are separated into an AC instability and an DC instability, named after that fact that the former defines an instability where oscillations grow and the latter refers to an instability where the bunch phase positions runs away in one direction.

The AC Robinson instability is nothing but the CBI with CBM 0 and a fundamental cavity mode as driving impedance. The small effect approximation of the AC Robinson instability was mentioned in Section 2.3.2. In the case of BESSY VSR, the shunt impedance of the fundamental modes of the SC cavities is in the order of $R_{s,0} = 1 \times 10^{11} \Omega$. With such an impedance, the argument of a small disturbance is not valid. In the contrary, the induced fields are theoretically in the order of $1 \times 10^{10} \text{ V}$, which is much more than the 1.5 MV that defines the nominal longitudinal dynamics. Hence, the small effect approximation in Section 2.3.2 is inapplicable.

A possibility would be to solve Eq. 2.23 directly to obtain the growth rate of the instability. However, in a realistic setup, the effective impedance as seen by the beam is significantly modified by the RF feedback, see for example [104], which is not covered in this thesis. As a consequence, the possible occurrence and strength of both Robinson

5. Predictions of Coupled Bunch Instabilities for BESSY VSR

instabilities strongly depends on the specific RF feedback parameters [2]. Hence, it is refrained from making any statements regarding AC or DC stability in this thesis, as the plausibility without the inclusion a realistic RF feedback would be too questionable.

5.6. Booster Synchrotron

An RF upgrade is also proposed for the BESSY II booster synchrotron to shorten the stored bunches in order to increase the injection efficiency into short bunches stored in BESSY VSR during top-up operation.

While ramping the SC RF cavities down shortly to lengthen the short bunches would be feasible from the beam dynamics point of view [91], it appears unfeasible as neither the RF can be detuned quickly, nor is the generator power sufficient to reduce the operating voltage [2].

The booster runs at a frequency of 10 Hz, where the beam is stored for about 45 ms from the point of injection to the first possible extraction point. With $f_{\text{rev}} = 3.125$ MHz, the bunches remain for about 1.4×10^5 turns in the synchrotron. This is long enough for CBIs to build up and the question of HOM driven CBIs in the booster synchrotron arises if additional cavities with potentially strong HOMs are installed in the ring.

CBIs in the booster synchrotron would lead to a reduced injection efficiency which must be avoided in terms of radiation safety.

With the relevant machine parameters of the BESSY II booster synchrotron given in Tab. 5.3, the impedance thresholds can be calculated using Eqs. 5.1 and 5.2 and compared to the impedance spectrum of the cavities considered for the RF upgrade. Note that the calculation is done at extraction energy and $f_s = 305$ kHz was chosen in the calculation which includes the RF upgrade. Below extraction energy, the beam may be more unstable due to the reduced rigidity and lower radiation damping rate. However, if the beam is unstable at the first extraction point, it is possible to extract at the second point to gain some time in a high energy regime for the damping mechanisms to stabilize the beam.

Figure 5.16 shows the booster threshold impedance for the longitudinal $m = 0$ case and the transverse $m = 1$ case for a threshold based on the radiation damping at high energy, see Tab. 5.3 and an estimated BBFB performance, see below. The thresholds are compared to the impedance spectra of the 1.5 GHz BESSY VSR cavity model “HZB 2c coax. coupler” and to a NC 3.0 GHz cavity option.

The impedance spectrum of the NC 3.0 GHz is extracted from preliminary studies with a NC 15-cell 3.0 GHz cavity [106] which was obtained by means of scaling a NC multi-cell 2.45 GHz MAMI structure [107].

The BBFB performance was estimated based on the BBFB performance of the BESSY II storage ring mentioned in Section 5.1, scaled up by a factor of 2.5 which corresponds to the ratio of circumferences of the storage ring to the booster synchrotron. This estimate assumes that a similar BBFB hardware including the kickers would be

Table 5.3.: Relevant machine parameters of the BESSY II booster synchrotron [2, 105]. Some numbers are rounded.

Parameter	Value
Energy E	1.7 GeV ^a
Momentum compaction factor α	0.033
Total beam current I_{DC}	2.5 mA
Circumference	96 m
Revolution frequency f_{rev}	3.125 MHz
Harmonic number	160
Fundamental RF frequency	500 MHz
Synchrotron frequency f_s , presently	38 kHz ^a
Synchrotron frequency f_s , after RF upgrade	305 kHz ^a
Betatron functions at cavities β_x, β_y	6 m
Longitudinal radiation damping time τ_{\parallel}	3 ms ^a
Transverse radiation damping time τ_{\perp}	6 ms ^a

^aAt extraction energy.

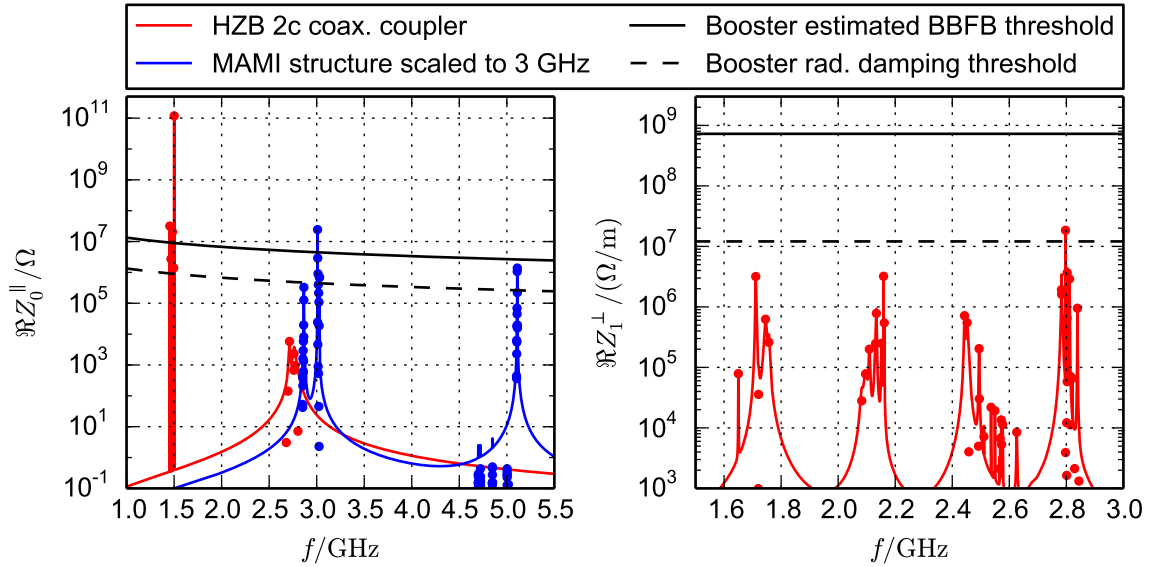


Figure 5.16.: Threshold impedances for CBIs at the BESSY II booster synchrotron in comparison with different cavity models. Left: Longitudinal $m = 0$ impedance. Right: Transverse $m = 1$ impedance. See text for details on the cavity models and threshold calculations.

5. Predictions of Coupled Bunch Instabilities for BESSY VSR

installed in the booster and that the damping rates would be faster simply because the bunches pass the kickers more frequently. It should be considered very preliminary, with the following numerical values:

$$\tau_{\text{fb}}^{-1} \Big|_{\text{very preliminary booster estimate}} \approx \begin{cases} 3.33 \times 10^3 \text{ s}^{-1} & \text{long.} \\ 10.0 \times 10^3 \text{ s}^{-1} & \text{trans.} \end{cases} \quad (5.20)$$

The following conclusions can be drawn from Fig. 5.16. The thresholds in the longitudinal plane are surprisingly large despite the relatively large α and small circumference of the booster. The main reason for the large threshold is the very high synchrotron frequency of $f_s = 305 \text{ kHz}$, which is a consequence of the increased longitudinal focusing of the RF upgrade, and the small current of 2.5 mA , see Eq. 5.1 for the scaling.

In comparison with the highly HOM damped cavity model “HZB 2c coax. coupler”, no longitudinal CBIs are expected even if only radiation damping is considered. However, the non-optimized NC 15-cell cavity without HOM dampers shows a mode spectrum with significantly larger impedances, which is not surprising as highest frequencies and large numbers of cells generally favor strong HOMs. This cavity might lead to longitudinal CBIs if only radiation damping is considered, thus, a BBFB system would be recommended in this case to ensure stability.

The thresholds in the transverse plane are also rather large due to the small current. Unfortunately, no studies of the transverse HOMs of the NC 15-cell cavity exists yet but for the “HZB 2c coax. coupler” cavity, it can be concluded that it is likely that no transverse CBIs will arise even if only radiation damping is considered.

6. Transient Beam Loading

This chapter covers the studies of transient beam loading. Section 6.1 introduces the general concept and presents methods for its calculation. In Section 6.2, a measurement performed at BESSY II is shown, analyzed and used for the verification of the calculation methods. Finally, Section 6.3 presents the calculations for BESSY VSR, where the effect on the short and long bunches are presented and consequences are discussed, such as an effect on the beam lifetime as well as possible longitudinal Landau damping.

6.1. Definition and Methods of Calculation

In this thesis, the term *transient beam loading* refers to a steady state where the net complex voltage seen by a probe at the nominal bucket positions is not equal for all buckets. This typically occurs through beam loading in active and passive cavities if the fill pattern is not even, e. g., if it exhibits a gap. The net voltage then shows a variation at the nominal bucket positions that does not change over time.

Furthermore, *beam loading* refers to the induced complex voltage in the fundamental mode of an active or passive cavity. In particular, the induced voltage may be real or imaginary, i. e., the beam loading may be called resistive, reactive or capacitive. Hence, beam loading solely depends on the beam and the properties of the impedance but not on other contributions to the state of the momentary phasor such as a generator.

In the following, different methods for the calculation of transient beam loading are discussed. The most insightful way is using a form of Ohm's law and the beam spectrum, whereas a tracking simulation is a straight forward approach with few pitfalls, see for example [63, 108].

6.1.1. Induced Voltage

The induced voltage in a cavity is basically given by Ohm's law, where the voltage equals the resistance times the current. In the case of a cavity, the resistance is replaced by the impedance, in turn yielding a complex voltage which contains additional information on the phase relation of the current to the induced fields. An additional factor of two is needed to account for the strongly bunched beam, i. e., a series of delta functions, and the circuit definition of the shunt impedance which is used in this thesis.

6. Transient Beam Loading

Together, the complex voltage V induced by a bunched beam with a DC (average) current I_{DC} at a beam harmonic ω_{beam} is given by

$$V|_{\omega_{\text{beam}}} = 2I_{\text{DC}}Z_0^{\parallel}(\omega_{\text{beam}}), \quad (6.1)$$

with the impedance Z_0^{\parallel} of the cavity defined in Eq. 2.10 via the shunt impedance $R_{s,0}$, the quality factor Q and the angular resonance frequency ω_r of the fundamental mode.

Equation 6.1 implies that Q is sufficiently large and that the system has reached a steady state with no beam oscillations. Both is true for the cases studied in this chapter.

Note that the induced voltage in Eq. 6.1 now oscillates at the frequency of the beam, i. e., ω_{beam} and not at the resonance frequency of impedance. The phase of the voltage relative to the beam current is given by $\arg V$ and the amplitude is given by $|V|$. At even fill, the only harmonics in the beam spectrum are multiples of the bunch frequency defined by the fundamental cavity, i. e., 500 MHz for BESSY II. Equation 6.1 further assumes that the bunches are so short that the drop of the amplitude at the beam harmonic I_p can be ignored at the angular frequency ω_r , i. e., $|I_p| = I_{\text{DC}}$, which is usually justified, see Fig. 1.8.

In case of uneven fill, the beam spectrum may have nonzero contributions at other revolution harmonics. The amplitude of each beam harmonic p is given by the complex amplitude of the beam spectrum I_p , defined in Eq. 2.38. The beam now induces a voltage at every revolution harmonic p according to the amplitude of the beam spectrum I_p ,

$$V|_{\omega_p} = 2I_pZ_0^{\parallel}(\omega_p), \quad (6.2)$$

with $\omega_p = 2\pi f_{\text{rev}}p$ the angular frequencies of the p -th revolution harmonic. The net effect on a bunch is then given by the superposition of all induced voltages oscillating at their individual frequencies.

The beam spectrum I_p is repetitive with respect to multiples of M , the number of buckets. As the cavity impedance is a rather narrow impedance, p can be restricted to the interval from 0 to M and the angular frequencies have to be chosen at a suitable interval that includes the resonance frequency of the cavity. For instance, a third harmonic cavity at BESSY II would be close to the harmonic $h = 3M = 1200$ and a suitable choice for ω_p would be

$$\omega_p = \begin{cases} 2\pi f_{\text{rev}}(3M + p) & , \quad 0 \leq p < M/2 \\ 2\pi f_{\text{rev}}(2M + p) & , \quad M/2 \leq p < M, \end{cases} \quad (6.3)$$

which defines a frequency interval with the resonance frequency of the cavity in its center.

6.1. Definition and Methods of Calculation

The net complex voltage V_m seen at a nominal bucket position m is then given by

$$V_m = \sum_{p=0}^{M-1} V|_{\omega_p} e^{2\pi i \frac{mp}{M}}, \quad (6.4)$$

the superposition of each contribution evaluated at the nominal bucket position. With the Fourier transform defined as $\mathcal{F}[x_k]_p = \sum_{k=0}^{M-1} x_k e^{-2\pi i \frac{kp}{M}}$, Eq. 6.4 can also be directly obtained from the fill pattern,

$$V_m = M\mathcal{F}^{-1}[2\mathcal{F}[i_k]_p \cdot Z_0^{\parallel}(\omega_p)]_m, \quad (6.5)$$

with the bunch current i_k of bunch k . Here, the length of the discrete series M (the number of buckets) is needed to cancel the normalization in the inverse Fourier transform $\mathcal{F}^{-1}[x_k]_p = M^{-1} \sum_{k=0}^{M-1} x_k e^{2\pi i \frac{kp}{M}}$.

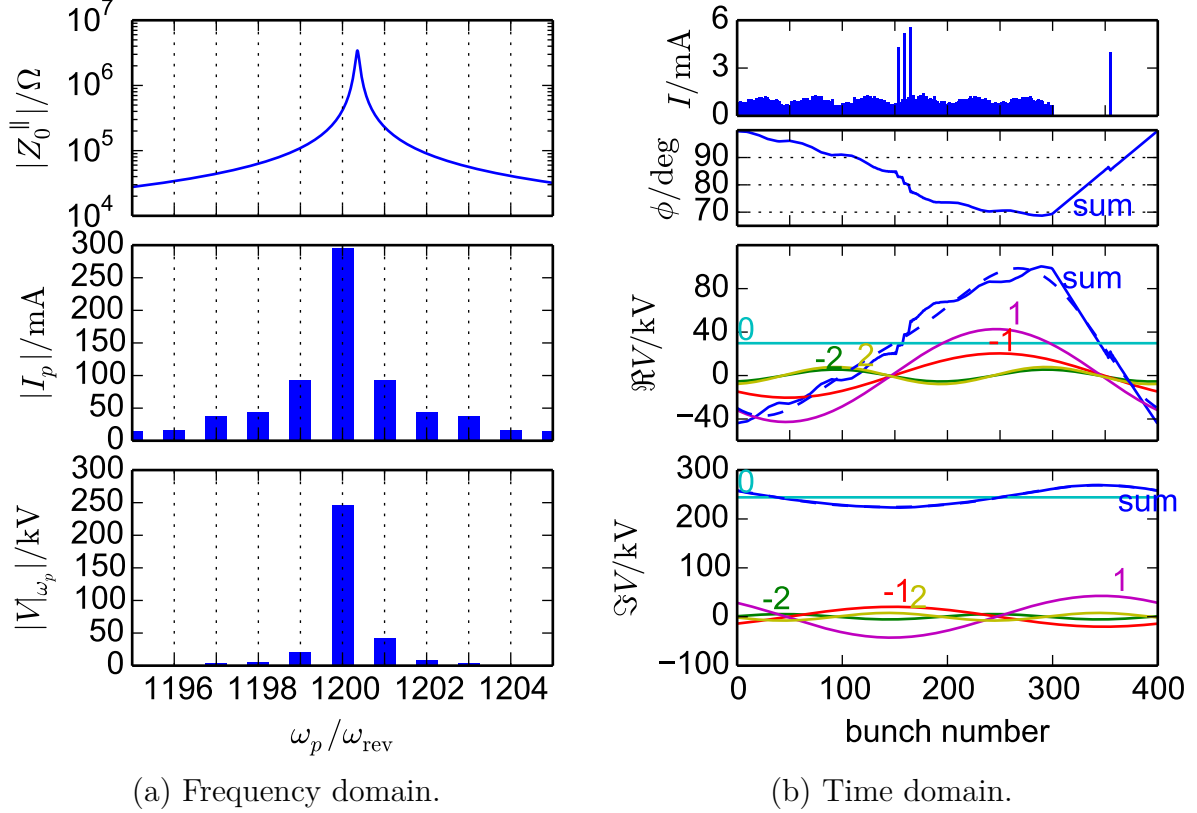
Equation 6.5 reveals the simplicity of the underlying physics, which is nothing but the calculation of the product of current and impedance to obtain a voltage. However, this needs to be done not only with a single DC current at one frequency, but simultaneously at all frequencies with their corresponding contributions. For this purpose, the multiplication is done in the frequency domain and then transferred back to the time domain.

Example

An example of this procedure is shown in Fig. 6.1 with graphs in the frequency domain in Fig. 6.1a and graphs in time domain in Fig. 6.1b. The example is performed with BESSY II parameters and a cavity that approximates the passive third harmonic Landau cavities of BESSY II with values set to $Q = 13\,900$, $R_{s,0}/Q = 247.48\,\Omega$ and detuned by $\Delta f_r = 443\,\text{kHz}$ above the 1200-th revolution harmonic so that bunch lengthening is achieved. The absolute value of the impedance of the cavity is shown in Fig. 6.1a top. The frequency axis has been limited to a few revolution harmonics around the resonance frequency of the cavity as the impedance drops quickly with the distance from its resonance frequency. The fill pattern used in this example, shown in Fig. 6.1b top, is a realistic BESSY II fill pattern.

The first step is to calculate the amplitude of the beam spectrum I_p by performing a Fourier transform on the fill pattern and choose the corresponding angular frequencies ω_p such that the resonance frequency is in the center of the interval. In this case, the choice given in Eq. 6.3 is made. The absolute value of I_p is shown in Fig. 6.1a center. As expected, $|I_p|$ is symmetric around the 1200-th revolution harmonic and because the fill pattern exhibits one large gap, the amplitudes of plus and minus one harmonic are relatively large.

6. Transient Beam Loading



(a) Frequency domain.

(b) Time domain.

Figure 6.1.: Visualization of the analytic calculation of transient beam loading with the steps in the frequency domain (a) and steps in time domain (b). (a) from top to bottom: Absolute value of resonator impedance (fundamental mode of Landau cavity), absolute value of amplitude of beam spectrum, absolute value of induced voltage oscillating at frequency ω_p . (b) from top to bottom: Bunch fill pattern, phase ϕ , real part and imaginary part of induced voltage at nominal bucket positions. In the latter three, lines annotated with a number refer to the contribution given by the beam harmonic indicated with the number whereas solid blue lines refer to the sum of all contributions and dashed blue lines refer to the sum of those contributions that are shown. See text for details.

Second, the impedance is multiplied with the amplitudes of the beam spectrum I_p , yielding the complex voltages $V|_{\omega_p}$, oscillating at their individual frequencies. The absolute value of those voltages is shown in Fig. 6.1a bottom. The strongly peaked shape of the impedance leads to the fact that only contributions very close to the resonance frequency induce a significant voltage. The visible asymmetry is caused by the detuning of the cavity.

Now, each $V|_{\omega_p}$ contributes to the voltage seen by a probe at the nominal bucket positions. The five strongest contributions are drawn in the bottom two graphs in Fig. 6.1b. The upper one of those graphs shows the real part of the voltage seen by a probe at the nominal bucket positions and is obtained by a cosine function with the amplitude given by $|V|_{\omega_p}|$, the angular frequency ω_p and a phase offset given by $\arg V|_{\omega_p}$. The real part of the voltage is the longitudinal accelerating voltage a particle experiences when it passes the cavity. The imaginary part of the contributions is plotted in the lower graph, obtained from the corresponding sine function. A particle at the nominal bucket position does not see the imaginary part of this voltage directly but the imaginary part is proportional to the time derivative of the acceleration voltage, hence it is the voltage gradient leading to longitudinal focusing or defocusing. The dashed blue lines show the sum of those contributions which are plotted in the same graphs. If all M contributions are considered, i. e., Eq. 6.4 is evaluated, the exact solution is obtained, which is drawn by the solid blue lines. The second graph from above in Fig. 6.1b shows additionally the phase of the induced voltage with respect to the beam spectrum. In this case, a phase of 90° describes a defocusing cavity, hence bunch lengthening is obtained.

Generally, it can be seen that the solid blue lines are not constant in the lower three graphs in Fig. 6.1b which is the manifestation of transient beam loading. If the fill pattern was completely even, all those curves would be constants as only the 0-th contribution would exist. Comparing the fill pattern with those graphs, direction relations can be seen. As the cavity is operated relatively far away from its resonance, beam loading is mostly reactive, i. e., inductive or capacitive. In other words, a bunch passing the cavity causes a phase shift rather than a change of the absolute value of the cavity voltage. This behavior can be clearly seen in the graphs that show a strong variation in phase and much larger imaginary parts than real parts.

Note that the algorithm assumes that the current that induces the voltage is bunched and located exactly at the nominal bucket positions. Of course, the real bucket position is determined by the shape of the accelerating voltage and if this voltage is different at each bucket, the bucket position and consequently the position of the bunch must be different for each bunch. In turn, if the bunch position deviations from the nominal bucket position, the bunch passes the cavity at a different phase and a different induced voltage is expected. In some cases, e. g., BESSY II standard user mode, this effect is non-negligible, as will be shown later in this thesis along with methods of its calculation.

Extension

One possibility of including realistic bucket positions in the analytic formulas is the following extension. If the current of each bunch i_k is considered to be a complex value, it contains additional information about the phase between the bunch and the phasor, hence also with respect to the resulting complex induced voltage. With this approach, the relative position of the individual bunches to the nominal bucket center can be taken into

6. Transient Beam Loading

account by rotating i_k by an angle equivalent to the relative position, expressed as the phase difference at the resonance frequency of the cavity. It has been shown by calculation that this approach leads to self-consistent solutions. In order to find the self-consistent solution, a recursive algorithm can be used, as explained in the next section.

6.1.2. Algorithm to Obtain Synchronous Phase Positions

Other studies regarding the analytic relationship between synchronous phase positions of the bunches and fill pattern are available [41, 109], however with the limitations of a linear voltage gradient, small induced voltages and approximately equidistant bunches.

In this section, a recursive algorithm is presented that overcomes all of the above limitations. It is based on the idea that the relative position Δt_k of each bunch k with respect to its nominal bucket position can be expressed by the argument of the complex current i_k of each bunch. Each iteration of the algorithm goes through the following steps:

1. Take the bunch positions Δt_k of the previous iteration and calculate the corresponding phase with respect to the resonance frequency ω_r and take it as argument of complex bunch current i_k ,

$$i_k = |i_k| e^{-i\omega_r \Delta t_k}. \quad (6.6)$$

For the first iteration, start with $\Delta t_k = 0$ for all k .

2. Calculate the net complex voltage V_m seen at the nominal bucket positions by means of Eqs. 6.3 and 6.5.
3. Repeat the first two steps for all cavities. An active cavity can be approximated by adding an additional complex current i_{gen} to all buckets, including empty ones, before step 2 is performed for the cavity, i. e., $i_k = i_k + i_{\text{gen}}$. For a cavity operated near zero crossing, i_{gen} can be approximated as purely imaginary and chosen so that the real part of the induced voltage has a sign that corresponds to acceleration rather than deceleration. This then changes the voltage transient of the cavity. However, for realistic scenarios, the use of i_{gen} is a rather small correction.
4. Calculate the new bunch positions Δt_k by evaluating the sum voltage of all cavities in the vicinity of each nominal bucket position. For instance, without radiation losses, the zero crossing has to be found. If the solution is not unique, the one macro-particle model is an inadequate approach¹. If desired, the focusing gradients at the new bunch positions can also be obtained directly by evaluating the time derivative, i. e., the imaginary part, of the sum voltage at Δt_k .

¹Two solutions may exist if the defocusing of a higher-harmonic cavity exceeds the focusing of the fundamental cavity and a double bucket with two synchronous positions appears.

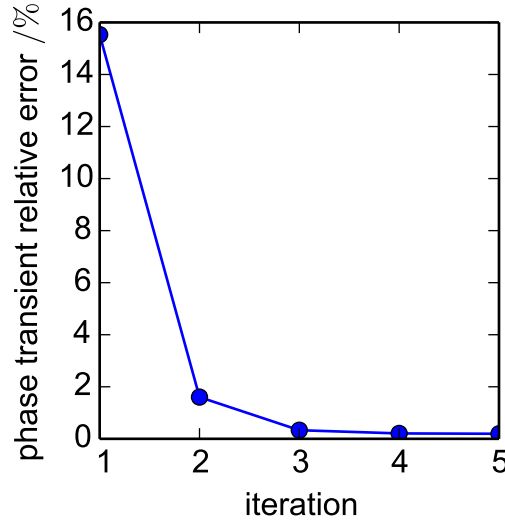


Figure 6.2.: Relative error of the total phase transient of the algorithm described in Section 6.1.2 with respect to tracking simulations as a function of the iteration step. The setup is a realistic BESSY II scenario with active fundamental cavities and passive Landau cavities.

The algorithm has been successfully verified with tracking simulation for a BESSY II setup with active fundamental cavities and passive Landau cavities where it shows very rapid convergence to the tracking simulation, see Fig. 6.2. In principle, the remaining difference is only given by the discrete nature of the tracking simulation.

Note that the question of absolute phases and relative phases of multiple cavities is not resolved in the algorithm above. For a single cavity, the absolute bunch position may run away with the iterations. This can be compensated by a phase offset applied on i_k according to the frequency detuning of the cavity or by a generator current i_{gen} . For more complex cavity setups, such as BESSY VSR the relative phases seem to have a stronger influence on the behavior of this algorithm and its results. The question of how this algorithm is applied to such cases is left to future studies. To date, the exact choice and possible restrains of the relative phases of the cavities in BESSY VSR is an open question, currently under investigation from a beam dynamic's point of view and also from the RF control's point of view.

6.1.3. Tracking

Transient beam loading is readily obtained from tracking simulations. The interaction of the beam with a longitudinal resonator, as described in Section 3.1.1, is fully applicable to the case of fundamental cavity modes as there are no approximations made that would

6. Transient Beam Loading

exclude very high shunt impedances.

In this thesis, the longitudinal stand-alone tracker described in Section 3.2.2 is used for all tracking simulations regarding transient beam loading. As mentioned in Section 3.1.1, the tracking code considers only one macro particle per bunch. This approximation is well justified as long as the bunch length is much smaller than the resonance frequencies of the cavities and as long as the bunch shape does not deviate much from a Gaussian shape. The latter may occur if the gradient, i. e., the time derivative of the accelerating voltage, is non-linear, which is usually the case only if it becomes very small at one point. For all cases shown in this thesis, this effect is negligible unless explicitly stated. For BESSY II, this approximation is also well justified. Calculations with this tracking code have been published in [2, 71].

6.2. Experiments at BESSY II

As BESSY II is typically operated with a gap of about 200 ns in the fill pattern, transient beam loading is expected. Furthermore, four passive 1.5 GHz Landau cavities are usually operated in bunch lengthening mode to increase stability and beam lifetime. With their poor ratio of peak accelerating voltage to normalized shunt impedance, namely $V_{\text{acc}}^{\parallel}/(R_{\text{s},0}/Q) < 1 \text{ kV } \Omega^{-1}$ [110] relatively strong transient beam loading is expected [63]². In such operation modes, the total phase transient, i. e., the range of the synchronous phase positions, is about 80 ps [71]. The following discussion repeats the results presented in [71].

6.2.1. Observation

Figure 6.3 shows simulations and measurements of two of the most visible effects of transient beam loading for a BESSY II standard user setup typical for the year 2014. The top panel shows the bunch fill pattern, obtained from the control system by measurement. The center plot shows the longitudinal location of the bunches, more precisely, the deviation of the bunch position from its nominal bucket position, Δt , measured as a time difference. It is also known as the *phase transient* or *synchronous phase positions*. The bottom plot shows the synchrotron frequency for each bunch.

As expected, the gap in the fill pattern of 200 ns causes a strong phase transient. The transient is almost linear along the bunch train, with small variations correlated to the small unevenness in the fill with a period of about 100 ns. The high current bunches in the bunch train locally increase the slope of the phase transient. The single high current

² The argument here is that for time scales shorter than the characteristic fill time, $\tau_c = \frac{2Q}{\omega_r}$, Eq. 6.1 is not valid but the induced voltage is proportional to the normalized shunt impedance $R_{\text{s},0}/Q$ which appears in the wake function, Eq. 2.10.

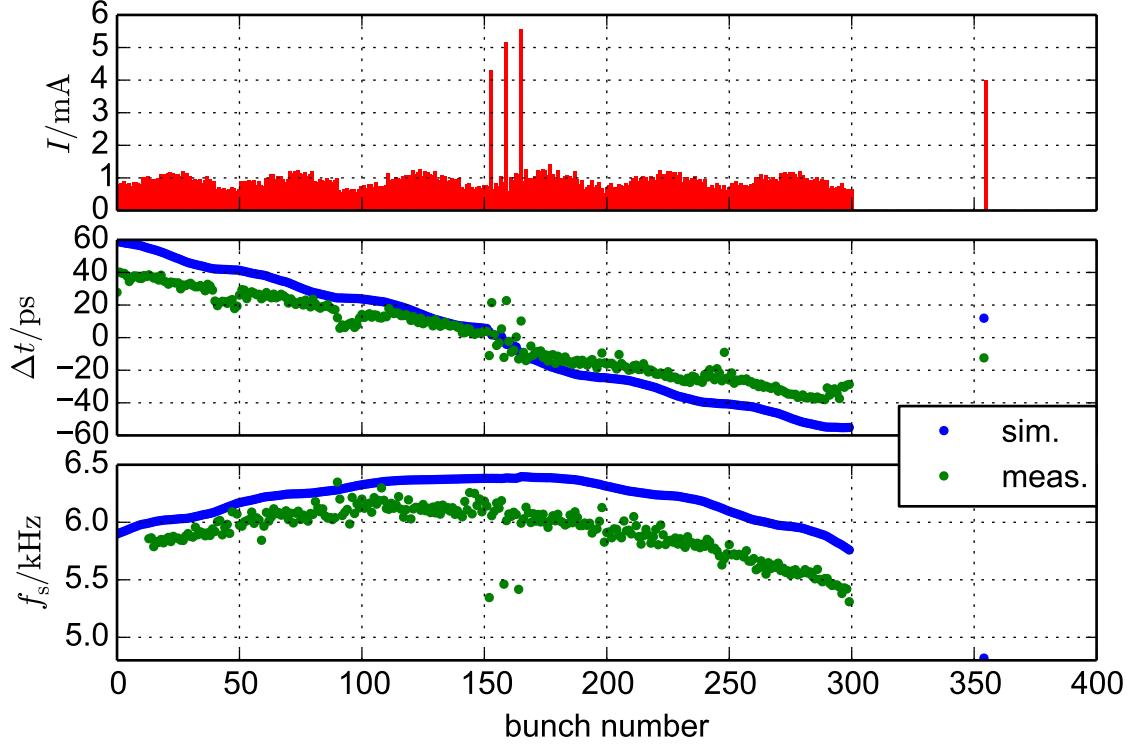


Figure 6.3.: Tracking simulation (blue dots) and measurements (green dots) showing effects of transient beam loading of a typical BESSY II standard user setup of 2014 with the fill pattern shown in the top panel. The bunch position, measured as deviation from its nominal bucket position Δt is shown in the central panel. The bottom panel shows the synchrotron frequency. See text for more details and discussions of the outliers.

bunch is already in the recovering slope with less displacement from its nominal bucket position than other bunches.

The behavior of the synchrotron frequency is less intuitive. Both, measurement and simulation show that the synchrotron frequency is largest in the center of the bunch train and smallest at its tail and front. Analogously, the bunches are shorter in the center of the bunch train compared to its tail and head.

6.2.2. Setup of Simulation and Measurements

The simulations are performed with the stand-alone tracking code, as mentioned in the previous section. The input parameters to the simulation are BESSY II standard parameters from Tab. 1.1 with the fill pattern as measured and shown in Fig. 6.3 top panel. The shunt impedance and quality factor of the Landau cavities were taken from [110].

6. Transient Beam Loading

The Landau cavities were detuned such that the dissipated power and the average voltage approximately matches the values that the control system returned during the measurement. Herein lies a possible source of uncertainty as the measurement of the voltage is rather imprecise and also the measured dissipated power is not entirely accurate. While the uncertainty of the value for the shunt impedance could not be obtained, the quality factor of the four Landau cavities has been measured, see Appendix A.6. It is about 5% less than the number quoted in [110]. However, as it is unclear if the normalized shunt impedance or the shunt impedance should be considered as the more accurate number and considering the fact that the detuning was chosen to match control system parameters, the simulation was performed exclusively with numbers stated in [110]. The damping time was set to $\tau_{\parallel} = 8 \times 10^{-5}$ s instead of $\tau_{\parallel} = 8 \times 10^{-3}$ s which does not change the equilibrium state but accelerates its approach. With those settings, tracking for 1500 turns is enough to reach the equilibrium state and allows the extraction of the bunch positions Δt and the focusing gradient V' at each bunch position via Eq. 3.12. The synchrotron frequency is then obtained by scaling according to Eqs. 1.3 and 1.5,

$$f_s = 8 \text{ kHz} \sqrt{\frac{|V'|}{2\pi \times 1.5 \text{ MV} \times 0.5 \text{ GHz}}}. \quad (6.7)$$

Both, the bunch positions and the synchrotron frequency were measured with the diagnostics of the BBFB systems [50]. The longitudinal feedback unit can measure the bunch positions by digitizing a signal that is approximately proportional to the arrival time difference from a reference clock and approximately proportional to the charge of the bunch. To obtain Δt , the digital signals were multiplied with a calibration constant and divided by the bunch currents. The non-perfect calibration is a source of uncertainty for the measured data. Looking at the center panel in Fig. 6.3, it can be seen that the measurements at and around the high current bunches in the bunch train deviate significantly from the local trend. This might be explained by a non-linear current dependency of the signal generation in the chain of signal processing. Furthermore, it can be seen that those high current bunches also distort the measurement of neighboring bunches, which is explained by non-perfect compensation of the ringing of the pickup signal.

The synchrotron frequencies of each bunch are obtained with the horizontal BBFB system. The horizontal tune spectrum is measured for each bunch individually and averaged over some time, see Fig. 6.4. As the chromaticity is non-zero, the horizontal and longitudinal bunch motion are coupled and the spectrum shows a betatron signal with synchrotron side bands. The distance from the central peak to the side bands is considered to be the synchrotron frequency, which is only an approximation. In this analysis, only the left side band was used to obtain the synchrotron frequency, as it proved to have a better signal to noise ratio compared to the right side band, see Fig. 6.4. For each bunch, a Gaussian fit was applied on the central peak and on the left side band and the difference in their central values is then plotted as the synchrotron frequency in Fig. 6.3 bottom panel. The

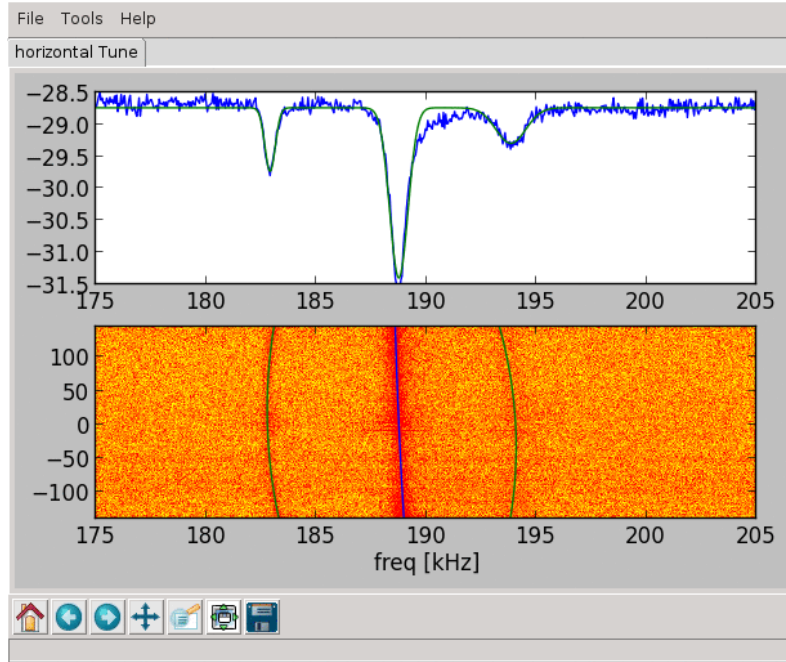


Figure 6.4.: Screen capture of the control panel of the bunch-by-bunch tune measurement in the horizontal plane at BESSY II. The top panel shows the spectrum averaged over all bunches with a central peak corresponding to the horizontal betatron oscillation and the side bands corresponding to a horizontal-longitudinally coupled motion. In the bottom panel, the amplitude of the spectrum is given by the color code for a selection of about 300 bunches (vertical axis). The smooth lines correspond to fit results that are not used in this thesis. Figure reproduced from [50].

three outliers correspond to the three high current bunches in the bunch train. Possible reasons for the deviation might be a current dependent tune shift.

Despite the numerous possible sources of uncertainties, the agreement of simulation and measurement can be considered satisfying. The major features of the transient beam loading, i.e., the magnitude of the phase transient and the magnitude and shape of the synchrotron frequency as a function of bunch number, are well reproduced by the simulation. The remaining discrepancy is believed to stem from the numerous uncertainties, both in the input parameters to the simulation as well as in the measurement.

6.2.3. Understanding the Physics

To understand the transient beam loading in the case of BESSY II, it is convenient to look at the simulation where the time behavior of all voltages can easily be extracted.

6. Transient Beam Loading

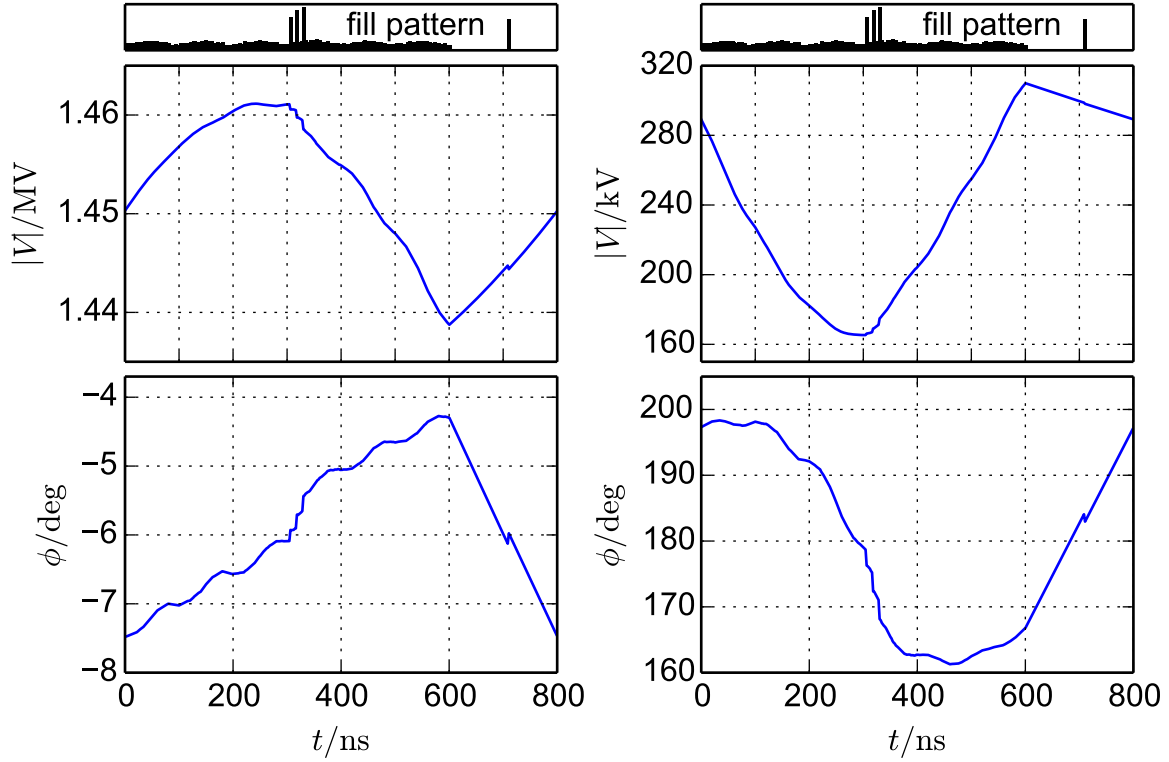


Figure 6.5.: Absolute value of voltage and phase w. r. t. their resonance frequencies of the 500 MHz main RF cavity (left panels) and 1.5 GHz Landau cavity (right panels) at the nominal bucket positions, extracted from the tracking simulation shown in Fig. 6.3. In this case, a phase close to zero indicates zero crossing with a focusing gradient.

Absolute value of voltage and the phase are shown Fig. 6.5 for both cavity systems. With a phase variation of less than 4° and an amplitude variation of less than 2 %, the main RF system shows a rather small relative modulation. This is due to its favorable ratio of peak accelerating voltage to normalized shunt impedance, namely $V_{\text{acc}}^{\parallel}/(R_{\text{s},0}/Q) \approx 3 \text{ kV } \Omega^{-1}$ and the lower frequency, also scaling with the induced voltage, see Eq. 2.10 and Footnote 2 on Page 116. The dominating effect regarding transient beam loading comes from the Landau cavities. According to this simulation, the amplitude of the voltage varies by almost a factor of two along the fill pattern with its minimum around the center of the bunch train. The phase varies by almost 40° along the bunch train, centered around 180° , which corresponds to zero crossing with defocusing gradient. From those graphs, it is evident that the net accelerating voltage and focusing gradient a bunch sees in the vicinity of its nominal bucket position strongly depends on its position in the bunch fill pattern.

Experiments at BESSY II confirm that the Landau cavities are the dominant cause

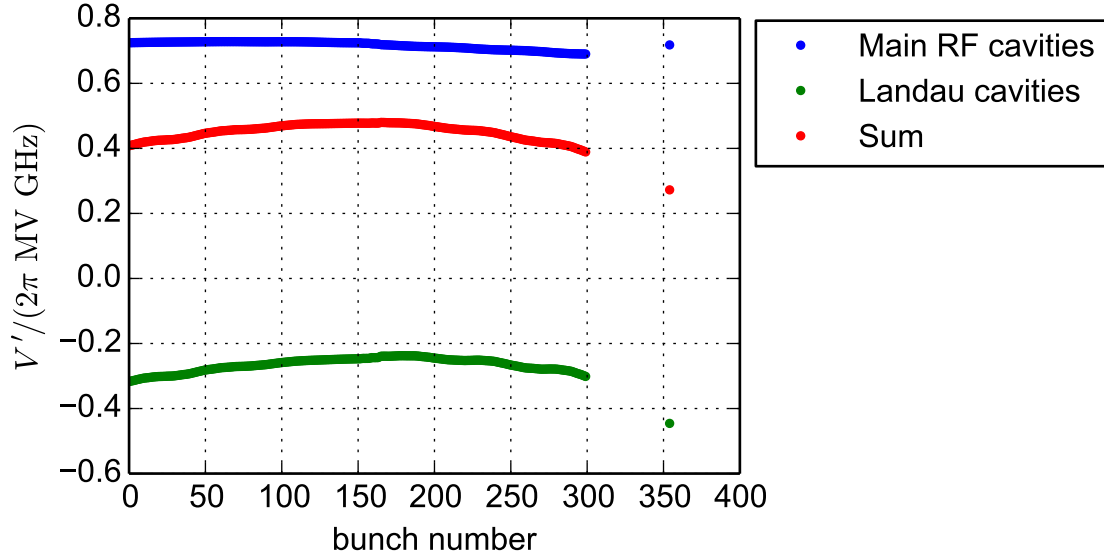


Figure 6.6.: Contributions and sum of the focusing gradient seen at the synchronous bunch positions, extracted from the tracking simulation shown in Fig. 6.4.

for the transient beam loading effect. If the Landau cavities are tuned to their home positions, i. e., tuned to a frequency exactly between two revolution harmonics, and at different harmonic, all of them away at least one harmonic away from 1200, the total phase transient over the entire bunch train is reduced by a factor of approximately 5.

The synchronous phase positions, shown in Fig. 6.3 center panel, are generally a consequence of radiation damping and energy loss per turn. In equilibrium, each bunch takes a longitudinal position where the energy loss per turn is exactly compensated by the net accelerating voltage of all cavities so that the bunch is neither accelerated nor decelerated. For BESSY II, the energy loss is about one tenth of the amplitude of the main RF, i. e., the over-voltage factor is approximately 10, hence the bunch position is close to zero crossing. With transient beam loading, the shape of the net voltage is different for each bunch and consequently the equilibrium position differs from bunch to bunch.

The time derivative of the net voltage at the equilibrium positions of the bunches finally determines the synchrotron frequency and bunch length. The contributions of the Landau cavities and the main RF system to the total focusing gradient are shown in Fig. 6.6. It can be seen that the variation in the main RF system is not very strong but again, the variation coming from the Landau cavities is significant. As deduced earlier, the gradient is largest around the center of the bunch train and falls off towards its ends.

6.3. Predictions for BESSY VSR

Having understood the general behavior of transient beam loading in theory, simulation and experiment at BESSY II, predictions for BESSY VSR can be made.

6.3.1. Simulation Setup

The simulation is based on the BESSY VSR standard parameters given by Tabs. 1.1 and 1.2 and the BESSY VSR baseline fill pattern shown in Fig. 1.4. For easy comparison, the bunch fill pattern is shown again in Fig. 6.7 top panel. The detuning of the 1.75 GHz cavity and in turn its average voltage was changed to a value slightly different from the nominal position. The relative phases of the cavity systems were chosen to be equal each turn at the beginning of the bunch fill pattern. This choice approximates a realistic scenario where the SC cavity systems are operated very close to the setting of passive cavities, i. e., no net energy transfer from or to the beam.

The damping time was reduced by a factor of 100 to $\tau_{\parallel} = 8 \times 10^{-5}$ s which does not change the equilibrium state but accelerates its approach. Furthermore, the quality factors of the SC cavities were set to $Q = 2 \times 10^6$ which accelerates the approach of the equilibrium state and ensures that the implementation of the simplified cavity feedback remains stable. The change of Q has little influence on the effects of transient beam loading discussed in this chapter, as they depend primarily on $R_{s,0}/Q$ which was kept unchanged. In this simulation, precise detuning of the cavities was not necessary as the generator power was not limited. Instead, the amplitudes and phases were set such that the average bunch length is maximized while no net energy transfer from or to the beam occurs. This reflects the realistic scenario.

Both, coherent and incoherent synchrotron radiation losses are simulated by constants that are subtracted from the electron energy every turn. The coherent synchrotron radiation of short bunches at BESSY VSR is expected to have a significant contribution to the electron losses. In this simulation, the net energy loss per turn is set to 178 kV for the long bunches (no coherent radiation) and to 689 kV for the single bunch located in the gap and to 603 kV for the short bunches in the bunch train [2].

Figure 6.7 shows the transient beam loading in all three cavity systems induced by the fill pattern shown in the top panel. It can be seen that the relative variation of the absolute value of the voltage (center panel) is small for all cavity systems. This is expected as all cavity systems are operated close to zero crossing. The variation of the phase (bottom panel) is also rather small, especially if compared to Fig. 6.5. This can be explained by a relatively large ratio of voltage to normalized shunt impedance, which makes the BESSY VSR setup generally less prone to transient beam loading than the present BESSY II setup with its Landau cavities.

However, the small phase shifts are enough to have a strong impact on the long bunches in BESSY VSR. At the nominal bucket positions of the long bunches, the weak focusing

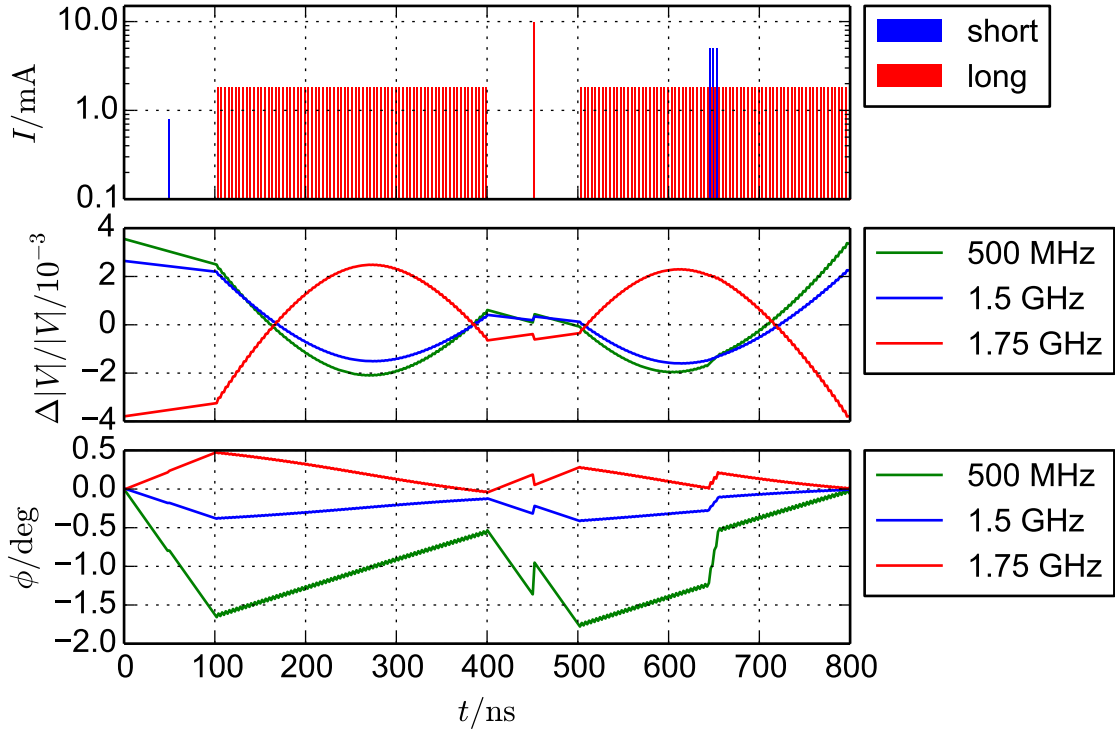


Figure 6.7.: Simulations of transient beam loading in BESSY VSR. Bunch fill pattern (top), relative variation of absolute value of voltage (center) and cavity phase w. r. t. its resonance frequency (bottom).

gradient is achieved by the cancellation of two large numbers. A small relative variation then causes a relatively large effect on the result of the subtraction, as discussed in the next section.

6.3.2. Synchronous Phase and Bunch Length

The modulation in phase and amplitude of all three cavity systems over the bunch fill pattern shown in Fig. 6.7 has an effect on the net voltage at each nominal bucket position.

As an example, the long bunches at the nominal bucket position 51 (beginning of first bunch train), 133 (center of first bunch train) and 399 (end of second bunch train) are shown in Fig. 6.8 along with the sum voltage and voltages of the individual cavity systems in their vicinity. The sum voltage is dominated by the SC cavities, hence the 500 MHz cavity system can be ignored in the following argumentation. The small phase shifts of the SC can be seen in the figures, manifested in an increasing difference in the zero crossings of SC cavity systems from left to right. In turn, the sum voltage is altered and the synchronous positions and the slope of the voltage at the synchronous position changes.

6. Transient Beam Loading

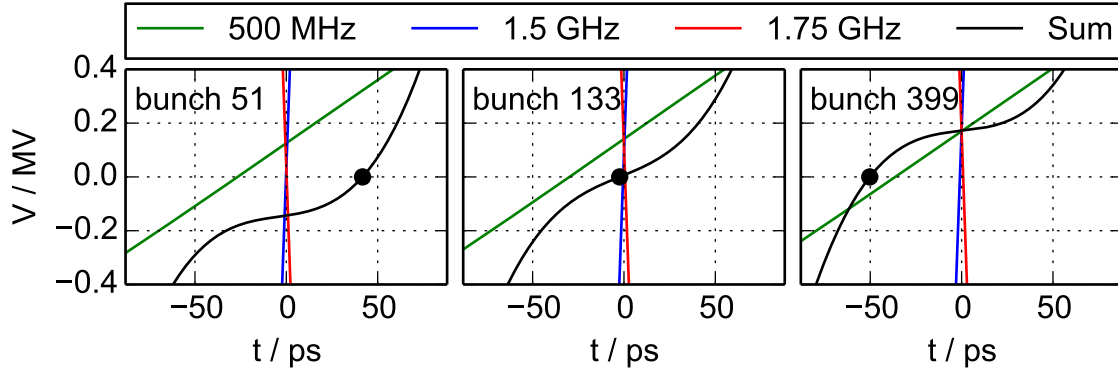


Figure 6.8.: Sum voltage and voltage of the individual cavity systems in the vicinity of the nominal bucket position of three selected bunches in the simulations of transient beam loading in BESSY VSR. The black dot indicates the synchronous bunch position. The constant synchrotron losses are subtracted.

In Fig. 6.8, the constant synchrotron losses are subtracted so that the synchronous phase position is found at zero voltage.

The bunch position relative to the nominal bucket position is shown for all bunches in Fig. 6.9 top row. The synchrotron frequency is shown in the center row, obtained by means of Eq. 6.7. In addition, the bottom row shows the relation of the zero current bunch length σ_0 to the nominal zero current bunch length of BESSY II, $\sigma_{0,\text{BESSY II}} = 10$ ps,

$$\frac{\sigma_0}{\sigma_{0,\text{BESSY II}}} = \sqrt{\frac{2\pi \times 1.5 \text{ MV} \times 0.5 \text{ GHz}}{|V'|}}, \quad (6.8)$$

calculated by means of Eqs. 1.1 and 1.3. The bunch length scales inversely to the synchrotron frequency calculated in Eq. 6.7.

6.3.3. Discussion

The results presented in Fig. 6.9 show that the effects of transient beam loading are expected to be strong for the long bunches in BESSY VSR. On the other hand, the effect on the short bunch is weak and can most likely be ignored.

The long bunches show a strong phase transient, in total more than 80 ps along the bunch fill pattern. This itself does not seem to be of particular concern, as it is in the same order as the present phase transient of BESSY II, see Fig. 6.3.

In addition, a variation in the synchrotron frequency and consequently in the bunch length is found with the consequence that the maximum average bunch length seems to be limited. The bunch length of the long bunch is a critical parameter as it determines the Touschek lifetime [111] of the long bunches which is of concern in BESSY VSR [2].

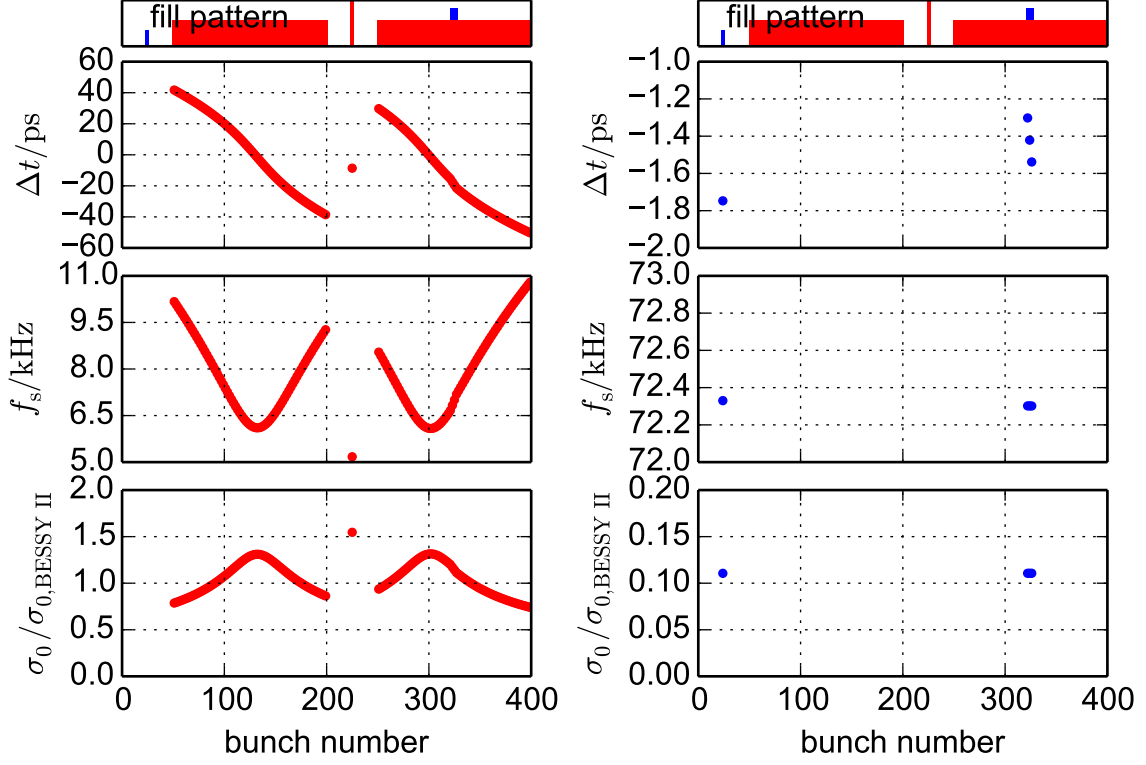


Figure 6.9.: Key parameters of the long bunches (left column) and short bunches (right column) of the simulations of transient beam loading in BESSY VSR. Top row: Bunch positions relative to the nominal bucket positions. Center row: Synchrotron frequency. Bottom row: Single current bunch length relative to the nominal zero current bunch length of BESSY II.

Furthermore, the bunch length changes the frequency up to which impedance interactions take place, resulting in heating issues of the beam pipe if the bunch length becomes too short at high currents stored in those bunches.

The simulation setting presented here is already optimized to maximize the average bunch length which yields an average bunch length approximately equal to $\sigma_{0,\text{BESSY II}}$. However, as the number of long bunches halves in BESSY VSR compared to BESSY II, the Touschek lifetime will be reduced by a factor of two even if the bunch length is unchanged. A more detailed discussion on the Touschek lifetime in BESSY VSR is found in [2].

The process of the optimization is illustrated in Fig. 6.10, where the cavity voltage of the 1.75 GHz cavity is used as the free parameter to change the resulting net focusing for the long bunches. Other parameters can be used analogously. If the voltage of the 1.75 GHz cavity is increased, the defocusing becomes stronger and a longer bunch is generally expected. However, as seen in the left panel of Fig. 6.10, this is true only for a

6. Transient Beam Loading

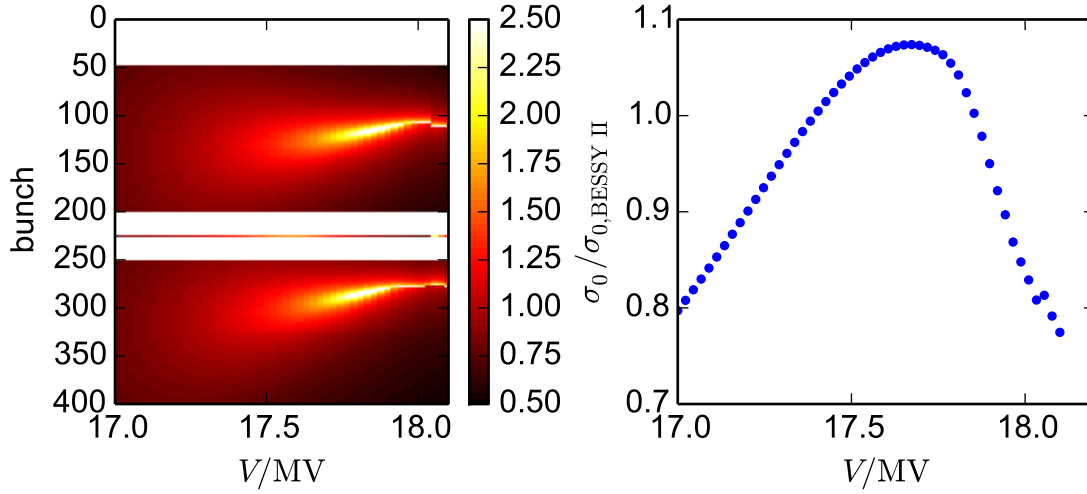


Figure 6.10.: Scaled bunch length (color code) of all bunches (left panel) and averaged (right panel) as a function of the voltage of the 1.75 GHz cavity system.

small number of bunches, while the rest of the bunches experience an enhanced focusing and become increasingly short. The optimum for this setup in terms of averaged bunch length can be read out from the right panel of Fig. 6.10.

It is clear that an approximately even fill pattern, i. e. without significant gaps, would significantly reduce the effect of transient beam loading. In turn, the gradient for the long bunches could be reduced more easily for a larger number of bunches and the average bunch length of the long bunches would increase.

As a consequence of these findings, intense feasibility studies have been launched to assess the necessity of the gaps in the fill pattern. This includes accelerator physical studies [112] and studies from the point of view of synchrotron users [113, 114], where the gaps are needed for pulse separation.

6.3.4. Landau Damping of Coupled Bunch Instabilities

Another consequence of the transient beam loading is the relatively large variation of the synchrotron frequency of the long bunches, seen in Fig. 6.9 left column, center panel. This bunch-to-bunch f_s spread causes Landau damping, as discussed theoretically in Section 2.5.

Figure 6.11 shows the f_s histogram of the long bunches from the same simulation as in Fig. 6.9. Figure 6.12 depicts the graphical solutions of the dispersion relation $d(\Omega)$, defined in Eq. 2.42. The rms value of this distribution is about 1.34 kHz. If the distribution was continuous and approximated as normally or uniformly shaped, simplified expressions for the expected Landau damping could be used [29, Ch. 5]. This is not done here, instead, the formalism presented in Section 2.5 is used which is applicable to discrete f_s distributions

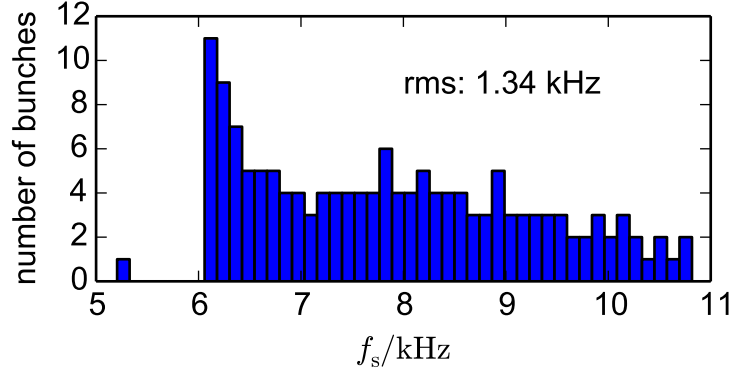


Figure 6.11.: Histogram of synchrotron frequencies of the long bunches in the simulation of transient beam loading for BESSY VSR.

of arbitrary shape.

The solid lines are the dispersion function as defined in Eq. 2.43, i. e., $(i \frac{\tilde{\mu}}{M} \sum_{q=1}^M (\omega_{sq}^2 - \Omega^2 + 2i\delta_n\Omega)^{-1})^{-1}$, drawn for all real Ω in a reasonable interval around the unperturbed synchrotron frequency, i. e., solutions at the threshold where the growth rate is exactly zero. This function contains the information about the f_s distribution and the dissipative damping term. The top panel of Fig. 6.12 shows two examples with radiation damping as the only dissipative damping, which is very similar to the study presented in [71]. The blue line is calculated with the f_s distribution shown in Fig. 6.11 and the green line with a constant synchrotron frequency of $f_s = 8$ kHz for all bunches, i. e., no Landau damping. The bottom panel of Fig. 6.12 shows two examples with the longitudinal BBFB damping with $\tau_{fb}^{-1} = 1.33 \times 10^3 \text{ s}^{-1}$ as the dissipative damping with the red line including the f_s distribution discussed above and the magenta line with a constant $f_s = 8$ kHz for all bunches, i. e., no Landau damping.

The dashed lines in Fig. 6.12 represent the r.h.s. of the dispersion relation, i. e., $I_{DC}\omega_{beam}Z_0^{\parallel}(\omega_{beam} + \Omega)$ in the worst case approximation for HOMs where the resonance frequency is not exactly known, thus becoming a circle. It is drawn at the threshold current, i. e., the very I_{DC} at which the circle interacts with the solid line given by d , according to the corresponding dispersion function (color lines matching).

It can be seen in Fig. 6.12 top panel, that the Landau damping stemming from the f_s distribution increases the threshold current by a factor of approximately 15 compared to a constant synchrotron frequency of $f_s = 8$ kHz, if radiation damping is considered the only dissipative damping mechanism.

If a BBFB with the performance of the present BBFB feedback of BESSY II is considered as the dissipative damping mechanism, the gain from Landau damping appears to be a factor of approximately 4.

The results are summarized in Tab. 6.1 and suggest that Landau damping can be sig-

6. Transient Beam Loading

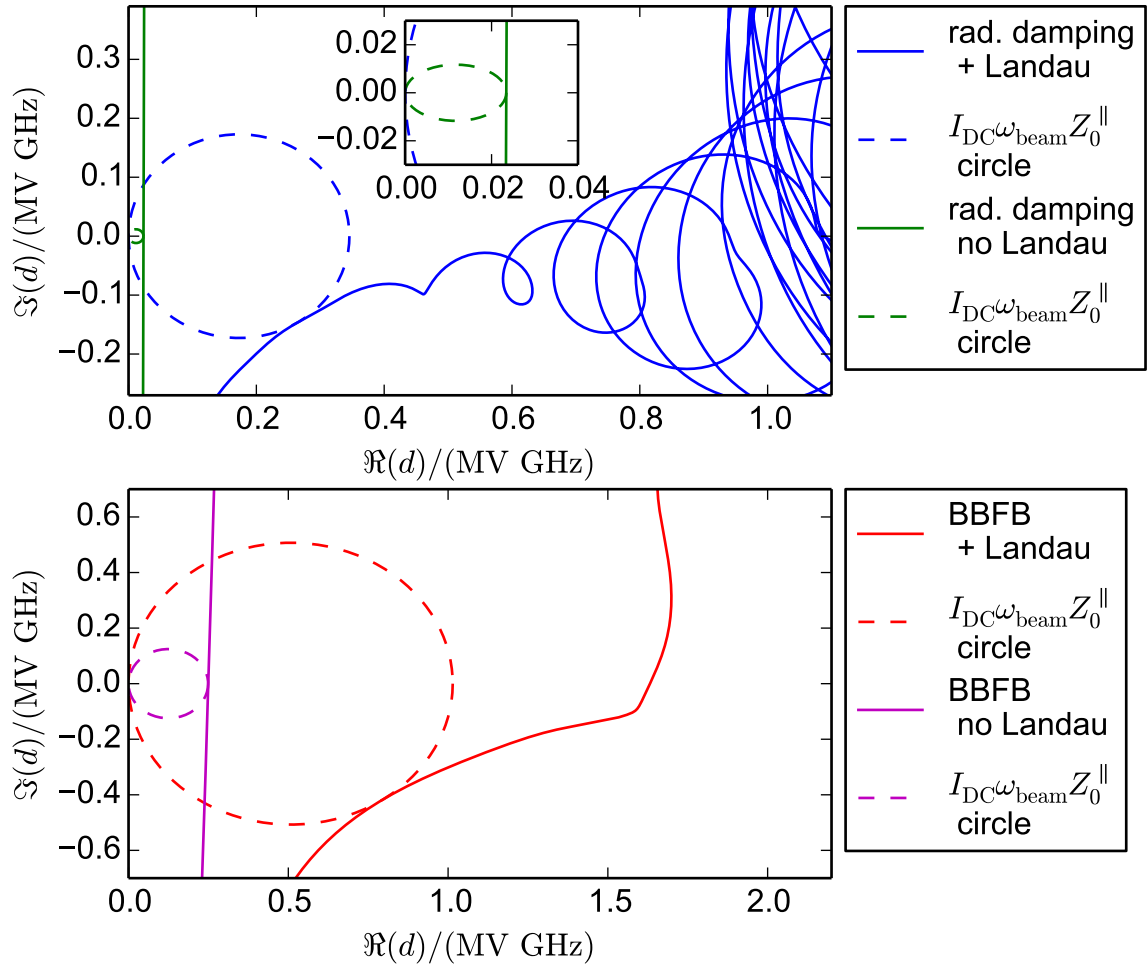


Figure 6.12.: Graphical solution of the dispersion relation of Landau damping (Eq. 2.42) for different combinations of radiation damping, damping provided by the BBFB and Landau damping produced by a f_s distribution obtained from the expected transient beam loading of BESSY VSR. See text for details.

nificant and may add a convenient additional safety margin to the over-all longitudinal damping performance of BESSY VSR. Nonetheless, it should be noted that it is not experimentally confirmed that the formulas applied in this study are reliable to make predictions in a regime where Landau damping exceeds radiation damping by up to two orders of magnitude. In this sense, it is recommended to perform further studies on the subject of Landau damping in BESSY VSR, e. g., aided by tracking simulations or measurements if possible.

Table 6.1.: Results of the graphical solutions of the dispersion relation of Landau damping for BESSY VSR with the expected transient beam loading for the baseline fill pattern.

Damping mechanisms	Threshold	
	$I_{\text{DC}}\omega_{\text{beam}}R_{\text{s},0}$ MV GHz	$R_{\text{s},0}^a$ k Ω
Synchrotron radiation	0.023	12.4
Synchrotron radiation and Landau	0.355	188.3
BBFB	0.249	132.1
BBFB and Landau	1.043	553.3

^aAt $I_{\text{DC}} = 300$ mA and $\omega_{\text{beam}} = 2\pi \times 1$ GHz for direct comparison with Eq. 5.4.

7. Conclusion

In the context of this thesis, a novel challenge for beam dynamics has been addressed, the operation of high frequency SC multi-cell cavities at high currents in an electron storage ring based synchrotron light source that enables new experimental possibilities for the users of synchrotron radiation. More explicitly, the important question of coupled bunch effects has been studied for BESSY VSR, serving as an example for this new class of machines.

The coupled bunch effects are separated into the study of CBIs, see Chapter 2, and the study of transient beam loading, see Chapter 6. For the calculation of CBIs, a number of numerical formulas and simulation algorithms are presented along with ready-to-use code for simulation, see Chapter 3. Additionally, software for the data analysis of CBI measurements is presented in Chapter 4. Explicit formulas for transient beam loading are presented along with software to simulate advanced setups of multi cavity systems at arbitrary fill pattern. In this thesis, the tools are applied to BESSY VSR for the study of HOM driven CBIs, see Chapter 5 and transient beam loading induced by the baseline fill pattern in Chapter 6.

For BESSY VSR, the HOM driven CBIs are evaluated based on the latest BESSY VSR 1.5 GHz cavity model, suggesting that they are likely to be under control if damping is provided by a BBFB system performing equally well or better than the present BBFB system of BESSY II, as discussed in Chapter 5. This is also true for the proposed low- α operation in BESSY VSR, which is expected to be even more stable, as shown in Section 5.4. Furthermore, it was shown in Section 5.3 that the bunch fill pattern generally has little direct influence on HOM driven CBIs. This includes the baseline fill pattern of BESSY VSR.

In the longitudinal plane, the HOMs are about one order of magnitude below the impedance threshold defined by the BBFB system, see Section 5.1. The longitudinal SPMs exceed this threshold, but as they have a very high Q paired with a small normalized shunt impedance, a correction on the calculation of its strength should be applied, as discussed in Section 3.3.4. Thus, only one SPM exceeds the threshold, which, being a small number in combination with its narrow peak, may be an acceptable risk regarding the question of the likelihood it is driven by the beam.

For the most part, the transverse dipole HOMs of the latest BESSY VSR cavity model are below the BBFB threshold. A single HOM exceeds the threshold, which, for the same reasons as above, may be an acceptable risk. If needed, improvements to the transverse BBFB by means of hardware upgrades are possible with no foreseeable limit, as long as

7. Conclusion

space for additional kickers is made available in the storage ring. The hazard of transverse quadrupole HOMs has been studied for three possible extreme cases of beam parameters. In all cases, the impedance threshold is at least one order of magnitude above the HOMs, thus making it unlikely that quadrupole CBIs will appear.

It should be noted that all predictions for BESSY VSR are stated on the condition that the cavity model “HZB 2c coax. coupler” is an adequate representation of the reality. As discussed in Section 5.1.5, the model is still under development, the 1.75 GHz cavity is not designed yet, studies of the HOM spectrum of the super-structure are not finalized and comparative measurements with copper or niobium prototypes have not been performed yet. Hence, it is recommended that the evaluations presented in this thesis are repeated as soon as more accurate data is available. Nonetheless, the consequences of fabrication uncertainties in terms of scattered HOM frequencies were studied in Section 5.2 for the present model with the result that narrow HOMs that exceed the instability threshold can still allow stable operation, with the likelihood of stability scaling approximately as 0.92^n with n the number of such HOMs.

The influence of transient beam loading on the longitudinal beam dynamics of BESSY VSR has been studied in Chapter 6, where a strong effect on the long bunch was found. Due to the fact that the long bunch is achieved by the cancellation of the two large gradients of the SC cavity systems, relatively small transient changes in the phases and amplitudes cause a relatively large disturbance of the longitudinal phase space. The consequence is the hindrance of an elongation of the long bunch in BESSY VSR compared to BESSY II as long as a fill pattern with large gaps is applied. This leads to increased Touschek losses, i. e., reduced beam lifetime, and more impedance interactions at high frequencies. Another, rather beneficial consequence of the transient beam loading is a bunch-to-bunch spread in the synchrotron frequency, causing Landau damping that may significantly mitigate longitudinal CBIs, as discussed in Section 6.3.4. Analytic estimations on the damping performance are given, where the threshold is up to four times increased compared to BBFB damping only. However, experimental verification is recommended before reliable consequences should be drawn from this effect.

The formulas and algorithms presented in this thesis, as well as the software for predictions and data analysis of measurements developed in the course of this thesis, are ready to be applied to future studies, including other cavity setups and electron storage rings. They will continue to serve as an important tool for the benchmarking of the BESSY VSR cavities and the prediction, understanding and analysis of coupled bunch effects in BESSY VSR during its design phase, commissioning and beyond.

A. Appendix

A.1. Transverse Moments in Cartesian Coordinates

The transverse m -th moment of the beam or a single bunch, M_m , is defined in Eq. 2.1. With the trigonometric identities

$$\cos m\theta = \sum_{k=0}^m \binom{m}{k} \cos^k \theta \sin^{m-k} \theta \cos \left(\frac{1}{2}(m-k)\pi \right) \quad (\text{A.1})$$

$$\sin m\theta = \sum_{k=0}^m \binom{m}{k} \cos^k \theta \sin^{m-k} \theta \sin \left(\frac{1}{2}(m-k)\pi \right), \quad (\text{A.2})$$

and the relations

$$x = r \cos \theta \quad (\text{A.3})$$

$$y = r \sin \theta, \quad (\text{A.4})$$

the expression can also be given in Cartesian coordinates. If $m > 0$, the freedom of choosing θ_0 results in two components of the m -th moment in Cartesian coordinates, a normal and a skewed moment. They can be obtained by means of the following two equations,

$$r^m \cos m\theta = \sum_{k=0}^m \binom{m}{k} x^k y^{m-k} \cos \left(\frac{1}{2}(m-k)\pi \right) \quad (\text{A.5})$$

$$r^m \sin m\theta = \sum_{k=0}^m \binom{m}{k} x^k y^{m-k} \sin \left(\frac{1}{2}(m-k)\pi \right), \quad (\text{A.6})$$

where the first equation is used for normal moments and the second equation for skewed moments. The first six moments are shown in Tab. A.1.

Table A.1.: First six transverse moments M_m in Cartesian coordinates.

m	Normal	Skewed
0	$\langle +1 \rangle$	
1	$\langle +x \rangle$	$\langle +y \rangle$
2	$\langle -y^2 + x^2 \rangle$	$\langle +2xy \rangle$
3	$\langle -3xy^2 + x^3 \rangle$	$\langle -y^3 + 3x^2y \rangle$
4	$\langle +y^4 - 6x^2y^2 + x^4 \rangle$	$\langle -4xy^3 + 4x^3y \rangle$
5	$\langle +5xy^4 - 10x^3y^2 + x^5 \rangle$	$\langle +y^5 - 10x^2y^3 + 5x^4y \rangle$

A.2. Longitudinal Higher Order Motion

This section studies longitudinal higher order motion, i. e., the possible motion arising if bunches of finite longitudinal extension are considered instead of longitudinal point charges, as done in Chapter 2.

In a longitudinally extended bunch, the electrons can also perform longitudinal intra-bunch oscillations, i. e., density oscillations. The lowest order of this intra-bunch motion, $l = 2$, is the quadrupole oscillation. Analogously to the motion of the center of mass, the dipole oscillation $l = 1$, the higher order oscillations can also be written down in an equation of motion and the question of an instability can be studied. The longitudinal impedance Z_0^{\parallel} couples to all those modes but the disturbance of the complex synchrotron frequency decreases with the order l . The exact scaling depends on the bunch shape. For a uniform bunch distribution, the so called “water-bag model”, the scaling can be expressed analytically. For disturbances not too strong, the growth rate of the multi-bunch instability for the longitudinal oscillation of order l is given by [30, Eq. 8.41]

$$\tau^{-1}_l = \frac{l}{(l!)^2} \left(\frac{\omega_r \hat{\tau}}{2} \right)^{2l-2} \tau^{-1}_{l=1}, \quad (\text{A.7})$$

with ω_r the angular resonance frequency of the impedance, $\hat{\tau}$ the half bunch length and $\tau^{-1}_{l=1}$ the growth rate of longitudinal dipole oscillation which is studied in detail in Chapter 2.

The rms bunch length of the long bunches at BESSY VSR is expected to be not larger than $\sigma = 20$ ps. Assuming the strongest HOM to be at $f_r = 3$ GHz and approximating the Gaussian bunches with the “water-bag model” by setting the half width equal to the half with half maximum of the Gaussian distribution, $\hat{\tau} = \text{HWHM} = \sqrt{2 \ln 2} \sigma$, the following

scaling factors for the higher orders is obtained:

$$\tau^{-1}_l \approx \tau^{-1}_{l=1} \times \begin{cases} 1/40 & \text{for } l = 2 \\ 1/5000 & \text{for } l = 3 \\ \dots & \end{cases} \quad (\text{A.8})$$

The $l > 1$ oscillation cannot be damped by a BBFB system which only acts on the center of mass. Therefore, radiation damping and Landau damping must be sufficient to ensure that $l > 1$ oscillations are not growing. With the parameters assumed above, the longitudinal quadrupole instability is expected to be less critical than the longitudinal dipole instability. Higher orders are suppressed even more.

If strong HOMs with frequencies significantly larger than 3 GHz are assumed, the growth rate of the longitudinal quadrupole instability may exceed the radiation damping rate while the dipole instability is still under control with the BBFB system. This would necessitate Landau damping to reach stability or the mode-coupling of $l = 1$ with $l = 2$ is strong enough to allow the BBFB system to damp the quadrupole oscillation sufficiently well.

A.3. Principle of Phasor Addition

The iterative approach used in Section 3.1 is based on the idea that any sum of wake functions of the same resonator impedance can be exactly reduced to a single expression with the mathematical form of a single wake function of the resonator impedance. The proof can be made by calculating the sum voltage given by two bunches of charge q_1 and q_2 passing the impedance at times t_1 and t_2 using Eq. 3.4 and complex phasor notation:

$$V(t) = a_1 e^{i\omega_r(t-t_1)} e^{-\frac{\omega_r(t-t_1)}{2Q}} + a_2 e^{i\omega_r(t-t_2)} e^{-\frac{\omega_r(t-t_2)}{2Q}} \quad (\text{A.9})$$

$$= e^{i\omega_r t} e^{-\frac{\omega_r t}{2Q}} \underbrace{\left[a_1 e^{i\omega_r(t_1)} e^{-\frac{\omega_r(t_1)}{2Q}} + a_2 e^{i\omega_r(t_2)} e^{-\frac{\omega_r(t_2)}{2Q}} \right]}_X \quad (\text{A.10})$$

$$= |X| e^{i \arg X} e^{i\omega_r t} e^{-\frac{\omega_r t}{2Q}}, \quad (\text{A.11})$$

with $a_{1,2} = q_{1,2} \frac{\omega_r R_{s,0}}{Q}$ and X constants.

A.4. Minimal Demonstrative Tracking Code

Source code of $m = 1, 2$ tracker used in Section 3.2.1 to be interpreted with Python 2.7:

```

1  from pylab import *
2
3  # BESSY II / BESSY VSR Parameters
4  frev = 1.25e6 # revolution frequency
5  q = 2.4e-07 # beam charge, corresponding to 300mA
6  E = 1.7e9 # beam energy
7  beta = 4.0 # value of beta function
8  c = 3e8 # speed of light
9  omegabeta = 17.85 * frev * 2*pi # angular betatron frequency
10
11 # a single point-like bunch with y=0 initial values
12 def track(omegar, omegabeta, Q, Rs, x=1e-3, m=2, xoffset=0, beta=4.0, N=1001):
13     V = 0 # phasor
14     ax = []
15     aV = []
16     for i in xrange(0,N):
17         # transform phasor
18         V = V * exp(omegar/frev * (1j - 1.0/2/Q))
19         # betatron phase advance
20         x = x * exp(1j * omegabeta/frev)
21
22         # optional shift HQM center w.r.t. reference orbit
23         xreal = x.real - xoffset
24
25         # transverse kick on bunch
26         if m == 1:
27             xkick = - c/omegar * V.imag
28         elif m == 2:
29             xkick = -2.0 * xreal * c/omegar * V.imag
30         x = x + 1j * beta/E*xkick
31
32         # new phasor after bunch passage
33         V = V - xreal*m * q * omegar * Rs / Q
34
35         ax.append(x)
36         aV.append(V)
37     return ax,aV
38
39 ##### demo 1 (m=1) #####
40 Rs1 = 1.898653e+08 # should result in 4 kHz growth rate..
41 omegar = 782*frev*2*pi + omegabeta
42 # arrays with complex coordinate and phasor used for plot in thesis
43 ax, aV = track(omegar, omegabeta, Q=1e4, Rs=Rs1, m=1, x=1e-3, N=501)
44 # ...
45
46 ##### demo 2 (m=2) #####
47 Rs2 = 1e13
48 omegar = 765*frev*2*pi + 2*omegabeta
49 xstart = 1e-3
50 # arrays with complex coordinate and phasor used for plot in thesis
51 ax, aV = track(omegar, omegabeta, Q=1e4, Rs=Rs2, m=2, x=xstart, N=501)
52 # ...

```

A.5. Justification of Margin a in the Statistical Approach

This section tries to justify the use of the extra safety margin a in the calculation of the width of a resonator impedance in the statistical approach in Section 5.2.

The statistical approach is based on the idea that the probability of stability should be valid for the entire time of deployment of a cavity in BESSY VSR, i. e., several years. Furthermore, the stability should cover the majority of possible operation modes. This means that operational changes in the cavity, i. e., change of HOM resonance frequencies, and changes in the beam, i. e., change of beam spectrum should be included.

In the following, a list of effects that influence the relation of beam spectrum to resonance frequency of the HOMs is given and the size of the effect is quantitatively estimated:

1. The synchrotron frequency may vary depending on the desired operation mode and the fill pattern, see also Chapter 6. The range is estimated to be from zero to 15 kHz. This adds a span of $\Delta f = 15$ kHz to the frequencies at which the beam samples a longitudinal impedance.
2. The betatron frequencies are controlled by the quadrupole magnets and are usually kept at fixed values. However, the betatron frequencies change if a different magnet optics is applied, e. g., the so called low- α mode or other special purpose modes presently in development or consideration [2, 113, 114]. For simplicity, the range is estimated to be the same as for the synchrotron frequency, leading to a span of $\Delta f = 15$ kHz to the frequencies at which the beam samples a transverse impedance.
3. The master oscillator, also known as master clock, is changed continuously during operation to account for different machine settings and long term drifts. Figure A.1 shows the variation of the frequency of the master oscillator at BESSY II during beam storage as a function of time. Annual variations are visible as well as short term changes accounting for a change in the machine settings. The span of the variation in the considered time frame, beginning of the year 2013 until May 2015, amounts to 14.4 kHz.

The master oscillator is fed to all cavity systems, thus the resonance frequency of the SC cavities has to follow the change, scaled with the harmonic factor of the cavities. For a 1.5 GHz cavity this amounts to a span of 43.2 kHz. When the fundamental frequency of a cavity is changed, the resonance frequency of the HOMs shift by a factor that strongly depends on the mode and the exact variation of the geometry by the tuner system. Depending on the mode, the shift can be of the same or opposite sign, and also smaller, equal or up to four times larger than the shift of the fundamental frequency [115]. For the bands that typically contain the strongest HOMs, namely TM_{110} and TM_{010} , the magnitude of the shift is not larger than approximately a factor of two of the fundamental mode [115]. Combined, this adds

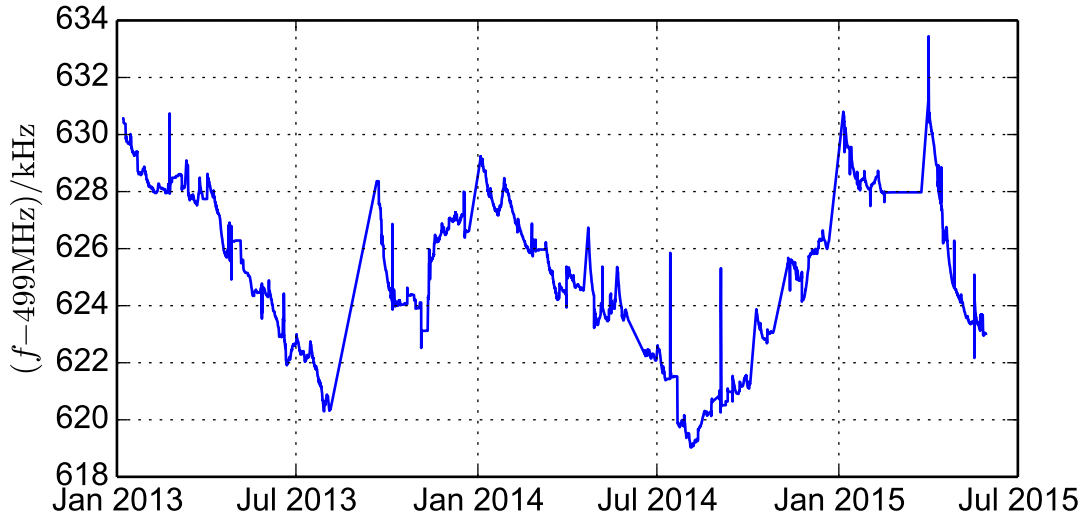


Figure A.1.: Archive data of the master clock frequency during beam storage at BESSY II from beginning of the year 2013 to May 2015.

a span of $\Delta f = 3 \times 2 \times 14.4 \text{ kHz} = 86.4 \text{ kHz}$ to the frequencies at which the beam samples an impedance.

4. The drifts of HOM frequencies due to temperature, helium pressure and other mechanical influences are rather small and can be ignored in comparison to the effects mentioned above [116].

The spans above can be added to account for the worst case where all shifts add up in the same direction, yielding a total span of approximately $\Delta f = 100 \text{ kHz}$. Note that this estimation is a rather coarse guess.

The extra margin a , added to the width of an impedance on both sides, then takes the value $a = 50 \text{ kHz}$, see Section 5.2 for its application.

A.6. Quality Factor Measurements of Landau cavities at BESSY II

In the course of investigations towards improving the accuracy of simulations of transient beam loading at BESSY II, Section 6.2, the quality factor the Landau cavities of BESSY II was obtained from measurements.

The spectrum of the four Landau cavities was measured during beam storage with a spectrum analyzer connected to a pickup in each of the cavities [117]. A Lorentzian three

A.6. Quality Factor Measurements of Landau cavities at BESSY II

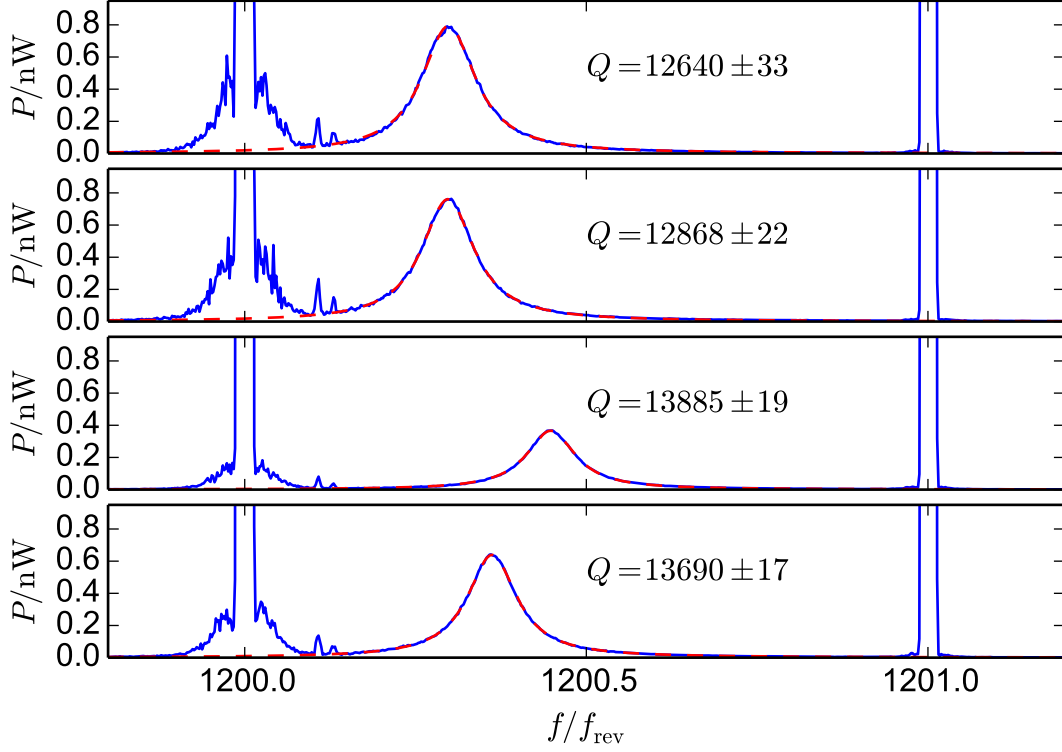


Figure A.2.: Power spectra (blue) of the four Landau cavities of BESSY II, measured with a spectrum analyzer connected to voltage pickups in the Landau cavities in April 2015. Lorentzian fits (dashed red lines) are applied to the resonance curves of the Landau cavities, which are tuned between the 1200-th and 1201-th revolution harmonic, i. e., they are operated in a bunch-lengthening mode. The resulting Q values with standard deviation errors are displayed for each cavity.

parameter fit is applied on the data to obtain the quality factor by means of

$$Q = \frac{f_r}{f_{\text{FWHM}}}, \quad (\text{A.12})$$

with the resonance frequency f_r and the full width half maximum f_{FWHM} . Fig. A.2 shows the spectrum along with the Lorentzian fit curves and the resulting Q value for all four cavities. The average value is found to be $Q = 13271 \pm 47$, i. e., a relative error of 0.36%. The average value is about 5% less than the value quoted in [110].

References

- [1] E. Jaeschke et al., “Lattice Design for the 1.7-GeV Light Source BESSY II”, in: *Proceedings of PAC1993* (1993), pp. 1474–1476 (cit. on pp. 1, 4).
- [2] A. Jankowiak et al., eds., “BESSY VSR – Technical Design Study”, Helmholtz-Zentrum Berlin für Materialien und Energie GmbH, June 2015, DOI: 10.5442/R0001 (cit. on pp. 1, 6, 9–11, 24, 47, 50, 80, 83, 84, 104, 106, 107, 116, 122, 124, 125, 137).
- [3] F. R. Elder et al., “Radiation from Electrons in a Synchrotron”, in: *Phys. Rev.* 71 (11 June 1947), pp. 829–830, DOI: 10.1103/PhysRev.71.829.5 (cit. on p. 1).
- [4] Basic Energy Sciences Advisory Committee (BESAC), “Next Generation Photon Sources for Grand Challenges in Science and Energy”, tech. rep., U.S. Department of Energy (DOE), May 2009 (cit. on pp. 1, 2).
- [5] R. Klein et al., “Operation of the Metrology Light Source as a primary radiation source standard”, in: *Phys. Rev. ST Accel. Beams* 11 (11 Nov. 2008), p. 110701, DOI: 10.1103/PhysRevSTAB.11.110701 (cit. on p. 2).
- [6] E. M. Rowe and F. E. Mills, “Tantalus I: A Dedicated Storage Ring Synchrotron Radiation source”, in: *Part. Accel.* 4 (1973), pp. 211–227 (cit. on p. 2).
- [7] R. Bartolini, “Design, status and road map of next generation low emittance rings”, Conference Website, ESLS XXII Workshop, Nov. 2014 (cit. on p. 2).
- [8] M. Eriksson et al., “The MAX IV Synchrotron Light Source”, in: *Proceedings of IPAC2011* (2011), THPC058, pp. 3026–3028 (cit. on p. 2).
- [9] B. W. J. McNeil and N. R. Thompson, “X-ray free-electron lasers”, in: *Nature Photonics* 4.12 (Dec. 2010), pp. 814–821, DOI: 10.1038/nphoton.2010.239 (cit. on p. 3).
- [10] D. H. Bilderback et al., “Energy recovery linac (ERL) coherent hard x-ray sources”, in: *New J. Phys.* 12 (2010), p. 035011, DOI: 10.1088/1367-2630/12/3/035011 (cit. on p. 3).
- [11] J. Knobloch, “BERLinPro – addressing the challenges of modern ERLs (a status report)”, in: *Beam Dynamics Newsletter No. 58*, ed. by W. Chou and E. Métral, vol. 58, IDFA Beam Dynamics Newsletter, Springer Berlin Heidelberg, 2012, pp. 118–131 (cit. on pp. 3, 92).

References

- [12] U. Bergmann et al., “Science and Technology of Future Light Sources: A White Paper”, tech. rep. SLAC-R-917, ANL-08/39, BNL-81895-2008, LBNL-1090E-2009, Argonne National Laboratory, Brookhaven National Laboratory, Lawrence Berkeley National Laboratory, SLAC National Accelerator Laboratory, Dec. 2008 (cit. on pp. 3, 4).
- [13] Helmholtz-Zentrum Berlin et al., “BESSY VSR Scientific Case”, tech. rep. First Version, Helmholtz-Zentrum Berlin (HZB), Apr. 2013, see also: BESSY-VSR - Workshop "The Variable pulse length Synchrotron Radiation source", 14.10. - 15.10.2013, HZB, Berlin (cit. on p. 3).
- [14] X. Huang, T. Rabedeau, and J. Safranek, “Generation of picosecond electron bunches in storage rings”, in: *Journal of Synchrotron Radiation* 21.5 (Sept. 2014), pp. 961–967, DOI: 10.1107/S1600577514010509 (cit. on p. 3).
- [15] A. Zholents et al., “Generation of subpicosecond X-ray pulses using RF orbit deflection”, in: *Nucl. Instrum. Meth.* A425 (1999), pp. 385–389, DOI: 10.1016/S0168-9002(98)01372-2 (cit. on p. 3).
- [16] A. Zholents, “A new possibility for production of sub-picosecond x-ray pulses using a time dependent radio frequency orbit deflection”, in: *Nucl.Instrum.Meth.* A798 (2015), pp. 111–116, DOI: 10.1016/j.nima.2015.07.016 (cit. on p. 3).
- [17] Y. Shoji et al., “Circulation of a Short, Intense Electron Bunch in the NewSUBARU Storage Ring”, in: *Proceedings of EPAC2006* (2006), MOPCH055, pp. 163–165 (cit. on p. 3).
- [18] A. Zholents and M. S. Zolotarev, “Femtosecond X-Ray Pulses of Synchrotron Radiation”, in: *Phys. Rev. Lett.* 76 (6 Feb. 1996), pp. 912–915, DOI: 10.1103/PhysRevLett.76.912 (cit. on p. 3).
- [19] E. Weihreter, “Status of the European HOM Damped Normal Conducting Cavity”, in: *Proceedings of EPAC2008* (2008), THXM03, pp. 2932–2936 (cit. on pp. 6, 76).
- [20] T. Atkinson et al., “Commissioning of the 50 MeV Preinjector Linac for the BESSY II Facility”, in: *Proceedings of IPAC2011* (2011), THPC108, pp. 3140–3142 (cit. on p. 4).
- [21] M. G. White, F. C. Shoemaker, and G. K. O’Neill, “A 3-Bev High Intensity Proton Synchrotron”, in: *CERN Symposium on High-Energy Accelerators and Pion Physics. Proceedings, 1st International Conference on High-Energy Accelerators, HEACC 1956, v.1-2*, 1956, pp. 525–529 (cit. on p. 4).
- [22] H. Wiedemann, “Particle Accelerator Physics; 3rd ed.” Berlin: Springer, 2007, DOI: 10.1007/978-3-540-49045-6 (cit. on pp. 6–8, 25).
- [23] Y. Cai, “Theory of Microwave Instability and Coherent Synchrotron Radiation in Electron Storage Rings”, in: *Proceedings of IPAC2011* (2011), pp. 3774–3778 (cit. on p. 8).

- [24] M. Ries, “Nonlinear Momentum Compaction and Coherent Synchrotron Radiation at the Metrology Light Source”, PhD thesis, Humboldt-Universität zu Berlin, 2014 (cit. on pp. 8, 64).
- [25] B. W. Zotter, “Potential-well bunch lengthening”, tech. rep. CERN-SPS-81-14-DI, 1981 (cit. on p. 9).
- [26] G. Wüstefeld, J. Feikes, and P. Kuske, “Towards Sub-picoseconds Electron Bunches: Upgrading Ideas for BESSY II”, in: *Proceedings of EPAC2006* (2006), MOPCH053, pp. 157–159 (cit. on p. 9).
- [27] G. Wüstefeld et al., “Simultaneous long and short electron bunches in the BESSY II storage ring”, in: *Proceedings of IPAC2011* (2011), THPC014, pp. 2936–2938 (cit. on p. 9).
- [28] A. Hofmann, “Beam instabilities”, in: *Advanced accelerator physics. Proceedings, 5th Course of the CERN Accelerator School, Rhodes, Greece, September 20-October 1, 1993. Vol. 1, 2*, CERN-95-06-V-1, 1993 (cit. on p. 13).
- [29] A. W. Chao, “Physics of Collective Beam Instabilities in High Energy Accelerators (Wiley Series in Beam Physics and Accelerator Technology)”, 1st ed., Wiley-VCH, Jan. 1993 (cit. on pp. 17, 19–21, 23, 26, 28–30, 38, 126).
- [30] K. Y. Ng, “Physics of Intensity Dependent Beam Instabilities”, World Scientific Publishing Company, Dec. 2005 (cit. on pp. 17, 19, 22, 28, 34, 38, 40, 134).
- [31] A. W. Chao, “Lecture Notes on Topics in Accelerator Physics”, tech. rep. SLAC-PUB-9574, Nov. 2002 (cit. on p. 18).
- [32] J. B. Murphy, S. Krinsky, and R. L. Gluckstern, “Longitudinal Wakefield for Synchrotron Radiation”, in: *Proceedings of PAC1995* (1995), TPQ14, pp. 2980–2982 (cit. on p. 18).
- [33] B. Riemann, A. Neumann, and T. Weis, “Alternative Approaches for HOM-Damped Cavities”, in: *Proceedings of LINAC2012* (2012), MOPB066, pp. 330–332 (cit. on pp. 19, 24, 54).
- [34] W. K. H. Panofsky and W. A. Wenzel, “Some Considerations Concerning the Transverse Deflection of Charged Particles in Radio-Frequency Fields”, in: *Review of Scientific Instruments* 27.11 (1956), p. 967, DOI: 10.1063/1.1715427 (cit. on p. 19).
- [35] S. Heifets, A. Wagner, and B. Zotter, “Generalized Impedances and Wakes in Asymmetric Structures”, tech. rep. SLAC-AP-110, Jan. 1998 (cit. on p. 20).
- [36] H. Padamsee, J. Knobloch, and T. Hays, “RF Superconductivity for Accelerators”, 2nd Edition, Weinheim: Wiley-VCH, 2008 (cit. on pp. 24, 25, 44, 47).

References

- [37] A. Vélez et al., “Hom Damping Optimization Design Studies for BESSY VSR Cavities”, in: *Proceedings of IPAC2015* (2015), WEPMA013, pp. 2774–2776 (cit. on pp. 24, 26, 27, 80, 92, 103).
- [38] S. Belomestnykh and V. Shemelin, “High-beta Cavity Design: A Tutorial”, tech. rep. SRF-060424-03, Presented at the 12th International Workshop on RF Superconductivity (SRF2005), Ithaca, NY, July 2005, Cornell University, 2006 (cit. on p. 25).
- [39] A. Velez et al., “BESSY VSR 1.5 GHz Cavity Design and Considerations on Waveguide Damping”, in: *Proceedings of LINAC2014* (2014), MOPP071, pp. 221–223 (cit. on p. 26).
- [40] K. W. Robinson, “Stability Of Beam In Radiofrequency System”, tech. rep. CEAL-1010, Feb. 1964, DOI: 10.2172/4075988 (cit. on pp. 32, 105).
- [41] S. Prabhakar, “New Diagnostics and Cures for Coupled-Bunch Instabilities”, tech. rep. SLAC-R-554, PhD thesis, Aug. 2001 (cit. on pp. 34, 64, 114).
- [42] L. Emery, “Required Cavity HOM deQing Calculated from Probability Estimates of Coupled Bunch Instabilities in the APS Ring”, in: *Proceedings of PAC1993* (1993), pp. 3360–3362 (cit. on p. 35).
- [43] L. Emery, “User’s Guide to Program `clinchor`”, tech. rep., May 2006 (cit. on p. 35).
- [44] R. Brun and F. Rademakers, “ROOT: An object oriented data analysis framework”, in: *Nucl. Instrum. Meth. A* 389 (1997), pp. 81–86, DOI: 10.1016/S0168-9002(97)00048-X (cit. on p. 35).
- [45] G. Guennebaud, B. Jacob, et al., “Eigen v3”, 2010 (cit. on p. 35).
- [46] L. D. Landau, “On the vibrations of the electronic plasma”, in: *J. Phys. (USSR)* 10 (1946), [*Zh. Eksp. Teor. Fiz.* 16, 574 (1946)], pp. 25–34 (cit. on p. 35).
- [47] O. Naumann, “Landau Damping of Longitudinal Multi-Bunch Instabilities in Electron Storage Rings”, PhD thesis, Technische Universität Berlin, 1999 (cit. on p. 35).
- [48] J. C. Bergstrom, “Jack’s Book (On Beam Instabilities and Other Things)”, tech. rep. 5.17.38.1 Rev. 2, Canadian Light Source Inc., Nov. 2006 (cit. on p. 38).
- [49] B. Zotter and F. Sacherer, “Transverse Instabilities of Relativistic Particle Beams in Accelerators and Storage Rings”, in: *Proceedings, International School Of Particle Accelerators of the 'Ettore Majorana' Center for Scientific Culture, Erice, Italy, 10-22 Nov. 1976* CERN 77-13 (1976), pp. 175–218 (cit. on p. 39).
- [50] A. Schälicke et al., “Status and Performance of Bunch-by-bunch Feedback at BESSY II and MLS”, in: *Proceedings of IPAC2014* (2014), TUPRI072, pp. 1733–1735 (cit. on pp. 40, 73, 76–78, 80, 118, 119).

- [51] R. G. Heine, “Untersuchung der Wechselwirkung intensiver Elektronenstrahlen mit höheren Resonatormoden an Delta”, PhD thesis, Universität Dortmund, 2006 (cit. on pp. 40, 72, 80).
- [52] B. C. Yunn, “A Beam Breakup Instability in a Recirculating Linac Caused by a Quadrupole Mode”, in: *Proceedings of PAC2003* (2003), RPPG033, pp. 3246–3248 (cit. on p. 40).
- [53] C. Song and G. Hoffstaetter, “Beam Breakup Simulations for the Cornell X-ray ERL”, in: *Proceedings of PAC2007* (2007), TUPMS022, pp. 1227–1229 (cit. on pp. 40, 92).
- [54] C. Song and G. H. Hoffstaetter, “Transverse Quadrupole BBU Threshold Current in the Cornell X-ray ERL”, tech. rep. Cornell-ERL-07-10, July 2007 (cit. on p. 40).
- [55] Y. Petenev, “Analysis of injection and recovery schemes for ERL based light source”, PhD thesis, Humboldt-Universität zu Berlin, 2014 (cit. on p. 40).
- [56] P. B. Wilson, “High-energy Electron Linacs: Applications to Storage Ring RF Systems and Linear Colliders”, in: *AIP Conf.Proc.* 87 (1982), pp. 450–555, DOI: 10.1063/1.33620 (cit. on p. 44).
- [57] P. B. Wilson et al., “Bunch Lengthening and Related Effects in SPEAR II”, in: *IEEE Trans. Nucl. Sci.* 24 (1977), pp. 1211–1214, DOI: 10.1109/TNS.1977.4328899 (cit. on p. 44).
- [58] T. Wangler, “RF Linear Accelerators (Wiley Series in Beam Physics and Accelerator Technology)”, 1st ed., Wiley-VCH, 1998 (cit. on p. 44).
- [59] M. Klein, “Investigation of transverse beam instabilities in the MAX IV 3 GeV ring using the multibunch code mbtrack”, Conference Website, Contribution to TWIICE2014, 2014 (cit. on pp. 45, 47, 50).
- [60] J. Byrd, “Simulation of the ALS Longitudinal Multibunch Feedback System”, in: *Proceedings of PAC1993* (1993), pp. 2349–2351 (cit. on p. 47).
- [61] M. Borland, “elegant”, Advanced Photon Source LS-287, Sept. 2000 (cit. on p. 47).
- [62] S. Khan, “Simulation of Longitudinal Coupled-Bunch Instabilities in BESSY-II”, in: *Proceedings of EPAC1998* (1998), THP15G, pp. 966–968 (cit. on p. 47).
- [63] J. M. Byrd et al., “Transient beam loading effects in harmonic rf systems for light sources”, in: *Physical Review Special Topics - Accelerators and Beams* 5 (2002), p. 092001, DOI: 10.1103/PhysRevSTAB.5.092001 (cit. on pp. 47, 109, 116).
- [64] M. Höner et al., “Investigation of Beam Instabilities at DELTA using Bunch-by-bunch Feedback Systems”, in: *Proceedings of IPAC2014* (2014), THPME104, pp. 3486–3488 (cit. on p. 47).

References

- [65] M. Höner, “Investigation of transient processes at the DELTA electron storage ring using a digital bunch-by-bunch feedback system”, PhD thesis, Technische Universität Dortmund, 2015 (cit. on pp. 47, 74).
- [66] T. Berenc and M. Borland, “Modeling RF Feedback in Elegant for Bunch-Lengthening Studies for the Advanced Photon Source Upgrade”, in: *Proceedings of IPAC2015* (2015), MOPMA006, pp. 540–542 (cit. on p. 47).
- [67] A. Neumann et al., “RF Feedback and Detuning Studies for the BESSY Variable Pulse Length Storage Ring Higher Harmonic SC Cavities”, in: *Proceedings of IPAC2015* (2015), MOPHA010, pp. 798–801 (cit. on p. 47).
- [68] A. Neumann, “Compensating microphonics in SRF cavities to ensure beam stability for future free-electron-lasers”, PhD thesis, Humboldt-Universität zu Berlin, 2008 (cit. on p. 47).
- [69] R. Nagaoka et al., “Studies of Collective Effects in SOLEIL and Diamond Using the Multiparticle Tracking Codes sbtrack and mbtrack”, in: *Proceedings of PAC09* (2009), FR5RFP046, pp. 4637–4639 (cit. on pp. 49, 50).
- [70] M. Ruprecht et al., “Analysis of Coupled Bunch Instabilities in BESSY-VSR”, in: *Proceedings of IPAC2014* (2014), TUPRI043, pp. 1659–1661 (cit. on pp. 50, 80, 86–88).
- [71] M. Ruprecht et al., “Influence of Transient Beam Loading on the Longitudinal Beam Dynamics at BESSY VSR”, in: *Proceedings of IPAC2015* (2015), MOPWA022, pp. 141–143 (cit. on pp. 50, 116, 127).
- [72] M. Klein and R. Nagaoka, “Multibunch Tracking Code Development to Account for Passive Landau Cavities”, in: *Proceedings of IPAC2013* (2013), MOPWO003, pp. 885–887 (cit. on p. 50).
- [73] D. Sagan, “Bmad: A relativistic charged particle simulation library”, in: *Nucl. Instrum. Meth. A* 558 (2006), pp. 356–359, DOI: 10.1016/j.nima.2005.11.001 (cit. on p. 51).
- [74] M. Lonza, “Multi-bunch feedback systems”, in: *CAS - CERN Accelerator School: Course on Beam Diagnostics, Dourdan, France, 28 May - 6 Jun 2008*, CERN-2009-005, 2009, pp. 467–511 (cit. on pp. 59, 62, 63).
- [75] A. Schällicke, F. Falkenstern, and R. Müller, “Bunch-by-Bunch Feedback and Diagnostics at BESSY II”, in: *Proceedings of IBIC2013* (2013), TUPC16, pp. 399–402 (cit. on pp. 59, 60).
- [76] Dimtel, Inc., “iGp12”, San Jose, CA, United States, 2013 (cit. on pp. 59, 60, 64).
- [77] Dimtel, Inc., “BPMH-20-2G”, San Jose, CA, United States, 2012 (cit. on p. 59).
- [78] Dimtel, Inc., “FBE-500LT”, San Jose, CA, United States, 2011 (cit. on p. 60).

- [79] T. Knuth et al., “Longitudinal and Transverse Feedback Kickers for the BESSY II Storage Ring”, in: *Proceedings of PAC1999* (1999), TUA33, pp. 1147–1149 (cit. on p. 60).
- [80] S. Prabhakar et al., “Phase space tracking of coupled bunch instabilities”, in: *Phys. Rev. ST Accel. Beams* 2 (1999), p. 084401, DOI: 10.1103/PhysRevSTAB.2.084401 (cit. on p. 64).
- [81] The MathWorks, Inc., “MATLAB”, Natick, MA, United States, 2015 (cit. on p. 64).
- [82] F. Pérez and B. E. Granger, “IPython: a System for Interactive Scientific Computing”, in: *Computing in Science and Engineering* 9.3 (May 2007), pp. 21–29, DOI: 10.1109/MCSE.2007.53 (cit. on p. 65).
- [83] C. Pasotti et al., “Coupled Bunch Modes Measurement System at ELETTRA”, in: *Proceedings of PAC1998* (1998), THP03E, pp. 990–992 (cit. on p. 72).
- [84] National Instruments Corporation, “LabVIEW”, Austin, TX, United States, 2015 (cit. on p. 72).
- [85] D. Teytelman, “Architectures and Algorithms for Control and Diagnostics of Coupled-Bunch Instabilities in Circular Accelerators”, tech. rep. SLAC-R-633, PhD thesis, June 2003 (cit. on p. 75).
- [86] F. Marhauser et al., “Impedances in Slotted-Pipe Kicker Magnets”, in: *Proceedings of EPAC2006* (2006), WEPLS115, pp. 2649–2651 (cit. on p. 76).
- [87] F. Marhauser and E. Weihreter, “Impedance Measurements of the HOM-Damped 500 MHz Metrology Light Source Cavity”, tech. rep. bessy-034-january-2007, BESSY GmbH, Jan. 8, 2007 (cit. on p. 76).
- [88] J. Byrd, “Study of Coupled-Bunch Collective Effects in the PEP-II B-Factor”, in: *Proceedings of PAC1993* (1993), pp. 3315–3317 (cit. on p. 80).
- [89] F. Marhauser et al., “HOM Damped 500 MHz Cavity Design for 3rd Generation SR Sources”, in: *Proceedings of PAC2001* (2001), MPPH033, pp. 846–848 (cit. on p. 80).
- [90] R. Heine, P. Hartmann, and T. Weis, “Characterisation of the EU-HOM-damped Normal Conducting 500 MHz Cavity from the Beam Power Spectrum at DELTA”, in: *Proceedings of EPAC2006* (2006), THPCH035, pp. 2856–2858 (cit. on p. 80).
- [91] M. Ruprecht et al., “Single Particle Tracking for Simultaneous Long and Short Electron Bunches in the BESSY II Storage Ring”, in: *Proceedings of IPAC2013* (2013), WEOAB101, pp. 2038–2040 (cit. on pp. 80, 106).
- [92] F. Marhauser, “JLab High Current Cryomodule Development”, Conference Website, WG307, 2009 (cit. on pp. 80, 92, 103).
- [93] R. A. Rimmer et al., “Recent Progress on High-Current SRF Cavities at JLab”, in: *Proceedings of IPAC2010* (2010), WEPEC076, pp. 3052–3054 (cit. on p. 80).

References

- [94] J. Heller, “Solving Maxwell’s equations for complex structures using the State Space Concatenation Scheme”, KOSEI Verbundforschungstreffen, Dortmund, July 22, 2015 (cit. on pp. 85, 86).
- [95] N. R. Valles, “Pushing the Frontiers of Superconducting Radio Frequency Science: From the Temperature Dependence of the Superheating Field of Niobium to Higher-Order Mode Damping in Very High Quality Factor Accelerating Structures”, PhD thesis, Cornell University, 2014 (cit. on p. 86).
- [96] G. H. Hoffstaetter and I. V. Bazarov, “Beam-breakup instability theory for energy recovery linacs”, in: *Phys. Rev. ST Accel. Beams* 7 (2004), p. 054401, DOI: 10.1103/PhysRevSTAB.7.054401 (cit. on p. 86).
- [97] I. Bazarov and G. Hoffstaetter, “Multi-pass Beam-breakup: Theory and Calculation”, in: *Proceedings of EPAC2004* (2004), WEPLT153, pp. 2197–2199 (cit. on p. 86).
- [98] N. Valles, D. Klein, and M. Liepe, “Beam Break Up Studies for Cornell’s Energy Recovery Linac”, in: *Proceedings of SRF2011* (2011), MOPO056, pp. 229–231 (cit. on p. 86).
- [99] B. Riemann, “Status of the design and HOM calculations for the BERLinPro main linac cavity”, Conference Website, Contribution to HOMSC12, 2012 (cit. on p. 92).
- [100] G. H. Hoffstaetter, S. M. Gruner, and M. Tigner, eds., “Cornell ERL: Project Definition Design Report (PDDR)”, Cornell University, June 13, 2013 (cit. on p. 92).
- [101] S. Prabhakar, J. D. Fox, and D. Teytelman, “New Diagnostics and Cures for Coupled-Bunch Instabilities”, in: *Proceedings of PAC2001* (2001), WOAA002, pp. 300–304 (cit. on pp. 95, 102).
- [102] M. Wang, P. Chou, and A. Chao, “Study of uneven fills to cure the coupled-bunch instability in SRRC”, in: *Proceedings of PAC2001* 3 (2001), pp. 1981–1983 (cit. on pp. 102, 104).
- [103] P. Goslawski et al., “The Low-alpha Lattice and Bunch Length Limits at BESSY-VSR”, in: *Proceedings of IPAC2014* (2014), MOPRO058, pp. 216–218 (cit. on p. 105).
- [104] A. Mosnier, F. Orsini, and B. Phung, “Analysis of the Heavily Beam-loaded SOLEIL RF System”, in: *Proceedings of EPAC1998* (1998), WEP28G, pp. 1720–1722 (cit. on p. 105).
- [105] M. Abo-Bakr et al., “The BESSY II Booster Synchrotron”, in: *Proceedings of EPAC1996* (1996), TUP007G, pp. 527–529 (cit. on p. 107).
- [106] A. Jankowiak et al., “Manufacturing and Testing of 2.45 GHz and 4.90 GHz Bipariodic Accelerating Structures for MAMI C”, in: *Proceedings of EPAC2006* (2006), TUPCH118, pp. 1292–1294 (cit. on p. 106).

- [107] A. Neumann, Private Communication, Helmholtz-Zentrum Berlin (HZB), Mar. 31, 2015 (cit. on p. 106).
- [108] S. De Santis, J. M. Byrd, and R. Bartolini, “Transient Beam Loading in the DIAMOND Storage Ring”, in: *Proceedings of EPAC2006* (2006), THPCH066, pp. 2937–2939 (cit. on p. 109).
- [109] S. Prabhakar et al., “Calculation of Impedance from Multibunch Synchronous Phases: Theory and Experimental Results”, in: *Proceedings of EPAC1998* (1998), THP33C, pp. 996–998 (cit. on p. 114).
- [110] W. Anders and P. Kuske, “HOM Damped NC Passive Harmonic Cavities at BESSY”, in: *Proceedings of PAC2003* (2003), TPAB004, pp. 1186–1188 (cit. on pp. 116–118, 139).
- [111] A. Piwinski, “The Touschek effect in strong focusing storage rings”, tech. rep. DESY-98-179, 1998 (cit. on p. 124).
- [112] P. Goslawski, Private Communication, Helmholtz-Zentrum Berlin (HZB), Apr. 20, 2015 (cit. on p. 126).
- [113] P. Goslawski, “Bunch separation with resonant island buckets for BESSY VSR”, Conference Website, ESLS XXII Workshop, Nov. 2014 (cit. on pp. 126, 137).
- [114] M. Ries et al., “Transverse Resonance Island Buckets at the MLS and BESSY II”, in: *Proceedings of IPAC2015* (2015), MOPWA021, pp. 138–140 (cit. on pp. 126, 137).
- [115] A. Neumann, Private Communication, Helmholtz-Zentrum Berlin (HZB), June 13, 2014 (cit. on p. 137).
- [116] S. Posen and M. Liepe, “Mechanical optimization of superconducting cavities in continuous wave operation”, in: *Phys. Rev. ST Accel. Beams* 15 (2012), p. 022002, DOI: 10.1103/PhysRevSTAB.15.022002 (cit. on p. 138).
- [117] P. Goslawski, Private Communication, Helmholtz-Zentrum Berlin (HZB), Apr. 23, 2015 (cit. on p. 138).

Acknowledgment

First, I would like to thank Prof. Dr. Andreas Jankowiak for the opportunity to work in his group, the supervision of my thesis and the support throughout my doctoral studies. I further thank Prof. Dr. Thomas Weis for his support since the beginning my doctoral studies and Prof. Dr. Jens Knobloch and Prof. Dr. Riccardo Bartolini for discussions and reviewing this thesis.

I am especially grateful to Dr. Godehard Wüstefeld, who has closely guided me from the beginning, taught me many aspects of accelerator physics and answered an innumerable amount of questions.

In addition, I would like to thank my coworkers, Dr. Markus Ries, Dr. Paul Goslawski, for their discussions, support with experiments and feedback on this thesis.

I am grateful to Dr. Jörg Feikes, Dipl. Phys. Tobias Tydecks and Dr. Ji Li for discussions and especially for their support during experiments at the MLS.

Furthermore, I thank Dr. Andreas Schälicke, Dr. Peter Kuske and Dr. Roland Müller for discussions, joint feedback studies and help with experiments at BESSY II.

Moreover, I am grateful to Dr. Axel Neumann and Dr. Adolfo Vélez for numerous discussions and contributions regarding cavities, RF and control theory.

I also thank Prof. Dr. Aleksandr Matveenko for his lecture on collective effects and further discussions.

I would like to express my gratitude to Dr. Ryutaro Nagaoka (SOLEIL) for the opportunity to visit his group, and together with Dr. Marit Klein for the rewarding discussions on challenging topics.

I further thank the group of Prof. Dr. van Rienen at Universität Rostock, the group of Prof. Dr. Thomas Weis at Technische Universität Dortmund, and other colleagues at the HZB, at other institutes around the world and friends who have helped me to complete this thesis.

Selbständigkeitserklärung

Ich erkläre, dass ich die vorliegende Arbeit selbständig und nur unter Verwendung der angegebenen Literatur und Hilfsmittel angefertigt habe.

Berlin, den 25. September 2015

Martin Ruprecht